

**OBSERVATION AND MODELLING OF FLUID TRANSPORT INTO  
POROUS PAPER COATING STRUCTURES**

by

**JOACHIM SCHOELKOPF**

A thesis submitted to the University of Plymouth  
in partial fulfilment for the degree of

**DOCTOR OF PHILOSOPHY**

Department of Environmental Sciences  
Faculty of Science

In collaboration with Omya AG, Oftringen, Switzerland

**July 2002**

# **Abstract**

**by**

**Joachim Schoelkopf**

## **Observation and modelling of fluid transport into porous paper coating structures**

In paper printing, one of the most important aspects for consideration is the control of ink setting rate. Ink setting, depending on ink and press type, is a function of evaporation, curing and removal of the liquid phase by capillary mechanisms steered by the porous substrate. In most cases, absorption by the substrate is the dominating mechanism. Many paper or board substrates are coated with a layer of pigment particles and binders. It is recognised that the void network between these particles has the most important influence on the absorption dynamics.

Many aspects of liquid absorption into porous networks are poorly understood. It is shown that it is necessary to characterise both the pore-level structure and the permeability of the network simultaneously.

To remove indeterminate effects caused by the usually uneven thin layers of coatings adopted in practice, a novel methodology was developed in this work comprising of a range of unique techniques such as the formation of porous tablet-like blocks of  $\text{CaCO}_3$ . By applying variable compression forces to a compact of fine-ground mineral, a wide range of usable porosities were obtained whilst keeping the surface chemistry and skeletal-defined pore geometry constant. The samples were characterised using mercury porosimetry. The methodology included techniques to study interactions of the structures with industrially and environmentally relevant liquids. An Ink-Surface Interaction Tester (ISIT) was used to analyse ink setting behaviour as a dynamic measure of ink rheology and solids content. This device was modified to provide a measure of the time-dependent extensional strain that is applied to the ink layer in addition to the normally obtained ink tack force values.

The importance of the inertial flow regime beyond that of pure viscous flow and its impact in an interconnected network structure, where liquid does not imbibe continuously in a steady laminar flow behaviour at the wetting front, are demonstrated. Mechanisms are proposed which account for the uneven wetting line and its action in leaving parts of the pore network unfilled. Along with other findings, deviations from Lucas-Washburn (LW) scaling are elucidated. These findings are discussed in the context of paper printing and give direction for developing beyond the current limits encountered using environmentally friendly minerals and ink constituents.

# List of contents

Copyright statement .....	i
Title page .....	ii
Abstract .....	iii
List of Contents .....	iv
List of Figures .....	viii
List of Tables .....	xiii
List of Equations .....	xiv
Acknowledgements .....	xvi
Author's declaration .....	xvii
1 Introduction .....	1
1.1 Hypotheses .....	1
1.2 Background summary .....	1
2 Theory, application and literature review .....	8
2.1 Paper technology background .....	8
2.1.1 Brief history of papermaking .....	8
2.1.1.1 Pigments in paper manufacturing .....	9
2.1.2 Characteristics of Calcium Carbonate ( $\text{CaCO}_3$ ) .....	11
2.1.3 Particle size: its importance, definition and production control .....	13
2.1.4 Coating application to the paper .....	14
2.1.5 Investigation of coating structure .....	14
2.1.5.1 Paper specific permeation/imbibition approaches .....	16
2.1.6 Printing of coated paper .....	19
2.1.6.1 Ink constitution .....	21
2.1.6.2 Three basic post-print mechanisms .....	22
2.1.6.3 Tack reflects the rheological characteristics of ink during application .....	24
2.2 Environmental situation for print media .....	25
2.2.1 Fibre versus pigment .....	25
2.2.2 Low and high waste pigments .....	25
2.2.3 Calcium carbonate ( $\text{CaCO}_3$ ) .....	26
2.2.4 New concepts in printing processes and ink formulations .....	26
2.2.4.1 Offset-inks: mineral versus vegetable oils and derivatives .....	27
2.2.5 Waterborne inks .....	29
2.2.5.1 Flexographic printing .....	29
2.2.5.2 Ink-jet .....	29
2.3 Interfacial theory .....	31
2.3.1 The nature of surface free energy .....	32
2.3.2 Dispersive and polar components of surface free energy .....	33
2.3.3 Liquids .....	34
2.3.4 Solids .....	35
2.3.4.1 The surface tension of crystallite particles .....	36
2.3.4.2 Calcium carbonate ( $\text{CaCO}_3$ ) .....	36
2.3.5 Phase interactions .....	38
2.3.6 Influence of surface micro-topography .....	40
2.3.7 Contact angle measurement .....	41
2.3.7.1 Measuring small contact angles .....	43
2.3.7.2 Contact angle during imbibition .....	43
2.3.7.3 Practical relation to the problem of measuring contact angle on compressed powders .....	44
2.3.8 Absorption – wetting, a glossary .....	45
2.3.9 Dynamic wetting .....	48
2.3.9.1 Applied surface wetting and spreading .....	49
2.3.9.2 Capillary imbibition .....	51
2.3.10 A chronology of imbibition science .....	54
2.3.11 Summary of proposed single capillary phenomena .....	57
2.3.12 Further observations made in simple capillary experiments .....	58
2.3.13 Complex single capillary shapes .....	60
2.3.14 The Lucas-Washburn equation .....	62
2.3.15 Inertia and the Bosanquet equation .....	63
2.3.16 Dimensionless numbers in fluid dynamics .....	64
2.3.17 Droplets, films – finite liquid systems .....	65
2.4 Porous media .....	67
2.4.1 Characterisation of porous media .....	68

2.4.1.1	Modelling approaches to visualise pore shapes.....	71
2.5	Transport processes in porous media.....	73
2.5.1	Diffusion, vapour adsorption and film flow.....	73
2.5.2	Transitions in film flow – meniscus movement.....	74
2.5.3	Imbibition into porous media.....	75
2.5.3.1	Transplanar imbibition, EMCO device.....	76
2.5.3.2	Planar wicking.....	77
2.5.3.3	Imbibition into an unconsolidated particle framework.....	79
2.5.3.4	Imbibition into consolidated porous media.....	80
2.5.3.5	Experimental approaches combining imbibition with independent pore size evaluation.....	81
2.5.3.6	Micro-model observations.....	82
2.5.4	Permeation.....	83
2.6	Pore-network models and simulators.....	83
2.6.1	The computer network simulator used in this work.....	84
2.6.1.1	The unit cell.....	84
3	Experimental techniques.....	87
3.1	Confocal laser scanning microscopy (CLSM).....	87
3.2	Surface tensiometry.....	89
3.3	Contact angle measurements.....	90
3.4	Mercury porosimetry.....	92
3.5	Rheology.....	92
3.5.1	Viscoelasticity measurements.....	92
3.5.2	Interpretation of stress sweep measurements.....	94
3.5.2.1	Elastic or storage Modulus $G'$ .....	94
3.5.2.2	Viscous or loss Modulus $G''$ .....	95
3.5.2.3	Phase angle $\delta$ .....	95
3.6	ISIT Ink Surface Interaction Tester.....	95
3.6.1	Interpretation of the tack curves.....	97
4	Preparation and characterisation of porous pigment samples.....	100
4.1	Introduction.....	100
4.1.1	Why do compressed particles stick together ?.....	101
4.1.2	Evaluation of method.....	101
4.2	Materials.....	102
4.3	Development of compaction method and devices.....	103
4.4	Sample preparation for imbibition experiments.....	108
4.5	Characterisation of the formed structures.....	109
4.6	Approaches to visualise pore geometry.....	109
4.7	Observation of macroscopic inter- particular imbibition.....	113
5	Advances in modelling imbibition.....	115
5.1	Analysis of volume absorption rates.....	115
5.2	Looking for an imbibition equation ( <i>Schoelkopf, Gane, et al. 2000</i> ).....	118
5.2.1	Simplistic assumptions in the approach.....	118
5.2.2	Liquid inertia as a factor in flow mechanisms.....	118
5.2.3	Comparing the Bosanquet and LW equations for a simple bundle of capillaries.....	119
5.2.4	Reynolds numbers during imbibition.....	125
5.3	The next step to realism – the network model.....	127
5.3.1	The wetting algorithm.....	128
5.3.2	Limitation of imbibition model compared to reality.....	130
5.3.3	The permeability algorithm ( <i>Matthews et al., 1993</i> ).....	131
5.4	Transition to experiment.....	132
6	Equilibrium distributions of imbibed droplets ( <i>Gane, Schoelkopf, et al. 2000</i> ).....	134
6.1	Introduction.....	134
6.1.1	Spreading and absorption mechanisms.....	135
6.2	Method development.....	136
6.2.1	Selecting a suitable dye.....	136
6.2.2	Findings.....	138
6.2.3	Droplet application method.....	139
6.2.3.1	Obtaining a smooth surface and uniform spread.....	140
6.3	Sample structures.....	142
6.4	Observations and results.....	142
6.4.1	Discussion.....	145
6.4.2	Intermediate conclusions.....	146
6.5	Modelling applications to droplet observations.....	147
6.6	Regimes of absorption.....	148
6.6.1	By-pass effect.....	148

6.6.2	Film flow phenomena .....	149
6.6.3	Laplace competition.....	149
6.6.4	Inertial flow.....	149
6.6.5	Discussion of the results in correlation with pore networks.....	150
6.6.6	Implications.....	153
7	Equilibrium distributions of imbibed supersource liquids ( <i>Gane, Schoelkopf, et al. 2000</i> ).....	156
7.1	Introduction.....	156
7.2	Liquids .....	156
7.3	Sample structures .....	158
7.4	Method.....	158
7.5	Results and discussion.....	160
7.6	Visualisation of the imbibing liquid front on the sample-scale.....	161
7.7	Conclusions.....	163
8	Equilibrium pressure-driven flow of liquid through saturated samples .....	164
8.1	Introduction.....	164
8.2	Experimental method development.....	165
8.2.1	Calculation of necessary pressures.....	165
8.2.2	Construction of the pressure cell.....	166
8.2.3	Method optimising .....	167
8.2.4	Embedding materials and sample preparation method.....	167
8.2.4.1	Sample structures .....	168
8.3	Results and discussion.....	168
8.3.1	Theory of entrapped bubbles.....	172
8.3.2	Comparison of experimental and modelled permeabilities .....	173
8.4	Conclusions.....	174
9	Dynamic behaviour of imbibing supersource liquids.....	176
9.1	Introduction.....	176
9.2	Materials .....	177
9.2.1	Preparation of the porous samples.....	177
9.2.2	Calcite crystal surface .....	178
9.2.3	Characterisation by mercury porosimetry .....	179
9.2.4	Liquids .....	180
9.3	Experimental method development.....	181
9.3.1	Wetting apparatus.....	181
9.3.2	Imbibition data treatment .....	182
9.4	Experimental imbibition of apolar liquid into samples of different porosities ( <i>Schoelkopf, Gane, et al. 2002</i> ).....	185
9.4.1	Imbibition into samples of different porosities and the same skeletal size distributions.....	185
9.4.1.1	Sample structures .....	185
9.4.2	Results and discussion.....	186
9.4.3	Imbibition into samples of different porosities and different skeletal size distributions.....	190
9.4.3.1	Sample structures .....	190
9.4.4	Conclusions with regard to apolar liquid imbibition .....	194
9.5	Imbibition of a mineral/vegetable oil mixture.....	194
9.6	Experimental imbibition of a polar liquid ( <i>Schoelkopf, Ridgway, et al. 2000</i> ) .....	195
9.6.1.1	Sample structures .....	196
9.7	Results, discussion and comparison to modelling.....	197
9.7.1	Sensitivity analysis.....	200
9.7.2	Effective hydraulic radius ( $r_{ehc}$ ) approximation .....	202
9.7.3	Comparability of modelled and experimental processes .....	203
9.7.4	Comparison between both the simulated and experimental imbibition, and the effective hydraulic radius prediction.....	205
9.7.5	Intermediate conclusions.....	206
9.8	Experimental imbibition of different polar liquids ( <i>Ridgway, Schoelkopf, et al. 2001</i> ).....	207
9.8.1	Comparing cylindrical and convergent computer network simulator throat geometries with experiment.....	209
9.8.1.1	Comparison between simulations and experiment .....	209
9.8.1.2	Summary of simulation and comparison.....	213
9.9	Application to previous experiments with apolar oil .....	214
9.10	Overall comparison of hydraulic radii "ehc" and uptake gradients.....	215
9.11	Conclusions from dynamic supersource imbibition.....	218
9.12	Absorptive removal of oil from an offset ink ( <i>Schoelkopf, Gane, et al. 2001</i> ) .....	220
9.12.1	Sample structures .....	220
9.12.2	Ink vehicle removal under supersource conditions .....	220

10	Extension to a complex system – dynamic behaviour of ink on coated paper ( <i>Gane, Schoelkopf, et al. 2000</i> ).....	225
10.1	Introduction.....	225
10.2	Materials and methods.....	226
10.3	Rheological study of oil "loss" from ink.....	226
10.4	A new approach using the ISIT force-time integral.....	229
10.4.1	The tack force development of an ink film on a substrate.....	229
10.4.2	Relevant parameters for the ink film separation.....	231
10.4.3	Tack measurements on non-absorbent substrates.....	232
10.4.4	Tack measurements on paper.....	234
10.4.5	Invoking the filtercake model.....	236
10.4.6	Using an extensional model.....	240
10.4.7	The ink rheology as it sets – obtaining the solids content as a function of time on the paper.....	242
10.4.8	Conclusions.....	244
10.5	Comparing LW and the tack-based absorption equation.....	244
10.5.1	Conclusions of the tack-based absorption prediction compared with the gravimetric approach.....	250
10.6	Conclusions: offset ink imbibition.....	250
10.7	Development of a laser-based strain sensor for ISIT.....	252
10.8	Devices.....	254
10.9	Measurement procedure.....	256
10.10	Results and discussion.....	258
10.11	Summary and conclusions ISIT strain measurements.....	260
11	Conclusions.....	261
11.1	Environmental.....	261
11.2	Scientific.....	261
11.3	Paper technology.....	264
11.4	Summary.....	265
11.5	Future work.....	268
	List of used symbols and abbreviations.....	270
Appendix A	Tables.....	272
Appendix B	Fitting equations.....	283
Appendix C	Compilation of footnotes.....	285
Appendix D	Miscellaneous.....	286
	References.....	287

## List of figures

Fig. 1	Structural overview of the thesis.....	5
Fig. 2	Conceptual schematic overview.....	6
Fig. 3	Commonly found forms of synthetically precipitated CaCO <sub>3</sub> : (a) rhombohedral calcite, (b) prismatic, (c) scalenohedral, (d) clustered aragonite, (e) aragonite, (f) agglomerated aragonite, (images taken from Gane, 2001).....	12
Fig. 4	(a-c) "crystal rebuild" CaCO <sub>3</sub> , (d,e) amorphous CaCO <sub>3</sub> , vaterite type, (d) containing also calcite needles, (f) V40, commercial co-structured pigment, talcum platelets with CaCO <sub>3</sub> particle coating. ..	12
Fig. 5	Double coated paper viewed in cross-section. A fine pigment layer on top gives gloss, the coarser precoat acts as a levelling and functional "primer". Below, the base sheet consisting of fibres and filler-pigments can be identified. ....	15
Fig. 6	An enlargement of Fig. 5. ....	15
Fig. 7	Stochastic print screen as used in modern sheet fed offset (a skin tone).....	20
Fig. 8	The filtercake model described by ( <i>Xiang and Bousfield, 1998</i> ) (for a detailed discussion and explanation of the parameters see section 10.4.1).....	24
Fig. 9	A layer of superabsorbent gel. (It remains unclear if the microcracks are an artefact of the electron beam or if they are a functional component of the layer).....	30
Fig. 10	A pigmented ink-jet coating layer.....	31
Fig. 11	Influence of different phase interactions (L = liquid, S = solid) and their effect on contact angle. ....	34
Fig. 12	The crystal structure of calcite. This schematic diagram shows both (left) the true unit cell, the acute rhombohedron, which contains 2[CaCO <sub>3</sub> ] and (right) an alternative cell based on the cleavage rhombohedron ( <i>Gane, 2001</i> ).....	37
Fig. 13	Balance of tensions acting on a sessile drop as viewed in cross-section.....	39
Fig. 14	Lotus effect on Lupin ( <i>Lupinus polyphyllus</i> ) in the author's garden.....	41
Fig. 15	The geometric schematic of a meniscus in a tube ( $r_c$ is the capillary radius and $r_m$ the radius of the meniscus curvature). ....	52
Fig. 16	Imbibition stopper $\alpha + \theta = 90^\circ$ , the radius of curvature of the meniscus is infinite. ....	53
Fig. 17	Comparisons of solutions to the equations of Szekely, Sorbie, Bosanquet and Washburn for water and capillaries of 10 $\mu\text{m}$ and 100 $\mu\text{m}$ , (taken from <i>Ridgway et al., 2001</i> ).....	57
Fig. 18	Schematic overview of influences on meniscus-driven imbibition from a reservoir (left) into an evacuated capillary tube.....	58
Fig. 19	Equilibrium edge of a drop of glycerol (dark image) on a naturally smooth surface of calcite. More details see Fig. 20.....	65
Fig. 20	CLSM (Confocal Laser Scanning Microscope) picture of the edge of a drop of glycerol placed on a roughened surface of calcite. Wicking in and through the surface roughness causes the drop to spread. Left: 20 s after drop application, right: 120 s. Scale bar for all images is approx. 150 $\mu\text{m}$ .....	66
Fig. 21	Examples of (a) a permeable automotive-foam: polymer, filled with CaCO <sub>3</sub> , SEM Picture, scale bar is 2000 $\mu\text{m}$ , (b) polished section of wood (probably <i>Libocedrus decurrens</i> ) from a pencil with parallel capillary pores, CLSM reflection picture, scale bar is 50 $\mu\text{m}$ . ....	67
Fig. 22	Synteape cross-sectional view of the internal laminate structure, showing a strongly anisotropic porosity, no transplanar permeability.....	69
Fig. 23	Schematic of some different morphological properties: (1) closed pores, no permeability and zero connectivity, (2) strongly anisotropic structure, permeable only in x,y plane, (3) unidirectional capillaries, connectivity $\approx 2$ but no tortuosity, (4) same as (3) but different number average $d_{50}$ pore diameter despite similar porosity, (5) no connectivity but high tortuosity, (6) small connectivity with high tortuosity, permeability is strongly non isotropic (7) showing features of distinct pores and throats, multimodal pore size distribution, monomodal throat size distribution, low connectivity, high tortuosity, reduced permeability, (8) distinct pores and throats, multi-modal pore and throat size distributions, high connectivity, medium tortuosity, high permeability.....	70
Fig. 24	Cubic packing (a), its pore space (b), an individual pore with throats (c) and the connection graph (d). In arbitrary units, the particle radius is 1.1 and interparticle centre-centre separation 2.0. ( <i>Toivakka and Nyfors, 2001</i> ).....	72

Fig. 25	Hexagonal close packing (a), its pore space (b) and the two different types of pores (c). Particle radius is 1.1 and closest neighbour centre-centre separation 2.0, given in arbitrary units, ( <i>Toivakka and Nyfors, 2001</i> ).....	72
Fig. 26.	Examples of pores from particle packing. Co-ordination number is 4 in (a) and 9 in (b). Three views from each pore are shown, ( <i>Toivakka and Nyfors, 2001</i> ).....	72
Fig. 27	Schematics of the mechanisms ranging from diffusion to capillarity, (skeletal particles are shown in blue, liquid and liquid vapour in yellow).....	73
Fig. 28	A simple experiment showing at the same time: (1) liquid film (dyed squalane) flowing in a glass pipette, (2) unstable regime, a bulge forms, (3) the necking process, two menisci have just formed, (4) an isolated slug of liquid.....	74
Fig. 29	Mechanisms between film flow and meniscus movement: (1a-3a) standard condition, (1b-2b) as described by Bernadiner ( <i>Bernadiner, 1998</i> ), (3b) as described by Fisher and Lark ( <i>Fisher and Lark, 1979</i> ), (1c, 2c, 3c and 1d) author's observations in simple capillary tube, (2d) the important consequence of (3b and 1d). (Blue arrows indicate direction of interface motion, white arrows direction of liquid flow).....	75
Fig. 30	CLSM schematic.....	88
Fig. 31	CLSM topographic image from a resin cast of CaCO <sub>3</sub> tablet.....	89
Fig. 32	Ring measurement schematic, showing for simplicity a cross-section of the ring. In light blue is the hydrostatic liquid volume needing correction. The arrows show the direction of force vectors acting at maximum measured pull force.....	90
Fig. 33	Calcite crystal used for contact angle measurements prior to surface grinding. (Note the birefringence).....	91
Fig. 34	Some thumbnails from the drop images.....	91
Fig. 35	Principle of oscillation measurements.....	93
Fig. 36	IGT Inking unit, shown without applied ink. On the right hand side the rubber distribution rolls are in place and the print wheel is on top.....	96
Fig. 37	Ink surface interaction tester ISIT (SeGan™).....	97
Fig. 38	Schematical tack curve graph with regimes I, II and III.....	98
Fig. 39	Test strips indicating pull-offs and the observation of adhesion via the retained print density under the pull-off. Test start at the bottom of each strip, the footprint area is highlighted (arrow).....	99
Fig. 40	Particle size distributions of the coarse and fine CaCO <sub>3</sub> powders used for consolidation of porous tablets expressed as cumulative mass % less than an equivalent Stokesian diameter.....	103
Fig. 41	Schematic cross-section of the die showing the plastic lining and cellulose membrane.....	104
Fig. 42	Development of dies from left to right. (i) The first prototype, found to be too heavy and steel quality too soft, the design also omitted any end-butted screws to help push the two sections apart. (ii) Improved lighter version but wore out after the production of ≈ 200 tablets. (iii) Die with a smaller piston diameter to achieve higher pressures, dimensions did not withstand the high pressure and deformed.....	104
Fig. 43	The present die design. In front left the die with improved dividing mechanism, front right the piston, behind it the template as an option to push the formed tablet out by the press. Little image top left, top-view of the improved dividing slit.....	105
Fig. 44	Custom-made hydraulic press for tablet compaction. On the bottom is shown the hydraulic unit, top right the electronic steering unit and the press-frame with the hydraulic cylinder exerting a force up to 600 kN.....	106
Fig. 45	SEM image of tablet surface.....	107
Fig. 46	Automated grinding machine (Jean Wirtz, Phoenix 4000). On the disc at the back are the custom-made grinding jigs. Front left: sample embedded in resin for permeability measurement, middle: half of a pigment tablet, right: sample ground to finished dimensions ready for the imbibition experiment.....	108
Fig. 47	Achieved porosities as a function of applied compaction pressure for the coarse CaCO <sub>3</sub> .....	109
Fig. 48	Back-scattered electron image of embedded pigment structure.....	111
Fig. 49	Particulate porous tablet formed with Inducarb V, a coarse calcite filler for plaster. Black resin is imbibed into voids showing the pore shapes in cross-section after grinding and polishing.....	112



Fig. 50	Particulate porous tablet formed with sea-sand. Black resin imbibed into the voids shows the pore shapes in cross-section. ....	112
Fig. 51	Dyed linseed oil wetting front imbibing into a coarse quartz particle layer.....	113
Fig. 52	Comparison of inertial and viscous equations and Bosanquet's solution for propandiol. The plot shows the length of the fluid column, $x$ , in a capillary with a diameter as shown in legend, after time, $t$ . ....	120
Fig. 53	Regions of behaviour of inertial and viscous dominated flow for 1,3-propandiol. The plot also shows the distribution of imbibition lengths for the array of throat diameters used in the modelling by the pore-level simulation in 9.7.....	121
Fig. 54	Methyleniodide absorption length into a distribution of capillary sizes as described using the LW equation.....	121
Fig. 55	Methyleniodide absorption length into a distribution of capillary sizes as described using the Bosanquet relation.....	122
Fig. 56	Nonane absorption length into a distribution of capillary sizes as defined by the LW equation.....	123
Fig. 57	Nonane absorption length into a distribution of capillary sizes as defined by the Bosanquet equation. ....	123
Fig. 58	Nonane wetting front velocity entering an array of capillary sizes depicted by the LW relation. ....	123
Fig. 59	Nonane wetting front velocity entering an array of capillary sizes calculated from the Bosanquet equation.....	124
Fig. 60	Volume absorption distribution in capillaries defined under LW for nonane. ....	124
Fig. 61	Volume absorption distribution in capillaries as defined by the Bosanquet equation for nonane. Note the kink from the viscous regime on the left hand side to the retarded one on the right. ....	125
Fig. 62	The Reynolds number during viscous imbibition as function of the travelled distance by the liquid front, $x$ , in a range of capillaries of radius parameter $r$ . ....	126
Fig. 63	Reynolds number over a range of viscosities and pore radii at an assumed liquid density of $855 \text{ kgm}^{-3}$ . ....	127
Fig. 64	Artefact of artificially regular unit cell structure and the iterative way of stepping through the algorithm computing the flow rate through the unit cell in respect to the repeat boundary condition of its nearest neighbours.....	129
Fig. 65	The right ratio of surface spreading/bulk imbibition is important for ink-jet printing. The picture on the right shows insufficient spread, resulting in bad colour coverage.....	134
Fig. 66	Some of the dried dyed droplets seen as stains on the compressed pigment block.....	136
Fig. 67	Cross-sectional grinding through a tablet after a chromatographic experiment.....	136
Fig. 68	The picture displays the cross-section view under the fluorescence microscope of the dyed tablet space after imbibition of a blend of equal amounts of Rhodamine B (retarded) and Aluminiumphthalocyanine-sodiumsulphonate (advanced). This shows dramatically the chromatographic effect. (Magnification 50x).....	139
Fig. 69	With grit 1 200, polished surfaces show maximum shape factor which means maximum roundness/uniformity of the droplet stain. ....	140
Fig. 70	Different stained liquids show strong influence of surface scratches (ground with 60 grit paper). ....	141
Fig. 71	Supersource water-soaked tablet shows a blurred dyed droplet front (distribution by diffusion rather than capillary absorption).....	141
Fig. 72	Droplet dots on tablet surface.....	143
Fig. 73	Droplet dots viewed in cross-section after grinding.....	143
Fig. 74	Ratio of surface diameter to maximum penetration depth of a droplet shown as a function of the mercury porosity as measured from the identical series of compressed tablets. For comparison the depth of penetration is also shown. ....	143
Fig. 75	Spheroidal approximation of the penetration volume. ....	144
Fig. 76	The comparison of $V_{\text{simdyed}}$ and $V_{\text{theoryed}}$ , expressed as difference ( $V_{\text{simdyed}} - V_{\text{theoryed}}$ ), shows a marked transition as a function of the mercury porosity. ....	145
Fig. 77	Schematic showing the balance between total pore filling and either excluded pores or potential pore drainage/side-wall wetting. ....	146

Fig. 78	Fractional excluded pore volume ( $V_{\text{simdyed}} - V_{\text{theodyed}}) / V_{\text{simdyed}}$ during droplet absorption as a function of measured porosity given in % .....	150
Fig. 79	The "ridge" of maximum absorption velocity for water (z-axis) as a shaded log/log/log plot, the base z-plane is $1 \text{ ms}^{-1}$ . Fig. 80 shows the same data as a mesh plot. ....	151
Fig. 80	Bosanquet pore size differentiation favours the pore size which corresponds to the maximum absorption velocity $\partial z / \partial y$ in $\text{ms}^{-1}$ for water as a function of time. ....	151
Fig. 81	Schematic of a computer network simulator cell filling under inertially controlled exclusion and wetting for water and a high porosity structure ( $\Phi = 28.02 \%$ , $Q = 1.26 \mu\text{m}$ , see Table 6. Note the non-uniform wetting front and the potential for a preferred wetting pathway. Dark grey indicates fluid filled features. ....	153
Fig. 82	Schematic of a computer network simulator cell filling under inertially controlled exclusion and wetting for water and a low porosity structure ( $\Phi = 19.26 \%$ , $Q = 1.31 \mu\text{m}$ , see Table 6). Note the relatively uniform wetting front. ....	153
Fig. 83	Schematic representation of the absorption steps controlling the tackification and surface drying of an offset ink. ....	155
Fig. 84	Chemical structure of squalane. ....	157
Fig. 85	Chemical structure of trioleine, triglyceride of oleic-acid. ....	157
Fig. 86	Comparison of $\phi_{\text{absorbed}}$ for some polar fluids, $\phi_{\text{Archimedes}}$ , and mercury porosimetry $\phi_{\text{Fig}}$ as a function of sample tablet compaction pressure. ....	160
Fig. 87	One-to-one correlation of imbibed liquid volume with porosity for both the polar and apolar fluids as determined from the generalised correspondence shown in Fig. 86, including water at two arbitrarily chosen porosities. ....	161
Fig. 88	A scan of the dyed liquid imbibition, view of sample from the side in the wet state, liquid imbibing from right to left (actual experiment performed vertically): (1) liquid front (fuzzy appearance), (2) regime of void filling and liquid distribution, (3) the line shows the meniscus boundary, above it a regime of surface wicking, (4) the dark area is the regime of liquid influx. ....	162
Fig. 89	Imbibition of water into a $\text{CaCO}_3$ porous compressed tablet. In this case the cationic dye is adsorbing onto the anionic carbonate surface. ....	163
Fig. 90	Permeability measurement cell : (1) lid with pressure inlet, (2) sealing O-rings, (3) liquid cell; outer diameter = 40 mm, (4) porous sample embedded in resin disc of diameter = 30 mm, (5) fixing ring compresses the o-ring which seals the resin disc, (6) security shroud and drop collector, (7) drop captor (Teflon tubelet), (8) dish on micro-balance. ....	166
Fig. 91	Non- linear flow at constant pressure, left: 7.22 bar, 23.02 %, porosity, right: 5.10 bar, 24.63 % porosity. ....	169
Fig. 92	Hysteresis of flow as a function of pressure: fractional porosity = 0.3298. ....	169
Fig. 93	Typical permeation curve, porosity = 26.34 %, $P = 4.82 \text{ bar}$ . ....	170
Fig. 94	Permeation gradients in a single sample as a function of applied pressure (legend shows fractional porosities as measured by mercury porosimetry. ....	171
Fig. 95	Permeation gradients in a single sample as a function of applied pressure (legend shows fractional porosities as measured by mercury porosimetry. ....	171
Fig. 96	Hydraulic radii not tracking with porosities (fractional porosities shown in legend). ....	172
Fig. 97	Experimental permeability $K$ calculated using Eq. 33 as function of fractional porosity. The errorbars indicate the variation under different experimental pressures as shown in Fig. 96 Comparison is given to two different network simulations involving conical and cylindrical throats. ....	174
Fig. 98	Samples for imbibition: cuboid blocks of compressed porous structures with wax barrier around basal edges to prevent surface wicking. ....	178
Fig. 99	Experimental and simulated mercury intrusion curves for sample 61. ....	179
Fig. 100	3D plot overview of liquid properties * for comparison only. ....	180
Fig. 101	Gravimetric wetting apparatus with the sample / liquid cell. ....	181
Fig. 102	Schematic of wetting. ....	183
Fig. 103	We see that the wax barrier reduces strongly the wetting jump (contrast the curve without wax ("w/o wax") to the curve with wax ("wax barrier")) and also the subsequent surface wicking. Moreover, the	

	curve "wax barrier" shows a slight increase in lifted mass while the "only setup" (including liquid but no sample contact) curve shows a significant smaller change in mass. So it is unlikely that evaporation or balance drift are the main causes for fluid loss from the bulk. It is concluded that this is imbibition into the residual small porosity of the solid marble (liquid: propandiol) .....	184
Fig. 104	(a) The absorption data for oil as detected by the balance, (b) the final stage of absorption, namely the saturation of the sample. The structure shown has a porosity of 32.26 % .....	186
Fig. 105	(a) Imbibition curves for the different porosities translated to $[V(t=0)/A]=0$ , (b) the slopes of $x$ , described as (i) $x$ = experimental Darcy length and (ii) as $x$ = LW-calculated imbibition length, respectively, tracking with porosities .....	187
Fig. 106	The $d_{50}$ -diameter, which is the capillary diameter at 50 % intrusion volume of the-corrected Hg-intrusion curves as a function of porosity. ....	188
Fig. 107	A schematic drawing (omitting interconnectivity) showing (a) the preferred pathway effect and (b) an idealised more equilibrated uptake, both having the same Darcy length (dotted line) but clearly different wetting lines. ....	189
Fig. 108	Both structure series, differing in pore size distribution only, show slightly different volume rate imbibition as a function of porosity. ....	191
Fig. 109	The measured $r_{50}$ -radius as a function of porosity for structures made from the two different skeletal particle size distributions .....	192
Fig. 110	LW-derived (volume based) $r_{ehcV}$ as a function of porosity shows quite similar behaviour for the two structure series, but the difference in pore size distribution delivers a constant shift in the $r_{ehcV}$ against porosity relationship .....	193
Fig. 111	LW-derived (volume based) $r_{ehcV}$ as a function of $r_{50}$ . Note the multiplicative scaling. ....	193
Fig. 112	Imbibition of a 1:1 blend of mineral oil at 6/9 and linseed oil. No deviation from $\sqrt{t}$ linearity is observed, porosity = 32.98% .....	195
Fig. 113	Typical plot of observed and corrected mass change around the wetting jump. ....	197
Fig. 114	Repeatability shown as gradients $d(V/A)/d(\sqrt{t})$ for 1,3-propandiol for 4 similar samples. $V/A$ is volume uptake per unit area of sample cross-section, (see Table 14 for sample details) .....	198
Fig. 115	The computer network simulator unit cell showing imbibition (dark shading) of 1,3-propandiol at 100 ns. Partial filling is shown by partial shading of the features, but this should not be interpreted as the absolute position of the fluid in such features, (sample 66) .....	199
Fig. 116	Imbibition into the unit cell at (a) 10 $\mu$ s and (b) 100 $\mu$ s after fluid contact (sample 66) .....	200
Fig. 117	Simulated ( computer network simulator with cylindrical throats) and experimental imbibition expressed as Darcy length, together with sensitivity analysis as explained in the text (sample 66, see Table 14 for details) .....	201
Fig. 118	Sensitivity of modelled absorption to change in liquid density .....	202
Fig. 119	Comparison of boundary condition of simulation and experiment. ....	203
Fig. 120	Original experimental imbibition curves shown as volume uptake per unit cross-sectional area. At $t = 0$ note the wetting jump, (see Table 14 for details) .....	207
Fig. 121	Uptake curves plotted as a function of the square root of time and determinations of gradients as $d(V/A)/d(\sqrt{t})$ , (see Table 14 for sample details) .....	208
Fig. 122	Experimental absorption curves shown in comparison with $r_{ehc}$ , (see Table 14 for sample details) ..	208
Fig. 123	Simulated absorption curves, (see Table 14 for sample details) .....	209
Fig. 124	Imbibition relative to the $r_{ehc}$ approximation for octanol and butanetriol with $r_{ehc} = 24.8$ nm, (see Table 14 for sample details) .....	210
Fig. 125	Size distributions of pores and throats for the cylindrical throat computer network simulator structure and the conical throat structure, each for sample 61. ....	210
Fig. 126	Imbibition of butanetriol, shown as dark shading, from top face of the unit cell for sample 59 at $t = 200$ $\mu$ s .....	211
Fig. 127	The same as described in the legend to Fig. 126 but now at 8 ms after contact .....	212
Fig. 128	Overview of experimental and simulated uptake curves (conical throats, if not otherwise indicated) for a range of different polar liquids, (see Table 14 for sample details) .....	214

Fig. 129	Comparison of slopes $dx/d\sqrt{t}$ show at some points a very good parallel between the absorption simulation in the porosimetry data-based structure and the experimental slopes of exactly the same structures. For comparison, included is the LW prediction from Fig. 105(b) based on $r_c = d_{50}$ .....	215
Fig. 130	Uptake gradients as a function of LW parameters. Points from left to right: butanetriol, butanediol,-propanediol, ethanediol, octanol, mineral oil af 6-9. The error bars indicate of the influence of $\theta \pm 15^\circ$ .	216
Fig. 131	The $d_{50}$ diameters of all structures used, plotted as a function of structure porosity.....	216
Fig. 132	Comparison of descriptive radii derived from different experimentations. All <i>ehc</i> values are for the mineral oil af 6/9.....	217
Fig. 133	Uptake curves from the ink shown as $V(t)/A$ normalised to $[V(t = 3 \text{ s})/A] = 0$ .....	221
Fig. 134	Typical curve of mass change with characteristic perturbation phenomena due to the low fluidity of the offset ink.....	222
Fig. 135	Approach attempting to make use of the Gibbs hinging inequality to try to overcome delayed meniscus formation.....	223
Fig. 136 a)	The preadjustment of $\theta$ , b) the regime of absorption after the indication arrow, which is used for the extrapolated fit back to shorter time. The porosity of the sample in this case was 27.04 % .	224
Fig. 137	Eq. 83 is fitted in the form of $y = a + b\sqrt{t}$ . The fit is not satisfactory. Sample 70, porosity = 27.04 %.....	224
Fig. 138	Overview of shear viscosity at $30 \text{ s}^{-1}$ and subsequent relaxation monitored by stress oscillation in the linear visco-elastic (LVE) regime as a complex viscosity, $\eta^*$ . The dilution of the ink with the mineral oil is shown in % w/w.....	227
Fig. 139	Ink structure recovery regime fitted with Eq. 84 (11.7 w/w % added oil).....	228
Fig. 140	Comparison of $\eta^*(0)$ and $\eta^*(\infty)$ as a function of <u>added</u> oil content of the ink $\Delta \Phi_{oil}$ (w/w%) - the extrapolation of $\eta^*(0)$ ( $a=4.78, b= -0.122$ ), on the right, to reduced oil content, is used as the basis for the viscosity comparison with ink tack measurements.....	229
Fig. 141	Schematic view of tack set-up under the assumed formation of a filtercake with thickness $\lambda$ .....	229
Fig. 142	Tack curve on smooth substrates.....	232
Fig. 143	Receding ink droplets on PTFE (spinoidal or nucleated dewetting) as seen using confocal laser scanning microscopy in reflected light mode.....	233
Fig. 144	Tack force on PTFE in relation to roughness/smoothness. The $x$ -axis shows the sandpaper grit. The value of 4 000 is arbitrarily attributed to the untreated smooth surface.....	234
Fig. 145	Cavitation: on the left, a rough substrate means less ink contact and enables air access: on the right, cavitation at initial fast separation with meniscus retreat as extension progresses (dependent on $\eta$ ) .	234
Fig. 146	Overall mean tack curve for test paper.....	235
Fig. 147	The tack rise in the form of a "process viscosity", values are shown in Table 17.....	235
Fig. 148 (a)	schematic pull-off curve with integrated area, (b) typical curve from a point of Fig. 142 showing 2 regimes: probably cavitation and viscous ones, (c) typical pull-off curve from a point of Fig. 147.	236
Fig. 149	Mobile ink layer thickness as a function of time obtained from gravimetric ink splitting experiments.	237
Fig. 150	Total remaining ink layer thickness.....	239
Fig. 151	Ink layer remaining on paper as a function of print density after tack test as a function of time.....	239
Fig. 152	The proposed differential oil content of the ink from Eq. 103 as a function of time in contact with the paper surface.....	243
Fig. 153	A fit based on the prediction (Eq. 106) to compare with Fig. 137 which is based on a LW expression Eq. 83, The fitting parameters are given in the Appendix B 3. Sample 70, porosity = 27.04 %.....	245
Fig. 154	Diluted ink mass removal curve for sample 186, porosity = 26.34 %.....	246
Fig. 155	Fit of the prediction (Eq. 106), i.e. prediction from ink tack force-time integral applied to supersource diluted ink. In this case, shorter timescales can be encompassed by the use of the more fluid ink, matching the timescale of tackification with that of supersource. Sample 186, porosity = 26.34 %.	246

Fig. 156	LW type fit applied to supersource imbibition of diluted ink (Eq. 83). We see a similar deviation from observations as for the undiluted ink. Sample 186, porosity = 26.34 %.....	247
Fig. 157	The fit of the prediction (Eq. 106) over shorter timescales. Sample 186, porosity = 26.34 %.....	248
Fig. 158	The poor fit of the LW approach (Eq. 83). Sample 186, porosity = 26.34 %.....	248
Fig. 159	Fit of the prediction (Eq. 106) with now an excellent $r^2$ of > 0.999. Sample 186, porosity = 26.34 %.....	249
Fig. 160	Showing the poor fit of the LW approach (Eq. 83). Sample 186, porosity = 26.34 %.....	249
Fig. 161	Schematic of the laser cantilever: (1) tack wheel moving a distance $x_w$ , (2) thin pivoting mirror guided by the extended axis of the tack wheel. The red lines indicate the laser beam, (3) is the plane on which the projected laser dot motion is monitored by means of a high-speed camera, (4) represents the printed paper stripe with the ink-film (blue) and the elongated ink filament (greatly exaggerated for clarity).....	253
Fig. 162	The laser setup on the ISIT device (no ink or paper applied): 1) the $xz$ -table holding the mirror, (2) tack wheel with extended axis pivoting the mirror, (3) beam steering unit (4) diode laser. The laser beam is drawn schematically into the image.....	253
Fig. 163	Detail view of the mirror (glass slide) and the tack wheel, Nr.2 in the previous figure.....	254
Fig. 164	Micrometer screw with adapter. For the calibration of the ISIT tack wheel motion it is mounted in place of the coil spring in the picture.....	255
Fig. 165	Calibration of laser point to tack wheel displacement. 0 on the $x$ -axis represents the point where the tack wheel touches the roll of the ISIT device. StdErr = 4.92 $\mu\text{m}$ .....	256
Fig. 166	The displacement, $X_{La}$ , of the laser point on the projection plane as recorded by the high-speed camera. 257	
Fig. 167	Magnification of regime B, the effective pull-off in Fig. 166.....	258
Fig. 168	The regime B, the effective pull-off transformed to the tack wheel displacement using Eq. 108.....	258

## List of tables

Table 1	Today's most important fluid ink-based printing processes.....	19
Table 2	Overview of typical ink compositions [ink pigment size is in the range of 0.05 - 0.5 $\mu\text{m}$ ]. .....	21
Table 3	Dimensionless numbers in fluid dynamics. Note, that $r$ represents a characteristic length of interface. In many cases the radius $r$ is used but also $D (=2r)$ is employed. ....	64
Table 4	Conversion table of applied forces to resulting pressures. ....	107
Table 5	Chromatographic behaviour of dyes. Adsorption: yes = little to no mobility of dye, medium = dye moved away from starting line, no = dye moved from starting line to endline. * all the dyes except the commercial named dyes are available from Fluka. ....	138
Table 6	Overview structures for droplet experimentation. The porosities as given in the text allow for clear identification. $K_{\text{sim}}$ is given for cylindrical throats. For an extended version and explanations refer to Appendix A, Table A 1 .....	142
Table 7	Proposed regimes of droplet imbibition and filling distribution. ....	148
Table 8	Properties of the test fluids for equilibrium supersource imbibition. ....	157
Table 9	Overview structures for equilibrium supersource experimentation. The porosities as given in the text allow for clear identification. $K_{\text{sim}}$ is given for cylindrical throats. For an extended version and explanations refer to Appendix A, Table A 1.....	158
Table 10	Overview of structures for permeability experimentation with oils. The porosities as given in the text, allow for clear identification. For an extended version and explanations refer to Appendix A, Table A 1 .....	168
Table 11	Overview of test liquids for dynamic supersource experiments * only used for simulation purposes, ** contact angle used in simulation, † measured on a ground Calcite crystal in the presence of a dispersant as described in section 9.2.2.....	180
Table 12	Overview of structures for experimentation with oils. The porosities as given in the text, allow for clear identification. For an extended version and explanations refer to Appendix A, Table A 1.....	186
Table 13	Overview of additional structures oil imbibition. The porosities as given in the text allow for clear identification. For an extended version and explanations refer to Appendix A, Table A 1. ....	190
Table 14	Overview of structures polar fluids imbibition. The porosities as given in the text allow for clear identification. For an extended version and explanations refer to Appendix A, Table A 1. ....	196
Table 15	Overview of structures for offset ink experimentation. The porosities as given in the text allow for clear identification. $K_{\text{sim}}$ is given for cylindrical throats. For an extended version and explanations refer to Appendix A, Table A 1.....	220
Table 16	Symbols, abbreviations and values used in the relevant calculations. Number of measurements for film thickness = $n$ .....	232
Table 17	Comparison of viscosity values obtained from different approaches.* mobile layer is determined from splitting experiments. ** $h_{\text{T}}$ is the remaining ink layer determined from print densities, † normalising constant $k = 0.1117$ , ‡ Keiter's expression gives results of similar dimensions.....	242

## List of equations

Eq. 1.....	13
Eq. 2.....	13
Eq. 3.....	32
Eq. 4.....	32
Eq. 5.....	33
Eq. 6.....	33
Eq. 7.....	39
Eq. 8.....	39
Eq. 9.....	40
Eq. 10.....	40
Eq. 11.....	40
Eq. 12.....	42
Eq. 13.....	44
Eq. 14.....	44
Eq. 15.....	44
Eq. 16.....	48
Eq. 17.....	49
Eq. 18.....	49
Eq. 19.....	49
Eq. 20.....	49
Eq. 21.....	51
Eq. 22.....	51
Eq. 23.....	52
Eq. 24.....	53
Eq. 25.....	53
Eq. 26.....	54
Eq. 27.....	62
Eq. 28.....	63
Eq. 29.....	63
Eq. 30.....	63
Eq. 31.....	63
Eq. 32.....	63
Eq. 33.....	83
Eq. 34.....	92
Eq. 35.....	93
Eq. 36.....	93
Eq. 37.....	94
Eq. 38.....	116
Eq. 39.....	116
Eq. 40.....	116
Eq. 41.....	117
Eq. 42.....	117
Eq. 43.....	117
Eq. 44.....	118
Eq. 45.....	119
Eq. 46.....	119
Eq. 47.....	119
Eq. 48.....	119
Eq. 49.....	125
Eq. 50.....	125
Eq. 51.....	125
Eq. 52.....	126
Eq. 53.....	132
Eq. 54.....	132
Eq. 55.....	144
Eq. 56.....	144
Eq. 57.....	144
Eq. 58.....	145
Eq. 59.....	145
Eq. 60.....	159
Eq. 61.....	159
Eq. 62.....	159

Eq. 63.....	160
Eq. 64.....	166
Eq. 65.....	166
Eq. 66.....	182
Eq. 67.....	182
Eq. 68.....	182
Eq. 69.....	183
Eq. 70.....	184
Eq. 71.....	187
Eq. 72.....	187
Eq. 73.....	190
Eq. 74.....	191
Eq. 75.....	191
Eq. 76.....	192
Eq. 77.....	192
Eq. 78.....	215
Eq. 79.....	218
Eq. 80.....	218
Eq. 81.....	218
Eq. 82.....	218
Eq. 83.....	218
Eq. 84.....	218
Eq. 85.....	223
Eq. 86.....	227
Eq. 87.....	228
Eq. 88.....	230
Eq. 89.....	230
Eq. 90.....	230
Eq. 91.....	230
Eq. 92.....	231
Eq. 93.....	231
Eq. 94.....	235
Eq. 95.....	236
Eq. 96.....	237
Eq. 97.....	237
Eq. 98.....	238
Eq. 99.....	240
Eq. 100.....	240
Eq. 101.....	240
Eq. 102.....	240
Eq. 103.....	241
Eq. 104.....	241
Eq. 105.....	242
Eq. 106.....	243
Eq. 107.....	243
Eq. 108.....	243
Eq. 109.....	243
Eq. 110.....	255
Eq. 111.....	258
Eq. 112.....	259
Eq. 113.....	259
Eq. 114.....	259



## Acknowledgement

Very special thanks to my external supervisor Dr. P. A. C. Gane for his belief in me, his continual support, his inputs, his friendship and finally for actually making this study possible.

I would like to thank Dr. G. Peter Matthews, my internal supervisor for his great support and flexibility. Thank you also to the other members of our research team, Dr. Cathy Ridgway for her accompanying work and help, for introducing me to a number of techniques (including pool billiards), for helping to proof-read this thesis, and finally for saving me from sleeping on a park bench when the hotel inadvertently gave my room away, and Dr. Daniel C. Spielmann for endless discussions and countless cigars.

Many thanks to OMYA, especially to its president Mr. Max Schachenmann, for providing the financial support and facilities for this research co-operation. Also to all the people in OMYA's research laboratories especially Thomas Kozlik, Silvan Fischer, Christina Eng and Daniel Frey for all the help, photos, discussions and for being good friends. I would also like to acknowledge Bruno Wullschleger from the workshop for not losing his nerves even after making numerous modifications to the novel experimental apparatus we put together. The Pore-Cor unit cell graphics software was programmed by Joseph Matthews. Thanks to all my fellow researchers in the group at Plymouth who helped make my visits to the University more comfortable.

To my wife Esther and my family for always believing in me and giving me the time and the space I needed, and to all my friends in Switzerland for appreciating that my time was often very limited, thank you.

## AUTHOR'S DECLARATION

At no time during the registration for the degree of Doctor of Philosophy has the author been registered for any other University award.

This study was financed by Omya AG, Switzerland, and carried out in collaboration with Omya's Oftringen - laboratories under the local supervision of Dr. P. A. C. Gane.

Relevant scientific seminars and conferences were regularly attended at which work was often presented; external institutions were visited for consultation purposes and several papers prepared for publication.

### Publications:

- 1 Gane, P. A. C., Schoelkopf, J., Spielmann, D. C., Matthews, G. P. and Ridgway, C. J., "*Fluid transport into porous coating structures: some novel findings*", Tappi Journal, 83(5), 2000, p77-78
- 2 Schoelkopf, J., Ridgway, C. J., Gane, P. A. C., Matthews, G. P. and Spielmann, D. C., "*Measurement and network modelling of liquid permeation into compacted mineral blocks*", Journal of Colloid and Interface Science, 227, 2000, p119-131
- 3 Gane, P. A. C., Schoelkopf, J. and Matthews, G. P., "*Coating Imbibition Rate Studies of Offset Inks: A Novel Determination of Ink-on-Paper Viscosity and Solids Concentration using the Ink Tack Force-Time Integral*", Proceedings 2000 TAPPI International Printing & Graphic Arts Conference, Savannah, GA, Tappi Press, Atlanta, 3-10-2000, p71-88. Accepted for publication in Tappi Journal
- 4 Schoelkopf, J., Gane, P. A. C., Ridgway, C. J. and Matthews, G. P., "*Influence of Inertia on Liquid Absorption into Paper Coating Structures*", Nordic Pulp and Paper Research Journal, 15(5), 2000, p422-430
- 5 Schoelkopf, J., Gane, P. A. C., Ridgway, C. J., Spielmann, D. C. and Matthews, G. P., "*Rate of vehicle removal from offset inks: a gravimetric determination of the imbibition behaviour of pigmented coating structures*", Tappi 2001 Advanced Coating Fundamentals Symposium Proceedings, San Diego, Tappi, Atlanta, 2001, p1-18. Accepted for publication in Tappi Journal
- 6 Gane, P. A. C., Ridgway, C. J. and Schoelkopf, J., "*Absorption Rate and Volume Dependency on the Complexity of Porous Network Structures*", Transport in Porous Media, 2002, in press
- 7 Ridgway, C. J., Gane, P. A. C. and Schoelkopf, J., "*Effect of capillary element aspect ratio on the dynamic imbibition within porous networks*", Journal of Colloid and Interface Science, 2002
- 8 Ridgway, C. J., Schoelkopf, J., Matthews, G. P., Gane, P. A. C. and James, P. W., "*The effects of void geometry and contact angle on the absorption of liquids into porous CaCO<sub>3</sub> structures*", Journal of Colloid and Interface Science, 239(2), 2001, p417-431
- 9 Schoelkopf, J., Gane, P. A. C., Ridgway, C. J. and Matthews, G. P., "*Practical observation of deviation from Lucas-Washburn scaling in porous media*", Colloids and Surfaces A: Physicochemical and Engineering Aspects, 206(1-3), 2002, p445-454
- 10 Ridgway, C. J., Schoelkopf, J., and Gane, P. A. C., "*A new method for measuring the liquid permeability of coated and uncoated papers and boards*", Journal of Pulp and Paper Science, submitted 2002.
- 11 Schoelkopf, J., Gane, P. A. C., and Fischer, S., "*Determination of elongational strain during ink-on-paper tack measurement: a novel technique to measure work of cohesion and adhesion of thin films*", TAGA Journal, submitted 2002.

- 12 Schoelkopf, J., Gane, P. A. C., and Ridgway, C. J., "Observed non-linearity of Darcy permeability in compacted fine pigment structures", Symposium: In Memory of Dr. Bernie Miller, TRI Princeton 2002,

### 13 Presentations and Conferences Attended:

Wetting and Flow in Porous Media Fundamental Concepts and Industrial Perspectives, Sept. 10-12 1998, Utö, Stockholm, Sweden. Attended.

Seminar SCA Graphics Research Centre, Sept. 9 1998, Sundsvall, Sweden. Oral presentation.

International Symposium on Paper Coating Coverage- Visions for Coating Development, Feb. 16-17 1999, Helsinki. Attended.

Tappi Advanced Coating Fundamentals Symposium April 30 May 1, 1999 Toronto. Oral presentation.

Tappi Coating Conference, May 2-5 1999, Toronto. Attended.

Research seminar (Env. Sci.) - Cleaner technology: wetting of paper coating formulations, University of Plymouth, Nov. 26 1999. Oral presentation.

International PhD Programme in Pulp and Paper Science and Technology (PaPSaT), January 10-14. 2000., Åbo Akademi, Turku, Finland. Invited lecture.

2000 Tappi Metered Size Press Forum, III, April, 27-29, 2000, Washington D.C. Attended.

TAPPI Coating Conference May 1-4 , 2000, Washington D.C. Attended.

International Workshop - Wetting: from microscopic origins to industrial applications, May 6-12, 2000, Hyeres France. Poster presentation.

Paper Coating Chemistry Symposium, Stockholm June 6-8, 2000. Oral presentation.

27th IARIGAI Research Conference, Advances in Paper and Board Performance, September 10-13. 2000, Graz, Austria. Attended.

2000 International Printing & Graphic Arts Conference, October 1-4, 2000, Savannah GA. Oral presentation.

Tappi Advanced Coating Fundamentals Symposium May 4-5, 2001, San Diego. Oral presentation.

TRI/Princeton International Workshop - "Nanocapillarity: Wetting of Heterogeneous Surfaces and Porous Solids", June 25-27, 2001, Princeton, NJ. Poster presentation.

12th Symposium "The Science of Papermaking", Keble College, Oxford, September 16-21, 2001. Attended.

Third International Symposium on Contact Angle, Wettability and Adhesion, Providence, Rhode Island (USA); May 20-22, 2002. Attended.

### **External Contacts**

Omya Research Centre, Meeting with Prof. E.L. Akim and Mr. A. E. Shvarts, Publishers of Russian paper magazines, November 30, 2000, Oftringen, Switzerland. Oral presentation.

Omya Research Centre, Contact meeting with Prof.'s H. Paulapuro and J. E. Laine, Helsinki University of Technology, December 19, 2000, Oftringen, Switzerland. Oral presentation.

Modelling pore volume of idealised structures - seminar and contribution to microscopy studies (joint programme with Assoc. Prof. Dr. Martti Toivakka, Åbo Akademi, Finland and Dr. P.A.C. Gane, Omya AG).

Involvement in joint research project "Improving Printability of matt-coated papers" YKI (Institute for Surface Chemistry), Dr. J. Grön, Prof. Dr. F. Tiberg, Stockholm, Sweden and Dr. P.A.C. Gane, Omya AG.

Advisory capacity in joint research project, "Chromatographic behaviour in Paper Printing Liquid Absorption" with S. Rousu and Prof. D. Eklund, Åbo Akademi, Finland and Dr. P.A.C. Gane, Omya AG.

Advisory capacity in joint research project "Preparation of micro particles with high refractive index and studies of optical properties" , with IPCMS (Institut de Physique et Chimie des Materiaux de Strasbourg, France, Prof. Dr. S. Vilminot and Prof. Dr. Ch. Hirlimann, Dr. H. Parant, Omya SA, Drs. D.C. Spielmann and P.A.C. Gane, Omya AG).

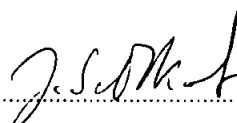
Joint research project : DSC probing of preferred pore sizes in liquid imbibition with Helsinki University of Technology, Prof. Dr. H. Paulapuro and Prof. Dr. J. E. Laine, Dr. P.A.C. Gane, Omya AG.

Involvement in joint research project "Dry Coating for paper" with KCL Finland, Dr. M Väha Nissi and BASF Ludwigshafen, Dr. J. Schmitt-Thümmes, Dr. A. Pfau, Dr. H. Kröner, Dr. W. Gaschler, Dr. W. Schädler, Dr. K.H. Etzbach, and Omya AG, Dr. P.A.C. Gane, Dr. D. Spielmann.

Involvement in confidential joint research project "Spray coating for paper" with the companies Raisio Latexia, Stora Enso, Metso and Omya.

## Membership of Professional Organisations

Since 2000 - Member of the TAPPI Coating Fundamentals Committee .

Signed.....   
Date..... 19.11.2002

# 1 Introduction

This thesis presents experimentation and modelling of the static and time dependent interactions between fluids and porous structures as found in fine mineral compacts. The target is to further the understanding of ink-paper relationships so as to utilise better the potential of environmentally sustainable high-win naturally-occurring  $\text{CaCO}_3$  resources.

## 1.1 Hypotheses

The fundamental hypotheses which are tested are:

- that the description of the extent of imbibition as dependent on the square root of time, and hence describable by the Lucas Washburn equation, is simplistic and misleading, and masks interesting and useful details of the imbibition process,
- that additional information can be gained about imbibition by using improved and novel experimental methods applied to specifically prepared experimental samples,
- that insights into the fine structure of the imbibition process can be gained by use of a computer model of a 3-D network.

## 1.2 Background summary

All interactions between solids and their environments occur at surface interfaces. What happens at these interfaces affects most aspects of life, from cell membranes to the biospheric interface of our planet to the cosmos.

The field of solid/liquid interactions has attracted much interest from researchers. Many processes, not only in biology and medical sciences, but also in industrial and agricultural applications, depend heavily on these mechanisms. Despite the wealth of research done in the past, there are still many open questions when it comes to the details of traditional theories applied to specific problems. This work is stimulated by issues of the print media industry. More specifically, the complex interactions between an ink and a pigmented paper surface are of importance, and here the influence of the pigment particles is the focus of attention.

Solid fine particulate pigments, which are in most cases of mineral origin, and therefore inorganic by nature, are used in many industries. Fillers are particles used to change the bulk properties of a material like its density, stiffness, opacity or porosity, or just to make a product cheaper by acting as an extender. The term pigment is mostly used when we are dealing with particles which improve the optical properties of a surface such as gloss (or mattness), opacity and colour. It is interesting to note that many pigments which are used to make a product brighter, are in the condensed bulk intrinsically transparent. This property can be likened to the transparent nature of water. The transmission of light through calcite, for example, is well-known for its well-defined crystallographic response to polarised light. However, the use of  $\text{CaCO}_3$  as a pigment makes use of the light scattering properties of fine particles at their crystal interfaces with air, as also for water in the case of snow.

This work is dealing with paper coating pigments which are not only used to improve the optical properties of the paper, but also to control and to optimise the receptivity of printing inks. The coating is applied in a thin layer ( $\approx 5\text{-}30\ \mu\text{m}$  depending on grade) as a coating colour - a water suspension containing pigments, binders and additives, often on fast running coating machines (up to  $2\ 200\ \text{mm}\cdot\text{min}^{-1}$ ).

For such pigments to be called environmentally friendly, depends mainly on the energy needed to process it, the scars its winning through mining leaves on the landscape, and the chemical or toxicological character of the pigment itself. Furthermore, an environmentally friendly paper manufacturing process, based on renewable fibre sources, yielding chemically stable paper, is needed to satisfy today's demands for both permanency and recyclability. It is recognised that pigments requiring an acidic paper production process do not meet the criterion of permanence, as witnessed by the decay of many valuable manuscripts. The responsible use of neutral or alkaline papermaking has meant that fillers and pigmented coating layers are now becoming dominated by the use of  $\text{CaCO}_3$ . To maximise the suitability of  $\text{CaCO}_3$ -based coating structures, a fuller and more complete understanding of its interactional role with ink is of prime importance to overcome some of the remaining difficulties in controlling ink setting and adhesion to the surface of paper, which often manifest themselves as deposits on the printing press and as print rub or scuff from matt surfaces.

The use of  $\text{CaCO}_3$  in a paper surface coating also has advantages from a paper-technical point of view. It shows an excellent brightness and good opacity at optimum particle size distribution. Furthermore, it is won at reasonable cost and very little mining waste. In some cases, such as with deposits of the purest marbles, the win is actually 100 %. Compared with primary kaolin extraction, for example, where the win is typically 15-20 %,



the amount of mine reclamation is greatly reduced. That  $\text{CaCO}_3$  has a great variety of crystal shapes and forms has a further potential in chemical and morphological modifications.

Another point of environmental focus is the use of inks based on sustainable vegetable oils instead of mineral oils, and the emerging use of waterborne inks. Attention is therefore paid to the comparison of alkanes (representing mineral oil-based traditional offset-inks) with vegetable oil-based and aqueous systems.

Parallel to the environmental issues is the scientific merit derived from these studies. The above-mentioned micromechanisms of liquid front movement and liquid distribution in an inter-particle void network are still not fully understood. One specific challenge is to investigate experimentally and theoretically the physical reasons why some coating structures with fine pores absorb liquid remarkably faster in some processes than coatings with bigger pores. This phenomenon, long observed in the printing industry, runs contradictory to the well-established Lucas-Washburn (LW) equation. Until now, many researchers have been using the LW solution assuming a "bundle of capillaries" to model absorption. Its eminent failure to explain the rate phenomena in printing leads to the generation of so-called 'effective parameters', which are nothing more than modified parameters to fit experimental data, often giving values far removed from independently measured surface energy values. Not only in the field of papermaking but also in textiles and geological formations, the difficulties in applying consistent parameters to LW throughout a series of similar experiments is known. It has to be recognised that the detailed processes are on a quantum mechanical and nano- scale and are intractable beyond the use of ensemble averaging. Therefore, continuous classical mechanics have still to be applied. This work, as in the classical literature, is based on simplifying assumptions which allow for a better isolation and understanding of some of the potential single contributing mechanisms. To this end, the effect of interconnecting pores of differing size and geometry forms a core part of this study.

The Environmental and Fluids Modelling Group, Plymouth have developed over the last ten years a pore space simulator named Pore-Cor<sup>1</sup>, based on a system of pores and interconnecting throats. Parallel to the author's work, Dr. C. Ridgway and co-workers at the University of Plymouth implemented a novel absorption algorithm into the computer network simulator, based on a short timescale solution, proposed by Dr. P. Gane of Omya AG, of the Bosanquet inertial model. Model development also considered the effect of pore geometry, adopting conical diverging and converging throats to simulate imbibition retardation and acceleration, respectively. A substantial component of this thesis is devoted to the design and development of experimentation to test the validity of the

---

<sup>1</sup> Pore-Cor is a software package developed by the Environmental and Fluid Modelling Group of the University of Plymouth, Devon PL4 8AA, U.K.

resulting computer network simulations, including a range of novel techniques, such as the formation of compressed porous structures of fine ground  $\text{CaCO}_3$ . Using this structure formation technique, a wide range of porosities and mean pore diameters can be achieved without changing the surface chemistry or intrinsic pore geometry. This range of structures is seen to contribute a unique series to the literature upon which consistent studies of imbibition and permeation are made, finally establishing the failure of an over-simplistic application of LW in respect to size and porosity scaling.

The experimental procedures for liquid imbibition and permeation include:

- a droplet method using dyes, and subsequent cross-sectional grinding, to determine the macroscopic equilibrium liquid distribution within the porous network by image analysis,
- a static supersource imbibition test to measure equilibrium liquid uptake and to calculate a pore volume filled by imbibed liquid,
- a dynamic supersource imbibition method to investigate the rate dependence of imbibition on liquid density, viscosity and surface tension, and
- a hydrostatic approach for direct measurements of steady state unidirectional permeability.

Rheometry, microscopy, tensiometry and contact angle measurements have been used to provide characterisation of interaction between test liquids and solid surfaces.

Extending the study to ink interactions directly on paper involved the use of the Ink Surface Interaction Tester (ISIT<sup>2</sup>) devising a new method of in-situ analysis, based on extensional viscosity, to derive the rate of fluid loss from a printed ink layer into a porous coating structure.

---

<sup>2</sup> ISIT is a product name of SeGan Ltd., Perrose, Lostwithiel, Cornwall PL22 0JJ, U.K.

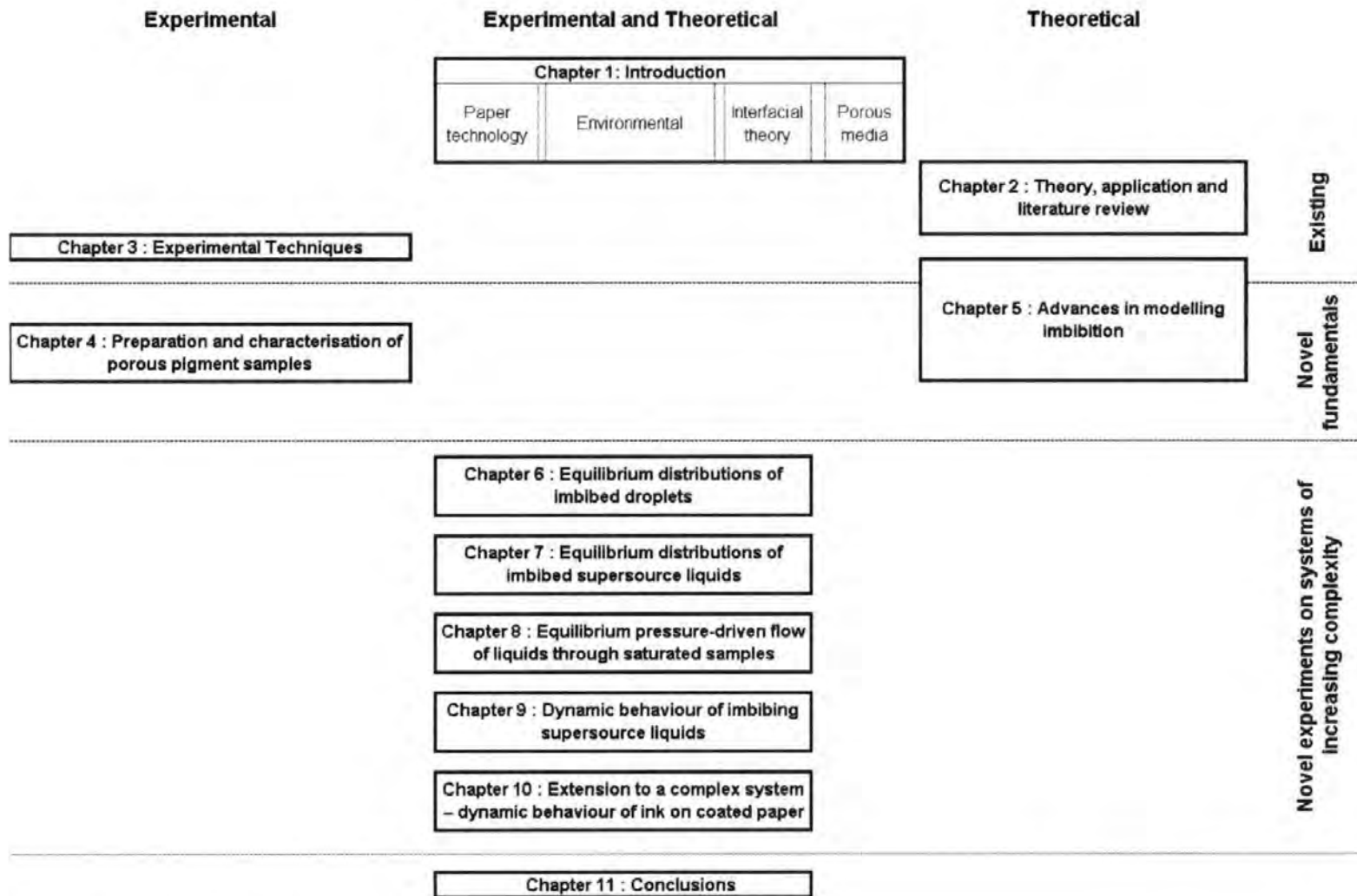


Fig. 1 Structural overview of the thesis.

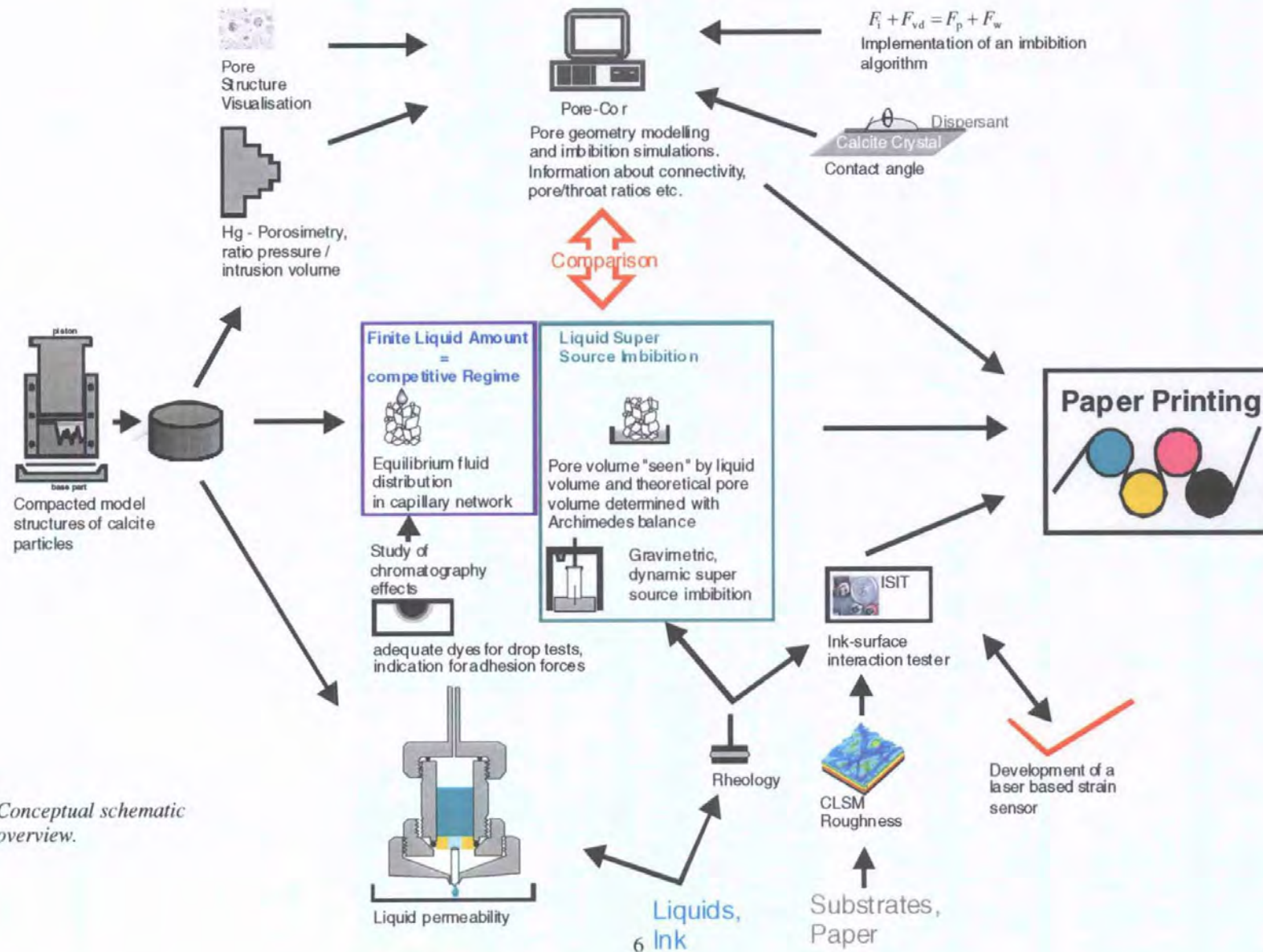


Fig. 2 Conceptual schematic overview.

This thesis is placed also in the context of other current research projects within the Fluid Interactions Group at the University of Plymouth, led by Dr. G. P. Matthews, and at the Research Laboratories of Omya AG, sponsor of this study, led by the Research Director, Dr. P.A.C. Gane. These include, Paul Bodurtha's work at Plymouth dealing with high aspect ratio, platy clay pigments, and an adaptation of the computer network simulator to provide for modelling slit-shaped pores, and the continued development of Pore-Cor in application to paper coatings by Dr. C. Ridgway, now at Omya AG. Dr. Gane's Omya group is also involved in other research projects, among which the work of Sanna Rousu-Leinonen, Åbo Akademi, Finland, investigating the chromatographic separation of offset ink components during the imbibition into a coating layer, is of significant interest, as is a joint project worked on by Maurizio Laudone, University of Plymouth and Omya, considering the effect of the forming pore structure of paper coatings on binder shrinkage during drying. Dr. Ridgway has conducted further absorption studies using the methodology developed by the author, extending the work to flexographic and newsprint inks as well as studies of the porous fibrous structures of papers and wood.

In the following chapter some fundamental theory and previously published work are reviewed, with special attention given to contributions in the field of interactions between liquids and porous media.

## **2 Theory, application and literature review**

This chapter covers both an overview of paper technology, and especially paper coating and printing, and a review of general work done in the field of liquid - solid interactions with special attention to capillarity.

We start with a review of papermaking, coating and printing to arrive at the environmental aspects surrounding the raw materials, in particular pigments used for paper coatings, which are designed for common printing technologies. This review reveals the need for a better understanding of ink absorption in the post-print process. Therefore, we review the theoretical aspects of some of the work done in the past, including the modelling of imbibition processes, and experimental approaches to analyse the capillarity of simple and complex systems. A focus is given to approaches specific to paper science.

### **2.1 Paper technology background**

#### **2.1.1 Brief history of papermaking**

Papermaking began in China around 105 AD, and its invention is generally attributed to a court official called Cai Lun. The first paper was made from a blend of different materials, including non-wood fibres and mulberry bark. This invention, an obvious improvement over the predecessors, such as cave walls, clay tablets and parchment, revolutionised the art and science of writing and drawing. The knowledge of papermaking then spread to the Middle East through central Asia and reached Europe in the 12th century.

A wide selection of fibres has been involved in papermaking, but in the years up to the 18th century, relatively large quantities were being made from linen rags. At that time, each individual sheet was hand shed separately. The papermaker would dip a mesh known as a forming screen into a tub containing a suspension of water and fibre (the stock). A sheet of paper would then be formed on the screen solely through the natural bonding of the fibres. This occurred as the screen was lifted out of the water/fibre solution and drained by gently shaking the screen to help fibre felting, which is the crucial process in sheet forming leading to mechanical interlocking and hydrogen bonding of the fibres. The sheet was then pressed and dried. Today, paper is still produced in this way by papermaking crafts' people and is specially valued for artistic use.

At the end of the 18th century the process of papermaking made a major step forward in output terms with the introduction of continuous forming. The Fourdrinier brothers in Britain introduced a practical continuous former in 1810, following development work carried out in France.

While papermaking has made many advances since the introduction of continuous forming and become an advanced industry, the basic steps in the process are essentially the same as those used in the early craft. These steps are:

- preparation of the stock - a solution containing fibre and water, as well as pigment fillers and chemical additives,
- forming the sheet on a woven screen,
- pressing the sheet to remove most of the remaining bulk water,
- drying to remove the remaining interstitial water,
- surface sizing and/or coating to improve the paper's printing quality and other properties,
- calendering to smoothen the surface and reduce porosity and permeability.

The last two steps are mainly responsible for the surface structure of the paper which is the issue of interest for this work.

#### **2.1.1.1 Pigments in paper manufacturing**

For a long time minerals in paper have been considered almost as "cheating", i.e. artificially extending the fibre with a cheaper, lower quality inert substitute. This attitude changed in the 19th century when the positive influence of properly selected minerals on brightness, opacity and smoothness of the paper was recognised. At that time Gypsum, China-clay, Satinwhite and Barite were in use in an acid papermaking environment, while high brightness  $\text{CaCO}_3$  became increasingly used after 1970 as a result of the revolution toward neutral and alkaline papermaking (see Table A 5 for pigment details and also 2.1.2 for more information about  $\text{CaCO}_3$ ).

Papers today contain high levels of mineral pigments, ranging from 35 %w/w in wood-containing supercalendered grades up to 50 %w/w in multi-coated woodfree grades. The level of pigmentation used simply

as filler is limited by loss of mechanical properties, such as strength and stiffness, and the propensity for dusting and piling in the printing and converting of the final product. It is because of these drawbacks, associated with uncoated papers relying on filling alone, that coated grades have emerged and flourished, (Gane, 2001).

Paper has been coated to improve its surface for better reproduction of printed images for over 100 years. The earliest examples could be more strictly defined as surface treated, for example with starch solutions. The introduction of half-tone and colour printing has created a strong demand for pigment coated paper. Coatings are applied to paper to achieve uniformity of surface for printing inks, lacquers, and the like, to obtain printed images without blemishes visible to the eye. Furthermore, they enhance opacity, smoothness, and gloss (or evenness of matt finish) of paper or paperboard, and to achieve economy in the weight and composition of basepaper stock by the upgrading effect of coating.

After 1970, a strong increase in coated paper production brought with it a number significant industrial impacts, not least the high demand for consistent mineral product, but also the economy of scale required in product form, such as slurried suspensions of mineral and the ability to run blade coaters at high speed continuously. Today, there are many qualities of coated papers on the market, and the world wide production is an estimated 37 million tonnes for 2000. The majority is used for quality magazines, catalogues, books and in the packaging industry. The pigment share for the above is approximately 30 – 50 %.

The chief components of the water dispersion used for coating paper are;

- pigment, increasingly  $\text{CaCO}_3$  in bright grades, they may still include clay for physical coverage, titanium dioxide for increased opacity, specialities such as satin white, plastic pigment etc. or combinations of these;
- dispersants (typically anionic polymers of acrylic acid) to give uniformity to the mixture (coating colour or "slip"); and an
- adhesive binder to give coherence to the finished coating.

Today, the binder is for most applications an anionically dispersed latex emulsion. Hydro-colloids, such as polyvinylalcohols and other derivatives or natural materials, such as starch, carboxymethyl-cellulose, guar gum, casein and proteins are often employed as cobinders to provide desired rheological properties and an ability to withstand waterloss from the coating colour in contact with the absorbent fibrous basepaper.



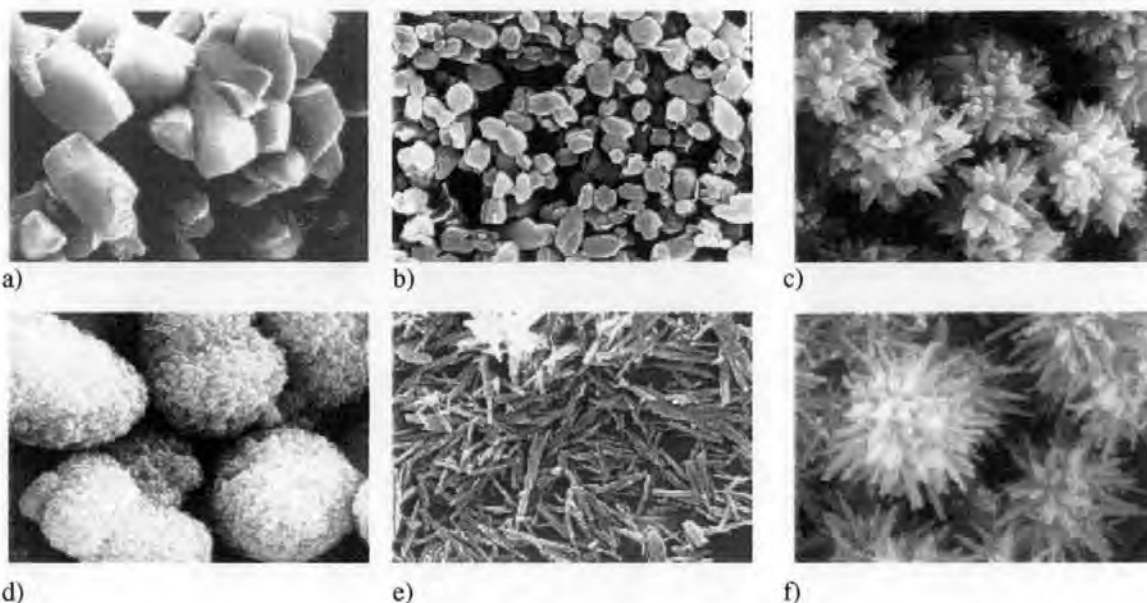
Pigments in paper are today designed especially to fulfil three major roles: providing the optical properties to enhance opacity and brightness of the paper, imparting improved end-use characteristics, such as smoothness and printability, the latter being a function of the inter-particle pore structure, and importantly, but often overlooked, the desired surface chemistry. They have maximum effect when incorporated in coatings with synthetic binder systems which also contribute to the structural and chemical properties. They have been, and continue to be, an economical and environmentally acceptable way of extending the fibre with reduced fibre content by replacing fibre with filler. This is especially the case for  $\text{CaCO}_3$ , which is a naturally renewable resource on a geological timescale.

A summary of some of the detailed properties of typical pigments in the paper industry is given in the Appendix A, Table A 5.

### **2.1.2 Characteristics of Calcium Carbonate ( $\text{CaCO}_3$ )**

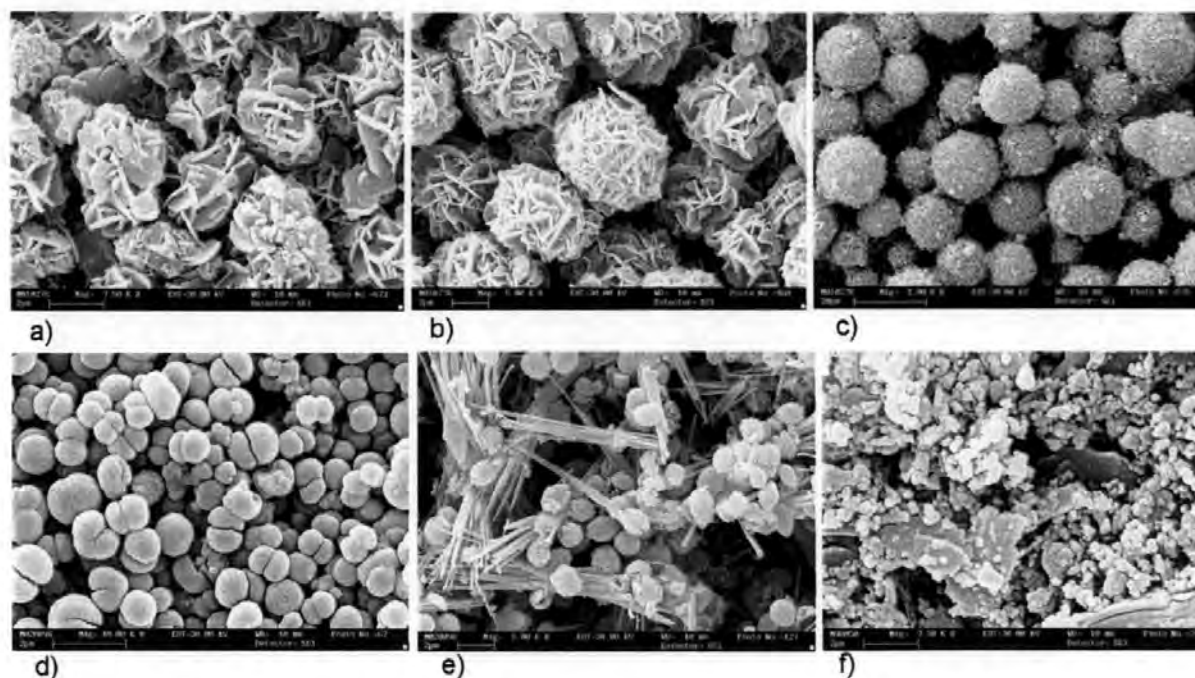
Gane (Gane, 2001) gives an overview about  $\text{CaCO}_3$ , which can be found in nature in a vast myriad of types and forms. It is a structural component of most skeletal creatures which have lived on earth and is part of an unbroken cycle, and so, in principle, is inexhaustible. The majority of deposits were formed by the capture of  $\text{CO}_2$  from the atmosphere by micro-organisms which combined the dissolved gas with calcium ions to form their exo-skeleton providing protection and structural support. Consumption by higher vertebrates resulted in captured mineral in their bone skeletal structures. Deposits of coccoliths formed chalk beds at the bottom of the sea which later and together with other crustacea became transformed under pressure to form limestone. In some cases high pressure and temperature promoted recrystallisation into marble, the hardest and brightest form of calcite.

Synthetic  $\text{CaCO}_3$  (pcc) is made by firstly reversing the natural process endothermically, driving off the  $\text{CO}_2$  once more, then subsequently slaking in water exothermically followed by reprecipitation of the carbonate by bubbling through  $\text{CO}_2$ . This can be made under carefully controlled concentration and temperature conditions to form any of the commonly useful crystal habits of  $\text{CaCO}_3$ : rhombohedral calcite (as found in marble), prismatic, spherically agglomerated and scalenohedral ("cigar"-shaped crystals occurring frequently in a clustered form), Fig. 3. The aragonitic (needle form) habit is more difficult to produce and is generally reserved for specialised coating applications. In practice, the batchwise precipitation process demands sophisticated control systems to maintain satisfactory consistency, and in coating applications this is an aspect which continues to limit its use severely, as ground carbonates progress to supplant kaolin completely in some woodfree grades.



**Fig. 3** Commonly found forms of synthetically precipitated  $\text{CaCO}_3$ : (a) rhombohedral calcite, (b) prismatic, (c) scalenohedral, (d) clustered aragonite, (e) aragonite, (f) agglomerated aragonite, (images taken from Gane, 2001).

Recent developments involve  $\text{CaCO}_3$  which is co-structured with other pigments (Gane *et al.*, 1999) and "crystal rebuild" pigments where the crystal lattice of  $\text{CaCO}_3$  is modified resulting in surfaces with platy / lamellar character on different scales of size (Beuleke and Burri, 1999) and amorphous modifications of  $\text{CaCO}_3$  (Minayoshi *et al.*, 1994). Examples are shown in Fig. 4.



**Fig. 4** (a-c) "crystal rebuild"  $\text{CaCO}_3$ , (d,e) amorphous  $\text{CaCO}_3$ , vaterite type, (e) containing also calcite needles, (f) V40, commercial co-structured pigment, talcum platelets with  $\text{CaCO}_3$  particle coating.

Functional pigments play an important role in papermaking, both for their properties as required by the end-use and for their process-enhancing qualities. Many are of high surface area acting as either speciality chemical

adsorbers, e.g. bentonite (montmorillonitic smectite) - a highly platy laminate structure of the 2:1 layer silicate type with a slight anionic charge density due to ionic substitution, or precipitated silica which combines high surface area with large interparticle pore volume. These latter types are often referred to as colloidal particles due to their microscopic nature and due to their tendency to interact with other microscopic species creating colloidally stabilised dispersions and gels.

### 2.1.3 Particle size: its importance, definition and production control

The particle size and distribution of sizes of a mineral pigment are determined traditionally using the sedimentation resistance of a particle of mass,  $m$ , flowing through a fluid of viscosity,  $\eta$ , reaching an equilibrium velocity,  $\mathbf{u}$ , under the action of a gravitational acceleration,  $\mathbf{g}$ , i.e. the Stokes' diameter or equivalent spherical diameter ( $d = 2a$ ), where  $a$  is the particle radius.

$$mg = -\mathbf{F} = -6\pi\eta a\mathbf{u}$$

Eq. 1

where  $\mathbf{F}$  is the sedimentation force. This is a practical but crude description when it comes to particles of complex shape and it assumes complete dispersion of the particles. Observation of the Stokesian dynamic can be made using either a simple extraction and density determination as a function of height, suitable for coarse pigments, or by measuring the absorption of X-radiation using the Beer-Lambert transmission intensity decay,  $I/I_0$ , as a function of path length through the particle,  $l$ , for an absorption constant of  $l/\tau$ ,

$$I = I_0 e^{-l/\tau}$$

Eq. 2

As we shall see later, optically and chemically active particulates have optimal particle size criteria based on the interaction with light and the activation energy distribution densities, respectively. Pore structures and geometries define the fluid absorption properties of paper. To achieve optimal properties it is necessary to control particle size and shape accurately and reproducibly. For synthetic pigments this is part of the precipitation or forming kinetics but for naturally occurring minerals various comminution techniques are used. The action of grinding can take several forms ranging from delamination of layered minerals, through frictional attrition to breakage.

## 2.1.4 Coating application to the paper

Today the main systems to apply the liquid coating colour to a basepaper are:

- blade metering, where an excess of colour is applied either by roll or nozzle jet and metered to the desired coat weight by removing excess using a blade inclined against the paper such that it trails the motion of the paper web.
- rollsystems (sizepress, premetered filmpress), in which a nip pressure is applied between the paper and the contacted colour to transfer the desired amount of coating.

Each system has its advantages and drawbacks. Rollsystems are mainly used for low viscosity coating colours and low application weights. Blade coating is generally used for higher viscosities and coating solids content. The flexibility of blade geometry can be used to provide a wide range of coat weight applications. The viscoelastic properties in association with the recently identified inertial dewatering characteristics (relaxation-induced dilatancy) of the coating colour must be held in control to ensure good runnability at the high coating speeds of today up to  $2\,000\text{ m min}^{-1}$  (Gane and Coggon, 1987), (Gane *et al.*, 1991), (Gane, 1997).

## 2.1.5 Investigation of coating structure

To visualise coating structure, the electron microscope provides one of the most informative images, as can be seen in the following cross-sections of multi-coated paper. The use of a coarse precoat  $\text{CaCO}_3$  and a fine topcoat, typical of so-called woodfree high brightness grades, can be readily identified.

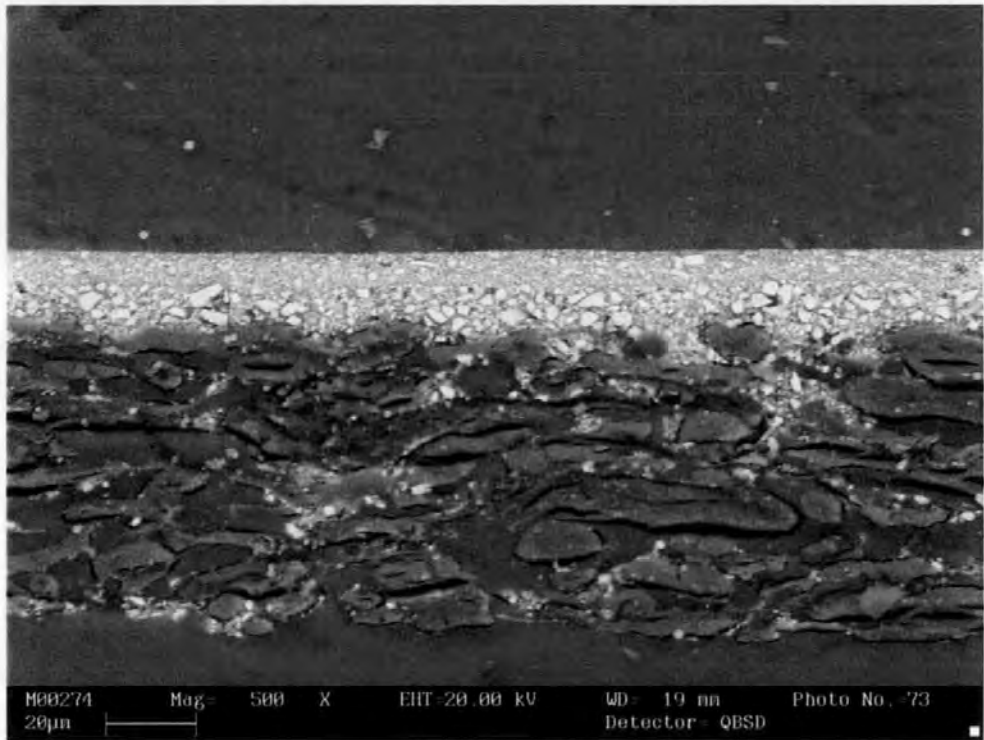


Fig. 5 *Double coated paper viewed in cross-section. A fine pigment layer on top gives gloss, the coarser precoat acts as a levelling and functional "primer". Below, the base sheet consisting of fibres and filler-pigments can be identified.*

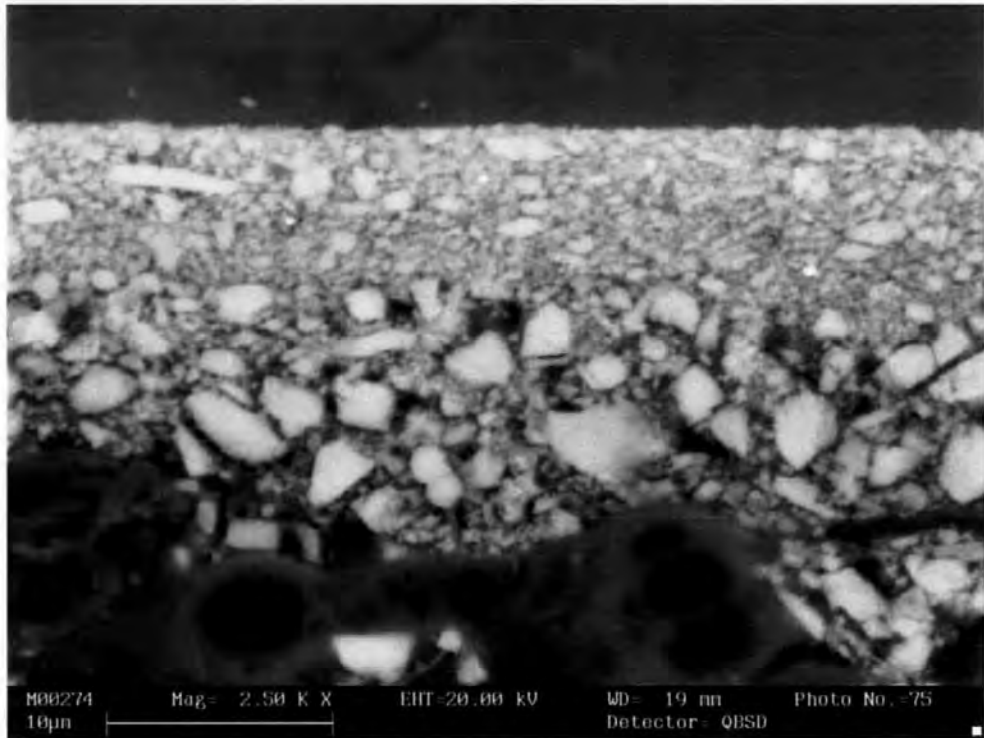


Fig. 6 *A sectional enlargement of Fig. 5.*

As well as the optical properties of pigment coatings, physical coverage of the relatively rough basepaper is an important criterion. Particles tend to become forced into the surface voids of the paper. A certain amount of coating penetration into the surface voids is desirable as it leads to synergistic light scattering effects with the surface fibre structure and helps the binding of the coating layer onto the basepaper. However, this must be limited so that the benefit of the coating on the surface can be maximised. This is termed coating holdout. In

many high quality grades, multi-coating is applied to achieve the balance between coating holdout and the desired properties of gloss (or mattness) and printability. A coarse pigment precoat, therefore, provides a better holdout than fine pigment and also forms a good foundation for the application of the topcoat.

Due to the strong interactions between coatings and basepapers, it is often necessary to study the intrinsic properties of coatings in isolation from the basepaper. This can be achieved, for example, by coating on foils or plastic paper, providing for ready measurement of intrinsic properties of the structure, such as light scattering, ink interaction etc. Further methods, and, in particular, the use of mercury porosimetry to probe the pore structure of coatings, are discussed in more detail later.

### **2.1.5.1 Paper specific permeation/imbibition approaches**

The investigation of paper structure-liquid interactions generally faces the problems of two-dimensionality with the dominance of interfaces. A simple measurement, widespread in the paper industry, is air permeability, represented by the Gurley-Hill S-P-S tester, (Gurley-Hill, 2001a), (ISO, 1994), or the L&W Bendtsen tester, (L&W, 2001b), (Heinemann, 1996). Drawbacks are that the transplanar flow, defined as the  $z$  direction through the cross-section of the sheet, is only through one sheet of paper, so even one pinhole will strongly influence the result. Also, the fluid used (air) is highly compressible and the sealing of the area to be measured is not trivial. A method has therefore been developed for the studies reported here to overcome the aforementioned drawbacks by using an incompressible fluid, i.e. liquid (mineral oil), that does not cause swelling or de-hydrogen-bonding of the fibres. A stack of paper is used in the form of a layered structure (more than 120 individual sheets are used) which are firmly embedded in a resin around their edges (see chapter 8).

It is problematic to link uni-directional permeability ( $z$  direction) directly with isometrically averaged porosity, as measured, for example, by oil saturation or mercury porosimetry, as is sometimes attempted. Paper is produced not only as a sheetlike formation but also under conditions of shear in the direction of the papermachine. This induces a strong directionality in the  $xy$  plane, following the machine direction. A paper structure is therefore similar in some ways to a mesophase crystal (liquid crystal) in that fibres become aligned in two dimensions. When the paper is coated, the structures formed are then not only directional but also layered.

Oil imbibition is frequently used to determine the porosity of paper. A silicone oil is generally used as a standard. As the oil imbibes it changes the overall optical properties of the paper by replacing air/solid interfaces, which are strong light scattering features, with oil/solid interfaces. As the refractive index of the oil is much

closer to that of the pigment or the fibre, the scattering potential is lost and the paper becomes less opaque and more translucent. The fall in opacity or increase in translucency is easily measured as a function of time during oil uptake. In the past, the majority of such work was carried out directly on papers. Only recently has the coating structure become the focus for specific analysis. Early work (Gate and Windle, 1973) studied the imbibition of oil into paper coatings. The general technique they developed is used in many later approaches.

Lepoutre (Lepoutre, 1978), investigated papers where the porosity was varied using different binder content and applying different calendering (compression of the paper). In the theoretical part he discusses the competitive capillarity between a consolidating ink on the surface and the pores within the coating structure. Oil was applied to the paper and, under a microscope, the progressive translucency was observed. This was achieved by viewing the progressive clarity through the sheet of an underlying dot pattern (actually a half-tone print pattern as might be seen on a newspaper picture for example). It was reported that the absorption rate decreased exponentially with latex content. In the explanation, a pore-throat picture was used. The role of latex was explained as blocking the throats or crevices and, therefore, changing the tortuosity of the structure.

Johnson *et al.* (Johnson *et al.*, 1999), (Johnson *et al.*, 1998), (Abrams *et al.*, 1996) investigated in a series of publications the porosities of different paper coatings on PET (polyethyleneterephthalate) films using mercury porosimetry. They stated the necessity for a correction for compressibility effects induced by the method. They also found a reduction in porosity with increasing latex content. In contrast to Lepoutre, they argue that shrinkage forces in the coating are promoted by the binder. This specific subject is being currently researched in more detail by a project between Omya AG and the University of Plymouth (Laudone, 2002) . Johnson *et al.* also compared mercury porosimetry with an oil imbibition method and found good agreement.

Larrondo and St. Amour (Larrondo and St-Amour, 1992), (Larrondo and St-Amour, 1995), compared mercury porosimetry to a stain imbibition method. The latter is performed by application of an excess layer of stained silicone oil. Light reflectance as a function of elapsed time was measured. Calculations involving paper caliper, sample weight and oil quantities were performed. Generally, a 10 % higher porosity of the coating layer was found using the stain method compared with mercury intrusion. Conversely, a 10 % higher porosity by mercury porosimetry was seen when testing the basepaper substrate.

The issue of the competitive spreading versus penetration of a droplet of ink into paper is discussed by Picollet *et al.* (Picollet *et al.*, 1998), for a rotogravure ink (see the following section on print methods). Some more details of this work are discussed later in the thesis in the context of droplet experiments (section 6.3).

Gane *et al.* (Gane *et al.*, 1996) also used mercury porosimetry with a compressibility correction method and involved the pore-space simulator Pore-Cor. As will be explained later in more detail, this model uses its pores and throats construction to account for shielding effects when calculating mercury percolation and subsequent permeabilities. One of the targets of this thesis is to address the validity of the permeability result from the model compared with independent experimental determination.

Karathanasis *et al.* (Karathanasis *et al.*, 2001), made a comprehensive practical study involving 20 different custom-produced papers which were printed on a six colour sheet-fed offset press. A wide range of pigment mixtures was used where the particle size distributions were analysed. The papers were also investigated using mercury porosimetry. Unfortunately, only a mean pore radius was evaluated and not a pore size distribution or a pore size gradient term. It was reported that ink setting increased with pore size but was not affected by calendering, a statement which is somewhat unclear as it was also stated that the calendering decreases pore sizes. This phenomenon was explained by the fact that probably the reduction in mean pore size was balanced by the reduced overall porosity, both parameters being governed by calendering.

The Bristow wheel is a tool specifically developed to investigate short time absorption phenomena on papers. The principle is that an applied volume of liquid imbibes into a strip of paper fixed on a rotating wheel. The wheel is brought into contact with a static fluid reservoir from which liquid flows out through a slit-shaped applicator and forms an extended stain on the moving paper. The stain length is a function of the rotation speed of the wheel and imbibition rate. Recent applications (Auslander *et al.*, 1998), (Picollet *et al.*, 1998) are still frequently found. Often a so-called wetting delay is seen, which is probably the influence of an air film captured within the paper roughness which has first to be displaced by the applied liquid.

Salminen (Salminen, 1988), studied the short time water absorption characteristics into uncoated papers with and without applying an external pressure. He used an enlarged version of a modified Bristow wheel. Results indicate a non-LW scaling. Often a more complex imbibition curve shape is observed and the rate power in time ( $t^x$ ) is observed to be greater than the expected square root ( $x > 0.5$ ). He proposed a diffusive mechanism wetting the structure ahead of the main capillary driven wetting front. The role of the external pressure in many practical applications is emphasised, especially as it overcomes any patchwork size (localised hydrophobising) in the paper.



## 2.1.6 Printing of coated paper

Table 1 gives an overview of some relevant print methods involving fluid inks and their applications. Many fundamental principles are valid for all the processes described.

Rotogravure	Flexo	Offset <i>Web offset (heatset)</i> <i>Sheet offset (non-heatset)</i>	News <i>Coldset web offset</i>	Ink-jet
Large circulation magazines and large quantity runs, especially seasonal mailorder catalogues. Some high volume books.	Packaging, paper board, e.g. food cartons, point-of-sale displays etc.	Magazines, books, advertising inserts.	Newsprint	Office, home, posters, digital photography

Table 1 Today's most important fluid ink-based printing processes.

The most important change identified during the last twenty years is the change from letterpress to lithographic or flexographic printing for the publishing market. Letterpress printing, the use of an inked typeface, dominated the market for the newspaper industry until the late 1980's. The progressive replacement by offset lithography and flexography has occurred in parallel with the development of news and information publishing methods, for example the use of digital computer-to-plate technology. This has led to increases in efficiency and something of a revolution in the newsprint industry.

The main trend in the publishing market involves the use of colour, particularly for magazine advertising and in newspaper supplements, both of which have increased in volume remarkably. Since the early 1990's there has been a dramatic increase in the number of magazines on the market. The increased diversity coming from the so-called "special interest" and "leisure" markets.

The main focus of this work is on offset printing (lithography) and is the most widespread large-scale printing process today. The lithography sector is also the most interesting sector in terms of volume growth. It comprises two types of lithographic printing which are called web offset (printed continuously from a reel) and sheet fed offset (printed discretely on sheets). The web offset process encompasses two types which are coldset and heatset, respectively. As the names suggest, the difference lies in the way the inks set-off or become "dry", as we will discuss later. The coldset inks are used for newspapers and the heatset inks are mainly used for magazines. Sheet fed lithographic printing inks are used mainly in the packaging market and the commercial high quality printing market.

The principle of offset printing is that the ink is transferred from a printing plate onto the paper having been offset via a rubber printing blanket in between. The plate consists of water-carrying and water-repellent areas, and the water repellent areas constitute the inked printed image. The aqueous solution applied to the plate is a so-called "fountain solution" or "fount" containing various additives, such as anti-corrosives, emulsifiers and wetting agents. The hydrophilic parts of the plate accept this fount. The printing rollers then apply the ink to the plate, which then transfers the ink and some of the fount to the offset blanket. The blanket then makes contact with the paper.

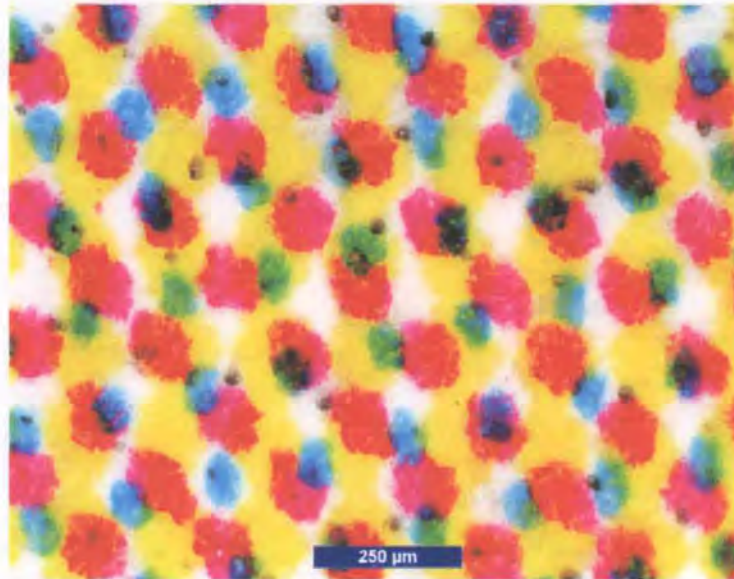


Fig. 7 Stochastic print screen as used in modern sheet fed offset (a skin tone).

The image itself can be a continuous ink film (full tone) or, to achieve a change in print density, in the form of printed dots. The print density can be changed either by adjusting the dot size or the frequency (screen) of dots. Modern technology employs a stochastic (randomly generated) screening method to avoid the regular patterning of an image, which is so readily picked up by the eye on traditional prints.

Offset inks are mixed suspensions and solutions of pigments, resins and polymer dyes in oils. The oils, known collectively as the ink vehicle, themselves are Newtonian liquids, but the rheology of the ink itself, as it interacts with the paper and the printing press, shows a complex behaviour. The absorption process of the oils into the coating layer is also complex, as the porous paper coating structure imbibes the liquid phase, leaving the solid and polymeric materials on the surface, and chromatographically separating the oils within the coating (Rousu *et al.*, 2000, Rousu *et al.*, 2001a, Rousu *et al.*, 2001b). This leads to an effective rise in viscosity of the ink and to a fast formation of an immobilised layer of binder and pigment particles on the coating surface and, therefore, to a decrease of mobile ink layer thickness. The solids rise on the paper surface leads to a tackification of the ink and eventual polymerisation of the resins completes the setting process. The rate of tackification in relation to

polymerisation is an important control parameter for ensuring good adhesion of the ink to the coating surface. The coating formulation, including binder (Rousu *et al.*, 2001b), provides the means to control this relationship.

A different situation is explained by Klemm (Klemm, 1999), who describes SC (supercalendered uncoated) paper, which has such an open, permeable porous surface that no separation of oil/resins occurs. There is no setting of the ink as such, but penetration of the whole ink body into the paper occurs. This also is the case for coldset newsprint - more ink is used, a different drying system is needed if the ink is to be set, e.g. UV sensitive resins, but usually the ink is left wet within the paper, some print gloss has to be sacrificed and the well-known smearing effect is ever present.

The advantage of coating paper with an uniform pigmented layer in respect to ink setting is clearly positive. It also assists recycling of paper fibre if the ink can be held on the coating pigment rather than having to de-ink the fibre itself. The control of tack is therefore crucial for the multicolour offset printing process. Tack is the pulling power or separation force of ink in its transfer from a press blanket to its intended printing surface. A tacky ink has high separation forces and can cause surface picking or splitting of weak papers.

### 2.1.6.1 Ink constitution

A review of recent industrial publications (Klemm, 1994), (Hanke, 1996) on printing inks, and the study of standard tests, indicate the following main liquid components of printing inks in the different print processes.

	Rotogravure	Flexo	Offset	News	Ink-jet
Solvents and oils	Toluene Xylene Ethylacetate	Water Ethanol Ethylene glycol Propylene glycol Ethoxy- and methoxy-propanol	Saturated short chain Alkanes ranging from Mineral oil fractions to vegetable oils such as Linseed oil	Mineral oils <i>new:</i> Oils from soya and linseed	Water Ethylene-glycol Diols Pyrolidone
Solid components (waxes and resins)	Polyethylene Waxes Natural Resin Talloresin Nitrocellulose Maleic-polyacrylic-vinyl resins	Maleic-, polyamide-, vinyl resins	Monoester of Fatty acids Alkyd resins	Waxes Bitumen derivates Natural resins	
Dyes		Alkali dyes			Direct dyes Acidic dyes

Table 2 Overview of typical ink compositions [ink pigment size is in the range of 0.05 - 0.50  $\mu\text{m}$ ].

The compilation in Table 2 is the base for choosing relevant test liquids for the experimentation being reported here.

### **2.1.6.2 Three basic post-print mechanisms**

The general framework of mechanisms of a process like printing is the same as for many applications where a multiphase suspension or dispersion is applied onto a solid surface which may be permeable and porous. The framework after initial application consists mainly of evaporation, absorption and curing.

Evaporation, a diffusive process, is dependent on vapour pressure and therefore strongly linked to temperature. The "escape" of volatile fluid molecules results in an increasing solids concentration at the liquid/vapour boundary; a skin formation is often observed.

Absorption on a fine porous substrate happens due to capillary forces where the Laplace pressure of the curved liquid menisci forms the driving force. Also non-Laplacian driven wetting is possible under all kinds of film flow situations, especially on uncoated papers. Furthermore, diffusion and effusion also contribute to absorption; the former relates to molecular or particulate transport into a non porous medium, e.g. a cured latex film, the latter is molecular and applies mainly to molecular mixing or exclusion. The consequence is an upconcentration of solid particles at the solid/liquid boundary by size exclusion effects. Even if the size of potential ink particles is much smaller than the mean capillary diameter it is likely that the ink particles block pore throats and junctions immediately (Toivakka *et al.*, 1992). This upconcentration of solids which can be thought of as a solidification is actually the build-up of a secondary porous layer, often with progressively reduced permeability due to small void spaces. Only in a potential final stage when liquid menisci are formed at the upper boundary of this packed solid does it start to act as a structure competing for liquid with the primary porous substrate.

Curing is a chemical process influencing often the later stages of the first two processes discussed above. The type of curing mechanism further complicates this issue. Oxidative and humidity initiated curing start from the boundary contact layer, and are applicable only for thin layer applications as access to the inner bulk is dependent on the diffusive permeability of the curing material. Light (infrared and ultraviolet), electron beam (EB) and heat-induced curing also start at the exposed surface and continue depending on the permittivity of the medium. Chemical curing, due to crosslinking or chainlinking reactions, starts everywhere in a medium at a given concentration. The impact of curing gives a further steady rise in viscosity and a potential change in temperature, although it may be only at surfaces exposed to the curing "starter". Curing also has the effect of

reducing the stickiness or adhesional properties of polymers changing them from a glue-type material to a multicrystalline spherulite solidus. The final impact is the ongoing formation of a network structure resulting in an immobilisation and solidification of the formerly fluid ink.

In this work the focus is on the offset or lithographic print process, where, after the initial pressure impulse applied to both sides of the paper from the printing nip, the above-mentioned three main mechanisms become active in the tackification and setting of an offset ink. Capillary forces and diffusion (plus limited evaporation later in the sequence of heatset web offset) remove the fluid phase from the applied ink layer causing a progressive concentration of solids towards the boundary between ink and the surface of the porous substrate. The curing (mainly oxidative) occurs ideally after the removal of the fluid components, resulting in a solidification of the ink film involving polymerisation and setting of resin binder components in the ink formulation. Previous work has shown that the assumption that the pores are in the form of a bundle of unconnected capillary tubes is insufficient to model the absorption process. Applying the LW equation with this assumption often leads to an unrealistic dimension of the effective pore radius. It also contradicts observation when comparing ink setting on fine gloss coating structures with those of coarser matt coatings. Donigian *et al.* (Donigian *et al.*, 1996), and Desjumaux *et al.* (Desjumaux *et al.*, 1998), observe this effect in specified cases, giving the explanation via the Laplace equation and the "sucking" potential of fine pores. Whilst this is an acceptable observation, no attempt was made to align this explanation with the traditional equation of flow, namely the LW equation, which predicts the contrary in terms of flow velocity.

In the case of offset inks, where the fluid is formed from alkanes in a mineral oil fraction, and/or vegetable oils, the viscosity is  $\approx 0.5 - 40$  mPas and the density  $\approx 730$  kg m<sup>-3</sup>. This, as will be argued by the author, maintains the relevance of the inertial timescale during the pore selection process within the porous network of a paper coating.

Xiang and Bousfield (Xiang and Bousfield, 1998) explained a further retardation of absorption into large capillaries by the increased drag offered by an assumed filtercake formation at the interface between ink and coating surface, associated with the large volumes of fluid absorbed by larger pores.

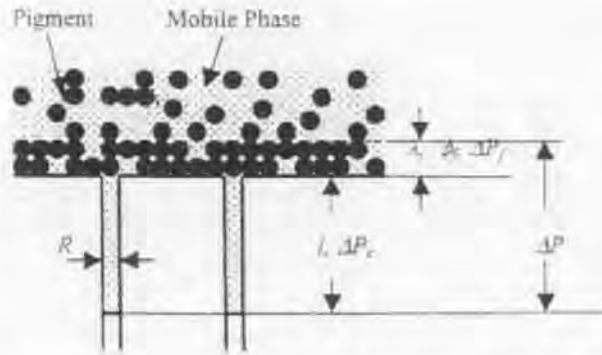


Fig. 8 The filtercake model described by (Xiang and Bousfield, 1998) (for a detailed discussion and explanation of the parameters see section 10.4.1).

However, this would also be inconsistent with the faster setting of inks on finer pore structures if it were the only retardational mechanism. To apply this model to the dynamic situation in a series of film splits, as the paper goes through a multicolour press, requires that it is possible to define an effective boundary between the immobilised filtercake and the remaining fluid ink. Work presented in this thesis demonstrates the shortcomings of the model for offset ink. Experimental evidence is presented to discredit the formation of a delineated filtercake in the offset process, except in the case of inks with an unusual high pigment content. An example of highly pigmented ink is used in the flexographic process and co-workers in the Omya AG laboratories have established the existence of a filtercake in such a case of water-based flexographic inks (Gane and Ridgway, 2001).

### 2.1.6.3 Tack reflects the rheological characteristics of ink during application

During the offset print process the ink experiences pressure-induced shear and several stages of film splitting where cavitation and filamentation can occur. The breaking length of the filaments depends on the "shortness" of the ink, a phenomenological term which is important for the printer. In order to achieve a level glossy ink film the microscopic levelling of the broken filaments, which are sometimes recognised on a macroscopic level as an orange peel effect is crucial. (The orange peel effect is more well-known in the context of paper filmpress coating.) Levelling can happen due to gravity on slow single colour presses but more strongly due to spreading forces if the surface energy of the substrate is high enough (Desjumaux *et al.*, 1998), and due to the elastic relaxation of the induced film split roughness (Xiang *et al.*, 1998). The process is retarded with growing viscosity or tack due to fluid loss and viscous structure rebuild, through oil removal from the ink by substrate absorption and rearrangement of the interactive polymer components. The latter results in a decreasing thickness of the mobile ink layer, and the phenomenological effect of tack build-up at the early stages of absorption will be related later in this work with the viscous properties of the ink during fluid loss.

## **2.2 Environmental situation for print media**

Printing on paper is basically a liquid-solid interaction occurring on a natural substrate. Attention here will be given to the origin of the solid and its implication for the interaction.

### **2.2.1 Fibre versus pigment**

Fibres used in paper manufacturing are coming mainly from renewable wood resources. The use of mineral filler and pigments was boosted by high and fluctuating pulp prices in the past. The production of natural ground pigments is more stable and significantly lower in their market pricing [about 22% of the fibre price, (Gane, 2001)] which reflects the lower total energy consumption and pollution of pigment production. From this point of view the use of mineral pigments can be logically promoted.

### **2.2.2 Low and high waste pigments**

First of all, paper pigments have to be classified following chemical/toxicological considerations which dissuade the use of barium, aluminium and titanium based compounds. (A compilation of candidate materials is given in Appendix A, Table A 5).

Talc, clay and calcium carbonate, the most widely used paper pigments, are all environmentally abundant as they are minerals widely present in deposits all over the world.  $\text{CaCO}_3$  is often used in agriculture and forestry to neutralise acidic soils (in Germany for example approx. 1.3 million tonnes per year).

The next potential argument is directly linked to environmental considerations in the domain of mining the raw material. Here we have to consider the amount of energy consumed in the manufacturing of the mineral pigments and to a certain extent the degree of de-naturing of a landscape.

Ground  $\text{CaCO}_3$  is a so-called low waste pigment, which means that normally 80-95 % of the raw stone material is used, lowering the cost of interim transportation and beneficiation engineering towards the usable pigment product. In primary clay mining the typical win from kaolinised granite is around 15 %, the situation for secondary clay deposits is somewhat better, as is the case of talc having a win of around 20-40 %, although exact numbers are difficult to obtain.

### **2.2.3 Calcium carbonate (CaCO<sub>3</sub>)**

For many years the use of clay was standard in the production process of paper under acid papermaking conditions. Clay is being rapidly superseded by calcium carbonate for technical reasons previously described.

Omya AG, formerly Plüss-Staufner, pioneered the use of natural ground carbonate as a paper filler and later as a coating pigment. Of course the use of CaCO<sub>3</sub> required the change from acidic to neutral paper production (or slightly basic). However, the conversion to neutral and alkaline papermaking has also had other beneficial effects. In particular, the permanence of paper against ageing has been dramatically improved by the change and buffering in pH. Tremendous efforts have to be undertaken to preserve and renovate ancient documents and literature, so it should therefore be self-evident that the use of neutral papermaking should be promoted and supported.

The summarised benefits of CaCO<sub>3</sub> usage are therefore:

- not toxic (can be easily purified to pharmaceutical quality if required),
- low waste production,
- produces chemically permanent (long term stable) paper.

These are the motivations for encouraging the study how to understand, improve and expand the use of this pigment in various printing applications.

### **2.2.4 New concepts in printing processes and ink formulations**

A further point of environmental interest is on the liquid side of the equation. Traditional ink formulations are challenged today; as mineral oil reserves tend to become exhausted, printing ink manufacturers are under pressure to reduce the content of mineral oil in their products in favour of vegetable oils. Another reason to replace mineral oil is the contribution of hydrocarbon emissions to the formation of "summer smog". A further argument is bio-degradability. Of course, these points do not remain undisputed. In the printing industry a debate is going on about the use of mineral oil. Different opinions are displayed for example on the Internet and some standpoints are discussed and summarised in the following.



#### 2.2.4.1 Offset-inks: mineral versus vegetable oils and derivatives

One main difference between mineral oil and the fatty acid esters proposed for substituting them lies in their evaporation behaviour. While mineral oil evaporates at acceptably high temperatures, fatty acid esters need much higher temperatures still and tend to decompose as heat is applied. With heat set web-offset inks, therefore, large problems remain. At least, web velocity has to be reduced and the drier temperature must be raised. Typically, the web temperature has to be raised from 120 °C to 150 °C. This is not only expensive, but also a clear disadvantage to the environment. It is also unlikely that evaporation actually plays an important role for heatset inks as the boiling points are so high and the residence time in a print drier is relatively short. Of more importance is the viscosity relationship with increasing temperature. The fall in viscosity speeds imbibition and so ink concentration. Simultaneously, so-called resins polymerise.

Generally, sheet-fed offset lithographic inks avoiding mineral oils are stated by the manufacturers to perform equally well. This is often not the case, and the questionable claims derive probably from the "environmental" marketing issues. To assist acceptance of such inks it is paramount to understand their interactions with coating and not to pursue one to one replacement.

Linked to these topics is the question of odour development. Positively, within the print shop, the cold set processes with vegetable oil-based inks are reported to give less discernible emissions.

The substances to replace mineral oil are not actually vegetable oils as such. Simple vegetable oils would have viscosities which are too high. They are instead fatty acid triesters of glycerol or fatty acid alcohol monoesters.

The micromechanisms of the absorption of different oils ranging from mineral to vegetable origins, in pure form and in various mixtures were studied recently by Rousu *et al.*, (Rousu *et al.*, 2000), (Rousu *et al.*, 2001a), (Rousu *et al.*, 2001b), (Rousu *et al.*, 2001c). The outcome is that, as a result of the chromatographic separation of the ink components, mineral oil was seen to form the wetting front ahead of the "slower" vegetable oil.

Dempewolf (Dempewolf, 1994) states that the properties of mineral oils are indispensable in the formulation of sheet-fed offset inks where fast drying is required and, in heat-set, a certain volatility. He also stresses in his pro mineral oil argumentation that the environmental impacts of an intensive rape or linseed cultivation must be considered. An emission of nitrogen oxides from such large-scale cultivation would contribute, he predicts, to the greenhouse effect some hundred times stronger than carbon dioxide. The same standpoint is defended by Siegrist (Siegrist, 1994). Also Theiler (Theiler, 1994) mentions the insufficient volatility of vegetable oils and

adds the drawback in deinking due to the partial hydrophilicity of the vegetable derivatives, and refers to acknowledged runnability problems. Klemm (Klemm, 1994) emphasises the inconsistent properties of vegetable-based products, where changes in the climate and the use of fertilisers leads to changing composition of the natural products and, therefore, to a potential quality fluctuation of the end product.

Lanet and Gandini (Lanet and Gandini, 1989) consider the waterless offset process where the non-image areas on the plate are not fountain solution wetted but covered with a PDMS (polydimethylsiloxane)-based compound (so-called Toray plate). A weak fluid boundary layer develops and enables the release of the ink film. Here a vegetable oil based ink showed a weak tendency to diffuse into the PDMS layer, an effect which in practice may prove to be detrimental in terms of ink release.

A field where vegetable oil-based inks are very popular is in newspaper printing, particularly in the US. American newspaper printers hold that the use of mineral oil-free cold set inks is not only environmentally friendly, but also increases product quality.

Among the advantages quoted are:

- less ink rub-off to the reader's fingers,
- more brilliant colours,
- no misting (formation of fine ink droplets around the distributor roller train),
- less ink consumption per unit area of print,
- lower hydrocarbon emissions.

The advantages they give over mineral oils include low volatile organic compounds (VOC), low toxicity and being supplied from renewable resources.

While European ink makers employ linseed oil as their favourite drying oil, and for dissolving the soft resins, American inks are more soyabean oil-based. This is not only because soyabean farmers are an important factor of the American economy, but also because soya oil esters are more similar to mineral oil than linseed products. The linseed oil dominance for Europe is recently challenged by rape seed oil and its esters, predominant in central Europe, and wood oil and its esters, more in Scandinavia and Finland.

## **2.2.5 Waterborne inks**

Waterborne inks today are mainly used in ink-jet and flexographic printing, although the apparent contradiction of a water-based ink in a waterless press has been used for UV curing inks on the waterless Toray plate.

Some aspects of ink-jet printing are discussed and partly analysed in chapter 6

### **2.2.5.1 Flexographic printing**

Flexographic printing, with its use of environmentally friendly water-based inks, is increasing in importance especially for 'point of sale packaging' due to the requirement to create marketing appeal for cartons and boxes. The development of flexography over the years has been described by Moir (Moir, 1994). High standards of print quality are nowadays expected and, because of this, coated grades of bleached board and unbleached Kraft liner are in increasing demand. For such printing using water-based flexographic inks, rapid drying characteristics are essential, and can be achieved through evaporative loss aided by additives which reduce surface energy and increase fluid phase partial pressure, and by providing strongly absorptive coating layers, which are of particular importance when considering multi-colour formats. Flexographic inks have been developed for use on a wide range of substrates, these include non-absorbent films and highly absorbent heavy weight coated packaging grades. The rheological behaviour of low-viscosity, water-reducible flexographic printing inks has been investigated by Havlinova *et al.* (Havlinova *et al.*, 1999). They conclude that the inks exhibit pseudoplastic flow behaviour. The ink drying characteristics are achieved by a combination of rapid evaporation of the water-based fluid phase together with some absorption where possible into a coating structure. The increasing diversity of print formats required for sophisticated aesthetically pleasing customer impression demands the design of complex multi-colour formats. Trends are emerging in which the control of the balance between feathering, fill-in and mechanical pin-holing means that increasingly reduced inks are being used (Finley, 1997). This places greater demands on the designed absorbency of coated substrates. A recent study based on some of the techniques developed and used in this thesis was performed by Gane and Ridgway (Gane and Ridgway, 2000).

### **2.2.5.2 Ink-jet**

Ink-jet printing is a strongly emerging technology. It was the breakthrough for the end consumer to get colour printing at a reasonable price and with steadily growing quality. A growth in the ink-jet market is expected as traditional film photography is slowly being displaced by digital technology. This allows the whole chain of

picture "creation" to be in the hand of the consumer, which includes a final ink-jet printout on a highly specialised paper. Qualities close to photographic paper standards are already possible. It is beyond the scope of this work to review the drop ejection technologies in use today. However, from the paper side, developments are only possible with a deeper understanding of the contributing mechanisms of liquid imbibition. The work presented in this thesis is invoking interest from several producers of high quality ink-jet papers. The inks are briefly discussed in section 6.2.1; one important parameter is the anionic charge of the dyes used in the ink.

Typical ink-jet paper works by one of the following two strategies:

1. Layers of hydrogels, superabsorbers etc., plus cationic charge over a bright substrate (Fig. 9). As an example, Yoldas (Yoldas, 1999) describes how to formulate a cationic sol-gel coating with high ink fluid (water) immobilisation properties. This is possible by a transient local swelling of the layer - as much as 600 - 700 %! This mechanism leads to a virtual dry state immediately and results in a dense and accurate dye deposition.

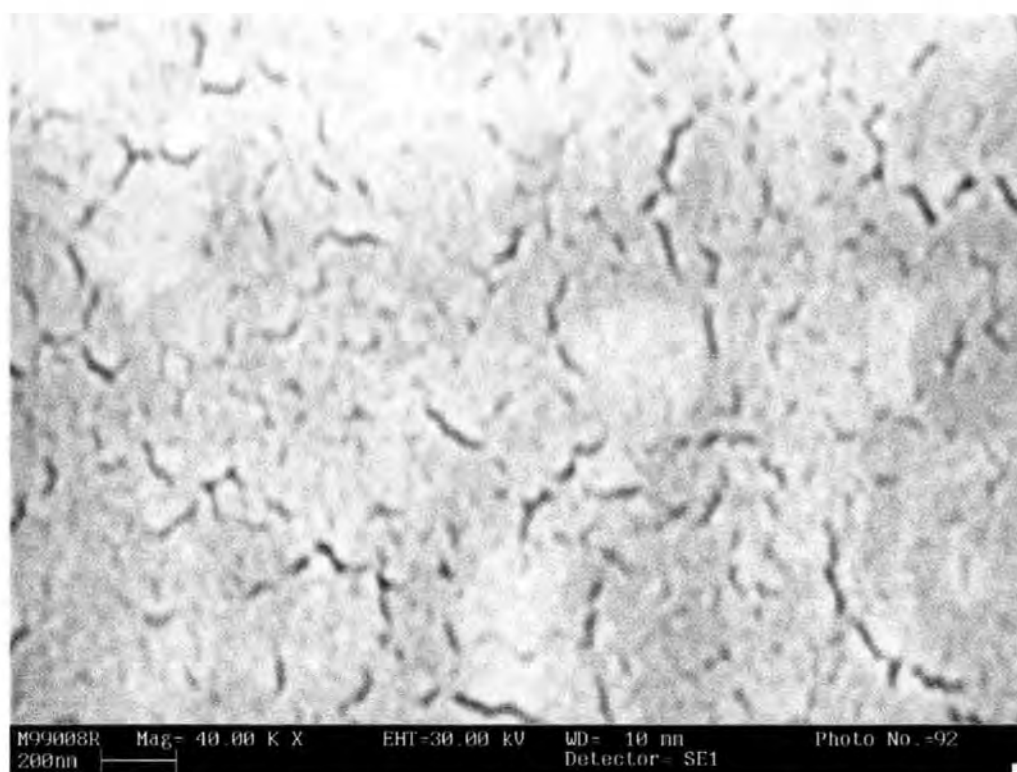
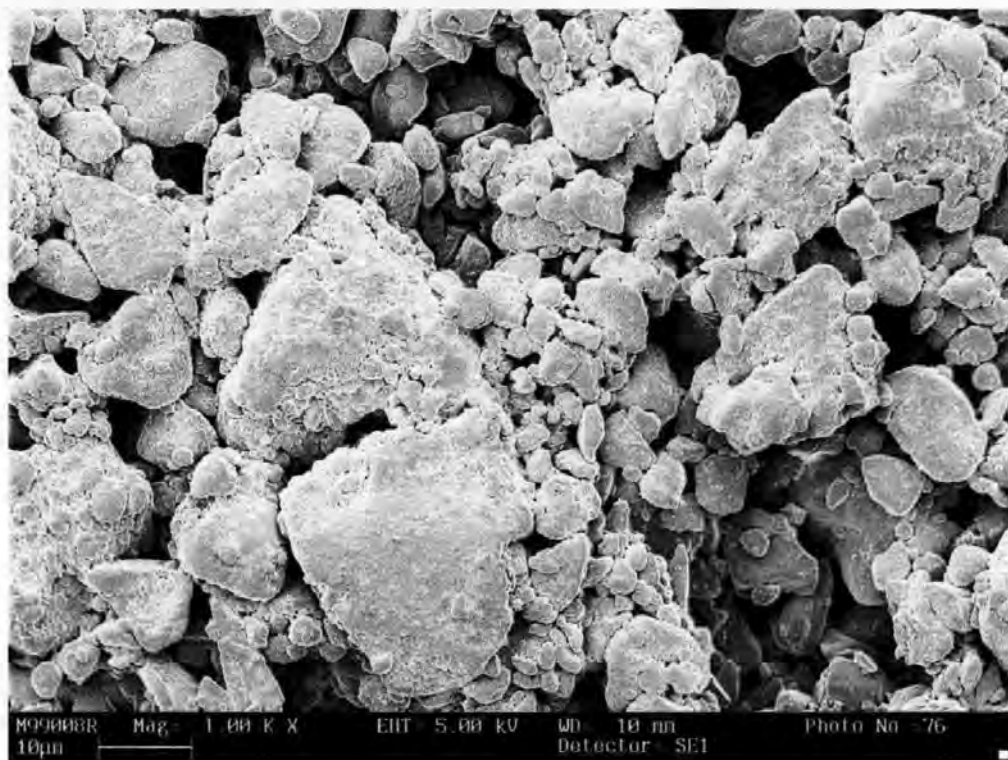


Fig. 9 A layer of superabsorbent gel. (It remains unclear if the microcracks are an artefact of the electron beam or if they are a functional component of the layer).

- Blend of coarse and super fine pigments, binder, additives plus cationic charge (Fig. 10). This approach today involves highly expensive porous, high surface area structures of precipitated silica. Replacement by  $\text{CaCO}_3$ -based pigmentation would bring significant savings.



*Fig. 10 A highly pigmented ink-jet coating layer.*

An application of ink-jet printing with far-reaching potential, which is under development by various industries, is to apply with ink-jet technology a thin layer of liquid having solid state semi-conductor properties onto a planar isolating substrate. In this way, planar microprocessors could be produced at very low prices.

### **2.3 Interfacial theory**

In the previous sections we have identified the important role of liquid-solid interactions in paper printing. Therefore, it seems desirable to expand this review beyond what was done exclusively in the field of paper science.

To understand the fascinating phenomena of wetting and capillarity it is worthwhile to have a look at some fundamental theory and previously published work to illuminate the mechanisms being proposed to explain them. For example Albert Einstein's first publication, written in Zürich, was dedicated to capillarity (Einstein, 1902). Although he was not researching capillary phenomena directly, he used surface tension and

thermodynamic argumentation to display and fortify the theory of molecules and atoms, which at that time was still in doubt.

Later, many interesting contributions were made linking fluid- and interactional parameters with the geometry of an encountered system. Let's start with one of the most important basic surface chemical parameters, namely the surface free energy.

### 2.3.1 The nature of surface free energy

Surface free energy,  $\gamma$ , is an acting potential derived from an excess of energy defined thermodynamically over a unit interfacial area. This excess is due to an imbalance of static and dynamic interparticulate (molecular) interactions at a boundary (interface) of a body in contrast to its bulk properties. It is assumed within the bulk that these interactions are spatially balanced and equilibrated. This may be expressed as:

$$\gamma = \left( \frac{\partial U}{\partial A} \right)_{N,S,V} = \left( \frac{\partial H}{\partial A} \right)_{N,S,P} = \left( \frac{\partial F}{\partial A} \right)_{N,V,T} = \left( \frac{\partial G}{\partial A} \right)_{N,T,P} \quad \text{Eq. 3}$$

where  $U$  is the internal energy (a sum of a vast array of energy forms, including translational, rotational, oscillatory, bond-energy, lattice energy etc.),  $S$  : entropy,  $H$  : enthalpy,  $F$  : is here the Helmholtz energy,  $G$  : Gibbs free energy,  $N$  : Avogadro's number,  $P$  : pressure,  $V$  : volume,  $T$  : absolute temperature and  $A$  : area.

Furthermore, the following relationships hold

$$H = U + PV, \quad F = U - TS, \quad G = H - TS = U - TS + PV \quad \mu_i = H_{m,i} - TS_{m,i} \quad \text{Eq. 4}$$

where  $\mu$  is the chemical potential, the subscript  $m$  is the number of moles and  $i$  stands for interface. The surface free energy ( $\text{Jm}^{-2}$ ), represents the work (energy) which is needed to form a surface i.e. to bring molecules from the interior of a continuous phase into the surface region. This is used directly, for example, when measuring the surface free energy of crystals by cleavage. In the case of solids, surface free energy is not only the work spent in forming the unit area of the surface but it also incorporates the surface stress which involves the work done in stretching a surface (Good and van Oss, 1992). The term surface tension, rather than surface energy, is somewhat more meaningful for liquids and vapours as it expresses the reformation potential of the surface to minimise free energy. The term surface tension ( $\text{Nm}^{-1}$ ) is used as a mathematical identity with surface free energy, i.e. it is convenient to handle thermodynamic problems as energies while hydrostatic approaches are more easily conceived in terms of tensions.

### 2.3.2 Dispersive and polar components of surface free energy

Intermolecular forces contributing to the origin of an effective surface energy are mainly van der Waals and Lewis acid-base interactions. An overview is given by Lee (Lee, 1993), reviewing the surface tension component (STC) theory developed by van Oss and co-workers (van Oss *et al.*, 1986), (van Oss *et al.*, 1988), (van Oss *et al.*, 1989), (Good and van Oss, 1992).

Lifshitz-van der Waals (LvW) interactions, (formerly called dispersive interactions) result from an uneven charge (electron density) distribution in (net) uncharged molecules and are relatively weak compared to other interactions, but they are ubiquitous, i.e. they act between all kinds of molecules and particles. These are the forces that hold a drop of liquid, such as water, on a vertical surface of absolutely hydrophobic material such as Teflon™. LvW interactions are composed of London dispersion forces, (<sup>d</sup>), caused by a fluctuating electron distribution (the only forces present in symmetrical non polar (here termed apolar) molecules like aliphatic alkanes etc.), Debye dipole-induced dipole polarisation, (<sup>i</sup>), and Keesom dipole-dipole orientation (<sup>p</sup>), as denoted in Eq. 5:

$$\gamma^{LvW} = \gamma^d + \gamma^i + \gamma^p \quad \text{Eq. 5}$$

Lewis acid-base (AB) interactions occur mainly through specific electron donor-acceptor interaction sites between uncharged surfaces and molecules, and mainly through the formation of hydrogen bonds (forming a strong contribution to polarity), themselves a special case of the hydrogen (or proton) donor-acceptor interaction.

$$\gamma^{AB} = 2(\gamma^+ \gamma^-)^{0.5} \quad \text{Eq. 6}$$

In addition, electrostatic Coulombic forces act between charged surfaces and ions.

A liquid contacting a solid surface forms an interaction based on the relative surface tension of the fluid, defined in relation to the surrounding vapour, the surface energy of the substrate, such that a balance is established between the surface wettability of the substrate by the liquid and the retaining surface tension forming a droplet being subject to external forces, such as gravity etc. This balance establishes a macroscopic contact angle. The way these forces (except Coulombic ones) interact, and the resultant impact on contact angle, is shown schematically in Fig. 11, (van Oss *et al.*, 1986). Experimentally the contact angle described by the STC theory is measured using a static, sessile, droplet.

---

™ PTFE (polytetrafluorethylene)

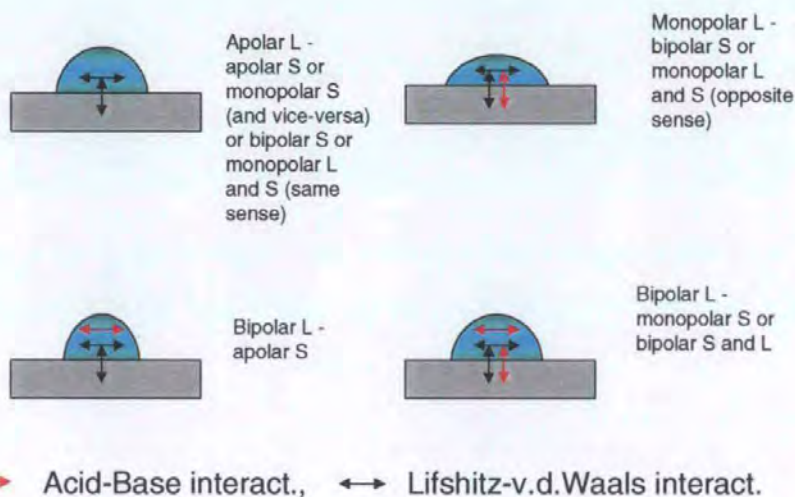


Fig. 11 Influence of different phase interactions ( $L = \text{liquid}$ ,  $S = \text{solid}$ ) and their effect on contact angle.

Regarding the studies undertaken in this thesis, the STC theory has some impact. Holysz and Chibowski (Holysz and Chibowski, 1994) analysed the polar and LvW- contributions to the surface energy of  $\text{CaCO}_3$  (as will be described in section 2.5.3.2). They found a strong monopolar surface with  $\gamma_s^- = 79 \text{ mJ m}^{-2}$  and a LvW component of  $48 \text{ mJ m}^{-2}$ .

The application of the STC theory explains why water can displace oil on some mineral surfaces. Normally, one would expect that the oil, having a lower surface tension (= lower cohesivity) than water, and therefore also a smaller contact angle, would spread or wet preferentially on a given solid. But if we consider a solid surface with a strong polar component, e.g. hydroxy-groups, then the hydrogen bonding forces, which of course can only be established to a polar molecule like water and not to an alkane, may be stronger than the omnipresent LvW forces (Robin, 2001).

The theory of separable surface tension components is not undisputed however. Neumann *et al.* have countered the STC theory using an equation of state approach. Recent examples are the papers of Kwok *et al.* (Kwok *et al.*, 1998) and del Rio *et al.* (del Rio *et al.*, 1998). This latter work uses dynamic contact angle hysteresis and a polynomial fitting algorithm of the droplet meniscus profile, using a technique called ADSA-P (axisymmetric drop shape analysis-profile) to identify slip-stick behaviour on a low energy, inert surface for some liquids. This behaviour would explain false or shifted readings using the stationary sessile drop technique.

### 2.3.3 Liquids

In a liquid the molecules are generally assumed to be randomly positioned and have an appreciable mobility. This picture precludes any debated effects of so-called memory effects in respect to dilute solutions of salts



and/or macromolecules. The mobility allows for quite simple measurements of the surface tension: using amongst others, the Wilhelmy plate, de Nouey ring, drop or bubble volume/detachment technique (a recent example is given by Miller *et al.* (Miller *et al.*, 1998) or a contact angle method. With these measurements, the interfacial tension can be determined, namely the liquid/vapour interface tension,  $\gamma_{LV}$ . For most cases, the obtained  $\gamma_{LV}$  can be assumed to be an approximation of  $\gamma_L$ , i.e. the cohesive "tension" of the liquid.

If only a small amount of liquid is present the microtechnique developed by Miller and Tyomkin (Miller and Tyomkin, 1992), is of interest. The method is based on a small liquid bridge between a sphere and a flat surface of known surface characteristic. A balance is used to measure the forces which oppose the separation of the sphere from the plate via the liquid bridge.

### 2.3.4 Solids

Adamson (Adamson, 1990) gives a thorough overview of the surface chemistry of solids. A solid, by definition, is condensed matter that is rigid and resists strain. A solid body responds to applied forces in the form of an elastic stress and its shape is determined more by its history than by surface tensional forces. The main reason for this is the low mobility of the surface atoms of a solid surface. If we imagine the formation of a fresh surface, let us say by cleavage, then at first the atoms stay in the same positions as they occupied in the bulk lattice. Then the atoms start to rearrange into their new equilibrium positions or begin to react with the environment in which they find themselves. In contrast, a liquid undergoes these steps virtually instantaneously under the actions of diffusion and convection. Therefore, a clean cleavage surface of a crystal will have a different surface energy than a ground or abraded surface of the same material. Grinding may induce local surface changes in general physical properties, e.g. density. In the case of quartz, for example, it is known that it forms a relatively deep amorphous surface layer. For metals this phenomenon is known as the Beilby layer which has the appearance of a viscous liquid which flows into surface irregularities such as scratches and cracks. Also, heat treatment will change surface properties.

A severe practical problem when discussing surface energetics of solids is that pure solid surfaces rarely exist. It is well known that high energy surfaces like mineral crystals immediately adsorb other species and whatever contaminants may come into contact onto their surface. Gao *et al.* (Gao *et al.*, 1998) go so far as to expect that an adsorbed liquid film is always present at any given solid interface.

In this work, the effect of surface contamination is illustrated by the behaviour of a calcite crystal. When the surface was freshly ground, it showed complete wetting by water, but after the crystal was left for some days in the laboratory atmosphere a defined contact angle  $> 45^\circ$  was measured. This issue complicates or even disables most equilibrium approaches to determine the intrinsic surface free energy of solids.

#### **2.3.4.1 The surface tension of crystallite particles**

Mineral particles, like many solids, consist of a multitude of small crystals or crystallites which form the solid mass. These crystals have different internal and cleavage planes which are determined by the geometrical structure of the atoms as they are bonded together in the condensed solid. The surface energies of these different crystal faces can differ dramatically (Adamson, 1990). The edge tension of a crystal, for example, is different from the surface energies of the planes, although calculations of these values are difficult and very sensitive to the form of lattice potential used. However, the edge tension is of special interest because of its influence on liquid as it progresses across a surface by creeping around or via the crystallite grain boundaries.

Crystals such as diamond, containing only covalent bonded atoms are quite rare and show very high cohesive forces. Many attempts have been made to calculate the surface energy of more common simple ionic crystals but without rigorous results. In the case of molecular crystals, including numerous salts with molecular ions, such as  $\text{CaCO}_3$  and a host of similar paper-related pigments, theoretical treatment is difficult because relatively long range van der Waals forces are involved. Surface distortion in molecular crystals, which can include reorientation effects, cannot be adequately modelled.

In practice, maybe the most helpful method is to measure the surface tension of a molten salt and to extrapolate to room temperature. Astoundingly this semi-empirical approach yields probably the most reliable results. Unfortunately, the method is not usable with salts that will decompose under elevated temperatures prior to reaching the melting point. Carbonates, for example, are known to split into oxides and  $\text{CO}_2$  at temperatures in the order of  $400^\circ\text{C}$ .

#### **2.3.4.2 Calcium carbonate ( $\text{CaCO}_3$ )**

The industrial modifications, properties and parameters of  $\text{CaCO}_3$  have been discussed earlier (section 2.1.2). Here we will shortly review some of the specific work carried out to determine the surface energy of  $\text{CaCO}_3$ .

In Fig. 12, the Ca cations (red), are at the corners and body centre position of a trigonal lattice with  $\alpha=46^\circ$  and a lattice parameter of 0.6361 nm. The planar  $\text{CO}_3$  (blue) anions are at about 1/4 and 3/4 the distance along the major diagonal. Each Ca atom has 6 closest oxygen atoms. The  $\text{CO}_3$  groups are arranged in a flat triangle with the C in the middle.

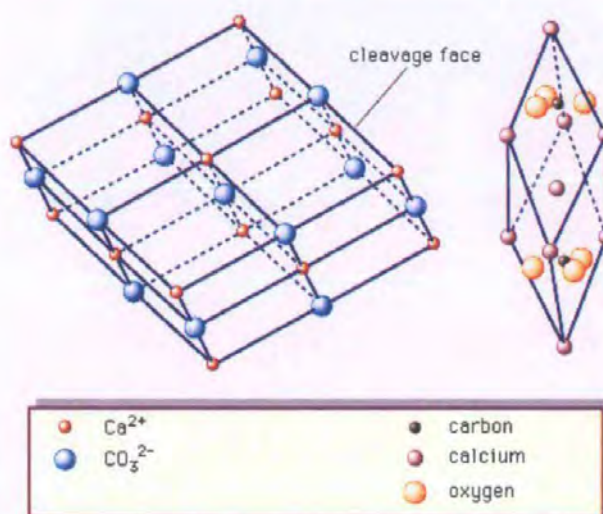


Fig. 12 The crystal structure of calcite<sup>3</sup>. This schematic diagram shows both (left) the true unit cell, the acute rhombohedron, and (right) an alternative cell based on the cleavage rhombohedron (Gane, 2001).

Stipp *et al.* (Stipp *et al.*, 1996) studied surfaces of a calcite crystal freshly after cleavage and during the following hours and days. They used different microscopy techniques, such as scanning force microscopy, and observed dynamic surface structural changes, such as hillocks and depressions or holes. As surface diffusion is considered unlikely for an ionic solid, the process was explained by an adsorbed water layer which they had observed earlier, even in ultra high vacuum. Chiarello *et al.* (Chiarello *et al.*, 1993) are cited, who found in one case a layer of water on  $\text{CaCO}_3$  with a thickness of 20 monolayers. The observed surface dynamics were thought to be caused by an equilibrium between this layer and the atmosphere. A consequence of this phenomenon is acidic attack on limestone and marble, and in particular on marble-clad buildings, this attack not being restricted to rainfall periods.

Holysz and Chibowski (Holysz and Chibowski, 1994) used a wicking technique and the Lucas-Washburn (LW) equation (Lucas, 1918, Washburn, 1921) to determine the surface free energy of  $\text{CaCO}_3$ . They calculated a Lifshitz-van der Waals interaction of  $48 \text{ mJ m}^{-2}$  and an acid-base electron donor parameter of  $79.0 \text{ mJ m}^{-2}$ . The

<sup>3</sup> Encyclopaedia Britannica.

sum of these values seems to be low when compared to other approaches. The possible causes are explained later in this work considering adsorbed contamination layers and insufficiency of the LW dynamics.

Papirer *et al.* (Papirer *et al.*, 1984) found  $58 \pm 6 \text{ mJm}^{-2}$  for the dispersive component of the surface energy of  $\text{CaCO}_3$  using inverse gas chromatography. The values reported by Keller and Luner (Keller and Luner, 2000), are quite different. Using the same technique they found surface energy values for ground chalk samples of 140-180  $\text{mJm}^{-2}$ , for marble and precipitated (PCC)  $\text{CaCO}_3$ , 55  $\text{mJm}^{-2}$  and for thermally treated PCC, 250  $\text{mJm}^{-2}$ . The differences are partially explained by adsorbed water; however, the difference relating to chalk samples remains open especially as trace element contamination was found to be minor (under 0.44%).

Janczuk *et al.*, (Janczuk *et al.*, 1986) used contact angle measurement (static sessile drop) on prepared marble surfaces and calculated theoretical values using the surface tension component theory. Preparation included pre-covering the surface with different organic liquids. They observed the build-up of an adsorbed water film around the applied water drop which lowers the marble surface energy to that of the value of water. They give values for marble as: a dispersive interaction of 64  $\text{mJm}^{-2}$  and a polar component of 106.6  $\text{mJm}^{-2}$ . Compounding the problem may be the influence of the crystal plane distribution which is affected by the sample production technique.

Adamson (Adamson, 1990) summarises a number of crystal cleavage experiments, among which, for  $\text{CaCO}_3$ , the value of 230  $\text{mJm}^{-2}$  is given for the 001 plane.

In summary, these results suggest that the high values approach those of the intrinsic values of the material, while the lower values report the surface free energy as it is reduced towards the value of the adsorbate present, which is probably water.

### **2.3.5 Phase interactions**

When two or more phases come in contact with each other a number of interactive phenomena occur. These involve liquid, vapour and solid phases which control miscibility and diffusivity, and in the case of solids and liquids, the resulting adhesion or failure to adhere, i.e. rejection (commonly expressed as reticulation). An equilibrium condition is established when cohesive forces at the liquid-vapour or gas interface balance the adhesion forces at the liquid/solid/gas interface and the external forces such as gravity. Viscosity acts to retard

any motion resulting from this equilibrium in capillaries or to dampen oscillation about this equilibrium on the surface as it forms a typical contact angle, Fig. 13.

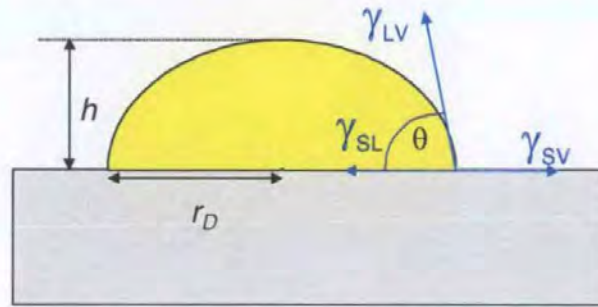


Fig. 13 Balance of tensions acting on a sessile drop as viewed in cross-section.

The force balance shown in Fig. 13 is known as the Young equation:

$$\gamma_{SV} = \gamma_{SL} + \gamma_{LV} \cos \theta$$

Eq. 7

where  $\gamma_{SV}$  is the surface free energy of the solid-vapour interface.

At the three phase confluence, the contact angle,  $\theta$ , describes the resultant of the mutual interaction of the liquid surface tension,  $\gamma_{LV}$ , and the adhesion forces of the solid/liquid interface attracting the liquid in an attempt to cover the solid and so reduce the apparent free surface energy. If complete wetting occurs,  $\theta$  is zero. Any deviation of  $\theta$  from zero lowers the wettability and therefore the intrinsic wetting force of the liquid front.

This relationship, (Eq. 7), is only fully valid on an absolutely smooth, pure and inert surface. Nevertheless, the equation is the basis upon which many approaches are based to calculate the surface free energy of the solid phase or, more precisely, the solid/vapour interfacial energy even if the solid is not smooth or chemically homogeneous by using a liquid of known surface tension characteristics. In practice,  $\gamma_{LV}$  is easily measurable, as previously mentioned, by means of the Wilhelmy plate or the de Nouey ring method, both based on a gravimetric determination of the "pull-force" of a well-defined wetting line (assuming full wetting). The remaining term  $\gamma_{SV} - \gamma_{SL}$ , however, is not easily separable. Therefore, there exist a range of semi-empirical models, like the Girifalco-Good-Fowkes-Young approach, Eq. 8, as referred in Adamson (Adamson, 1990). A table of such equations is given by Grundke *et al.* (Grundke *et al.*, 1991).

$$\cos \theta = -1 + \frac{2(\gamma_s^{LW} \gamma_L^{LW})^{0.5}}{\gamma_L}$$

Eq. 8

In the presence of a very thin film of adsorbed liquid, a surface parameter called the disjoining pressure should be taken into account in thermodynamic considerations. For such a thin film (< 10 nm) some of the assumed bulk properties of the same liquid are no longer valid. A recent view and contribution to the subject is given by Lee (Lee, 1999). The disjoining pressure,  $\Pi$ , is a function of film thickness and can be viewed as the difference between the normal component of the film pressure  $\Pi_N$  (in equilibrium with the vapour phase pressure,  $P_V = \Pi_N$ ) and the pressure in the bulk liquid phase,  $P_L$ .

$$\Pi(h) = \Pi_N(h) - P_L = P_V - P_L \quad \text{Eq. 9}$$

and

$$\Pi(h) = -\left\{(\delta G(h) / \delta h)\right\}_{T, \mu} \quad \text{Eq. 10}$$

where  $\delta h$  is the change in thickness of the film and  $\delta G$  is the change in Gibbs free energy according to the Frumkin-Derjaguin theory (Lee, 1993). The equilibrium macroscopic contact angle,  $\theta_e$ , is a function of the disjoining pressure:

$$\gamma_{LV} \cos \theta_e = \gamma_{LV} + \int_0^{\infty} \Pi(h) dh \quad \text{Eq. 11}$$

One consequence of the presence of adsorbed liquid films is that the curvature of a forming meniscus increases as a function of this film thickness  $h$ . Tuller *et al.* (Tuller *et al.*, 1999) make the link between adsorbed liquid films and film flow, the disjoining pressure, capillary condensation, meniscus dynamics and imbibition into complex pore geometries. Some of these mechanisms are discussed later.

### 2.3.6 Influence of surface micro-topography

It is known that the surface topography and roughness have a strong effect on contact angle. This is dramatically illustrated on some plant leaves, such as the Lotus flower and plants from the cabbage or Lupin family, as depicted in Fig. 14. The surface of the plant leaf is covered with dendritic wax crystallites, (Barthlott, 1990, Barthlott, 2000). The surface free energy of a wax is relatively low and a drop of water on a smooth surface of this wax material would show a contact angle  $> 90^\circ$  but probably  $< 120^\circ$ . The structural impact of the crystallites derives from the exposed tips and edges of the dendritic features which minimise the solid/liquid contact area, resulting in a dominance of the cohesive forces of the liquid drop striving for a spherical shape. As a result, a

complete repellence can be observed with a contact angle approaching  $180^\circ$  and the droplet rolls off the surface leaving no trace. This is an extreme example, actually referred to as the Lotus effect, of how surface roughness can strongly affect the contact angle and is creating strong industrial interest because of the potential as a dirt repellent and for developing self-cleaning properties of protective surfaces. Problems, however, arise from mechanical instability as artificial surfaces, unlike plant structures, are not self-renewing.



Fig. 14 Lotus effect on Lupin (*Lupinus polyphyllus*) in the author's garden.

A contrasting phenomenon is also known when the intrinsic contact angle is relatively low, say  $< 45^\circ$ . A designed textured surface can act to enhance the wetting, the apparent contact angle becomes  $0^\circ$  and the phenomenon is called super-wettability.

Lucassen *et al.* (Lucassen *et al.*, 1992) analysed the critical wetting on specially shaped surfaces. They showed that a solid surface can be designed in such a way that the contact angle is of indifferent character. This means that, dependent on the position of the liquid front in relation to the solid base plane, the behaviour may change from complete wetting to non-wetting. They used a Sinclair cuspid, machined from PVC and soap-films to demonstrate this behaviour. Possibilities are being discussed today arising from the potential use of surfaces, covered with specifically designed structures on a micro or even nano level.

### 2.3.7 Contact angle measurement

The contact angle of a droplet can be measured by viewing it from the side, either statically or dynamically. In the first case a droplet is positioned at the solid surface and after an equilibration time the contact angle is measured. In a dynamic measurement the time dependent formation process of the contact angle is monitored.

Alternatively, top view measurements can be performed determining the height,  $h$ , and diameter,  $2r_D$ , of a droplet. Also apex curvature determination and extrapolation may be carried out using confocal scanning or colloidal probe microscopy by applying Eq. 12 (see Fig. 13).

$$\theta = 2 \tan^{-1} \left( \frac{h}{r_D} \right)$$

Eq. 12

A recent example is given by Shiryaeva *et al.*, (Shiryaeva *et al.*, 1995), using a light microscope and an autocollimation procedure.

The observed contact angle is, therefore, in principle a measurable parameter although deeper investigation reveals problems. This has led to extensive discussions among researchers (Lee, 1993). Adamson (Adamson, 1990) considers at least three different contact angles for a given system which he calls  $\theta_m$ ,  $\theta_h$  and  $\theta_{app}$ .  $\theta_m$  is the microscopic angle between the liquid and the ridge of solid, it is the angle determined by surface stresses taking into account local deformations both of chemical and topographic nature. It is easy to define, but the experimental microscopic determination is in fact difficult to perform. The problems which have to be considered include: viscous retardation, volatility related to vapour phase establishment depending on the selected liquid, and optical focus limitations together with the problem of contact angle hysteresis depending on advance or retreat of the triple line. Furthermore, the resolution of the microscope is important and an advanced scanning electron microscopy technique may be required. The term  $\theta_h$  is the thermodynamically contact angle, sometimes also called  $\theta_c$  or  $\theta_Y$ , i.e. the Young's contact at equilibrium.  $\theta_{app}$  is the apparent contact angle which is the average macroscopical detectable contact angle which can be measured accurately on a sessile drop by the use of a goniometer or a camera and image analysis.

The distinction of an advancing and receding angle has also gained much attention (Grundke *et al.*, 1996), (Kwok *et al.*, 1998). The terms "advancing" and "receding" refer to the liquid front movement on the solid. Probably the most convenient way to obtain an advancing angle under continuous motion is to apply a steady feed of liquid into the drop (by the means of a micro syringe) which, when carefully manipulated, leads to a constant progress of the contact line. Sometimes the wetting motion is not constant and instead a slip-stick phenomenon may be observed. The opposite arrangement, where a drop is forced to recede from formerly wetted surface terrain, is obtained by pulling liquid back. Recording this process with a camera, one obtains a dynamic advancing and receding contact angle hysteresis. Kwok *et al.* (Kwok *et al.*, 1998) claim that on ideal solid surfaces (referring to low energy surfaces only) there is no contact angle hysteresis and the experimentally



observed contact angle is therefore equal to  $\theta_Y$ . They also introduced a new method based on automated drop contour analysis (del Rio *et al.*, 1998), where axisymmetric (Laplacean) drop shape analysis is contrasted to a polynomial fit program. The method, however, is only applicable to samples where a hole can be drilled through the base substrate, as the drop is fed or withdrawn through this hole respectively to obtain an advancing/receding contact line. They identify a fundamental phenomenon concerning some solid/liquid combinations which is again manifest as the slip-stick behaviour of the slowly advancing contact line. This means that in a static measurement the line may be measured in a held or pinned-down condition yielding a different contact angle than seen after a subsequent slip event.

### **2.3.7.1 Measuring small contact angles**

For contact angles lower than  $10^\circ$ , it is convenient to use other methods, for example interferometry studying the interference pattern observed under monochromatic light of known wavelength. An application is given by Gerdes (Gerdes, 1998). Also Hadjiiski *et al.* (Hadjiiski *et al.*, 1996) used a trapping technique where spherical solid or fluid particles are placed within a thin layer of liquid and a monochromatic light interferometric method is used to determine the three phase contact angle.

### **2.3.7.2 Contact angle during imbibition**

In an imbibition situation the contact angle is argued to be considerably different to the static one and dependent on the contact line velocity.

Interestingly, there seems to be little differentiation in the literature between a self wetting situation with a developed meniscus where the velocity is a function of the contact angle, and forced wetting, for example in an experiment where endless tapes of polymer (polyamide or polyester) are drawn into a container of wetting liquid. Furthermore, it seems to be unclear what the differences are in the dynamic contact angle depending on the existence and scale of a meniscus in a wetting situation. A suggestion is given by Ligenza and Bernstein (Ligenza and Bernstein, 1951), namely, if the hypothetical velocity of a precursor development and the rate of contact angle formation and wetting are faster than the rate of meniscus movement then there is no difference between the dynamic and the static contact angle.

A range of empirical relationships are given in the literature, where, basically, the dynamic contact angle  $\theta_d$  can be expressed in terms of the static contact angle,  $\theta_0$ , as

$$\theta_d = f(Ca, \theta_0)$$

Eq. 13

at least for the low capillary number ( $Ca$ ) regime. (See the glossary in section 2.3.8 for definition; dimensionless numbers).

Seebergh and Berg (Seebergh and Berg, 1992) found that surface roughness also promotes a stick-slip behaviour. No differences were found comparing liquid with LvW and AB interactions. They review past work and propose the general correlation (including systems with a slip-stick scatter)

$$H = 4.47 Ca^{0.42}$$

Eq. 14

where  $H$  is here a dimensionless function for the dynamic contact angle:

$$H = (\cos\theta_0 - \cos\theta_d) / (\cos\theta_0 + 1)$$

Eq. 15

Theoretical considerations suggest that very close to a surface a significant deviation from the expected meniscus shape must occur due to viscous stresses, slip behaviour and further effects of molecular length scales. Van der Zanden and Chesters (van der Zanden and Chesters, 1994) have experimentally found an increasing curvature for the meniscus approaching a capillary wall. The technique used is based on laser light reflection from the meniscus and works down to about 50 nm from the solid wall.

To describe the phenomenon in rigorous detail is therefore virtually intractable. The interface on the molecular and atomic scale demands resort to quantum mechanics, which for any but the simplest atomic pair interaction itself becomes intractable. We conclude at this point that the contact angle is a complex result of the interfacial relationship and of the history of the experimental process. It is of practical importance and is best described by empirical observation under the conditions best suited to the dynamics of the conditions under study. In the main, the approach of this work, in dealing predominantly with imbibition, avoids some of the many complications by using, to the best knowledge, fully wetting liquids for the solid skeletal materials under investigation. This is also justifiable to a large extent since the mineral surfaces in question have adsorbed polymeric dispersants, typically polymers of acrylic acid. These aid wettability of many of the liquids used in the printing process.

### 2.3.7.3 Practical relation to the problem of measuring contact angle on compressed powders

In addition to the influence of surface roughness of a solid, a powder surface made from non-deformable particles, even if compressed against a flat and smooth surface, retains the local morphology of the particles and

the packing characteristic between the particles. Normally, to calculate the surface free energy an expression of the form of, or similar to, Eq. 8 is used. The roughness is not, however, explicitly accounted for. The outcome is an effective surface energy which is very different to that considered physically realistic due to the retained surface morphology, as explained in section 2.3.6. For example, the surface free energy of stearic acid should be in the order of  $22 \text{ mNm}^{-1}$  (estimated). This may be compared with polytetrafluoroethylene, one solid with the lowest imaginable surface energy, having  $\approx 18 \text{ mNm}^{-1}$ . If, however, stearic acid is coated onto the individual particles of ground  $\text{CaCO}_3$  powder the measured contact angle, using a sessile drop of known surface tension, is in the range of  $4\text{-}7 \text{ mNm}^{-1}$ . Therefore, the morphology of the particles and/or the packing of different particle size distributions masks completely any difference in surface chemistry or degree of coating. Usable results can only be obtained from contact angle measurements of powders when comparing identical pigments with different adsorbed coatings. This could be shown by a series from an uncoated to a perfectly coated product of the same type.

Absorption of fluid into the packed powder structure also produces artefacts. These range from loss of fluid into the structure faster than it can wet across the surface, to liquid imbibing through the porous structure back to the surface, forming a precursor film there. This layer coalesces eventually with the liquid meniscus of the main droplet seen as movement along the surface independent of wettability of that surface material.

### 2.3.8 Absorption – wetting, a glossary

At this point it is useful to provide some qualitative definitions of the observable and material features of fluids and porous solids, and their interactions. The list is not meant to be a comprehensive compendium of terms nor to be rigorously interpreted for applications outside the field of study undertaken here. Many of these will be formulated more rigorously under applicable theoretical considerations at the appropriate points in the subsequent text.

Term	definition	comments
Absorption	A fluid being taken up into or between material of another phase, species or dimension.	Comprising imbibition, diffusion etc.
Adsorption	Chemical or physical binding onto a surface	Differentiated into chemisorption (chemical bonds) and physisorption (Lifshitz-van der Waals, Coulombic interactions).
Break through	The point (or time) when in a displacement process the displacing fluid is monitored at the outlet boundary.	
By-Pass Effect	Slow capillaries (or connected voids) being by-	Slowness is not only defined in the

	passed by faster ones. May result in entrapped vapour phase in a structural feature.	viscous sense, but also by inertia and geometry.
Capillary Condensation	The transition from adsorbed liquid films in capillaries or void networks to filled voids as a function of capillary/pore diameter, vapour pressure, temperature and adsorbed liquid layer thickness.	
Connectivity	The average number of interconnecting throats which a pore has to its nearest neighbours.	Has a strong impact on effective permeability and effective path length (tortuosity).
Darcy-Length	Porosity-averaged volume per area uptake, represents the non-tortuous, non-interconnected way the wetting front would be expected to travel through an idealised bundle of equally sized capillaries.	As an averaged value it removes any information about liquid movement via micro-connectivity mechanisms.
Diffusion	Particular or molecular transport initiated by thermal energy or concentration gradients.	
Dimensionless numbers	Capillary length Capillary number Reynolds number Bond Number Weber Number Ohnesorge number Suratman number	$H = \sqrt{\gamma(\rho g)^{-1}}$ $Ca = We/Re$ $Re = \rho v 2r \eta^{-1}$ $Bo = \rho g r^2 \gamma^{-1}$ $We = v^2 \rho r \gamma^{-1}$ $Oh = (We)^{0.5}/Re$ $Su = Oh^{-2}$ where $v$ is velocity, see also section 2.3.16
Displacement	One fluid being displaced by another. The driving force may be intrinsic (preferred wetting) for non-miscible processes or pressure-driven. Miscible displacement concerns mutually miscible liquids.	
Drainage	A gas/liquid displacement process.	
Effusion	Molecular transport.	
Film-Flow	Sometimes called wall flow or liquid creeping. It is a planar flow driven by intrinsic wetting forces of the wetting front.	
Fingering	A wetting front showing deviation from a uniform wetting line in the form of concentrated dendritic regimes (fingers) ahead of the main front.	Viscous fingering may be observed when a viscous fluid is displaced in a porous medium by a less viscous one.
Ganglion ( <i>PI</i> Ganglia)	A capillary intersection within a network - derived from the observation of nerve networks.	
Haines jump	Jump motion in a porous structure mostly due to film-flow pre-wetting, meniscus build-up, fast acceleration and pore filling.	
Geometrical hydraulic diameter	Ratio between cross-sectional area and perimeter of a hollow structure $\times 4$ .	
Imbibition	Spontaneous liquid / gas displacement process driven by wetting and capillary forces.	
Infiltration	The usually slow leaking, pressure-driven or concentration-driven entry of liquid into a porous structure.	
Interface roughening	The macroscopical wetting front showing positional and rate fluctuations as a function of time and distance. On the microscale, a similar phenomenon is called micro-fingering. We use the term preferred pathway flow when considering network structures.	
Intrusion	Pressure driven (non wetting) liquid transport into a porous structure.	
Invasion	A sudden breakthrough of a phase into another	

	as soon as a threshold is overcome.	
Laplace Pressure	The pressure difference across a meniscus - this is the driving force per unit cross-sectional area in a wetting situation. In a non-wetting context (Hg-porosimetry) it is the pressure needed to move the interface into a non-wetting void effectively overcoming the meniscus curvature defined by $\theta > 90^\circ$ .	
Layering	Liquid arranging microscopically into layers	
Marangoni flow	Gradients in surface tension (induced by temperature or composition gradients etc.) - causes a macroscopic fingering of the wetting front.	
Migration	A phase changing its location.	
Miscible Displacement	A fluid/fluid displacement with a chemically unstable interface, effected by diffusional mixing.	
Necking	Used in film-flow to describe the forming of a bulge(s), often at the wetting front due to an unstable (transitional) condition - the subsequent locally filling and associated breakdown of fluid continuity is termed snap-off.	
Penetration	Mostly term for forced, pressure driven transport	
Percolation	Mostly term for gravity driven liquid seeping through a porous, often loose substrate. Also used to describe the pathway advance of a fluid through a porous network due to a pressure that is greater than any wetting or non-wetting force, e.g. Hg intrusion porosimetry.	The basic idea of percolation theory is the existence of a sharp transition at which the long-range connectivity of the system disappears (or, going the other way, appears). This transition occurs abruptly when some generalised occupation density in this system reaches a critical value (percolation threshold).
Permeability	Defines quantitatively the extent to which a porous material allows a fluid to pass through under a given pressure differential. Absolute permeability covers one phase flow through a saturated sample, relative permeability is linked to multiple phases and their distribution characteristics within the porous network. A practical unit of permeability is the darcy which is equal to $0.987\mu\text{m}^2$ .	A material may be very porous but not permeable (e.g. a closed foam or use of an impermeable layer in sandwich constructions to hinder permeation, e.g. Syntape - the substrate used in this work - is impermeable through the sheet but has a porosity between two surface-impermeable non-interconnected layers.
Permeation	Deduced from the permeability	
Pinch-off	Term used for the sequence: film-flow, snap-off, interface movement	
Pore	That part of a porous structure forming a discrete geometrical void	If interconnected with other pores takes part in penetration, permeation, absorption etc.
Precursor	A liquid layer formed ahead of the bulk liquid front due to very fast diffusive phenomena	
Preferred pathway flow	See interface roughening.	
Saturation	In "porous" context: the degree of liquid content in pores - a saturated medium is completely filled with fluid.	
Segregation	The de-mixing of phases	
Snap-off	The transition jump from a liquid film within a capillary to a filled capillary showing breakage of the fluid column and the formation of internal menisci	
Sorption	General term for a process of fluid or solved species transition from a free state to an	

	interactional one, usually by ad- and/or absorption.	
Spinoidal dewetting	If a system, containing a continuous film of liquid, undergoes a critical condition, (i.e. film reduced below a critical film thickness), the film starts to become unstable with a subsequent dewetting process which leaves often a pattern of droplets.	Nucleated dewetting starts from a nucleus, a chemical or geometrical discontinuity. It is observed as a reticulation of the fluid.
Spreading	The planar distribution of a liquid on another phase subject to the forces of surface energy and external forces such as gravity.	
Throat	The section of smallest perimeter between two pores	
Tortuosity	Defines the extent of deviation from a straight line passage of fluid through an interconnected porous system.	
Trapping	A temporary fixation of one phase at a ganglion in a displacement process	
Triple Line	The confluence line where three phases meet	
Wetting	A solid/vapour interface being replaced by a liquid/solid one: mostly used for the general process of a fluid advancing on a solid	A situation is referred to as non-wetting if the contact angle is equal to or greater than 90°. Contact angle approaching 0 defines "fully wetting".
Wicking	The macroscopic process of displacing a gas within a planar or axial porous material by a liquid driven by meniscus and film-flow forces	

### 2.3.9 Dynamic wetting

We follow the suggestions of Kissa (Kissa, 1996), using the term wetting for the intrinsic process of a solid/gas interface being replaced by a solid/liquid interface, for example on a flat surface. For the wetting into a capillary void we use the term imbibition.

As already mentioned, we are dealing with an interface replacement process driven by the aim of a given system to minimise its surface free energy. This can be a liquid wetting a dry solid or, if it is on a prewetted solid, it is the interface of the adsorbed wetting film and the vapour replaced by the bulk liquid. Chibowski and Holysz (Chibowski and Holysz, 1997) express the interface replacement process generally as

$$\gamma_{i1} - \gamma_{i2} = |\Delta G| \tag{Eq. 16}$$

where  $\Delta G$  is the free energy change accompanying the process and  $i$  stands for interface. The four different possible cases for interface replacement are then:

1. The liquid completely wets the surface ( $\theta = 0$ ). A bulk film is present on the surface (possibly with an adsorption and/or diffusion precursor) and the following equation describes the displacement

$$|\Delta G| = \gamma_{SV} - \gamma_{SL} = \gamma_{LV}$$

2. Same liquid as above, but liquid advancing on the bare solid

$$|\Delta G| = (\gamma_S - \gamma_{SL} - \gamma_L) \text{ where } (\gamma_S - \gamma_{SL} - \gamma_L) = W_A - W_C$$

$W_A$  being the work of adhesion and  $W_C$  the work of cohesion.

3. Same case as 1, but the liquid showing a contact angle greater than zero

$$|\Delta G| = \gamma_{LV} \cos \theta$$

And finally,

4. Same as case 2, but also showing a contact angle greater than zero

$$|\Delta G| = (\Pi_c + \gamma_{LV} \cos \theta) \quad \text{where} \quad \Pi_c = W_A - W_C$$

The problem with cases 2. and 4. is that they contain parameters which are uncertain and need the involvement of semi-empirical equations. The intrinsic wetting force of a liquid front would, in this context, be correctly defined as: the appropriate form of interface displacement tension multiplied by the length of the wetting front.

Mainly two different approaches are found in the literature to describe the fundamental mechanisms of wetting as reviewed by Gerdes (Gerdes, 1998).

- The first uses classical hydrodynamics. It assumes no wall slip, but can apply an effective *slip length* (to account for observable deviation) or employ a cut-off at the wetting line and an assumed microscopical equilibrium contact angle. It treats the advancing fluid as a macroscopic wedge and applies Navier-Stokes equations deriving relations between the slope of the wedge and its moving velocity.
- The second approach adopts molecular kinetics theory. It involves a statistical mechanical description and system-specific molecular parameters to describe an adsorption/desorption process driven by an out of balance wetting force.

### 2.3.9.1 Applied surface wetting and spreading

The process of wetting, initiating and maintaining motion of a fluid on a solid surface, is seen in many situations which are of practical and industrial import.

Examples, in which bulk liquid (supersource) is present, are: the rise of liquid on a glass plate, many coating processes such as dip- and cast-coating, sizing, cleaning processes etc. To improve the wettability, surfactants are often used which lower the liquid surface tension. In the case of polar surfactants, arrangement of the surfactant molecules in such a way that their non-polar tails are exposed to the gas phase acts to reduce the polar component of the surface tension of a polar fluid. Conversely, they can be arranged so that the polar parts are exposed, thus raising the polar surface tension of an otherwise non-polar fluid. Non-polar surfactants can be chemi-sorbed onto surfaces to provide a surface energy match with a non-polar fluid.

Of greater importance is the spreading of limited amounts of liquid, such as droplets and thin films. Examples are: ink-jet digital printing and spray applications of paints, varnishes and biological agents, such as pesticides etc., where drop adhesion and spreading to a film is usually desired. Film applications are standard for continuous coating of planar substrates such as paper, tapes (audio, data storage), polymer films, fabrics, and non-wovens, and in the construction of composite materials such as artificial leather, conveyor belts, photo-paper and plastic laminates, for example Royalex<sup>TM</sup><sup>4</sup>.

In nature, completely planar, smooth and clean surfaces are seldom found. Roughness generally results in a continual change of contact angle which may lead to air entrapment at the surface if the contact angle is large. If macroroughness has a strong uni-directional component, such as a scratch, it acts like a half open capillary pulling a liquid droplet along it. Liquid concentrates on the sides of any raised linear or point-like features. Also chemical non-uniformity of a surface is common. Often many molecules from the surrounding environment are bound by adhesion/adsorption forces to the surface.

The following sections focus on the practical implications of wetting as it controls absorption and spreading on porous media. To develop this analysis it is necessary to consider the ubiquitous case of the capillary. Its geometry, although idealised can in principle be applied to capillary diameters down to approximately ten times the fluid molecule diameter within or upon a localised porous structure. The limitations of continuous capillary flow theory as feature dimensions decrease form the basis for expanding the modelling of fluid uptake to include phenomena that act on the short timescale and over distances which are too short for Poiseuille (viscous) flow to become established.

---

<sup>4</sup> Royalex is a trademark from Uniroyal ([www.uniroyal.com](http://www.uniroyal.com)) and is made of a hard foam core "sandwiched between layers of polyvinylchloride and acrylbutadienstyrene and has an excellent ratio of weight to mechanical properties like e.g. stiffness and impact strength



### 2.3.9.2 Capillary imbibition

The observed "pulling" of a liquid into a capillary is due predominately to the intrinsic wetting process of the capillary wall, (Wilhelmy, 1863), and the effect this has in creating a meniscus curvature. The pressure difference across the curved meniscus of the liquid/gas interface is then used as a descriptor for the capillary force.

In a parallel-walled capillary the liquid is enclosed by the solid. The cohesivity of the liquid competing with the liquid-solid adsorption process results in a curved liquid/gas interface, itself striving to minimise its surface area. The capillary geometry enables bulk flow towards the wetting front and, as a result, feeding it. The geometry of the capillary can be extended to consider non-parallel walls. In this case a curved interface will also try to move even in the absence of an intrinsic wetting force, for example in a construction involving a converging conical pore and a contact angle of  $90^\circ$ .

A vertical capillary rise experiment leads us to a force balance for the equilibrium liquid rise in a circular capillary of radius,  $r$ :

$$\rho gh = \Delta P \Rightarrow h = \frac{2\gamma \cos \theta}{rg\rho} \Rightarrow F_w = 2\pi r\gamma \cos \theta$$

Eq. 21

where the gravitational acceleration,  $g$ , the fluid density,  $\rho$ , and the height of rise,  $h$ , are balanced by the tension of the meniscus. Minimising this tension acts as the wetting force,  $F_w$ , and as this force is acting across a cross-sectional area, the phenomenon is termed the Laplace pressure,  $\Delta P$ , acting orthogonally across the interface. It is negative in a wetting situation, acting from fluid to vapour. The advantage of equations based on Eq. 21 is that  $r$  and  $\cos \theta$  can be analysed independently (Marmur and Cohen, 1997). For more arbitrary meniscus shapes the Laplace pressure can conveniently be expressed as

$$\Delta P = \gamma_{LV} \left( \frac{1}{r_1} + \frac{1}{r_2} \right)$$

Eq. 22

where  $r_1$  and  $r_2$  are the two principal radii. This is also a useful approximation for of an irregularly shaped meniscus. The tension within the meniscus leads to a pressure gradient according the Laplace expression (Davis, 1996).

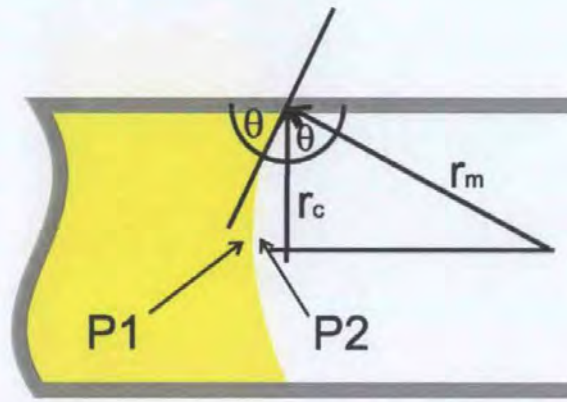


Fig. 15 The geometric schematic of a meniscus in a tube ( $r_c$  is the capillary radius and  $r_m$  the radius of the meniscus curvature).

An interesting detail is discussed by Zhang and Nakajima (Zhang and Nakajima, 1999), namely the nanometer deformation of the solid phase caused by the Laplace pressure and the possibility of its effect on surface tension measurements. Although it is difficult to support many of the assumptions used in molecular dynamics at this scale, nobody before had considered the force of very small menisci  $r_m \leq 10$  nm on solid surfaces. This force may lead to elastic deformation and changes in the geometry of the surface, distorting the classical equations. The influence is much stronger with water than with organic solvents. The implication for porous structures is also the potential of movement of particles which are not firmly anchored within the structure.

At this stage it is important to point out that for some cases, where a feature geometry leads to a flat meniscus,

$$\Delta P = \frac{\gamma_{LV}}{\infty} = 0$$

Eq. 23

as shown in Fig. 16. This case is called an imbibition stopper, and accounts for any case in which the meniscus radius of curvature is made infinite under the constraints of the contact angle. It was analysed, for example, by Kent and Lyne (Kent and Lyne, 1989). (The expanding cone of angle  $\alpha$  is used as a specific case later in the modelling in this work). It is, therefore, more comprehensive to describe the capillary wetting force with the curvature-linked Laplace pressure than using just the (intrinsic) Wilhelmy force.

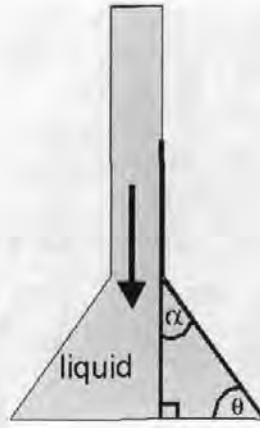


Fig. 16 Imbibition stopper  $\alpha + \theta = 90^\circ$ , the radius of curvature of the meniscus is infinite.

Mason and Morrow (Mason and Morrow, 1994) describe meniscus curvature in relation to contact angle in specific pore geometries surrounded by circular cross-sectional solid bodies (spheres, rods, tori etc.). Although the interesting case of an imbibition stopper, when curvature ( $1/r_m$ ) is zero, is not discussed, they show that, for a steadily converging-diverging pore the curvature is at maximum outside the throat minimum diameter. They suggested that this compensates partially for the contact angle effect known from imbibition/drainage hysteresis.

As we have discussed the driving force above we need to understand the "braking" forces which act against the infinite acceleration of the fluid. The first is viscous flow and is expressed by the equation of Hagen and Poiseuille which describes the laminar flow resulting in a parabolic velocity distribution within a liquid volume  $V$ , in time  $t$ , for a horizontal circular tube of length  $l$ , radius  $r$ , containing a fluid of viscosity  $\eta$ , flowing under a differential pressure  $\Delta P$ , as:

$$\frac{V}{t} = \frac{\pi r^4 \Delta P}{8 \eta l}$$

Eq. 24

Transforming this equation we obtain the viscous drag,  $F_{vd}$

$$F_{vd} = r^2 \pi \Delta P = \frac{8 \eta l V}{r^2 t}$$

Eq. 25

Balancing the driving force of Eq. 21 with the viscous drag in Eq. 25 yields the well known equation of Lucas-Washburn, as defined later in the text in section 2.3.14.

The second "braking force" is accounted for by Newton's second law which provides momentum (inertia of a body of mass  $m$ ) as a resistance to infinite acceleration.

Further dissipating forces of minor impact are due to non laminar streamlines at the regimes of flow transition such as capillary inlet, the zone of establishment of parabolic velocity distribution and close to the meniscus, as discussed further in section 2.3.11

### 2.3.10 A chronology of imbibition science

A brief review of historical contributions made to the field of fundamental capillarity forms a basis for the approaches which have been further analysed and compared in this thesis.

An early approach to analyse imbibition is reported by Bell and Cameron (Bell and Cameron, 1906), who found a square root dependency on time,  $t$ , (see Eq. 26) for imbibition length  $x$ , involving an constant  $k$  which was apparently also found independently by Ostwald in 1908, as reported by Lucas (Lucas, 1918).

$$x^2 = kt$$

Eq. 26

Lucas experimented with glass tubes and filter-papers to verify the equation he obtained combining the Laplace relation with Poiseuille's equation of laminar flow, Eq. 24. His focus was mainly to fortify the dependency on  $\sqrt{t}$  (in terms of the precision of the exponent 0.5). Washburn (Washburn, 1921), not being aware of Lucas' work, performing vertical and horizontal capillary experiments, derived the same equation as Lucas and discussed slip behaviour and the limits of Poiseuille flow at both ends of the liquid column. He also discussed the equation's applicability to porous substrates. In addition he notes the need for a film of liquid on the capillary wall to maintain the condition of a zero contact angle, even for fully wetting fluids.

The main drawback of the combined Lucas-Washburn approach is the lack of inertial terms, relating to the mass of fluid under motion, as was recognised by Rideal (Rideal, 1922). The impact of inertia is to modify the initial uptake dynamic or to impose variation on Lucas-Washburn when the geometry of the medium changes providing either acceleration or deceleration of the fluid flow, such as that shown in Fig. 16. Bosanquet (Bosanquet, 1923) complemented Rideal's solution, adding the inertial impulse drag effect associated with an accelerating fluid.

Peek and McLean (Peek and McLean, 1934) considering Bosanquet's attempt as irrelevant practically, tried to extend the LW equation for porous media, adding two parameters accounting for the pore size distribution. However their experimentation using strips of paper could only qualitatively verify the "character" of their approach.

Pickett (Pickett, 1944) calculates Reynolds number in a capillary and writes a differential equation based on Newton's law of motion which is identical to the Bosanquet solution. His conclusion was that Reynolds numbers are far too low for turbulent flow playing a role in capillary imbibition.

LeGrand and Rense (LeGrand and Rense, 1945) express that Pickett's view might be too simplistic discussing contact angle development, entrance turbulence, streamlines in the vicinity of the meniscus and wall slip. Furthermore, they published a set of data on capillary rise using a stroboscope.

It is interesting to note that Brittin (Brittin, 1946) seemed not to know of any of the earlier work, except from the previous century. Brittin gives a detailed analysis of theoretical flow regimes and derivations of equations for vertical and horizontal capillary imbibition and he adds an end drag term (turbulent flow at the inlet). The paper has a strong focus on the mathematical treatment of the differential equations of motion.

Ligenza and Bernstein (Ligenza and Bernstein, 1951) formulated an equation of vertical capillary uptake, apparently based on Bosanquet's equation adding Brittin's end drag condition. Experiments were performed using glass capillary tubes with markers and a stopwatch

Szekely *et al.* (Szekely *et al.*, 1971) did not refer to any of the early approaches except Washburn. They started from an energy balance and removed the initial infinity of the LW velocity, avoiding also the infinite acceleration condition of Bosanquet. Letelier and Leutheusser, (Letelier and Leutheusser, 1979), mentioned that, stripped of "arbitrarily" added corrective terms, the Szekely equation is identical to that of Bosanquet.

Levine *et al.*, (Levine *et al.*, 1976) introduced a sink flow towards the capillary entrance from the reservoir, referring to Szekely and adding some changes or improvements. They focussed on the low Reynolds number regime which they considered to be more practically relevant. Reference to the work of Levine (Levine *et al.*, 1980), shows a conflict with the writings of Ligenza as to who uncovered Bosanquet's publication. He went on to re-account for the deviation from Poiseuille flow in the vicinity of the moving meniscus by including a slip condition. Letelier and Leutheusser (Letelier and Leutheusser, 1979), (also not referring to Levine's papers) started from the Navier-Stokes equations, discussing both Szekely's and Bosanquet's work. They identified an incorrect coefficient in the second order term, and claimed to have given a more rigorous solution, with dimensionless variables, in the form of a series expansion. Batten (Batten, 1984), (not referring to Levine's papers) accepted Letelier's and Szekely's efforts as rigorous but remarked on their disagreement with experimental data (from capillary rise experiments). He added to Szekely's equation the dissipation of a kinetic

energy head and the dynamic establishment of a velocity dependent contact angle. He states that the Letelier approach ignored the correction for converging flow at the capillary entry. He compared his own equation, and the two others mentioned, with data from LeGrand and Rense (LeGrand and Rense, 1945). Ichikawa and Satoda (Ichikawa and Satoda, 1994) not referring to Levine's 1979 work claimed that Letelier did not account for inertia during the inlet acceleration. They started with an energy balance and arrived at an extended dimensionless Bosanquet relation.

Sorbie *et al.* (Sorbie *et al.*, 1995) identified the consequence of inertia in interconnected capillary features (a pore doublet), relating a modified Szekely equation to the individual capillary feature lengths and pointed out that short capillary features may fill predominantly in the inertial regime.

Marmur and Cohen (Marmur and Cohen, 1997) in turn separated surface tension and radius for individual analysis using an equation for vertical capillarity without specifying the origin. Moshinskii (Moshinskii, 1997), only referring to Russian authors, solved the Navier-Stokes equations using advanced methods to obtain his integro-differential equation. He did not consider the effects at the ends of the liquid column he described. When any of these latter equations are applied to a porous substrate, the number of unknown parameters tends to grow unmanageably.

It is with such a background that the work here is focussed on the following authors. First of all, the initial approach of Lucas (Lucas, 1918) and Washburn (Washburn, 1921), and then the classical mechanical approach of Bosanquet (Bosanquet, 1923), as taken further by Schoelkopf *et al.* (Schoelkopf *et al.*, 2000) and Ridgway *et al.* (Ridgway *et al.*, 2001). Sorbie *et al.* (Sorbie *et al.*, 1995) recognised the importance of competitive imbibition into a ratio of different capillary sizes. The competitive rates of absorption, as manifest by a pore-doublet using the Szekely equation, were shown (Sorbie *et al.*, 1995) to be related to the aspect ratio of the pores, defined as the length of the capillary representing the pore divided by its radius. The competitive effects in a range of capillaries and eventually network structures are compared by Ridgway *et al.* (Ridgway *et al.*, 2001) as modelled by the applications of the Bosanquet equation, the original Szekely equation and a modified Szekely equation derived by Sorbie *et al.* (Sorbie *et al.*, 1995), as shown in Fig. 17.

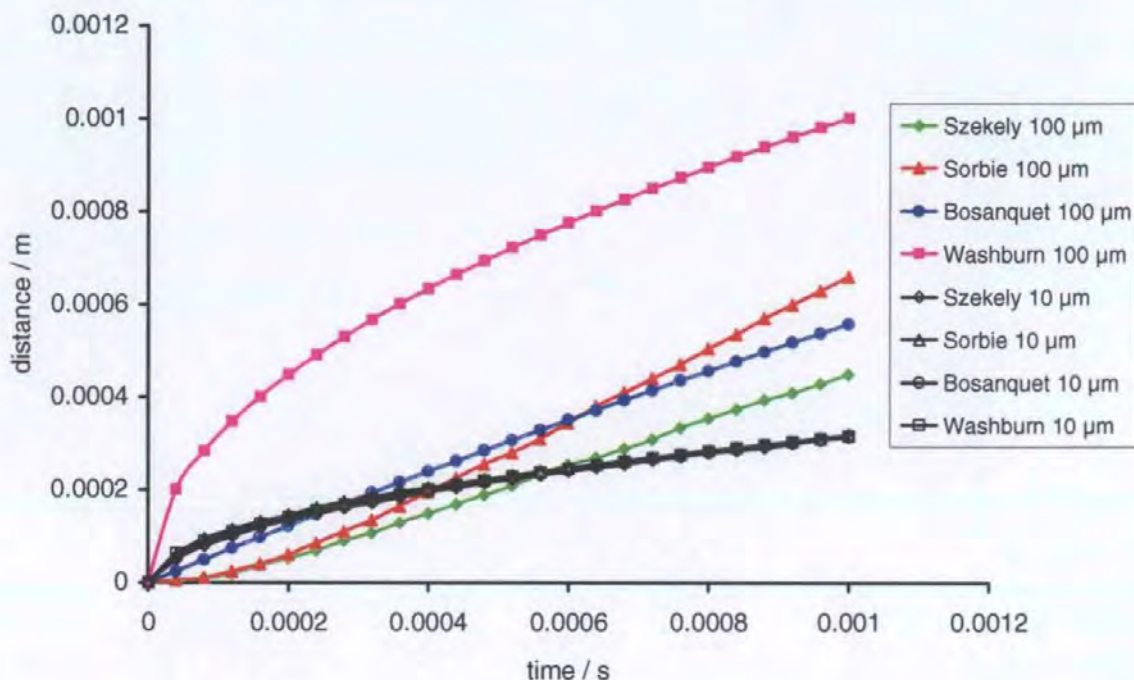


Fig. 17 Comparisons of solutions to the equations of Szekely, Sorbie, Bosanquet and Washburn for water and capillaries of 10  $\mu\text{m}$  and 100  $\mu\text{m}$ , (taken from Ridgway *et al.*, 2001).

The four equations give similar absorption rates for water in the 10  $\mu\text{m}$  radius capillary. Discrepancies arise for the absorption behaviour of the larger 100  $\mu\text{m}$  capillary.

### 2.3.11 Summary of proposed single capillary phenomena

As a conclusion of the work done in the field one could summarise the relevant physical details in terms of a schematic of the imbibition process. We see immediately, that even in simple tube experiments, as depicted in Fig. 18, there is still much uncertainty about the dynamic contact angle [12], (numbers in square brackets refer to Fig. 18), and the exact meniscus shape [8] which are related to the condition of the inner surface of the tube in terms of microroughness [10,11], cleanliness, precursor development and pre-wetting conditions [9], which can be anything from a fluid monolayer to a bulk film, and meniscus distortions and further viscous energy dissipation due to "fountain" flow or vortices close to the wetting front [7]. The dynamic effects at the entrance region [1-5] are also considered to be of similar complexity. We have a potential external pressure [1], edge-effects (turbulent flow) [2], the time regime of establishment of a meniscus [3], the reservoir sink flow towards the inlet [4] and the domain of inertial flow which is non-viscosity-affected and may be imagined as a plug flow. Molecular modelling approaches (Martic *et al.*, 2000) have shown a wavy meniscus shape [5]. This flow regime is within the focus of interest of this work and is discussed later in detail. [6] represents the established parabolic flow-velocity distribution which is the basis of Poiseuille flow.

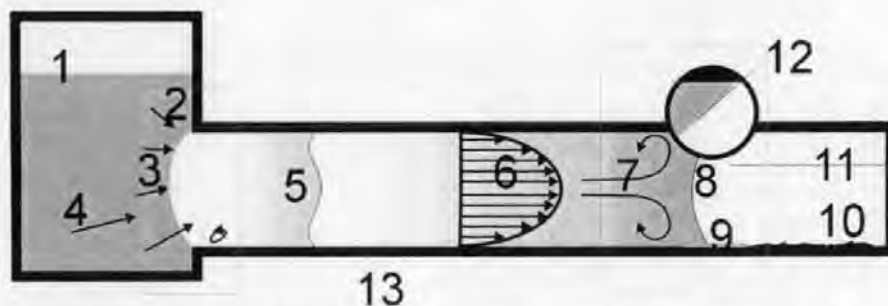


Fig. 18 Schematic overview of influences on meniscus-driven imbibition from a reservoir (left) into an evacuated capillary tube.

### 2.3.12 Further observations made in simple capillary experiments

Some of the details of imbibition, as summarised in Fig. 18, have been analysed experimentally over the years using glass capillaries mounted in a vertical or horizontal position. Early approaches, (Bell and Cameron, 1906), (Washburn, 1921), (Rideal, 1922) used stopwatches and marks on the glass, or a similar grid system, and had to use liquids with elevated viscosities to remain within the realm of observation. With time, detection systems improved and recent approaches use high-speed cameras and image analysis (Quere, 1997).

A step forward was the experimentation of LeGrand and Rense (LeGrand and Rense, 1945), who used a stroboscopic light to record on a photographic plate. Their data are used in many later theoretical approaches.

Ligenza and Bernstein (Ligenza and Bernstein, 1951) performed vertical experiments with capillaries of 20 and 50  $\mu\text{m}$  in diameter. For high viscosities the stopwatch was used. For lower viscosities, a device resembling an  $xy$ -recorder, which logged a manually triggered signal, as a function of time, was used. The precision of the experimentation was not good enough to trace inertial and end drag effects and it was concluded that the Washburn equation and the Poiseuille approximation hold for capillaries in the order of the used diameters. The zero contact angle assumption also seemed to hold for the system used. This was explained with the suggestion that the rates of contact angle formation and wetting are faster than the rate of meniscus movement.

Fisher and Lark (Fisher and Lark, 1979) tested and confirmed the LW equation for a range of capillaries with radii from 3 to 400  $\mu\text{m}$ . They used a microscope at different positions along the capillary and a stopwatch to determine the timescale for the meniscus to reach that point. Tests for capillaries with 0.3  $\mu\text{m}$  radius revealed an abrupt decrease in flow rate for water and the generation of air bubbles in the flow. The origin of the air bubbles is not clarified, but their effect is explained by the difference between advancing and receding contact angles of the liquid columns involved.



Mumley *et al.* (Mumley *et al.*, 1986) studied the meniscus motion for immiscible liquid/liquid systems with different ratios of densities, viscosities (remaining in the viscous stable regime) and surface tensions. The capillaries used were between 0.5 and 1 mm in diameter, and careful cleaning and pre-treatment of the surfaces was carried out. Dynamics of meniscus rise were recorded with a camera. They found dynamic contact angles differing from those at equilibrium. They also found in some cases flat menisci inclined relative to the capillary walls (without discussing inertial flow) and a rate slower than that predicted by the LW equation. The explanation given is that excess hydrodynamic forces and wetting front singularities, such as toroidal vortices at the meniscus boundaries, group into an excess-force term  $F^*$ . The dynamic contact angle is discussed as a consequence of meniscus deformation and it is pointed out that it is not a fundamental surface property.

Ichikawa and Satoda (Ichikawa and Satoda, 1994) used 0.5 to 4 mm diameter capillaries, rigorously cleaned and dried with nitrogen. The recording of the meniscus position was performed with a video camera. Resolution was 1/30 s in time and 0.5 mm in distance. A slower imbibition was found for a dry tube. They also performed a self-receding experiment which gave results that do not agree with any established theory.

Weislogel (Weislogel, 1997) experimented using straight and U-shaped tubes, partially hydrophobised on the inner surface, and partly in a gravity-free environment (drop tower). A liquid slug was placed in the tube with one meniscus on the coated side and one on the uncoated side of the glass tube. Due to the gradient in pressure of the two menisci, the liquid comes into a domain of steady motion which can be analysed quite precisely in terms of wetting force. Nevertheless, the contact angle difference was measured with an uncertainty of  $\pm \approx 25\%$ . The interpretation of the data was carried out by the extensive use of dimensionless numbers. The expected results confirmed the steady flow behaviour and that the strongest influence on  $Ca$ , capillary number, was surface condition/cleanliness.

Quere (Quere, 1997) used a high-speed camera (a picture each 5 ms = 200 s<sup>-1</sup>) to study the rise of different liquids in glass capillaries with a diameter of approximately 1 mm. It was possible to show the inertial regime which is linear in time for lowest viscosity liquids. However, the velocity in this regime is slower than predicted by an equation of inertial flow. It is explained by the dynamic contact angle which is a function of wetting line speed and greater than the static advancing contact angle which is zero in this case. The role of the dynamic contact angle was confirmed by prewetting the tube which gives rise to a higher velocity, closer to the theoretical inertial wetting value.

Most approaches agree on the fact that liquid wetting a completely dry capillary does not follow the expected quantitative behaviour. The concept of a dynamic contact angle is often discussed as a function of the capillary number. The possibility of using an adjusted driving force term, as proposed by Chibowski and González (Chibowski and González, 1993) based on a type of interface displacement as the driving force, expressed in terms of  $\Delta G$ , is in many cases limited due to unknown parameters. Therefore, we see that mostly the contact angle  $\theta$  is adjusted by researchers, such that it becomes a fitting parameter. Unfortunately, to our knowledge, nobody yet has given a clear visualisation of fast moving menisci shapes.

### 2.3.13 Complex single capillary shapes

It is important to remember that the theory given to this point concerns itself with geometrically regular and circular capillary elements. We have already intimated the impact of discontinuous geometrical changes, and this forms the next step towards a porous network, i.e. the analysis of capillaries of different cross-sectional shape.

A lot of work was done after 1985 investigating the dynamics of imbibition into angular capillaries. The cross-sectional shape covers different shapes from triangles to rectangles and polygons. Many of the publications are quite similar. Therefore, a chronological order of the work is given here.

Theoretical studies were carried out by Ransohoff and Radke (Ransohoff and Radke, 1988), pointing out the differential flow resistance in different cross-sectional domains of an angular capillary. The dimensionless flow resistance is shown to increase with increasing roundness and half angle of the corners.

Tang and Tang (Tang and Tang, 1994) did the same, focusing in a theoretical approach on the shape of the liquid tongue, (meniscus) being, due to local strongly increased curvature, much more advanced in the corners.

Ma *et al.* (Ma *et al.*, 1996) extended the study to the involvement of different contact angles and corresponding imbibition or drainage in regular polygonal tubes. Their aim was to understand filling/drainage mechanisms in the field of mineral oil recovery. In imbibition, an important derivation is that such a tube can be filled either by an advancing meniscus or by expanding the menisci from the tube corners.

A special case is analysed by Yost *et al.* (Yost *et al.*, 1997) investigating the wetting flow in narrow v-shaped grooves, an issue which is important to understand in soldering kinetics. Early flow regimes are reported not to follow a LW model. This effect is interpreted in terms of a dynamic contact angle.

Borhan and Rungta (Borhan and Rungta, 1993) consider the imbibition between periodically corrugated plates, and point out the influence of geometry. With growing amplitude of corrugation, the time needed to rise to equilibrium height increases.

Dong and Chatzis (Dong and Chatzis, 1995) pioneered the experimental study of flow in corners of square capillaries. The wetting front in the corners was ahead of the bulk phase, which was to be expected considering the local curvatures in the "corners". The general behaviour scales as the square root of surface tension over viscosity,  $\sqrt{\gamma/\eta}$ . Furthermore, the effect of cleanliness was seen most drastically in the corners. Even washing with acetone left some obviously adsorbed matter which leads to a higher contact angle and slowed imbibition. Reproducible multi-step cleaning and oven drying of the tube yielded a contact angle of  $23^\circ$  compared with the contact angle of  $0^\circ$  in a pre-wetted condition, the latter one of course being faster in imbibition. Also larger tube sizes increased the meniscus velocity as expected in the viscous regime. An interesting find was that the roundness of the corners retards the velocity of imbibition. The authors do not discuss the transition to a round tube where the wetting line length is minimised compared with those shapes having "corners".

Weislogel and Lichter (Weislogel and Lichter, 1998) used a drop tower to conduct gravity-free experiments in glass containers with interior corners (triangles and square cross-sections). They focused on the range of Ohnesorge number being greater than 1 (see section 2.3.16), a regime formerly not explored. In this regime, the inertia of the liquid plays a dominant role as the interface changes in shape. This is relevant for applications where liquids wet free from the limits of gravity. Incidentally, the understanding of this behaviour is crucial for technology in outer space.

A further step towards the reality of a real porous medium is the analysis of capillaries with longitudinal changes of shape. Levine *et al.* (Levine *et al.*, 1977) considered this case in an illustrative theoretical study also reviewing some earlier work. They showed the changes in meniscus curvature as it imbibes into a periodically corrugated capillary tube.

The work of Maisch and Sell *et al.* (Maisch *et al.*, 1981), (Sell *et al.*, 1984), (Sell *et al.*, 1986), (Maisch *et al.*, 1986) has the background of space technology. In a series of papers they use experiments involving two immiscible, but density and viscosity matched, liquids. The liquids show different contact angles to glass. This allows for the observation of meniscus behaviour and movement in macroscopic tubes as gravity no longer influences the interface. They use tubes with different shapes: straight, conical and periodically constricted. The meniscus motion is observed and photographed and compared with numerical results modelling the change in

meniscus shape in connection with the local tube geometry. When the tube is diverging, the meniscus flattens and imbibition is slowed. The opposite is observed for convergent tube sections. Streamlines and vortices and their effect on meniscus shape are discussed. Similar work was carried out later (Sharma and Ross, 1991) without reference to the work of Maisch *et al.*

Tuller *et al.* (Tuller *et al.*, 1999) go a step further, discussing comprehensively phenomena ranging from adsorbed liquid films to capillary condensation, interfacial configurations, saturation and liquid retention for pores of different cross-sectional shapes and longitudinal steps. This latter was actually a pore level model with interconnecting throats and slits. They propose a modified unitary approach to adsorption and capillary condensation (original work by Philip (Philip, 1977)) based on the augmented Young-Laplace equation (containing beside the capillary component an adsorptive one) and advanced interface science in the domain of adsorbed liquid films. This work has a soil science background, where the shape of pores depends on the particle shape of the soil, for example the platy nature of clay soils.

We now concentrate on the important equations used in this work, which will later be extended to the modelling of the geometrical description of porous media.

### 2.3.14 The Lucas-Washburn equation

Let us go back to the simplest case for the description of capillarity which is represented by a horizontal circular tube of definably small radius,  $r$ . The Laplace pressure across the meniscus of a fluid in the tube describes the force of imbibition of the capillary and is given by the curvature of the liquid/gas (air) meniscus. To obtain an equation of dynamic motion, the Laplace relation is traditionally incorporated into the Poiseuille equation of laminar flow and one obtains the well-known LW relation:

$$x^2 = \left( \frac{rt}{2\eta} \right) \gamma \cos \theta$$

Eq. 27

where  $x$  is the distance travelled by the liquid front in the capillary,  $t$  the time,  $\eta$  the fluid dynamic viscosity,  $\gamma$  the interfacial tension, i.e. liquid-vapour interfacial tension, referred to earlier as  $\gamma_{lv}$ , and  $\theta$ , the contact angle between the fluid and the solid walls of the capillary.

### 2.3.15 Inertia and the Bosanquet equation

Bosanquet (Bosanquet, 1923), complemented Rideal's solution (embodying Lucas-Washburn) adding the inertial impulse drag effect associated with an accelerating fluid, based on the following force balance:

$$F_i + F_{vd} = F_p + F_w \quad \text{Eq. 28}$$

where  $F_i$  is the inertial force according to Newton's second law, and equals  $d(mdx/dt)/dt$ , where  $m$  is the mass of the fluid in the capillary ( $=\pi r^2 \rho x$ ), and  $mdx/dt$  is the momentum, or inertia, of the fluid.  $F_{vd}$  is the force due to viscous drag, and follows Poiseuille's law, i.e.  $F_{vd} = r^2 \pi \Delta P = 8 \eta \pi x dx/dt$ .  $F_p$  is the force acting by an external pressure, if present, and is given by  $P_e/(\pi r^2)$ , and  $F_w$  is the wetting force, i.e.  $F_w = 2 \pi r \gamma \cos \theta$ . When the terms are brought into their dynamic form, one obtains Bosanquet's relation:

$$\frac{d}{dt} \left( \pi r^2 \rho x \frac{dx}{dt} \right) + 8 \pi \eta x \frac{dx}{dt} = P_e \pi r^2 + 2 \pi r \gamma \cos \theta \quad \text{Eq. 29}$$

where  $\rho$  is the fluid density. By integration, and letting

$$a = \frac{8\eta}{\rho r^2} \quad b = \frac{P_e r + 2\gamma \cos \theta}{\rho r} \quad \text{Eq. 30}$$

it can be shown that

$$x_2^2 - x_1^2 = \frac{2b}{a} \left\{ t - \frac{1}{a} (1 - e^{-at}) \right\} \quad \text{Eq. 31}$$

where  $x_1$  is the initial position and  $x_2$  is the position after time  $t$ .

Szekely *et al.* (Szekely *et al.*, 1971), also finding the Washburn equation to be inadequate at short times, went on to consider the energy balance at initial fluid uptake, deriving the following equation governing the advance of the wetting front in a capillary,

$$\left( x + \frac{7}{6} r \right) \frac{d^2 x}{dt^2} + 1.225 \left( \frac{dx}{dt} \right)^2 + \frac{8\eta}{\rho r^2} x \frac{dx}{dt} = \frac{1}{\rho} \left( \frac{2\gamma \cos \theta}{r} - \rho g x \right) \quad \text{Eq. 32}$$

where  $g$  is the acceleration due to gravity. The three terms on the left-hand side represent the net influx of kinetic energy, the formation of a *vena contracta* at the tube inlet and the work expended overcoming viscous forces.

The right-hand side consists of a capillary force term and a gravitational potential term, if applicable. Whereas both the Washburn and the Bosanquet approximations are insoluble at  $x = 0$  ( $t = 0$ ), predicting infinite velocity, the velocity singularity at  $t = 0$  is no longer a problem in the Szekely formulation since the initial conditions,  $x = \dot{x} = 0$  at  $t = 0$  do not form a discontinuity. Sorbie *et al.* (Sorbie *et al.*, 1995) have shown how this equation compares with that of Washburn by considering water displacing air in a capillary, i.e. external pressure differences are omitted and the effect of gravity over small height differentials is assumed negligible. Sorbie *et al.* (Sorbie *et al.*, 1995) also state that the factor of 1.225 in Eq. 32 can be alternatively derived as 0.225.

### 2.3.16 Dimensionless numbers in fluid dynamics

In many of the recent aforementioned studies, dimensionless numbers are used to analyse and visualise global relationships. Their aim is to distinguish transport phenomena into different regimes of impact from the omnipresent forces related to gravitational acceleration, viscous dissipation, inertia and surface free energy acting within a space-time dimensional system.

Capillary length	$H = (\gamma(\rho g)^{-1})^{0.5}$	actually not dimensionless but, as the name implies has the unit of length = m
Capillary number	$Ca = v \eta \gamma^{-1}$	$= We/Re$
Reynolds number	$Re = \rho v 2r \eta^{-1}$	balances inertial vs. viscous forces and indicates the onset of turbulent flow
Bond Number	$Bo = \rho g r^2 \gamma^{-1}$	balances surface tension forces vs. gravity forces
Weber Number	$We = v^2 \rho r \gamma^{-1}$	balances inertial vs. surface tension forces
Ohnesorge number	$Oh = \eta (r g \gamma \rho)^{-0.5}$	$= (We)^{0.5}/Re$
Suratman number	$Su = \gamma \rho r \eta^{-2}$	$= Oh^{-2}$

Table 3 Dimensionless numbers in fluid dynamics. Note, that  $r$  represents a characteristic length of interface. In many cases the radius is used as  $r$ , but also the diameter is employed as the characteristic length.

In this study generally the practical dimensions are retained in order to focus the application onto real dimensional systems. Furthermore, many of the phenomena, such as inertial effects, are not universal over all dimensionless space defined by these numbers. Therefore, it is necessary in this field to refer to dimensionless number regimes within specific constraints of the dimensions of the problem.

### 2.3.17 Droplets, films – finite liquid systems

Until now, all the approaches discussed deal with an infinite liquid source (supersource). In many practical applications a finite amount of liquid is invoked as drops or films.

First let us look at the spreading of droplets or films on a solid surface. While the numerous numerical and analytical modelling descriptions under different gravitational and energetical domains are somewhat beyond the scope of this review (an example can be found in Chebbi and Selim (Chebbi and Selim, 1997)) we look at some of the experimental and qualitative work done in this field.

Apel and Marmur (Apel and Marmur, 1999) analysed the spreading of liquids on rough surfaces, identifying the effect discussed previously as superwettability. The surface roughness acts to form a multitude of local menisci causing a drop to spread. In the studies contributing to this thesis, this effect was observed on a crystal surface of calcite using a drop of glycerol, where the naturally quasi-smooth crystal surface resulted in a defined equilibrium spreading contact angle, Fig. 19. However, a microrough surface resulted in the development of a macroscopic precursor. This is illustrated using Confocal Laser scanning Microscopy in Fig. 20, in which wicking in and through the roughness-contributing structure causes the droplet to spread. The final result is a macroscopic drop contact angle approaching zero.



*Fig. 19* Equilibrium edge of a drop of glycerol (dark image) on a naturally smooth surface of calcite. More details see Fig. 20.

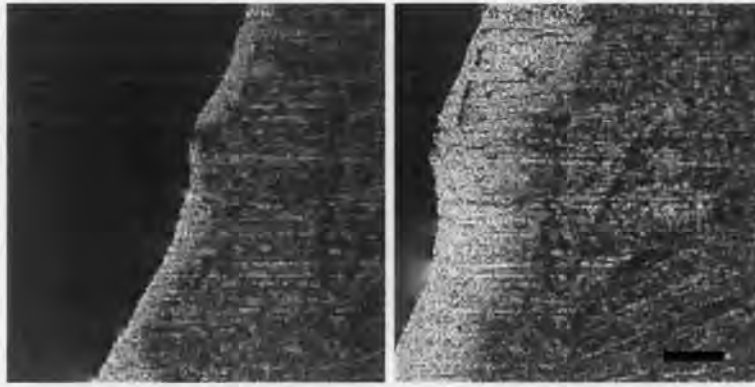


Fig. 20 CLSM (Confocal Laser Scanning Microscope) picture of the edge of a drop of glycerol placed on a roughened surface of calcite. Wicking in and through the surface roughness causes the drop to spread. Left: 20 s after drop application, right: 120 s. Scale bar for all images is approx. 150  $\mu\text{m}$ .

Gerdes (Gerdes, 1998) investigated the dynamics of spreading on a surface having different ordered patterns of capillary channels parallel and orthogonal to the direction of spreading.

Marmur *et al.* pioneered in a series of papers (Marmur, 1988), (Marmur, 1992), (Danino and Marmur, 1994) the influence of available liquid amount on the uptake into capillary structures. Factors discussed are the size of the porous medium, its pore size distribution and the shape of the liquid reservoir. If the liquid reservoir shows a curvature, as is the case with a liquid droplet, then the curvature causes a pressure inside the liquid which again contributes to a driving force (Marmur, 1988). The curvature grows as the liquid imbibes from the drop into the capillary. Another consequence is that when the contact angle is greater than  $90^\circ$ , imbibition still occurs. The influence of the pore size distribution on preferred wetting into some capillaries is identified. Also the consequence arises that the wetting front is subsequently becoming non-uniform creating a re-distribution effect, which accords with the postulation of differentiated absorption (Marmur, 1992). However, they make the traditional LW assumption that larger pores are filling initially faster than the smaller ones. Experimental evidence of the phenomena was deficient, as admitted, due to experimental constraints.

An important contribution comes from the discussion of the re-exposure effect, which plays a role when the porous substrate is very thin. Re-exposure refers to the delivery of fluid to the surface of the porous medium either by sideways wetting through the porous structure, regaining access to the surface or by local saturation effects. Under these conditions, the boundaries, or the interface to the environment (vapour phase), start to have considerable influence. One example exhibiting such behaviour is the radial penetration of liquid into paper. This was studied using different types of liquid supply (droplets and from a capillary, fed by an unlimited reservoir (Danino and Marmur, 1994). Imbibition from an unlimited reservoir fits the theory of a radial capillary (Marmur, 1992). If a limited liquid source is used, e.g. from a feeding capillary not connected to a reservoir, the findings are similar to that seen in the second stage of droplet penetration. The slow rate of uptake is then explained as a



re-distribution of liquid from large into small pores, assuming, initially, the preferential filling under LW of larger pores.

## 2.4 Porous media

Porous media are present everywhere in daily life. They take forms ranging from closed impermeable systems, like closed foams for lifejackets or Swiss cheese, to open permeable media, such as sugar cubes, bread, filter systems, fabrics and paper. Roughly, we may divide porous media into

- foams (a kind of an inverse particulate structure, where the voids are the nodes and the interstitial material the skeleton),
- biological substrates, like wood with vesicular voids, often poorly interconnected,
- mechanically created structures like stretched particle-filled polymer films, and finally
- particulate structures.

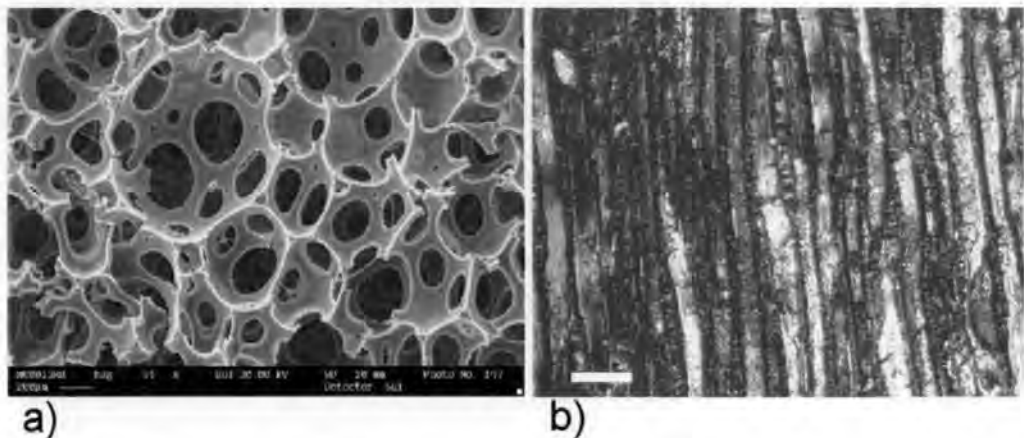


Fig. 21 Examples of (a) a permeable automotive-foam: polymer, filled with  $\text{CaCO}_3$ , SEM Picture, scale bar is  $2000 \mu\text{m}$ , (b) polished section of wood (probably *Libocedrus decurrens*) from a pencil with parallel capillary pores, CLSM reflection picture, scale bar is  $50 \mu\text{m}$ .

In this last important group, the spatial arrangement and local geometry of the pore network are of course dependent on the intrinsic shape of the contributing particles in the widest sense of solid objects on a meso- or micro-scale, such as fibres (unfilled paper, non-wovens, insulating material), yarns (fabrics), sheets or foils (laminates), platelets (ceramics, pottery), beads (air filters, sintered glass), solidified liquid droplets out of emulsion (Styropor - expanded polystyrene), micro-crystals of all kinds of shapes (tablets, stones, concrete, gypsum) and complex mixed systems (filled paper, soil). Gels and flocculated colloidal structures are a special

case, where a visco-elastic network is formed by interacting colloidal particles, and the capillary spaces in between are, during formation, filled with liquid. Sometimes the particles themselves are also porous, and occasionally a fractal scaling of structure goes down to molecular dimensions. In artificial particulate structures, the "binder" also plays an important role. Its action can range from film-forming and sealing the whole structure to pointwise binding, leaving the structure open and permeable. Hilfer (Hilfer, 1996) for example, gives an extensive review and overview of approaches and models concerning porous media regarding structural relaxation and transport phenomena. Focus is on mathematical definitions of set theory and geometrical descriptions of complex microstructures. He gives equations of pore-scale transport and discusses upscaling to macroscopic descriptions.

#### **2.4.1 Characterisation of porous media**

As the issue of porous media characterisation covers a vast area of research, this section focuses mainly on paper-related structures. Here also, only an overview is given and concentration is made on some selected publications.

Important porous media parameters include surface free energy and geometry/morphology. The structural properties which characterise the behaviour of a porous substrate are:

- a) porosity,
- b) pore size and size distribution,
- c) throat size distribution,
- d) connectivity,
- e) tortuosity,
- f) permeability,
- g) pore/throat shape (including aspect ratio).

While a) is directly measurable by an adequate porosimetry method and f) is experimentally quantifiable, b), c) and d) need a more sophisticated description. In particular c), d) and e) require to date the involvement of a simulator program (microtomography as a potential experimental method is discussed in the next paragraph). Furthermore, g) is best visualised by using an adequate method of microscopy, amongst which electron

microscopy is widely used, which does go some way toward determining d) and e) also, at least semi-quantitatively. Quantifying connectivity and pore arrangements in space are important issues which still need evaluation when a pore network simulator is involved as it ideally is necessary to reduce the number of ill-defined fitting parameters. Baldwin *et al.* (Baldwin *et al.*, 1996) using a magnetic resonance imaging technique (NMR) and image analysis, characterised binarized pictures in terms of pore morphology and fractal dimensions.

Direct experimental 3D digitised imaging is in its infancy. For example, microtomography has, as yet, limited resolution ( $> \approx 8 \mu\text{m}$ ) (Goel *et al.*, 2001), just outside the region of micrometers and below the resolution needed for paper coating structures. This, however, is a highly interesting new method which allows for an excellent 3D visualisation of porous structures and holds much potential for the future.

Some examples of electron micrographs for porous media are shown in Fig. 21, (in previous section), and Fig. 22 below. The example in Fig. 22 shows a synthetic polypropylene laminate which is  $\text{CaCO}_3$ -filled and stretched to form a synthetic paper, Synteape<sup>5</sup>, which is used later in this study as a non-interactive substrate for producing idealised coating structures. Microscopy is a direct means to verify the order of magnitude of the values of parameters measured by other methods.

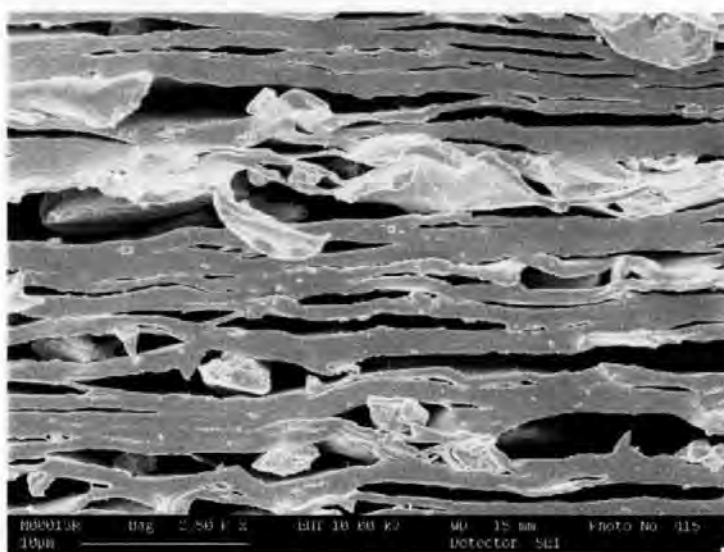


Fig. 22 *Synteape cross-sectional view of the internal laminate structure, showing a strongly anisotropic porosity, no transplanar permeability.*

More often it is found convenient to classify structures using a variety of pre-defined structure type definitions which serve to evaluate the images seen in microscopy. These are most applicable to the region of mesopores. Fig. 23 shows how some of these categories can be explained by the previous porous structure

<sup>5</sup> Synteape is a registered trade mark of Arjo Wiggins Limited, Gateway House, Basing View, Basingstoke, Hampshire, RG21 4EE United Kingdom.

definitions of a) through g). These examples illustrate the usefulness of the developed concepts and parameters in describing in words the visual internal appearance of a porous structure.

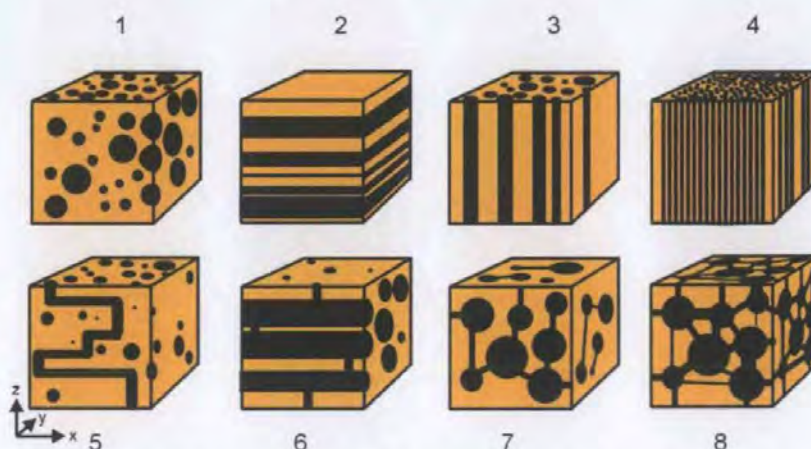


Fig. 23 Schematic of some different morphological properties: (1) closed pores, no permeability and zero connectivity, (2) strongly anisotropic structure, permeable only in  $x,y$  plane, (3) unidirectional capillaries, connectivity  $\approx 2$  but no tortuosity, (4) same as (3) but different number average  $d_{50}$  pore diameter despite similar porosity, (5) no connectivity but high tortuosity, (6) small connectivity with high tortuosity, permeability is strongly non isotropic (7) showing features of distinct pores and throats, multimodal pore size distribution, monomodal throat size distribution, low connectivity, high tortuosity, reduced permeability, (8) distinct pores and throats, multi-modal pore and throat size distributions, high connectivity, medium tortuosity, high permeability.

In many practical applications, the structure may only be determined approximately, applying a systematic probing or observational method and deriving some usable parameters. There are many such methods for studying paper, for example, air permeation measurements, equilibrium liquid saturation (such as the supersource method used in this study); a lot of them are in fact adapted to a specific application in the industry.

The most accepted method to investigate a porous structure is by intrusion/extrusion porosimetry, where the use of mercury as a test liquid is the most widespread technique, (Larrondo and St.Amour, 1995), (Abrams *et al.*, 1996), (Gane *et al.*, 1996), (Ellis and Fripiat, 1996), (Johnson *et al.*, 1999), (Bodurtha *et al.*, 2001). Mercury is an ideal liquid, as it shows a very high contact angle to most solid substrates and, therefore, the Laplace equation can be employed to relate an applied pressure with a relevant pore radius being intruded by the non-wetting liquid mercury. The main drawbacks of the method are the effects induced by the high pressure applied and the shielding of large pores by small access throats. To overcome these drawbacks a number of correction methods are suggested in the literature. The adoption of a network model, such as Pore-Cor, and the correction program Pore-Comp<sup>6</sup> (Gane *et al.*, 1996), such as are described later in the experimental chapter, provide ways to overcome such problems.

<sup>6</sup> Pore-Comp is a software developed by the Environmental and Fluid Modelling Group of the University of Plymouth, Devon PL4 8AA, U.K.

Methods related to mercury porosimetry include water intrusion porosimetry for strongly hydrophobic substrates (Fadeev and Eroshenko, 1997), and the liquid extrusion porosimetry introduced by Miller and Tyomkin (Miller and Tyomkin, 1994a), which monitors the extrusion of a wetting fluid from a pre-saturated structure.

Another method is frequently used to determine the surface area of a porous sample. It is the so-called BET, named after Brunauer, Emmett and Teller, and is based on nitrogen monolayer adsorption isotherms, (Adamson, 1990): the adsorbed quantity being proportional to the available surface area.

Thermo-porosimetry is another method with much potential in this area. It is based on the depression of the melting temperature of a frozen liquid in a pore compared to the bulk liquid. The depression of melting temperature is imposed by the boundary constraints of size in a given pore. This is effectively a semi liquid-crystal effect imposed by the surface order of the molecules of the fluid at the skeletal boundary. Two methods are applied to measure energy transitions attributed to the phase change as a temperature sweep is performed. Differential scanning calorimetry (DSC) was recently proposed to study paper structures by Maloney and Paulapuro (Maloney and Paulapuro, 2001) for the determination of pore size in regimes down to 10 nm. This method is currently being used for an independent confirmation of preferentially imbibed pore sizes. (Joint research project: Helsinki University of Technology and Omya AG).

Another method is NMR (nuclear magnetic resonance) cryoporometry which was recently applied to analyse paper coating structures by (Furo and Daicic, 1999). Direct comparison between the different methods, it seems, has not yet been made but an attempt is under way initiated by the author of the thesis. (Joint research project: Swedish Surface Chemistry Institute, YKI, Helsinki University of Technology and Omya AG).

#### **2.4.1.1 Modelling approaches to visualise pore shapes**

In order to assess the complex void spaces between particles, computer modelling approaches have been undertaken by various authors.

The approach of Baldwin *et al.* (Baldwin *et al.*, 1996) was driven further by Toivakka and Nyfors, (Toivakka and Nyfors, 2001), where by different simulated packings of spheres, followed by subsequent pore-centres determination by erosion and voxel-wise build-up, a model of the 3D-pore shape is attained. The animations in Fig. 24, Fig. 25 and Fig. 26 show impressively the different pore shapes and resulting connectivities.

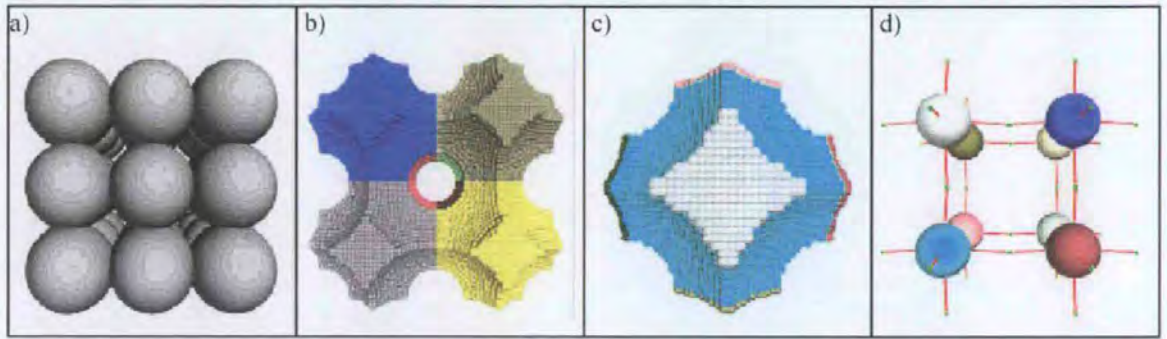


Fig. 24 Cubic packing (a), its pore space (b), an individual pore with throats (c) and the connection graph (d). In arbitrary units, the particle radius is 1.1 and interparticle centre-centre separation 2.0. (Toivakka and Nyfors, 2001).

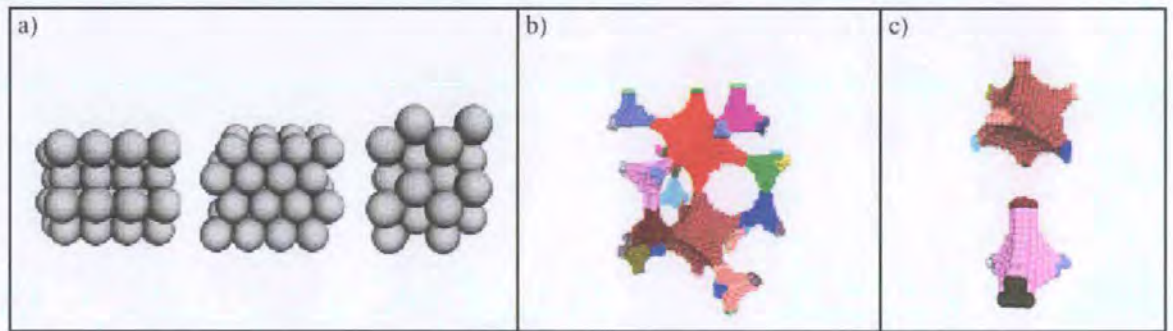


Fig. 25 Hexagonal close packing (a), its pore space (b) and the two different types of pores (c). Particle radius is 1.1 and closest neighbour centre-centre separation 2.0, given in arbitrary units, (Toivakka and Nyfors, 2001).

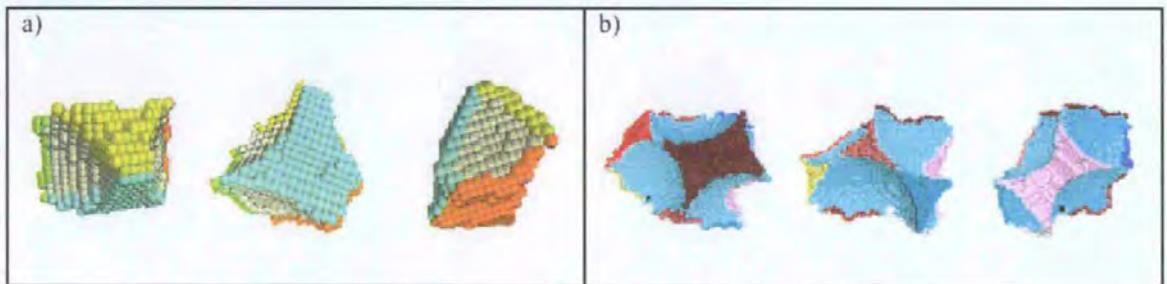


Fig. 26. Examples of pores from particle packing. Co-ordination number (connectivity) is 4 in (a) and 9 in (b). Three views from each pore are shown, (Toivakka and Nyfors, 2001).

These visualisations are very helpful when it comes to the understanding of real void shapes. Although they are a step further towards reality, compared with simpler simulations such as Pore-Cor (used in this thesis), it is, at the moment, not convenient to use the models as the basis for the skeletal surface in an imbibition simulation due to the level of complexity of the surface in relation to existing computing power. However, the final step to geometrical reality would be replacing the spheres by arbitrarily shaped particles. Of course, this approach still falls short of complex mixed systems, especially when the components of such systems interact with each other and with themselves. Furthermore, the impact of compressible species cannot be contemplated due to a lack of knowledge of shrinkage and condensation forces. Unfortunately, all of these aspects exist in a typical paper coating formulation and exhibit themselves at different stages of the coating formation.

## 2.5 Transport processes in porous media

### 2.5.1 Diffusion, vapour adsorption and film flow

Beside the main processes of capillarity, which this work deals with primarily, there are other mechanisms which play a role in porous media liquid absorption. The diffusive process of evaporation, as mentioned before, is relevant for many practical liquids. Some of the commonly encountered effects are summarised.

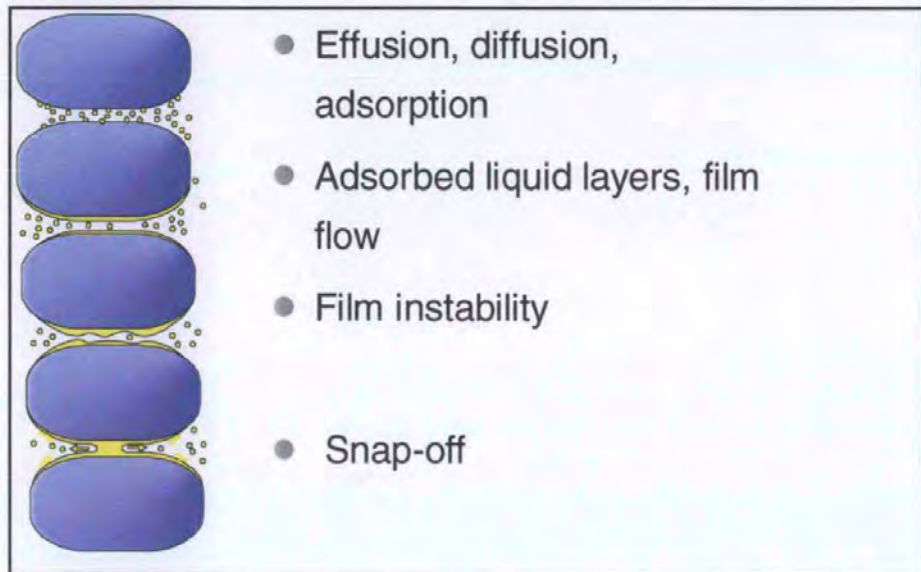


Fig. 27 Schematics of the mechanisms ranging from diffusion to capillarity, (skeletal particles are shown in blue, liquid and liquid vapour in yellow).

A typical sequence is shown in Fig. 27. Diffusion transports liquid molecules within the porous network where the solid pore walls start to adsorb liquid molecules and a liquid film forms. Good (Good, 1971) gives a generalisation of the LW equation including a film pressure term to explain the influence of adsorbed vapour inside a porous structure. The thickness of the film starts to grow, and through a wetting process the film may start itself to move. Film flow then could be defined as a flow parallel to the interface direction. When a critical thickness is reached in a capillary, the film becomes unstable and starts to show a wavy surface. Eventually, two adjacent liquid "waves" touch each other, a process known as snap-off. Two menisci form and move depending on liquid availability. The transition from a pore with adsorbed films to a pore filled with liquid is also referred to as capillary condensation in the field of adsorption science. Normally, these effects are confined to pore sizes which are large compared with the continuity conditions of a fluid meniscus. The continuity conditions are themselves dependent on fluid abundance, the rate at which fluid can be delivered into the pore from surrounding constraints and the internal fluid properties such as its inertia.

These phenomena are described in some publications in the fields of soil and petroleum science. A recent example of observation of these mechanisms is the work of Bernadiner (Bernadiner, 1998), and an application to a comprehensive pore level model is given by Tuller *et al.*, (Tuller *et al.*, 1999). It includes pores of different cross-sectional shapes, longitudinal steps, (actually a pore with two connecting throats) and slits. The transport mechanisms range from adsorbed liquid films to capillary condensation, interfacial configurations, saturation and liquid retention.

## 2.5.2 Transitions in film flow – meniscus movement

Beyond the described features above, there is evidence for further related phenomena. Simple experiments in a macroscopic glass capillary, where film flow is easily producible, show a range of interesting phenomena, such as multiple snap-offs leading to a chain of enclosed air bubbles, Fig. 28. This seems to be one potential mechanism for the explanation of unfilled pores or entrapped vapour bubbles in a porous substrate, a subject which is discussed later.

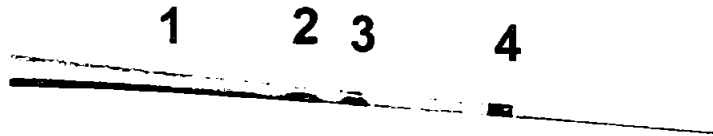


Fig. 28 *A simple experiment showing at the same time: (1) liquid film (dyed squalane) flowing in a glass pipette, (2) unstable regime, a bulge forms, (3) the necking process, two menisci have just formed, (4) an isolated slug of liquid.*

An incomplete assembly of the described and proposed mechanisms are compiled in Fig. 29.



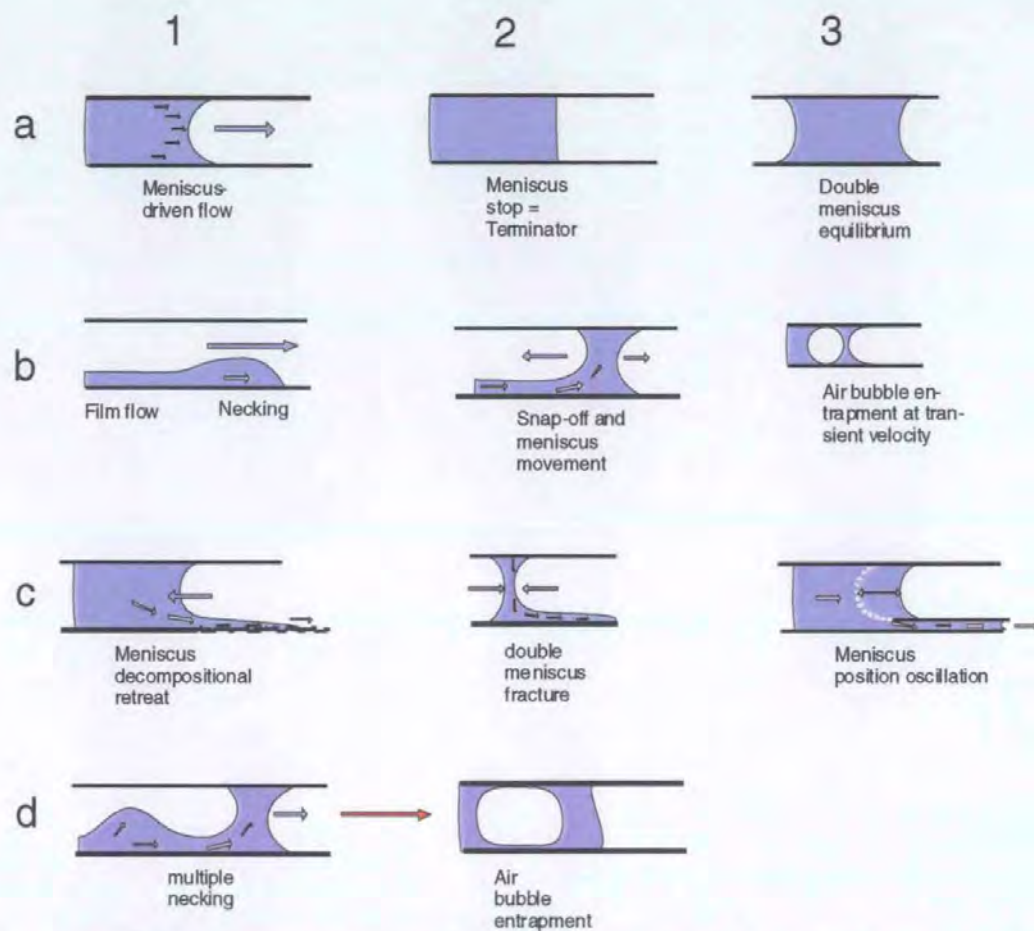


Fig. 29 Mechanisms between film flow and meniscus movement: (1a-3a) standard condition, (1b-2b) as described by Bernadiner (Bernadiner, 1998), (3b) as described by Fisher and Lark (Fisher and Lark, 1979), (1c, 2c, 3c and 1d) author's observations in simple capillary tube, (2d) the important consequence of (3b and 1d). (Blue arrows indicate direction of interface motion, white arrows direction of liquid flow).

In many applications, especially in the petroleum industry, the flow of three phases, one gas and two immiscible liquids, like brine and oil, is studied, often as a function of saturation level of the various phases, (Huang *et al.*, 1995), (Keller *et al.*, 1997), (Dixit *et al.*, 2000). Depending on their relative properties, such as density, viscosity and surface tension, a range of pore-scale phenomena lead to macroscopic flow patterns such as fingering. Although there are some application in paper science, for example in offset printing, the reported work here restricts itself to the study of one liquid phase.

### 2.5.3 Imbibition into porous media

Imbibition focuses on the "suction" of liquid into a capillary-like system: the system in question being a porous network structure. Again there are many contributions to the literature from a vast range of applications. An important part of this work, however, is the use of a convenient method to measure imbibition into porous media experimentally. Therefore, a review of some existing techniques and approaches is made, omitting work done specifically in the field of paper science which was reviewed earlier in section 2.1.5

Marmur and Cohen (Marmur and Cohen, 1997), use an equation for vertical capillarity into a porous medium which separates the unknown values of contact geometry,  $\cos\theta$ , and the effective capillary radius,  $r$ . The calculated parameters can then be compared with a horizontal model. They find a value for  $\theta$  which is greater than the expected intrinsic contact angle ( $\theta \approx 0$ ) for the fluid and surface used, even for low surface tension organic liquids being imbibed into sand and a filterpaper. They point out that this is a result of the fact that imbibition into a real porous medium is modelled using an equivalent cylindrical model capillary. The pore wall roughness and the changing pore geometry of the real structure lead in this model to a higher contact angle as a result, and supports the dynamic contact angle theory.

### **2.5.3.1 Transplanar imbibition**

Transplanar imbibition (transport perpendicular to the plane of a sheet-like material) is important for printing, gluing, dyeing and impregnation of substrates such as leather, fabrics and paper. The difficulties are often in respect to the short time and distance range of the processes, especially when thin films or microscopic droplets of fluids are applied.

Recently, the propagation and absorbency of an ultrasonic signal within a given medium was used to measure the characteristic properties of the medium as air in the voids is replaced by liquid. Changes in the air to liquid ratio result in absorbency and/or transmission variations of the ultrasonic signal. The thesis of Gabriel (Gabriel, 1999) describes and discusses this method to study paper and different liquids. Experimentally, a liquid (i.e. water, ink or coating colour) is imbibed into the substrate. During this process the transmission of the ultrasonic waves through the sample is recorded. The imbibing liquid replaces the air within the substrate and may cause structural changes as well. (Liquids propagate ultrasonic signals better than gases such as air). The ultrasonic receiver records even the smallest alterations of the signal as a result of changes in the porous sample. A computer calculates imbibition curves and provides characteristic data. At the present stage, the limits in frequencies involved for measurements prevent a comprehensive interpretation of the data. An ultrasonic spectral analysis could overcome this limitation. Another drawback is that the change in measured signal intensity can have many different physical reasons, including interference, which makes interpretation difficult.

An application of this method to consolidated pigment structures was considered at an early stage of this project but abandoned later due to the above-mentioned limitations in interpretation.

### 2.5.3.2 Planar wicking

Planar substrates, such as paper, tissues and fabrics, are easy to handle specimens for studying in-plane imbibition. However in many cases transplanar imbibition is more important, but is more difficult to measure. One drawback dealing with planar wicking experiments for fundamental research may be the large contribution of the linearly orientated interfaces and outer surfaces.

Kissa (Kissa, 1996) reviewed wetting and wicking with a focus on textile (fibrous substrates) applications. He proposed the term "wetting" only for the intrinsic process of replacement of a solid/vapour with a solid/liquid interface, while wicking is termed the secondary process of liquid being imbibed into a void structure. He pronounced the differences of finite- and supersource liquid reservoirs on imbibition processes.

Pezron *et al.* (Pezron *et al.*, 1995) investigated the imbibition into a fabric, finding the usual linearity with respect to the square root of time. They were able to separate the process of surface creeping, within the surface structure of the fabric, from the bulk uptake, and to quantify it to some extent.

Nederveen (Nederveen, 1994) considered highly porous non-wovens, which showed, in some cases, fibre swelling during imbibition and permeation experiments. For non-swelling systems, progress of the wetting front was observed to be linear with respect to the square root of time was also seen. A modified equation for swelling substrates was given. Experimentally the fibre mats are clamped between two transparent plates. On one edge, the plates are brought closer together to form a porosity gradient through the sample cross-section. At pre-defined times, the liquid front is marked on one of the plates and can be analysed in relation to the local density of the mat.

There are a couple of recent approaches, concerning what is called interface roughening. In other words, the macroscopic wetting front deviation from a straight line is analysed as a function of elapsed time and wetting velocity. This topic is linked to phenomena on the microscale, in this thesis called the preferred pathway flow, which is discussed later in sections 6.6.5, 7.6, 9.4.2 and 9.4.4.

Dubé *et al.* (Dubé *et al.*, 2000) give an overview of the theoretical and experimental work done in the last two decades. The main conclusion is that the scaling of moving interfaces is dependent on the fluctuation of the average capillary pressure gradient which sets the length-scale for interface roughening.

Horvath and Stanley (Horvath and Stanley, 1995) used an interesting test method to analyse the growth of the liquid/vapour interface during imbibition of liquids into paper. They use a video camera to monitor the wetting front in a long paper strip, and, via a computer, the wetting front is kept at a constant height using a stepper motor. The imbibition velocity is controlled by choosing different heights which yield a different gravity impact. The growth of the imbibing interface is analysed as a height-height correlation function  $C(t)$ . They report a stronger interface roughening with lower wetting front velocities and find that  $C(t) \sim t^\beta$  with  $\beta = 0.5600 \pm 0.0003$ . The interpretation of  $\beta$  is given in terms of anisotropic pinning and de-pinning of the meniscus, omitting any other potential mechanisms.

Van Oss *et al.* (van Oss *et al.*, 1992) introduced a new method using the LW equation to quantify the pore sizes and the contact angle by means of liquid imbibition into a porous substrate. They used thin layers of clay particles and packed columns of both the same clay and of monosized polymer particles. In other approaches they used thin layer plates coated with  $\text{CaCO}_3$  particles. With the use of liquids of known surface tension components, they obtained values for the acid-base and Lifshitz-van der Waals contributions. Chibowski, Holysz *et al.* (Chibowski and Holysz, 1992), (Chibowski and Gonzalez-Caballero, 1993), (Holysz and Chibowski, 1994), (Chibowski and Holysz, 1997), use this method applying it to thin layer coatings of particles on glass plates. Using different liquids they determine the surface energy of the solid and its components according to the theory of van Oss *et al.* (van Oss *et al.*, 1992). Using liquids with a contact angle of zero, they then determine an effective pore radius. This is subsequently used in a modified LW equation to obtain values for the surface energy of the solid. This approach is not undisputed. Here it is argued that too many factors influence the results, such as the "two-dimensionality" of the layer with a strong contribution of the interfaces, capillary condensation during the vapour pre-wetting process filling the smallest pores through a snap-off process, and flow micro-mechanisms including inertial contributions. An additional problem as discussed previously is that on mineralic surfaces there are in most cases adsorbed layers of contaminations including water (Gao *et al.*, 1998) giving a lower apparent surface energy than the intrinsic value of the pure surface. The results which are presented tend to differ strongly from what is found using other methods.

Troeger *et al.* (Troeger *et al.*, 1998) exploited the same method (LW wicking) to determine the surface free energy of microporous membranes. The pore geometry was evaluated using SEM pictures and described as a node-fibre structure for PTFE and PP (polypropylene) but UHMWPE (ultra high molecular weight polyethylene) being branched on different length scales. This difference was reported to have no influence on their surface tension measurements.

### 2.5.3.3 Imbibition into an unconsolidated particle framework

Packed beds of particles are quite easy to produce and therefore offer many opportunities to study imbibition. However, there is a drawback due to the remaining uncertainty in many cases regarding structural parameters which cannot be determined. At least it is possible to calculate packing porosities for spheres. Also, as previously reviewed, the forces of the liquid menisci (Zhang and Nakajima, 1999) may cause particles to move, as the author himself has observed under the microscope when using granular structures (section 4.7). A possibility to overcome this issue is described in chapter 4 to allow the formation of a rigid, consolidated structure

The above-mentioned methodology for the determination of the surface free energy of powders, by performing wicking experiments with thin layers of pigment applied to a planar carrier, (Holysz and Chibowski, 1994), has also been used for volume uptake experiments into graduated glass cylinders with a controlled powder filling to determine the effective surface free energy, (Grundke *et al.*, 1996). This last approach is a low cost procedure and may therefore be of some interest for a regular testing environment. It has to be taken into account that all the above-mentioned limitations influence the results and therefore careful and critical assessment of the data is needed.

Lu *et al.* (Lu *et al.*, 1994), (Lu *et al.*, 1995) used experimentation with glass beads. They analysed vertical and horizontal forces acting on a single spherical bead and on what they call packing units. The wetting force within such a porous packing changes not only its magnitude with liquid progression but also its direction. The total vertical force is therefore an attenuated wave function. This is seen as the origin of the Haines jump. Another aspect of the wave-like movement is that the liquid front reaches its equilibrium height only if the system (especially the initially dry system) remains undisturbed. In video sequences it was shown moreover, how, as a first wetting step, a thin film wets the glass bead.

Yang and Zograf, from a pharmaceutical background (Yang and Zograf, 1986a), showed results on imbibition into packed beds of monosized particles, and point out that the application of the LW equation gives wrong results when calculating the single surface tension and contact angle parameters even if linearity with respect to the square root of  $t$  is observed. Later (Yang and Zograf, 1986b), (Yang *et al.*, 1988) they reviewed the mechanisms of imbibition and permeability. Although they describe the Haines jump phenomenon they make no link to inertial contribution, but discuss the assumption of a uniform wetting front, which they term "slug flow".

and also the possibility of unsaturated flow. Furthermore, they experimented with packed beds of monosized beads with varying surface energy and known packing porosity. They found a  $\sqrt{t}$  dependence over a wide range of contact angles. Using octane, where the contact angle is essentially zero, experimental data have been used to calculate apparent dynamic imbibition angles. There is disagreement between these values. From a range of values, obtained with different liquids, they conclude that due to the complex flow patterns in powder beds or compacts, they cannot be expected to follow the bundle of capillaries model. Consequently, they state that any derived values, such as contact angles and pore radii, are physically meaningless. Another interesting discovery was reported, namely that the imbibition into a powder did not occur with contact angles between 70-80°. This confirms that pore geometries leading to flat menisci, imbibition terminators, are prevailing over the intrinsic wetting process.

A special case is treated by Heerjtes and Witvoet (Heerjtes and Witvoet, 1970), where the wetting and de-wetting of powders is studied under conditions of submersion. Here the liquid imbibition is influenced by the air escape properties of the porous sample. Air escape was observed to be dependent on spatial pore size distribution, where the larger pores need to be at the boundaries of the sample.

#### **2.5.3.4 Imbibition into consolidated porous media**

The work of Taylor *et al.*, (Taylor *et al.*, 2000) is close to the subject of this study. The analysed samples are natural limestones, as used in the building industry. The porosities of the samples were determined using a standard vacuum technique and ranged from 19 % to 29 %. A pore size distribution was not determined. 3 alkanes, 3 alcohols and water were the chosen experimental liquids. Many of the material samples had been dried at 105°C. The liquids and the limestone samples were conditioned for 16 hours before the experiment in the measurement cell. This last point raises the question about vapour diffusional pre-wetting and the potential for capillary condensation/snap-off in some relevant pores. The size of the sample used (in the order of 60x60x10 mm), however, does not suggest that an equilibrium condition could have been reached within 16 hours. The imbibed mass of liquid was not recorded continuously, on account of the large bulk of the samples, but weighed at convenient intervals while full saturation was obtained after 17 days. Another point in question is that it is not clear if a correction for air displacement was applied. The large sample size and the sealing of the planes perpendicular to the main flow direction, force the air to be displaced through the whole remaining void network which is likely to have influenced the data. The usual dependence on  $\sqrt{t}$  was observed for all liquids. All liquids except water showed complete wetting, while with water only partial wetting was found. This was

explained by naturally adsorbed contaminants which resist capillary water absorption, which is a desirable effect in the building industry. However, without a quantitative determination of the pore size distribution it is difficult to rule out other possible mechanisms.

Grattoni *et al.* (Grattoni *et al.*, 1995), performed imbibition studies with samples of sandstone, (sample length was 24.2 mm) and ethanol/water mixtures, using a supersource method and measurement of the liquid front position with a cathetometer and telescope. Like Taylor *et al.* (Taylor *et al.*, 2000), they suggest an organic contamination of the intrinsically high energy surface quartz particles to explain the low surface energy they measured. They also report a colour gradient along the porous wetted rock. The observations were discussed in terms of the influence of gravity. They postulated that at a given height, small capillaries take over the transport of the liquid front. For imbibition times  $t < 100$  s, the slopes of the curves were shown to differ from the further regime. This was explained with adsorbed films and inertial influence. The latter effect, however, was considered negligible for the rest of the experiment, "since laminar conditions are set up rapidly". As they use a "long" capillaries model, inertial impact for this *model* is in fact negligible. The summation of inertia in a network of short capillaries is mentioned, but not invoked.

Interestingly, the darkening of the samples quoted in the above work (Grattoni *et al.*, 1995), caused by the changed light scattering properties of pores in which the air is displaced by the liquid, showed a gradient towards the wetting front. This finding is in agreement with the observations of the author described later in section 7.6. The discussion of this pathway/saturation issue involved only the height rise velocities of the capillary flow (Laplace/Poiseuille) balance and the overtaking of the wetting front in small capillaries at a given height due to gravity-dependent retardation in larger ones. Grattoni notes that this point is argued differently by other workers, supposing that gravity has no relevant impact for this range of pore sizes and sample size.

#### **2.5.3.5 Experimental approaches combining imbibition with independent pore size evaluation**

There are few imbibition studies found in the literature where the porous sample is consolidated and the porosity and pore size distribution are well determined. The most convenient and comprehensive way of proceeding is to adopt the methods based on the Laplace equation for non-wetting fluids, for example mercury porosimetry for polar materials or water porosimetry for low energy structures, e.g. porous polymers. Such a methodology, as used in this work, gives an independent measure of the pore sizes which can be compared to imbibition data.

Einset (Einset, 1996) researched reactive melt infiltration, a promising technique, to process reinforced ceramic components. He compared imbibition rates of different liquids into particulate structures of C and SiC, which had been characterised by mercury porosimetry. The Washburn equation is used to describe the parabolic function of imbibition against time, but a discrepancy (1-2 orders of magnitude) was found comparing the pore radii thus obtained with those from mercury porosimetry. This was explained by the "network effect" and varying contact angles induced by contaminants. Dullien's extension (Dullien, 1992) of the Washburn model is applied using a pore with changing diameter (actually a pore and a throat).

Li *et al.* (Li *et al.*, 1994) used a variety of alkanes for wicking experiments into ceramic structures. They assumed that the contact angle was zero, and found an effective radius which was smaller than that afforded by mercury porosimetry by a factor of about 2. They questioned the mercury porosimetry result.

### **2.5.3.6 Micro-model observations**

A very interesting method is based on the use of micro-models. One approach is to apply techniques from integrated circuit production to print a pattern onto a glass plate. The pattern is of a material which protects the glass in the subsequent etching process using hydrofluoric acid. The pattern itself can be anything from a geometrical structure to a binary cross-sectional picture of a real porous substrate. A drawback is the two-dimensional character of the model, where the channel depth and depth profile is dependent on the etching process. Nevertheless, interesting observations can be made under a microscope. A recent example is given by Keller *et al.* (Keller *et al.*, 1997) observing a 3-phase system where the structure is derived from a sandstone and a set of displacement mechanisms are observed. Another representation is given by Bernadiner (Bernadiner, 1998), who describes in some detail the transitions from film flow to snap-off and meniscus movement. Also the mechanism of air entrapment (unfilled pores) are shown. Knackstedt *et al.* (Knackstedt, 1998), (Knackstedt *et al.*, 2000) have used micro-models to show the non-applicability to LW dynamics for many structures which are non-isometric on a microscale (for example as structure 6 in Fig. 23). A further advantage of the micro-model was highlighted i.e. the possibility to determine exactly the pore/capillary perimeter. Also some qualitative work was shown revealing the imbibition of a droplet into an etched "paper coating structure" model. The jump-wise fast pre-wetting of a precursor film, ahead of the wetting front, is visible.



## 2.5.4 Permeation

We briefly look at permeation, which is the motion of a liquid flowing through a porous substrate without a specification of an internal driving force. It is mostly defined for an external pressure-driven process. Hilfer (Hilfer, 1996) states that the permeability is the most important physical property of a porous medium in much the same way as porosity is its most important geometrical property. The permeability  $K$  is expressed using Darcy's Law (Darcy, 1856). This is a phenomenological, semi-empirical equation based on an analogy to the Poiseuillian volumetric flow rate  $q$  through a cylindrical capillary tube of radius  $r$ :

$$q = \frac{r^2 A \Delta P}{8 \eta l} \Rightarrow q = K \frac{A \Delta P}{\eta l}$$

Eq. 33

The fluid viscosity  $\eta$ , (Eq. 25) the driving pressure  $\Delta P$ , the total sample cross-sectional area  $A$  and  $l$  its length are the governing parameters. Darcy pioneered the concept of quantitative permeability, formulating the classical relationship given in Eq. 33. This equation has been widely adopted, and adapted to more complex situations. In soil and petroleum science,  $K$  is often employed in form of a permeability tensor to describe the permeation characteristics in a spatial (mostly macroscopic) context. Relative permeability describes permeation as a function of saturation with a third phase. Pigment-related work concerning the permeability of a growing filtercake of paper coating particles was recently reported by Lohmander *et al.* (Lohmander *et al.*, 1999). A lot of similar work has been carried out with fibres as the permeability of a fibre mat is, in fact, the basis of paper making.

The limits of the Darcy regime have also been analysed, which are mostly exceeded by turbulent flow, liquid circulating in pores (pore-level eddies), and entrapped ganglia of a different phase in small capillary features which may start to move at a pressure threshold value and at very low flow rates where interactions between the fluid and the pore walls become important, (Levine *et al.*, 1977), (Hilfer, 1996), (Seguin *et al.*, 1998a), (Seguin *et al.*, 1998b).

## 2.6 Pore-network models and simulators

A lot of work has been done in the past in this field. The approach is to assemble capillary features into a possible three-dimensional interconnected network. A computer based algorithm applies equations of phase movement within the features as a function of time. A not very recent but comprehensive evaluation is given by

van Brakel (van Brakel, 1975), and a more recent review is given by Ridgway (Ridgway, 1995). Much of this literature concentrates on areas of soil science, oil extraction and chemical effusion in porous media.

Here, it is worth concentrating on those contributions which bear direct relevance on the study area undertaken by the author. A valuable reference source is provided by the review of Matthews (Matthews, 2000). While pore-scale models are already discussed in section 2.3.13, three-dimensional networks have been little used as yet to model coating layers. A prime exception is the work of Pan *et al.* (Pan *et al.*, 1995). They use a fixed high value of 6 for the connectivity and arbitrarily shaped doughnut-hole throats, with also an arbitrarily chosen size range following a Rayleigh distribution. Toivakka and Nyfors (Toivakka and Nyfors, 2001) (see also section 2.4.1.1) obtain more realistic connectivity values from their virtual assemblage of particles into structures, rendering them the interparticle void shapes and their networking. A similar approach is used to model a paper network, using modelled fibres instead of spheres and a growth algorithm. An example is the work of Niskanen *et al.* (Niskanen *et al.*, 1999).

In the field of coating structures, modelling work was pioneered by Kettle and Matthews *et al.* (Kettle and Matthews, 1993), (Gane *et al.*, 1996), (Kettle *et al.*, 1997) using a mercury percolation data-based computer network simulator.

## **2.6.1 The computer network simulator used in this work**

A network model is, as the name implies, an interconnected system of voids. Pore-Cor is a computer network model that simulates the void-space structure of porous materials based on an array of pores and connecting throats. In the following the term "computer network simulator" is used instead of the brand name Pore-Cor<sup>1</sup>. It has been used to simulate the structures of a wide range of porous materials including sandstones (Matthews *et al.*, 1993), medicinal tablets (Ridgway *et al.*, 1997), and soil (Peat *et al.*, 2000). The structural properties of the computer network simulator are described in the following section, while the implementation of the imbibition algorithm is explained later.

### **2.6.1.1 The unit cell**

The computer network simulator uses a unit cell with 1 000 cubic pores in a three-dimensional 10x10x10 array, connected by up to 3 000 throats, which can either be cylindrical or double conical (Ridgway *et al.*, 2001), i.e. up to one connected to each cube face depending on the chosen connectivity. The centre of each pore is equally

spaced from its neighbouring pores by the 'pore row spacing'  $Q$ , and each unit cell is therefore a cube of side length  $10Q$ . Periodic boundary conditions are applied, i.e. each cell is connected to another identical unit cell in each direction. Connectivity, and therefore flow, is maintained between adjacent unit cells in the  $x$ ,  $y$ , and  $z$  directions. When modelling real systems, the pore- and throat-size distribution of the unit cell is optimised so that the simulated percolation curve fits as closely as possible to the corrected experimental mercury intrusion curve (Matthews *et al.*, 1995), (Gane *et al.*, 1996). The pore and throat size distribution is characterised by two parameters, 'throat skew' and 'pore skew'. The distribution of throat sizes is chosen to be log-linear. The throat skew is the percentage number of throats of the smallest size and the linear distribution between the minimum and the maximum size pivots about its mid-point at 1%. The positions of the pores and throats are random, being determined by a pseudo-random number generator. The throats are randomly positioned within the array and the pores are then generated to be the size of the largest throat entering them. The pore size is initially determined as the size of the largest throat connecting to that pore. The pore skew then increases the sizes of the pores by a constant multiple. However, the pores with the largest sizes are truncated back to the size of the largest throat, thus giving a peak at the maximum size.

The percolation characteristics of the network are insensitive to  $Q$ . Therefore, after convergence of the simulated percolation to the experimental percolation has been achieved by scanning through values of throat skew and connectivity,  $Q$  is adjusted so that the porosity matches the experimental value while ensuring that no pores overlap. It has been found that it is not normally possible to represent the overall complexity of the void network of a natural sample using the relatively simple geometry of a single unit cell. The size of the unit cell is often smaller than the representative elementary volume (REV) of the sample. Therefore, different unit cells must be generated using a different seed for the pseudo-random number generator. The model is designed so that different structural parameters in conjunction with the same seed of the pseudo-random number generator produce a family of unit cells which are similar to each other – for example, all may have a group of large pores in the same region. This aspect of the modelling is discussed in detail in a recent publication (Peat *et al.*, 2000). These different stochastic generations use a different pseudo-random number generator seed, and can either use the original computer network simulator optimisation parameters or can be re-optimised to the experimental data. The parameters and procedure are described in more detail in previous publications, (Matthews *et al.*, 1995, Ridgway *et al.*, 1997). As a result it must be recognised that the actual size relationships between pores, throats and throat length can be far removed from reality. The model matches the intrusion percolation and hence, as we

see later, the sample permeability. These are effectively linked via the realistic application of the pore shielding algorithm which plays an important role also in the description of permeability

In the case of paper and board coatings, however, the limitation of the unit cell size is usually manifest only in the  $xy$  plane parallel to the paper surface, whilst the dimension of the  $z$  direction of the unit cell is often sufficient to describe the thin layer properties of coatings and the relevant applied fluid volumes. When it comes to absorption modelling, if continuity of applied thin films of fluid is considered in the  $xy$  plane, or even droplets, the continuity of supersource conditions can be applied easily in relation to the  $xy$  dimensions of the unit cell and the uniaxial  $-z$  direction absorption is then well represented.

Details of the application of the computer network simulator in the context of developing a realistic wetting algorithm forms one of the themes of this thesis.

### 3 Experimental techniques

In this section, standard methods are described which have been used throughout this work. The novel techniques, developed in the course of the project, are explained in the relevant sections in later chapters.

#### 3.1 Confocal laser scanning microscopy (CLSM)

The CLSM (Confocal Laser Microscope) used was a standard Lasertec 1LM21<sup>7</sup>, and is based on a normal light microscope, Fig. 30, with lenses from 5 to 100 times magnification. Additionally, a factor of 16 x or 60 x is given by the two different laser camera heads. Therefore, the maximum magnification is 6 000 times.

The use of the monochromatic laser illumination allows for a very narrow focus range in the *z*-direction (depth of field). As the automated *xyz*-table of the microscope performs a *z*-scan, reflected light from the layer in focus is recorded (if there is an object) and assembled into a picture including the relevant points from all the layers (Fig. 31). The height information (*z*-axis) can be rendered as a grey level image. This image can be used to calculate an average microroughness or to obtain a topographic representation of a surface. The latter is shown in Fig. 31 for a replica of the surface of a CaCO<sub>3</sub> tablet.

---

<sup>7</sup> Lasertec 1LM21 is a product name of Lasertec Corporation, Unit 4, Wendell Court, 16/20 Wendell Road, London W12 9RT, UK.

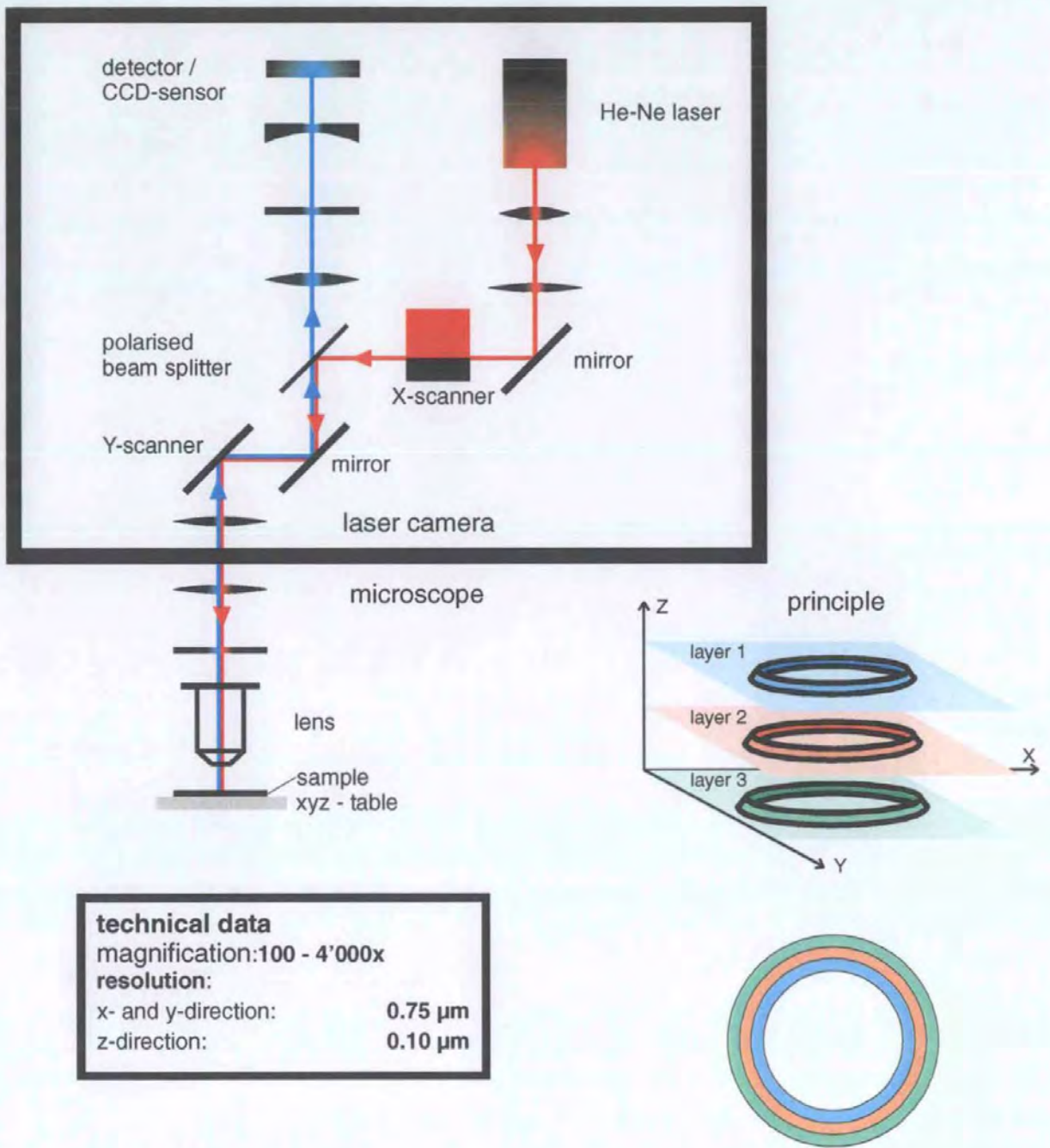


Fig. 30 CLSM schematic.

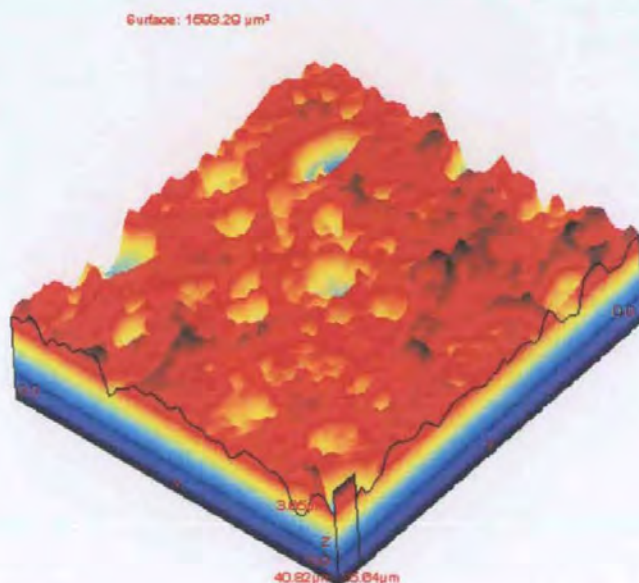


Fig. 31 CLSM topographic image from a resin cast of  $\text{CaCO}_3$  tablet.

### 3.2 Surface tensiometry

Some of the more "exotic" liquids used in this work are characterised with a digital Krüss™ tensiometer K10T<sup>8</sup> using the platinum ring method, the invention of which is attributed to Le Comte Du Nouey.

The surface tension is calculated using equation Eq. 21 where simply the wetted length attached to a platinum ring is balanced by the weight of lifted liquid. The weight of the excess lifted liquid (see Fig. 32) must be corrected for in the observed value.

The ring used has a mean radius of 9.545 mm and the radius of the platinum wire constituting the ring is 0.185 mm. The high surface energy of platinum guarantees a contact angle of zero. Lifting the ring through the interface results in the measured force going through a maximum, as the wetting tension acts tangentially to the ring.

<sup>8</sup> Krüss GmbH, Borsteler Chaussee 85-99a, D 22453 Hamburg, Germany

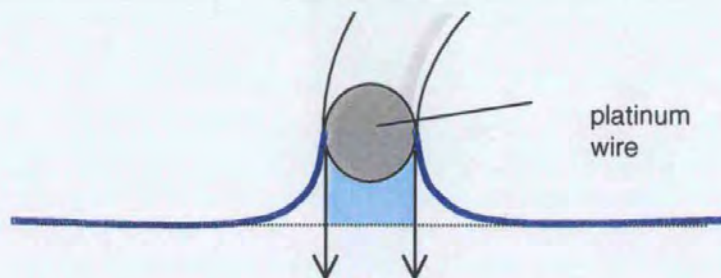


Fig. 32 *Ring measurement schematic, showing for simplicity a cross-section of the ring. In light blue is the hydrostatic liquid volume needing correction. The arrows show the direction of force vectors acting at maximum measured pull force.*

Cleanliness is of primary importance. The platinum ring is cleaned with demineralised water, then Acetone (pro analysis, Fluka<sup>9</sup>) and then gently heated to glowing in a weak gas flame. Measurements are carried out in a thermo-regulated environment (20°C) in triplicate and the deviation between the measurements is usually less than 0.2 mN m<sup>-1</sup>.

### 3.3 Contact angle measurements

To overcome the artefacts caused by a powder surface, the static contact angles for CaCO<sub>3</sub>/liquid systems were measured on a plane of a large crystal of Calcite, Fig. 33. The plane is wet surface ground and polished in the presence of the same polyacrylate dispersing agent as adsorbed onto the ground particulates in the absorption and porosimetry samples. For the detailed grinding procedure see section 4.4.

<sup>9</sup> Fluka products are available worldwide through Sigma-Aldrich. (see [www. sigma-aldrich.com](http://www.sigma-aldrich.com))



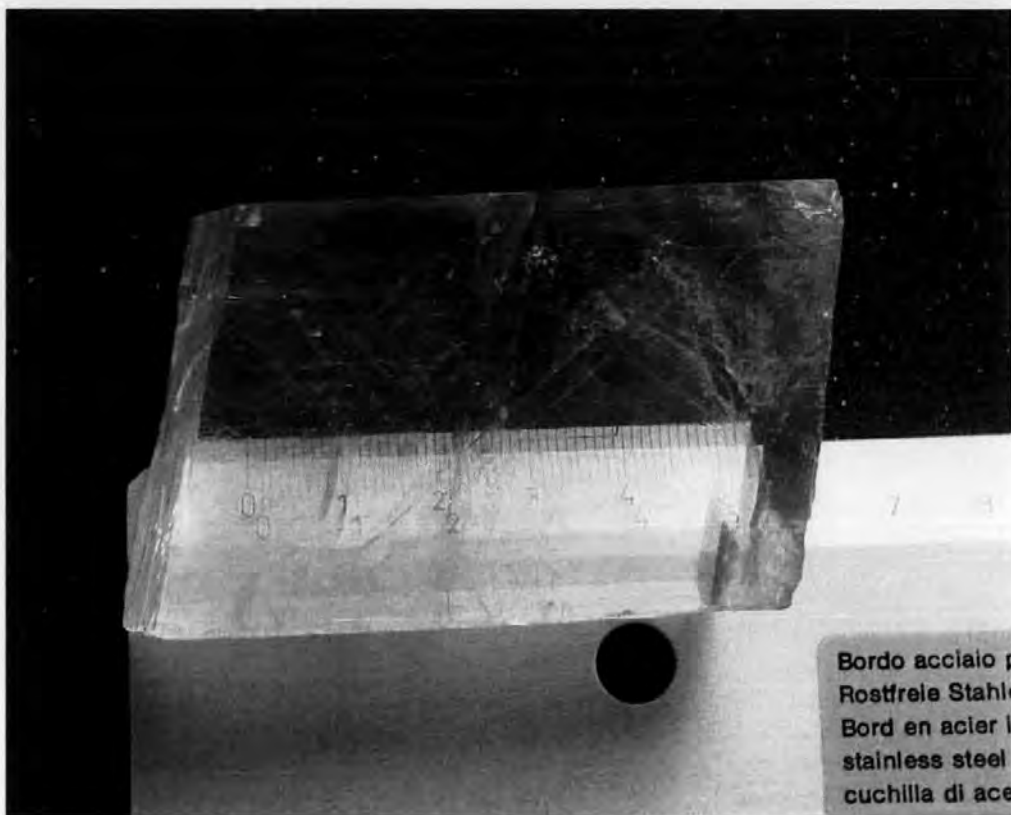


Fig. 33 Calcite crystal used for contact angle measurements prior to surface grinding. (Note the birefringence).

The set-up for observing contact angle was custom-made using a Philips<sup>10</sup> CCD camera (LHD 046200) and an xyz-table (constructed with elements from Phoenix-meccano<sup>11</sup>).

The pictures were captured with a PCI framegrabber (GrabBit<sup>TM</sup> <sup>12</sup>) into Image Access<sup>TM</sup> 3.1<sup>13</sup>, an image analysis and database software (Fig. 34). The contact angle was determined using Image Access' graphical angle measure function.

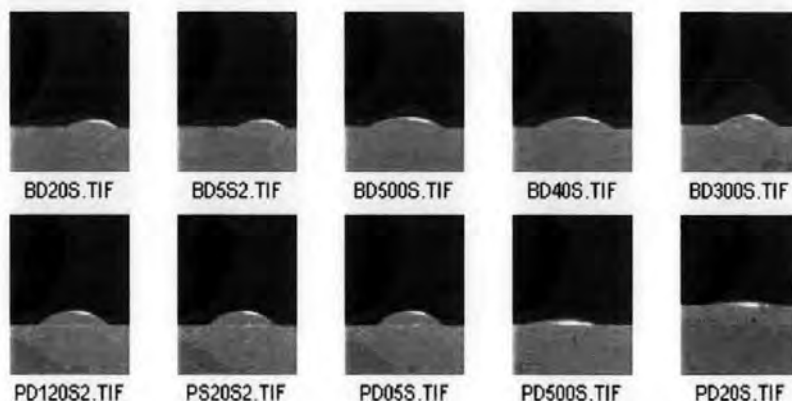


Fig. 34 Some thumbnails from the drop images.

<sup>10</sup> see [www.philips.com](http://www.philips.com) for local distributors

<sup>11</sup> Phoenix-meccano Phoenix Electronics Distribution Ltd., Castlehill Industrial Estate, Carlisle ML8 5UF, [www.phoenix1.co.uk](http://www.phoenix1.co.uk)

<sup>12</sup> GrabBit is a trademark of Soft Imaging System GmbH, Hammer Str. 89, 48153 Münster, Germany

<sup>13</sup> Image Access is a product of Imagic Bildverarbeitung AG, CH-8152 Glattbrugg, Switzerland

The microroughness of the surface was measured with the CLSM. The microscope scanned perpendicular to the surface at 4 780 points with a spacing of 0.38  $\mu\text{m}$ , and measured a surface roughness variance of 0.37  $\mu\text{m}^2$ .

### 3.4 Mercury porosimetry

A Micromeritics Autopore III mercury porosimeter<sup>14</sup> was used to measure the percolation characteristics of the samples. The maximum applied pressure of mercury was 414 MPa (60 000 psia), equivalent to a Laplace throat diameter of 0.004  $\mu\text{m}$ . Small samples were used, each of around 1.5 g in weight. The equilibration time at each of the increasing applied pressures of mercury was set to 60 seconds. The mercury intrusion measurements were corrected for the compression of mercury, expansion of the glass sample chamber or 'penetrometer' and compressibility of the solid phase of the sample by use of the following equation from Gane *et al.* (1996) and contained in the software package Pore-Comp<sup>6</sup> :

$$V_{\text{int}} = V_{\text{obs}} - \delta V_{\text{blank}} + \left[ 0.175(V_{\text{bulk}}^1) \log_{10} \left( 1 + \frac{P}{1820} \right) \right] - V_{\text{bulk}}^1 (1 - \phi^1) \left( 1 - \exp \left[ \frac{(P^1 - P)}{M_{\text{ss}}} \right] \right)$$

Eq. 34

$V_{\text{int}}$  is the volume of intrusion into the sample,  $V_{\text{obs}}$  the intruded mercury volume reading,  $\delta V_{\text{blank}}$  the change in the blank run volume reading,  $V_{\text{bulk}}^1$  the sample bulk volume at atmospheric pressure,  $P$  the applied pressure,  $\phi^1$  the porosity at atmospheric pressure,  $P^1$  the atmospheric pressure and  $M_{\text{ss}}$  the bulk modulus of the solid sample. The total volume of mercury intruded up to and including the maximum pressure, once corrected for sample compression effects, can be used to calculate the porosity of the sample.

Mercury intrusion curves of similar samples gave a repeatability to within  $\pm 0.8\%$  of the total void volume, averaged over the entire intrusion curve.

### 3.5 Rheology

#### 3.5.1 Viscoelasticity measurements

During the last two decades, since stress controlled rheometers became commercially available, viscoelastic measurements have developed to become a powerful means to determine flow properties of liquids in the

<sup>14</sup> Micromeritics, One Micromeritics Drive, Norcross, GA 30093-1877, U.S.A., [www.micromeritics.com](http://www.micromeritics.com)

industry. As a function of frequency or stress/strain the interaction forces of a liquid are probed from the regime of elastic (network-like) behaviour to the onset of flow and beyond.

The viscoelasticity measurements have been performed with the StressTech<sup>15</sup> Rheometer. Different measurement systems are available and described in the relevant experimental context.

For each measurement point, an oscillating shear stress in the form of a sinusoidal wave with a chosen frequency  $f$  (typically around 0.5 Hz), is experienced by the sample. The stress recorded on the sample cup is formed by a similarly oscillating applied strain supplied from the rotor, which in turn is feedback-controlled to develop the constant amplitude of sample stress. The resulting strain of the rotor in creating the constant stress is time-dependently detected, (Eq. 35).  $\gamma(t) = d/L(t)$  is the strain of the rotor, where  $d$  is the thickness of the sheared layer and  $L$  is the distance of displacement in shear direction.  $\tau(t) = F(t)/A$  (force per area) represents the stress.

$$\frac{\tau_0}{\gamma_0} = |G^*|$$

Eq. 35

where  $\tau_0$  and  $\gamma_0$  are amplitudes of stress and strain, respectively. The phase shift of the stress in relation to the strain curve results in the phase angle  $\delta$  (Eq. 36, Fig. 35). For the next measurement point either the frequency (frequency sweep) or the shear stress (stress sweep) is changed, depending on the method used.

$$|G^*| \cos \delta = G' \Rightarrow |G^*| \sin \delta = G'' \quad \text{where } G^* = G' + i G''$$

Eq. 36

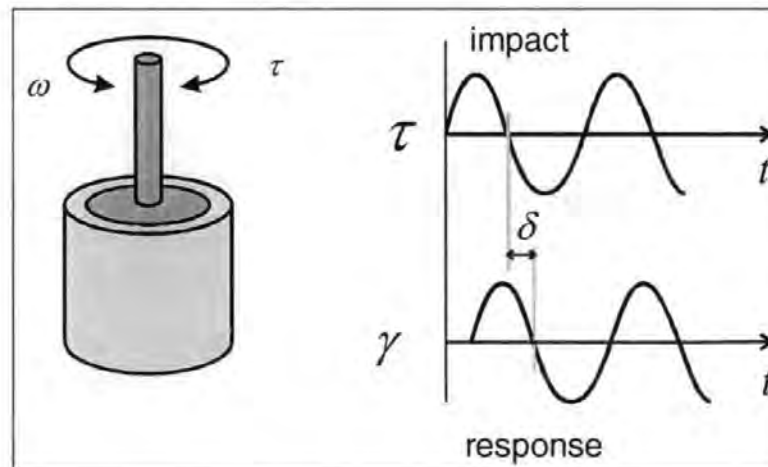


Fig. 35 Principle of oscillation measurements.

<sup>15</sup> StressTech® is a product name of ReoLogica Instruments AB, Lund, Sweden

The real  $G'$  and imaginary,  $G''$  parts of  $G^*$  can be determined referring to the storage and loss modulus, respectively. The complex viscosity  $\eta^*$  as used later in this work (section 10.3) is calculated using the angular velocity  $\omega$  as

$$\eta^* = \frac{G^*}{\omega} \quad \text{where} \quad \omega = 2\pi f$$

Eq. 37

### 3.5.2 Interpretation of stress sweep measurements

Stress sweeps are a useful tool to determine the interactions within a viscoelastic material which lead to a spatial network structure. Often this structure is so subtle (for example milk) that it could not be measured until a new generation of rheometers was developed during the last decade. The decomposition of this structure and the simultaneous onset of flow is often called the yield point. At low stresses, the elastic behaviour of the network structure is monitored. The interactions in the network keep particles in suspension and prevent settling. This is an important issue for many industrial and food applications. After the onset of flow, another important issue is the time which is needed for the re-establishment of the structure. The choice of the right oscillation frequency is linked closely to this aspect. While at low frequencies the interactions have enough time to "follow" the motion of the measurement system by breakdown and reformation of bonds, at higher frequencies this is no longer the case, and the measured liquid appears more solid-like because the motion in each direction is faster than the material can accommodate.

A separate observation and discussion of the elastic modulus  $G'$  and the viscous modulus  $G''$  over a range of applied stress or strain is meaningful. In practice the relation of these two moduli (phase angle  $\delta$ ) is a very important quantity.

#### 3.5.2.1 Elastic or storage Modulus $G'$

The elastic modulus  $G'$  indicates the elastic part of the viscoelastic behaviour. Suspensions and dispersions at higher solids contents show typically viscoelastic behaviour. The elasticity is caused by the interactions between the particles, between the particles and the suspending fluid, and between solved species like polymers. These interactions form a gel-like network structure. This is used to make suspensions stable during storage and transportation. Also important is the rate of re-establishment of the network structure once it has been destroyed

by shear. In this case the structure rebuild ensures that the material does not flow away from the site of application. Examples of this are ketchup, toothpaste and wall paint.

Furthermore, some polymers in aqueous solution, which are able to unfold and stretch, do have the ability to return to their original shape and show an elastic behaviour over a wide range of shear. This property is the cause of the often attributed "slimy" texture, for example that of an egg-white.

### **3.5.2.2 Viscous or loss Modulus $G''$**

The viscous modulus  $G''$  indicates the viscous (or 'plastic') part of the viscoelasticity. Newtonian behaviour is always purely viscous, but that does not mean that purely viscous behaviour has to be Newtonian. The thinner a dispersion is, for example an ink or coating colour at decreasing solids content, the more the viscous behaviour of the continuous phase predominates. A sufficient value of  $G''$  for an ink and/or paper coating colour seems to be important for the absorption of energy during the passage through under a metering blade or in a roller nip.

### **3.5.2.3 Phase angle $\delta$**

The phase angle,  $\delta$ , indicates the relation between the viscous and elastic part of the complex viscosity ( $\eta^*$ ), i.e. a high phase angle means that at the actual level of shear stress the viscous part dominates. The shape of the phase angle curve as a function of shear stress permits to a certain extent a prediction of the runnability of a paper coating colour. Normally, "typical" coating colours show a sigmoidal shape of the curve. Variations can lead to diverse problems on the coating machine.

## **3.6 ISIT Ink Surface Interaction Tester**

Ink-on-paper tack as measured by the ISIT<sup>2</sup> device is defined as the maximum force experienced by a contact disc (also named tack wheel), of material similar to an offset printing blanket, separating from a tackifying ink film measured using a solenoid, coil spring and load cell (Gane and Seyler, 1994), Fig. 37.



Fig. 36 IGT Inking unit, shown without applied ink. On the right hand side the rubber distribution rolls are in place and the print wheel is on top.

The ink film is applied via an inking unit (IGT Reptest<sup>16</sup>) shown in Fig. 36. The total exposed roller area was calculated to be 123 727 mm<sup>2</sup>. Typically an amount of 0.3 ml ink is applied by means of an IGT ink pipette<sup>16</sup>. Then the distributor is started (rotation speed approx. 1 s<sup>-1</sup>, not adjustable) and the ink spreads over the exposed roller area by film-splitting including the print disc rotating with the main rubber roller. Subsequently the print disc is manually transferred to the ISIT machine where the substrate stripe is attached to the sample carrier with a double-sided self-adhesive tape. The ISIT test cycle is started via a linked PC and in a revolution of the sample carrier the print disc transfers the ink to the paper. A print pressure of 500 N is applied with a printing speed of 0.5 ms<sup>-1</sup>. The sample carrier is then stopped momentarily.

The ink-free contact disc is then pressed against the print on the sample platen by the electromagnetic force acting on the solenoid. This action applies an extensional force on the coil spring mounted in parallel with the solenoid. Contact time and force can be varied by electronic controls to optimise adhesion between contact disc and print. At cessation of the electromagnetic force, the contact disc is retracted from the print by the strain force of the extended coil spring, strong enough to achieve separation of the disc from the ink film. Under small extensions, the coil spring provides a constant acceleration during the retraction of the disc. The acceleration can be additionally controlled by a chosen ramp-down function for the solenoid - an exponential rampdown can be chosen to provide zero acceleration (constant velocity) once the motion begins. This is a unique feature of this static test procedure. The strain gauge, fixed between contact disc and coil spring, generates a load-dependent

<sup>16</sup> IGT Reptest B.V., P.O. Box 4672, 1009AR Amsterdam, The Netherlands, [www.igt.nl](http://www.igt.nl)

signal which is recorded as the force during separation as a function of time. The maximum in this force is defined as the tack force at the given time of separation. The sequence is automatically repeated for a pre-defined number of cycles chosen to span the timescale regions of the tack force under study. The build-up of the tensile force required to achieve each individual separation is recorded with time (pull-off curve) and can be analysed through specifically designed software.

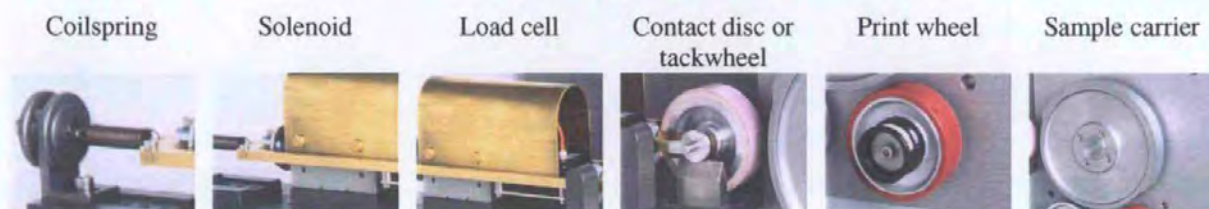


Fig. 37 Ink surface interaction tester ISIT (SeGan™).

### 3.6.1 Interpretation of the tack curves

The following description refers to the general features seen in a typical tack cycle curve as shown in Fig. 38, (Gane and Seyler, 1994).

I Tack rise time is a measure of the openness of the finest pores in the coating (confirmed by the modelling and observation provided in this thesis). Latex can have a diffusive absorbing effect also in this region. Latex may induce also a structural effect, either by packing or by swelling in contact with ink oils. Other structural effects can be observed, for example, a microfloculated or disordered coating consisting of fine particles will have quite a fast rise time. Sometimes this effect can lead to problems of "carry-over ink piling" on later printing station blankets (seen as a build-up of drying/tackified ink) and generally a too fast tack rise is associated with a poor print gloss.

II Maximum tack force is a measure of the cohesion in the ink competing against the "affinity" that the ink has for the coating surface. If removal of ink occurs at this maximum tack force, then the adhesion of the ink to the coating is poor and can also lead to potential piling problems. Too high a maximum leads to rupture at the weakest point in the paper.

III Surface tack decay is a measure of the total pore volume characteristic of the coating "as seen by the ink". It typically shows the level of coating consolidation that has taken place, for example, in calendering or during drying. Often, too fast a fall leads to poor ink curing and a tendency to rub off and too slow a fall indicates potential for set-off. Furthermore, if the sample shows post-tack adhesion failure, due to too fast a fall, then print abrasion is clearly suspect (Gane and Seyler, 1994).

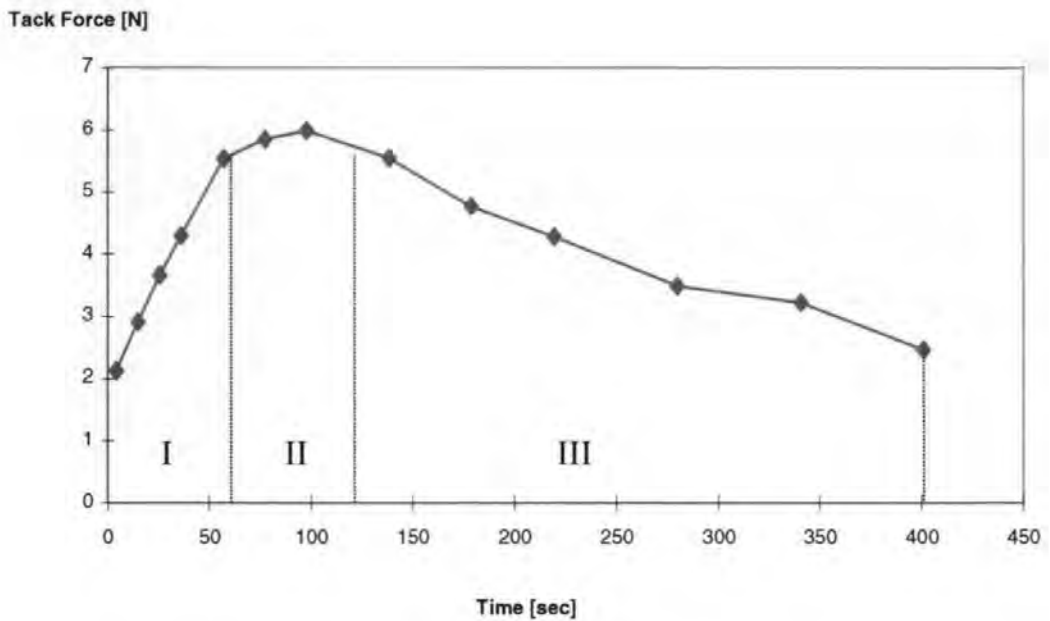
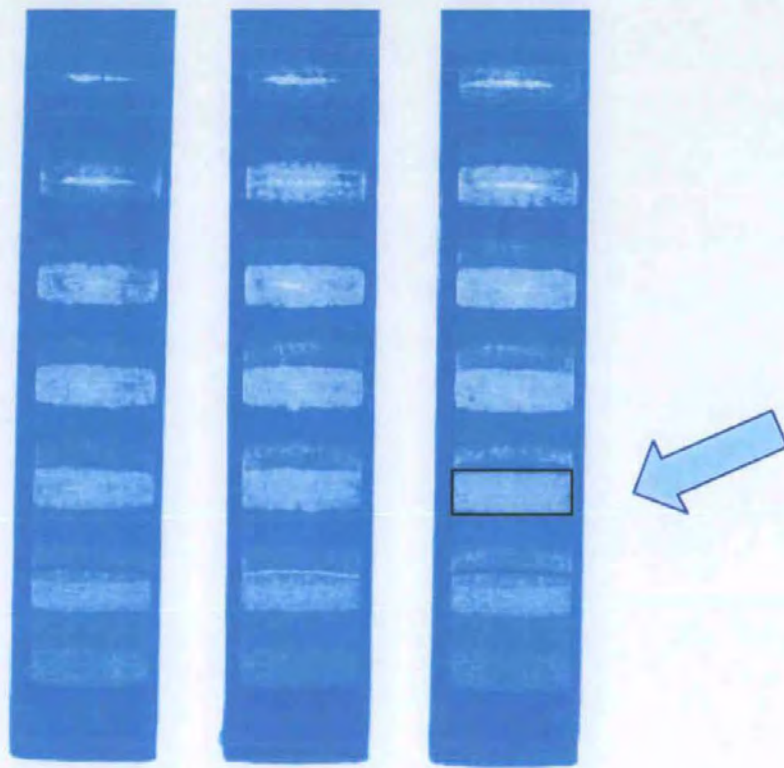


Fig. 38 Schematic tack curve graph with regimes I, II and III.

On the test strip the described development of the tack curve probed by the tack wheel is manifested by marks as shown in Fig. 39. Visual inspection of the marks confirms what is described above in I-III. The so-called footprint area is discussed later in this thesis, and is used as a parameter in a rheological modelling attempt.





*Fig. 39 Test strips indicating pull-offs and the observation of adhesion via the retained print density under the pull-off. Test start at the bottom of each strip, the footprint area is highlighted (arrow).*

## 4 Preparation and characterisation of porous pigment samples

### 4.1 Introduction

The core of this work is the use of macroscopic blocks of mineral coating pigments as model structures for paper coatings. Many valuable investigations have been performed directly on paper surfaces or on model coating layers. A paper coating has a thickness, depending on grade, of between 5-15  $\mu\text{m}$ , and a practical single ink layer is typically 0.25  $\mu\text{m}$  (or in total on a four colour press up to 1  $\mu\text{m}$ ). Even using volumes as small as a microlitre directly onto such a microscopic surface, the volume available in the thin layer pore structure is distinctly limited by saturation phenomena preventing the understanding the complexities of coating imbibition. Speaking more generally, if the porous substrate under study is too thin, then the influence of the interfaces to the environment become dominant. Marmur and Danino (Marmur, 1988), (Danino and Marmur, 1994) discussed one facet of this issue, calling it the re-exposure effect. They describe a thin porous planar substrate being exposed to the surrounding vapour phase of the test liquid. Due to the "thinness" it becomes energetically unfavourable and results experimentally in a lower equilibrium height rise than would be seen in the same porous medium of greater thickness. In the real case of the printing of coated paper, the fluid volume is too small to create an equilibrium vapour environment surrounding the whole planar structure. To investigate this dynamic correctly, therefore, novel experimental techniques are required.

It was decided to step away from thin coating layers, because of these limitations, and to consider the possibility of using macroscopic blocks of consolidated pigment formed over a range of compressions which allow for the equilibrium absorption of measurable droplet sizes without saturation.

A method was developed, derived from an extension of the preparatory work of the author in support of the studies made by Pennanen (Pennanen, 1996), in which consolidated pigment structures are formed. The formation of compressed structures out of powder is a common technique in pharmacology, an example is the work of Koehler (Koehler, 1970), studying the decay of tablets as a function of permeability, capillarity and tablet constitution. Ridgway (Ridgway *et al.*, 1997) formed tablets of lactose where the resulting samples have been used for pore-modelling based on mercury porosimeter data. For this work a similar methodology is employed, resulting in the formation of macroscopic porous structures of  $\text{CaCO}_3$ . By applying different consolidation pressures, a wide range of usable porosities can be obtained which lend themselves to being well characterised using mercury porosimetry. The key point is without change of the surface chemistry or intrinsic

skeletal geometry, a range of usable porosities and  $d_{50}$ -mean pore diameters can be achieved. Such a consistent base of experimental structures for use in various kinds of imbibition and permeation experiments, has not been reported before in the literature.

#### **4.1.1 Why do compressed particles stick together ?**

Loose powder already shows the establishment of some associated network structure, which in most application-based cases is highly undesirable as it reduces the powder flowability. During powder compaction, the single particles are forced so close together that increasingly interparticle interactions are established. A further step is the process of sintering or necking, which is possible because of the ability of metals, salts and other solids to show some bulk and surface mobility. An overview of structure consolidation and sintering, together with some simplified equations, is given by Petzold and Hinz (Petzold and Hinz, 1979). The reduction of total surface area, and hence of surface free energy, is one driving force. Thus, both bulk and surface diffusion generally become appreciable at the temperatures or pressures involved in sintering. This already occurs below the melting point temperature of a solid. Small ice spheres form a connecting neck at  $-10^{\circ}\text{C}$  if touching (Adamson, 1990). In the case of MgO, sintering rates are increased with increasing ambient humidity. The studies here confirm this finding.

#### **4.1.2 Evaluation of method**

Although there are many types of tablet presses on the market, and some of them have been evaluated for this study, the need was recognised to apply very high pressures to achieve rigid structures with the targeted range of porosities between 20 - 40 % (as are typically found in paper coatings). This was achieved using an hydraulic press. The first hydraulic press used had a sufficient range of pressures for an initial study of the method. However, its operation and physical bulk made it unsuitable in the longer term for sample preparation on a regular basis. Therefore, a second press was constructed and will be described in the following sections together with a suitable die for use with the press.

## 4.2 Materials

Two commercially available dry powder products were chosen, both derived from natural  $\text{CaCO}_3$ , ground under similar chemical conditions from the same limestone source (Orgon, France). The grinding was made in a wet state at consistent solids content using a polyacrylate dispersing agent applied in proportion to the specific surface area of the final pigment size distribution and subsequently dried. The dispersing agent was needed to achieve the necessary fine colloidal particles in the grinding process.

The choice of predispersed ground  $\text{CaCO}_3$  is supported by two main considerations. Firstly, it is widely accepted that mineralic solids adsorb other species from the surrounding atmosphere, and secondly, experiments show that the drop in apparent surface energy as contaminants are adsorbed can be monitored by contact angle measurements, (see section 3.3). Therefore, it made sense to use a material produced in such a way that there was a controlled and reproducible amount of a known pre-adsorbed species at the surface. Only a commercially available specialised product as would be used to form paper coatings ensures the right particle size distribution relevant for the experiments in respect to ink fluid components. The resulting range of pore sizes is crucial for the whole work.

The two particle size distributions of the respective products were chosen so that they were distinctly different in respect to the quantity of particles less than the  $2\ \mu\text{m}$  Stokesian equivalent hydraulic diameter. This was to avoid the interference of dispersant molecular weight and size in relation to subtleties in the distribution of the pigment size. The pigments were Hydrocarb OG, 60 % w/w  $< 2\ \mu\text{m}$ , and Setacarb OG (otherwise known as Hydrocarb 95), 95 % w/w  $< 2\ \mu\text{m}$ , defined as "coarse  $\text{CaCO}_3$ " and "fine  $\text{CaCO}_3$ ", respectively. The cumulative particle size distribution curves of the two materials, as measured by sedimentation<sup>17</sup>, are shown in Fig. 40.

---

<sup>17</sup> Measurements made on a Sedigraph 5100 from Micromeritics Instrument Corporation, one Micromeritics Drive, Norcross, GA 30093-1877, U.S.A.

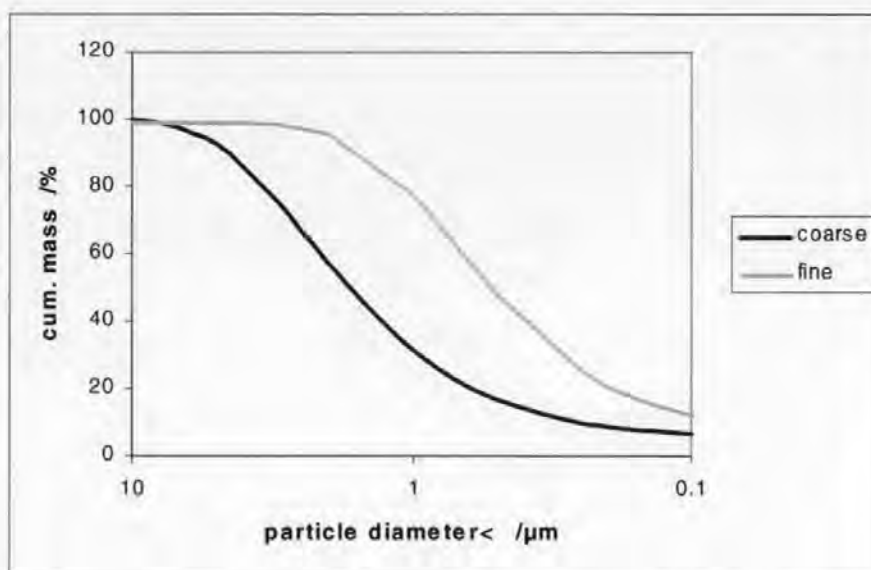


Fig. 40 Particle size distributions of the coarse and fine  $\text{CaCO}_3$  powders used for consolidation of porous tablets expressed as cumulative mass % less than an equivalent Stokesian diameter.

### 4.3 Development of compaction method and devices

For the preparation of the pigment tablet blocks, a cylindrical hardened steel die, attached to a baseplate, with a single acting upper piston was developed and shown to be suitable for a wide range of pigment particle sizes, chemistries and morphologies. The die is perpendicularly divisible into two sections to aid removal of the compacted pigment sample.

The removal of the formed tablet proved to be a critical issue due to strong sticking of the tablet to the die walls. It could be observed that under the applied pressure and the resulting friction, the  $\text{CaCO}_3$  was pressed into the steel. The worst situation was when powder particles entered the small gap between the piston and the die. To overcome this problem a number of approaches have been incorporated, such as using a harder steel quality, polishing the inner surfaces, applying different non liquid anti-sticking agents on the base, such as fluorinated or silicone waxes. However, it was found that only the protection of the inner walls with an inlaid strip of plastic film helped against sticking of the powder (Fig. 41). The development of the die design is shown and briefly explained in Fig. 42, and the present design is shown in Fig. 43.

With all the improvements, the problem partially remains that sometimes the formed tablet decays during the disassembling of the die. The cause is probably that the protective plastic strip does not stay in its original position and wrinkles too much, and subsequently unprotected die walls are exposed to the powder.

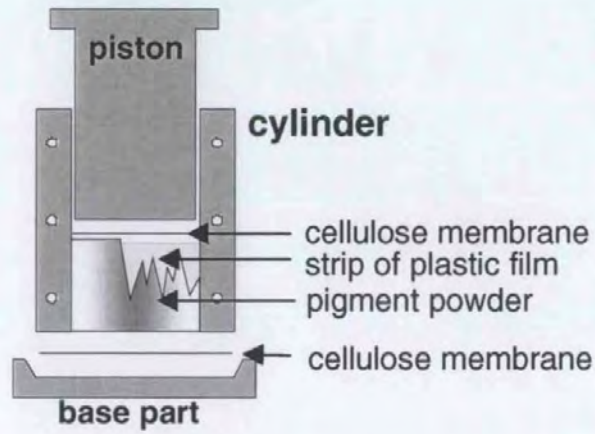


Fig. 41 Schematic cross-section of the die showing the plastic lining and cellulose membrane.



Fig. 42 Development of dies from left to right. (i) The first prototype, found to be too heavy and steel quality too soft, the design also omitted any end-buttet screws to help push the two sections apart. (ii) Improved lighter version but wore out after the production of  $\approx 200$  tablets. (iii) Die with a smaller piston diameter to achieve higher pressures, dimensions did not withstand the high pressure and deformed.



*Fig. 43 The present die design. In front left the die with improved dividing mechanism, front right the piston, behind it the template as an option to push the formed tablet out by the press. Little image top left, top-view of the improved dividing slit.*

The overall steps of improvement through the development are summarised below.

- The shape of the division slit. A design as shown in Fig. 43 helps to maintain the relative position of the two halves, therefore, omitting unnecessary stresses on the compact during the assembly and disassembly of the tool.
- The aids to help uniform separation (guiding bolts and separating bolts)
- The hardness and the surface polish of the steel which both reduced the mechanical friction and sticking of the powder.
- The overall size and weight of the press was reduced to improve the handling.
- A small ventilation channel was drilled into the piston to allow for improved air displacement.
- A second piston, slightly smaller in diameter and a support jig were constructed to push out the compact.

As previously explained, the progression to a second design of hydraulic press was necessitated by the need for a more rapid sample preparation and evaluation within the development laboratories of Omya AG. This press is now described as it formed the regular apparatus for the production of tablet samples (Fig. 44<sup>18</sup>). The press-frame was welded in the workshop. The hydraulic unit with the cylinder exerting a force up to 600 kN and the electronic steering unit were supplied from Cymax AG<sup>19</sup> and produced following the guidelines of the author of this thesis. The press components were put together onto a roll-table to provide mobility.



*Fig. 44 Custom-made hydraulic press for tablet compaction. On the bottom is shown the hydraulic unit, top right the electronic steering unit and the press-frame with the hydraulic cylinder exerting a force up to 600 kN.*

Each tablet was formed from 60 g of homogenised powder carbonate. The homogenising was carefully controlled using a powder mill, similar to a coffee grinder, and performed under consistent conditions. The pigment was then compacted for 5 minutes at a predetermined pressure. The range of applied press forces,  $F$ , the press area,  $A$ , and the resulting pressures are listed in Table 4.

<sup>18</sup> The pressing of pigments into tablets showed also, beyond the topic of this work, potential for AFM (atomic force microscope) sample preparation and for the evaluation of pigment hydrophobising quality.

<sup>19</sup> Cymax AG, Studbachstrasse 12, CH-8340 Hinwil, [www.cymax.ch](http://www.cymax.ch)



An important factor was the appropriate pre-conditioning of the powder. Non-conditioned powder (room temperature and background humidity) showed a high proportion of fracturing during removal of the tablets. After experimenting, it was found that equilibrating the pigment in an atmosphere of 100 % relative humidity at 23°C prior to tablet formation greatly increased the integrity of the formed tablets. It was assumed that, for a successful necking process between the particles, surface adsorbed water is advantageous.

Briscoe and Rough (Briscoe and Rough, 1998) reported non-uniform packing densities in highly compacted powders induced by wall friction effects. For the study reported here, however, this effect was considered to be negligible because of the relatively lower pressure ranges adopted and the broader particle size distributions of coating pigments resulting fortuitously in a certain micro-heterogeneity of the tablet. This micro-heterogeneity in turn accommodates for likely stress release within the tablet leading to a macro-homogeneity. The homogeneity was clearly monitorable by the consistency of droplet shape on the tablet surface after the surface was carefully formed by grinding the block such that the inner structure was revealed.

Cross-sectional area, $A = 17.35 \text{ cm}^2 (\pm 0.16)$	
Applied force $F$ / kN ( $\pm 5$ )	Effective pressure $P$ / MPa ( $\pm 2.7$ )
100	57.6
200	115.3
300	172.9
400	230.6
450	259.4

Table 4 Conversion table of applied forces to resulting pressures.

An electron micrograph of the surface of one of the tablets is shown in Fig. 45.

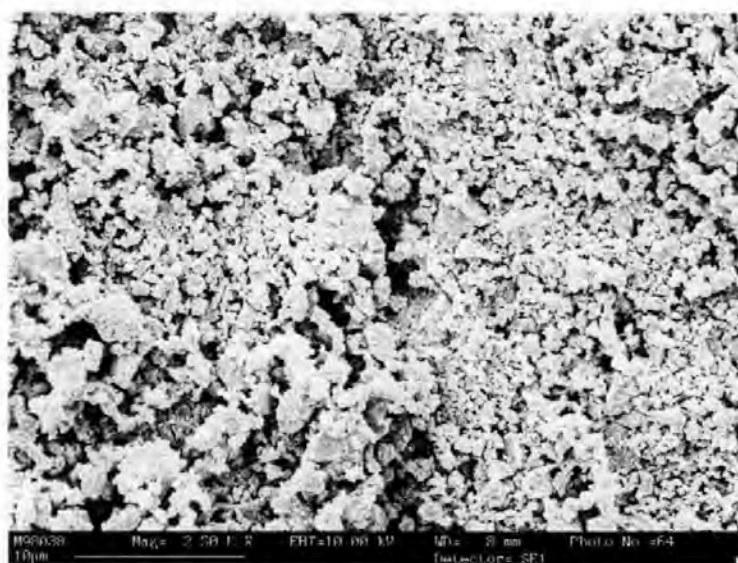


Fig. 45 SEM image of tablet surface.

#### 4.4 Sample preparation for imbibition experiments

The round tablets obtained by the previously described method have a diameter of 47 mm and a thickness of  $\approx 18$  mm. Part of each sample (typically  $125 \text{ mm}^3$ ) was studied by mercury porosimetry to determine its percolation characteristics as described in the next section.

The rest of the compact could then be shaped for the specific permeation experiment as described in each relevant chapter. Generally, the tablets were most easily cut by the use of a rectangular blade and gentle tapping with a hammer. The pieces obtained may be surface ground (dry) to the desired dimensions on an automated grinding machine (Jean Wirtz, Phoenix 4000<sup>20</sup>, Fig. 46) typically using 4 different grinding papers: 60, 150, 320, 1200 grit. Generally a grinding speed of  $100\text{-}250 \text{ min}^{-1}$  is used and an aspirator is employed in situ for dust removal. Alternatively, samples, such as a single calcite crystal, can be ground on a wet stage where tap water is continuously running over the grinding disc. Alternatively, a special solution containing dispersing agent may be used which has to be dosed by hand from time to time.



*Fig. 46 Automated grinding machine (Jean Wirtz, Phoenix 4000). On the disc at the back are the custom-made grinding jigs. Front left: sample embedded in resin for permeability measurement, middle: half of a pigment tablet, right: sample ground to finished dimensions ready for the imbibition experiment.*

<sup>20</sup> Jean Wirtz is a subsidiary company of of Buehler Ltd., 41 Waukegan Road, Lake Bluff, IL 60044, USA

## 4.5 Characterisation of the formed structures

The structures have been characterised with mercury intrusion porosimetry. The method was described in section 3.4 where also the repeatability was quantified. The relation between compaction pressure and achieved porosity is shown in Fig. 47. The observed scattering of the data is probably due to differences in powder filling "looseness" linked to the unadjustable initial velocity of the closing press. The macro-homogeneity of the samples is satisfactory as described in the previous section. It was therefore necessary to measure the mercury porosity of each tablet formed as there is not a direct relationship between applied pressure and porosity. Each structure is given an individual number (except the early equilibrium supersource series in chapter 7) which is referred in the text for clear attribution to a structure porosity

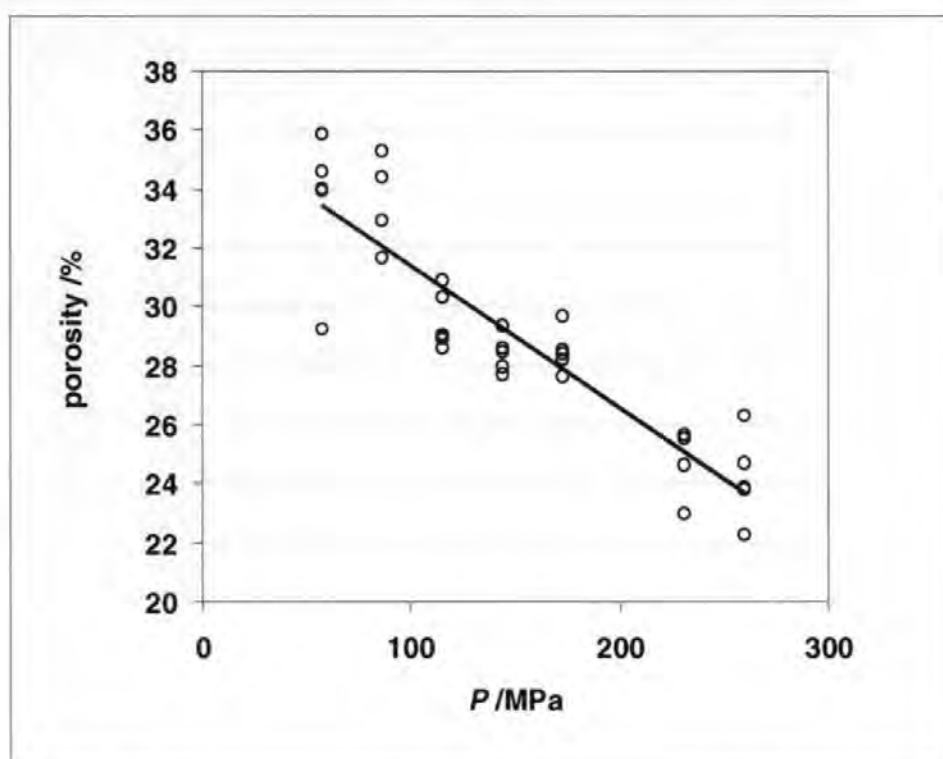


Fig. 47 Achieved porosities as a function of applied compaction pressure for the coarse CaCO<sub>3</sub>.

In the Appendix A, Table A1 summarises all the structures and the properties determined by mercury porosimetry and the parameters modelled by the porous network simulator as described in sections 2.4.1 and 2.6.1 and discussed here in chapter 4.

## 4.6 Approaches to visualise pore geometry

As outlined in section 2.4.1.1, interparticle voids generally have a complicated geometrical shape even if the geometry of the skeletal particles is relatively simply defined. Accompanying the main work of sample

preparation it was desirable to obtain qualitative information about the real voidage network within the compressed tablet samples.

The ideas considered to reproduce practically the void network included:

- To intrude under pressure Wood's metal at elevated temperatures, allowing it to solidify under a maintained pressure to obtain a metal-filled structure. This would be excellent for Scanning Electron-microscopy. The draw-back was that a pressure vessel, such as a porosimeter would have to be constructed or completely modified and this was considered impractical.
- To create macroscopic structures with soluble particles in the range of centimetres, cast the voidage in wax and solve or etch the particles away leaving the former void network as a wax structure. This negative mould could be used to cast a positive structure of the particles in transparent resin. This resin model could be used in gravity-free liquid displacement observations. Again this was considered to be out of the scope of the work as it would have involved the general problem of scaling the observations to micro dimensions. There is also the lack of correlation between large particle morphologies and those of the  $\text{CaCO}_3$  pigment particles.
- To let a curable resin imbibe, or pressure intrude, into the actual structure, or similar analogue structure, under investigation.

Following the third idea, an epoxy resin was poured into a shallow dish and the samples were placed into it (as described in section 7.3). The liquid resin was imbibed at least several millimetres into the structure before the progressive curing raised the viscosity such that absorption was slowed down and came to a stand-still. The permeated regime was ground flat and polished using the technique described in 4.4

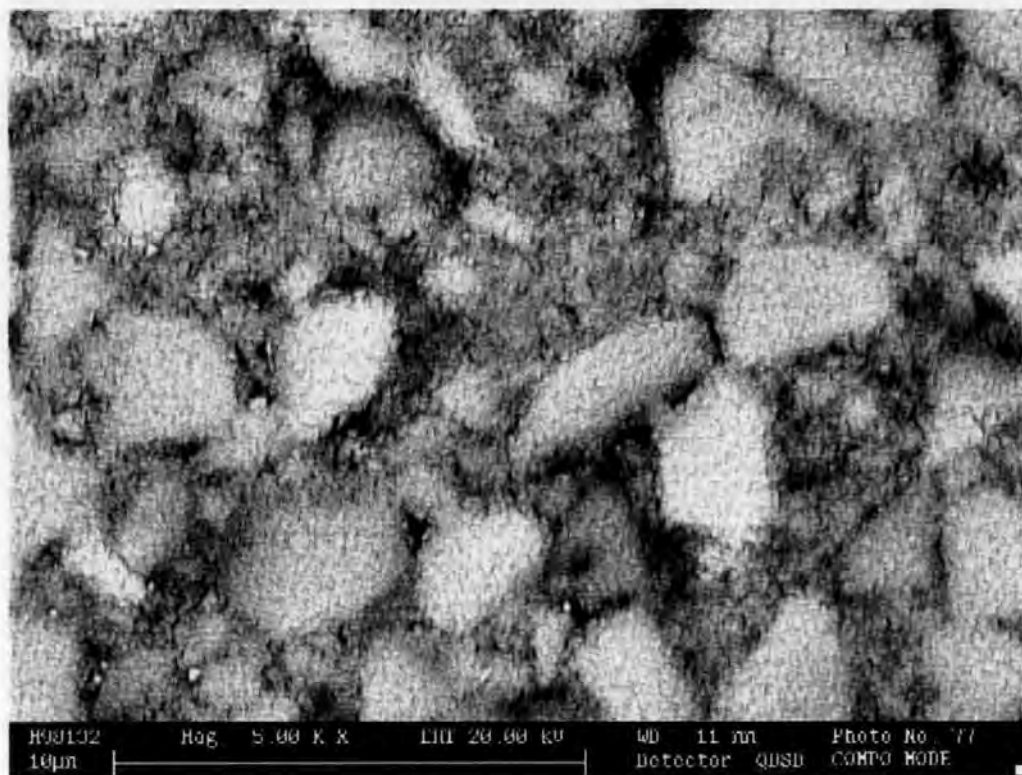


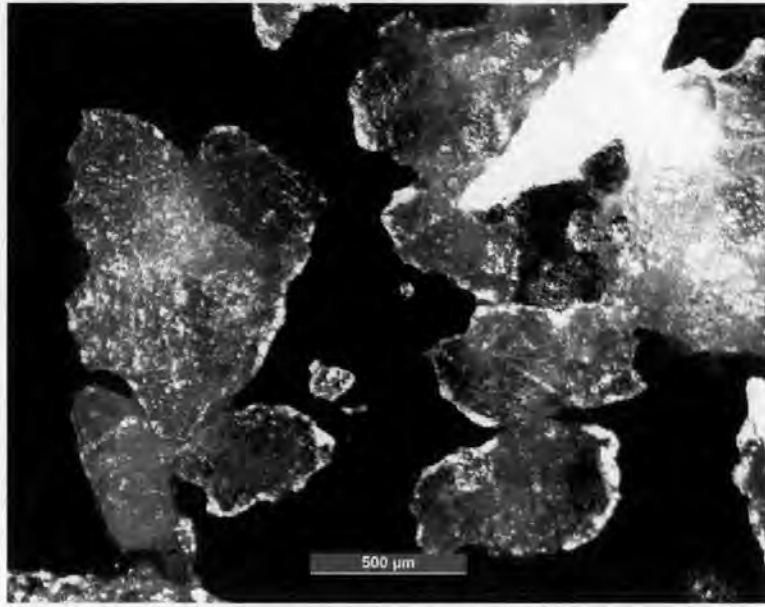
Fig. 48 *Back-scattered electron image of embedded pigment structure.*

Fig. 48 shows the type of image obtained after epoxy imbibition which reveal a general problem. Due to the small size of the individual particles, in the order of  $1\mu\text{m}$  and smaller, the back-scattered electron (BSE) mode of the electron microscope does not provide a satisfying resolution. The scanning electron microscopy (SEM) mode gives a much better resolved picture but does not distinguish between the materials, i.e. it cannot differentiate between the epoxy resin-filled voids and the  $\text{CaCO}_3$  particles. Changes in thickness of the gold plating did not substantially improve the quality of resolution.

Based on these results, the decision to step to structures of coarser particles of similar shape was made. A coarse  $\text{CaCO}_3$  (Inducarb V) was used having a particle size distribution of 96 %w/w < 2 mm, 5 %w/w < 1.25 mm. The granulate is not compactable into an integral tablet, therefore an inorganic "glue" was used, namely a solution of sodium silicate  $\text{Na}_2\text{Si}_3\text{O}_7$  of 41 %w/w (Fluka). The particles were tipped into a plastic beaker, enough of the solution of sodium silicate was added to saturate the particles. Then the beaker was put upside down on some layers of absorbing tissue to drain the solution out. After some hours the beaker was carefully removed and the structures were allowed to cure for 48 hours.

The structures obtained, Fig. 49, shift towards the macroscopic regime compared with the regular structures of Hydrocarb 90 OG, but basically they maintain their void shape and nature. To achieve a better optical contrast between the particles and the resin-filled voids, the resin was filled with carbon black (ca. 20 % by volume).

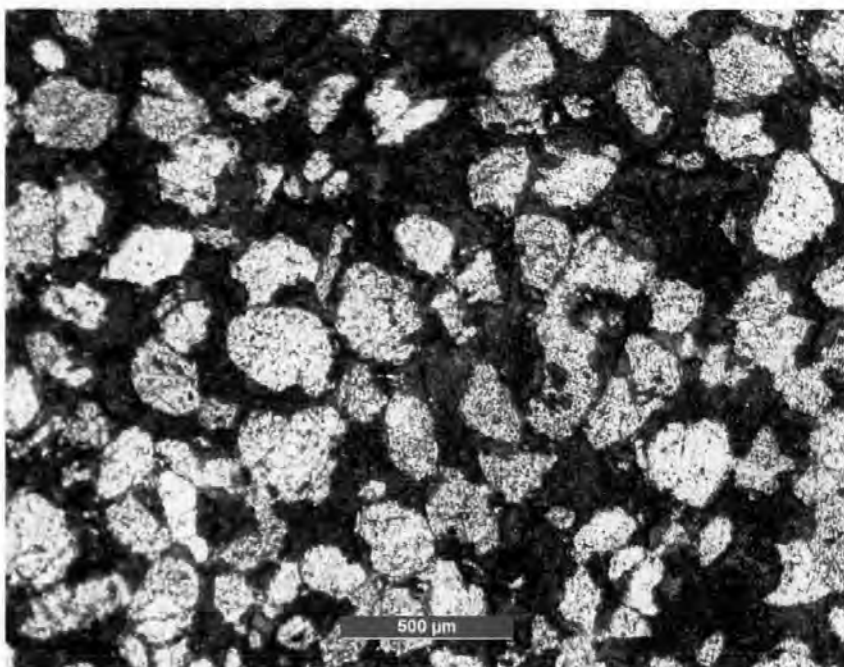
In parallel, structures were formed using the same technique based on a fine quartz sand (sea-sand, Fluka), Fig. 50, resulting in a kind of artificial sandstone.



*Fig. 49 Particulate porous tablet formed with Inducarb V, a coarse calcite filler for plaster. Black resin is imbibed into voids showing the pore shapes in cross-section after grinding and polishing.*

The pore shapes in Fig. 49 and Fig. 50 show complex forms with divergent/convergent sections as was schematically modelled by Toivakka and Nyfors (Toivakka and Nyfors, 2001) for random packing of simple spheres. This observation triggered the challenge to extend the computer network simulator's throat shapes to divergent/convergent profiles.

An approximate two-dimensional connectivity of  $> 4$  is also recognisable in the images.



*Fig. 50 Particulate porous tablet formed with sea-sand. Black resin imbibed into the voids shows the pore shapes in cross-section.*

## 4.7 Observation of macroscopic inter- particular imbibition

A layer of quartz particles (seasand, Fluka) with an average diameter of  $250\ \mu\text{m}$  was deposited on a microscopic slide. A large drop of dyed linseed oil (Fat red bluish, Fluka) was placed at an external boundary of the particle layer. The dynamic imbibition behaviour was observed under a microscope. During the early stages of observation the process was so fast that, in spite of the elevated viscosity of the oil, it was very difficult to follow the wetting front moving across the  $xy$  table of the microscope.

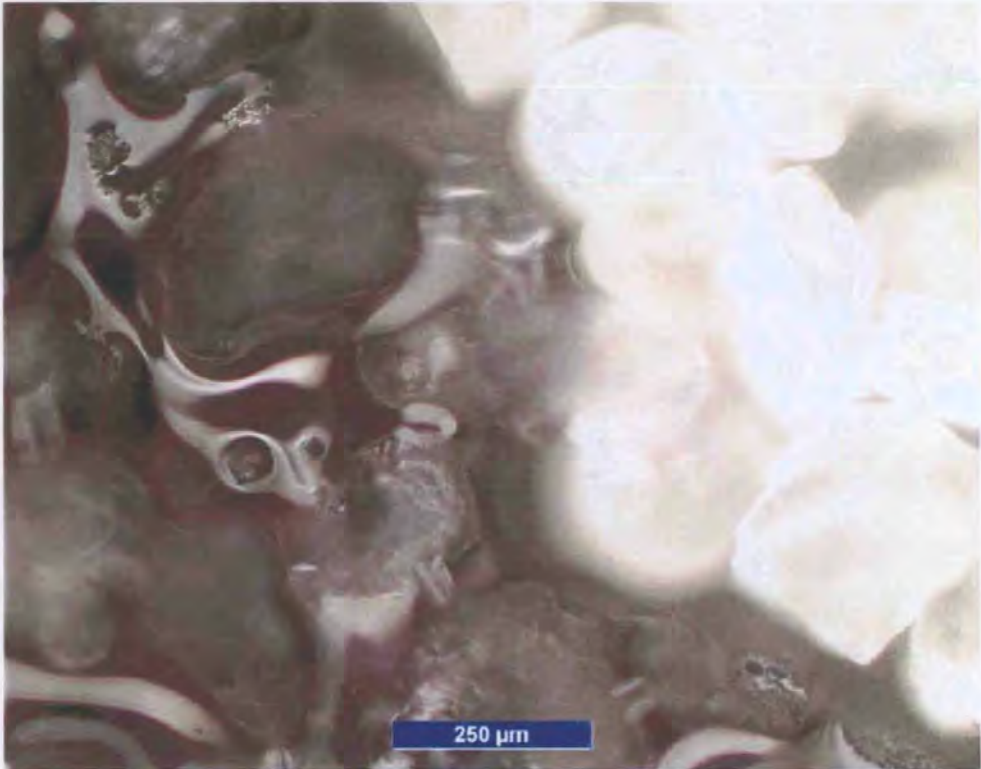


Fig. 51 Dyed linseed oil wetting front imbibing into a coarse quartz particle layer.

The image, Fig. 51, was taken in a final stage with little residual motion, mainly by Laplace pressure-driven redistribution. Nevertheless, the fact that the liquid front does not move with a uniform velocity was clearly visible. Haines-jump motions of the menisci could be observed. It also appeared that in the first stage of imbibition particles are surface-wetted by a liquid film and the meniscus jump followed subsequently. The experiment was repeated with a coarse  $\text{CaCO}_3$  powder on a glass slide giving the same behaviour. These observations are in agreement with studies of Lu *et al.* (Lu *et al.*, 1994), (Lu *et al.*, 1995) who worked with spherical glass beads. Also Knackstedt *et al.* (Knackstedt *et al.*, 2000) have observed this behaviour in etched micro-models.

What is obvious is that the jump-wise motion results in strong acceleration of that section of the liquid front involved in the jump. This means that there are inertial effects. An important condition for the jump to occur is, that enough free liquid is present to be accelerated. Big inter-particle voids seem to act as reservoirs for these

acceleration events. The observations made regarding imbibition into particle layers confirm earlier work describing a jumpwise motion of the liquid front (Nielsen *et al.*, 1986), (Lu *et al.*, 1994), (Lu *et al.*, 1995), (Bernadiner, 1998). The jumps represent strong acceleration of the liquid involved. Therefore inertia has an influence, as the mass of liquid is accelerated (and decelerated). This inertia has to be considered when modelling the corresponding imbibition dynamic. The application of an equation of imbibition containing an inertial term in a network simulator suggests a preferred pathway flow or effective micro-fingering (section 9.7) This is confirmed by dye imbibition which shows that the liquid front does not form a sharp line, but rather a "fuzzy" regime (section 7.6).



## 5 Advances in modelling imbibition

In this chapter initially a different way is examined to describe the macroscopically observed imbibition. A definition is looked for independently of any preconceived absorption theory, related only to volume uptake rates, section 5.1

Throughout the practical work based on observation, comparison with modelled data was continuously carried out concurrently with the experimental work. Therefore, the evaluation of an equation for imbibition is discussed in section 5.2. The main idea is to compare the LW equation with an equation that contains the inertial term. In section 2.6.1 the porous network simulator Pore-Cor was described and the implementation of a dynamic imbibition algorithm will be explained in section 5.3.1.

### 5.1 Analysis of volume absorption rates

Driven by the discussions above an attempt is made at defining an equivalent hydraulic radius,  $r_{ehcV}$  (Eq. 39), for an equivalent hydraulic capillary which provides an equivalent capillary radius that would contain the volume of fluid uptake as measured experimentally with an absorption length of  $x(t)$ , independently of any preconceived absorption theory. It is also possible to define an *ehc* based on apparent Darcy imbibition distance, or observed liquid front position into the structures as a function of time. We use  $r_{ehcV}$  for the volume based term while the Darcy-length based definition is termed  $r_{ehc}$  referring to the EHR model in earlier publications of the author and co-workers (Schoelkopf *et al.*, 2000), (Schoelkopf *et al.*, 2001). There a difference of a factor greater than 4 was found between the measured  $r_{50}$  ( $= d_{50}/2$ ) and the derived  $r_{ehc}$  for similar compressed tablets to those used in this section. The two *ehc* definitions are not in themselves totally compatible if for any reason the complete porosity of the sample is not being filled at a given time,  $t$ , behind the wetting front.

To understand the subtle differences a network makes when comparing the Darcy-length based definition  $r_{ehc}$  and that defined by volume,  $r_{ehcV}$ , let the porous structure that is actually filling be described first as a simple bundle of capillaries. This is only for convenience to visualise the relation between structure capillaries and the *ehcV*, and assumes nothing of the mechanism of a network structure. The real distance of the wetting front,  $x$ , absorbing into this bundle of capillaries is a function of surface energy comparison between the fluid and the skeletal surface; defined by  $\chi_{LV}\cos\theta$ , Eq. 7, where  $\chi_{LV}$  is the fluid surface tension between the meniscus and the

vapour phase (air) and  $\theta$  describes the contact angle between the advancing meniscus and the solid phase.

Defining  $\eta$  as the fluid viscosity and  $r_c$  as the individual capillary radius in the bundle, and  $t$  is the time, then

$$x = f(\gamma_{LV} \cos \theta, \eta, r_c, t) \quad \text{Eq. 38}$$

is an expression for the distance travelled in that capillary at time,  $t$ .

The volume,  $V(t)$ , of fluid absorbed per unit cross-sectional area,  $A$ , of the sample at a given time,  $t$ , is therefore equated between the capillary bundle and the  $ehcV$ ,

$$V(t) / A = \sum_{i=1}^N x_i(t) \pi r_{ci}^2 = x(t) \pi r_{hcV}^2 \quad \text{Eq. 39}$$

where  $N$  is the number of capillaries per unit area accessing the surface of the sample. This definition is purely intrinsic to the model. By contrast the Darcy length,  $x_{\text{Darcy}}$ , may be defined as

$$x_{\text{Darcy}} = \frac{V(t)}{A\phi} \quad \text{Eq. 40}$$

(see also Eq. 71), where  $\phi$  is the porosity of the sample.

To illustrate the difference between  $r_{hcV}$  and  $r_{hc}$ , now suppose all the capillaries have the same radius, then the actual wetting front distance  $x$  in the bundle will be the same as in just one capillary. The value of  $x_{\text{Darcy}}$ , however, is dependent on the sum of the volumes having entered into each capillary, i.e. the number of capillaries and the porosity these represent. Clearly, the porosity of a single capillary per unit area is far less than that of a bundle of  $N$  capillaries per unit area, hence the correction using the measured porosity takes care of this in a case where all the porous structure is simultaneously being filled behind the wetting front. When we have a distribution of capillary radii, the Darcy length now represents the distance of the wetting front in a capillary based on the geometric mean of the capillary radii.

Consider a complicated system of tortuous paths intertwined, but not interconnected, still giving the same measured porosity. Now again, Darcy length will not relate to the observed wetting front, i.e. how far the liquid has imbibed into a complex sample, but  $x_{\text{Darcy}}/x_{\text{observed}}$  represents a tortuosity. Therefore, the concept of Darcy length should not be confused with the progress observed in imbibition into real network structures, as it represents the length that would be present if the sample were modelled by a bundled distribution of straight

capillaries given by the function of the geometric mean of their radii. If we were to derive an *ehc* based on Darcy length, as defined by LW, it would follow

$$r_{ehc} = \left( \frac{V(t)}{A\phi} \right)^2 \frac{2\eta}{\gamma_{LV} \cos \theta t} = \left( \frac{d(V(t)/A)}{\phi d\sqrt{t}} \right)^2 \frac{2\eta}{\gamma_{LV} \cos \theta}$$

Eq. 41

The most important drawback using an  $r_{ehc}$ , (which includes an assumed porosity term), is, therefore, that it presupposes the complete filling of the available structure from the supersource up to the liquid front.

We now, therefore, return to defining an *ehcV* based on experimental volume uptake. The measurement from experiment is that of liquid mass uptake as a function of time into the porous compressed pigment tablets of defined porosities. The pigment/fluid interactional properties represented by a constant  $\gamma_{LV} \cos \theta$ , are the same in all experiments. The experimental parameters are therefore:

$$m(t) = V(t)\rho$$

Eq. 42

where  $m(t)$  is the mass uptake at time  $t$ , as defined by a volume  $V(t)$  of fluid of density  $\rho$ . We normalise to the cross-sectional area of the sample,  $A$ , such that the data become  $V(t)/A$ , the volume absorbed per unit cross-sectional area of the sample.

It is shown experimentally that the rate of volume uptake, as we see later (see Fig. 105), does indeed approximate to a  $\sqrt{t}$  relationship. Therefore, as the interest is primarily in rates of uptake, we can express each curve as a linear relationship between  $V(t)/A$  and  $\sqrt{t}$ , the gradient of which we can write as

$$\frac{d(V(t)/A)}{d\sqrt{t}} = \frac{d((m(t)/A)/\rho)}{d\sqrt{t}}$$

Eq. 43

and which can be obtained directly from the plotted data by a linear regression analysis.

This approach will be applied and tested with an additional set of experiments in section 9.4.3.

## 5.2 Looking for an imbibition equation (Schoelkopf, Gane, et al. 2000)

### 5.2.1 Simplistic assumptions in the approach

To allow for the computation to be tractable, it is necessary to begin with some assumptions that, although simplistic, nevertheless are realistic enough to move the discussion forward.

The main assumption for all the modelling work is that imbibition is driven by capillarity whereas diffusive processes are neglected. Furthermore, the capillaries are represented by tubes with a circular cross-section.

The basic equation of imbibition can be written in the form of

$$\Sigma \text{dissipating forces}(t) = \Sigma \text{driving forces}(t) \quad \text{Eq. 44}$$

The influence of the displaced fluid, in these cases the vapour in the porous network, the possibility of adsorbed liquid films in terms of film flow phenomena and the potentially increased meniscus curvature are all neglected.

The model used here details the mechanisms of inertial flow in addition to, and compared with viscous dissipated flow, resulting in a time dependent size selectivity of the pores. This leads in turn to preferred pathway flows.

### 5.2.2 Liquid inertia as a factor in flow mechanisms

The mechanism of inertial delay of imbibition is discussed, in which the mass of liquid resists the acceleration due to capillary forces. This is especially dominant at short times and in large diameter capillaries. The network of a coating also consists of entry features throughout the structure forming a continuity of connectivity between the pore entities. Inertia must be considered at each of these entry features where accelerations are high. This is not to be confused with the so-called wetting delay as observed in paper science, caused by surface molecular interactions such as arise from sizing of uncoated papers, where a low surface free energy barrier on the solid phase has to be gradually overcome by hydrative swelling.

### 5.2.3 Comparing the Bosanquet and LW equations for a simple bundle of capillaries

Taking Eq. 31, where for  $at \ll 1$ , i.e. short timescales, using a Taylor series expansion, it can be derived that

$$e^{-at} = 1 - at + \frac{a^2 t^2}{2} (at \ll 1) \quad \text{Eq. 45}$$

From Eq. 31 it then follows that

$$x_2^2 - x_1^2 = b t^2 \quad (at \ll 1) \quad \text{Eq. 46}$$

If the measurement co-ordinates are set such that  $x_1$  is zero and there is no applied external pressure  $P_e$ , then

$$x^2 = \frac{2\gamma \cos \theta t^2}{r \rho} \quad (at \ll 1, P_e = 0) \quad \text{Eq. 47}$$

This equation describes what is here referred to as 'inertial flow'. The distance travelled,  $x$ , is directly proportional to time  $t$ , in contrast to the Laplace-Poiseuille flow regime described by the LW equation, Eq. 27, for which  $x \propto \sqrt{t}$ . Also, in contrast, the distance travelled by inertial flow is independent of viscosity, but inversely related to the radius of the tube  $r$  and the fluid density  $\rho$ . From Eq. 47 the velocity may be differentiated as:

$$\frac{dx}{dt} = \left( \frac{2\gamma \cos \theta}{r \rho} \right)^{0.5} \quad \text{Eq. 48}$$

as also given by Quere (Quere, 1997).

Under the conditions of inertial uptake, the regime of Eq. 47 describes a monolithic block of fluid entering a tube, driven by the wetting force of the liquid contacting the initial side-walls of the tube.

The meniscus front of the fluid is assumed to be flat, although in practice the shape may be wavy (Fig. 18). All parts of the fluid within the tube move at the same rate – hence the independence from viscosity. The flow is retarded more for a high density fluid entering a large tube because the mass of fluid, and hence its inertia, is higher. Also, the higher the viscosity of the fluid, the faster the effect of viscous drag becomes apparent. This effect of inertial retardation and subsequent introduction of viscous drag is shown quantitatively in Fig. 52 for propandiol (viscosity 57.1 mPas) entering capillaries of contrasting radii of 1  $\mu\text{m}$  and 1mm respectively.

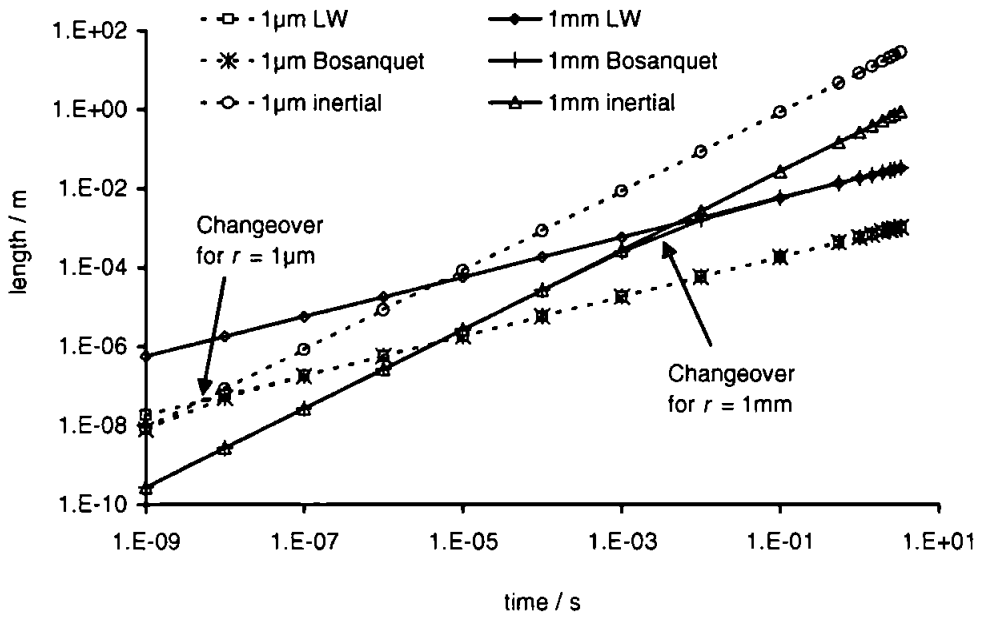


Fig. 52 Comparison of inertial and viscous equations and Bosanquet's solution for propandiol. The plot shows the length of the fluid column,  $x$ , in a capillary with a diameter as shown in legend, after time,  $t$ .

The graph shows how the proposed (Bosanquet) flow changes from inertial to LW flow as time and distance increase. For a tube of 1mm radius, the change-over begins at about 0.01 s and after 1 mm penetration, and for a tube of 1  $\mu\text{m}$  radius it starts at about 0.01  $\mu\text{s}$  and 0.1  $\mu\text{m}$  absorption distance. For even smaller tubes, the change-over will occur even faster and earlier, so that the flow will be accurately described by the LW solution in the finest of capillaries for supersource conditions once the fluid has travelled further along the capillary than its changeover radius. Also, with increasing fluid viscosity, whilst keeping fluid density and radii constant, the change-over will occur earlier. This effect shows that viscosity and radius are in a mutual relationship through frictional dissipation, whereas density and radius determine inertia.

For features of a particular radius, the curved lines in Fig. 53 show the distance filled at times ranging from 0.001  $\mu\text{s}$  to 1  $\mu\text{s}$ . The right hand side of the boundary shows behaviour in the remaining larger pores dominated by inertial retardation effects, and in this region features of a smaller radius fill faster than those with a larger radius. At the boundary the behaviour changes to viscous flow which can be described by the LW equation, and the distance filled now decreases as the radius decreases.

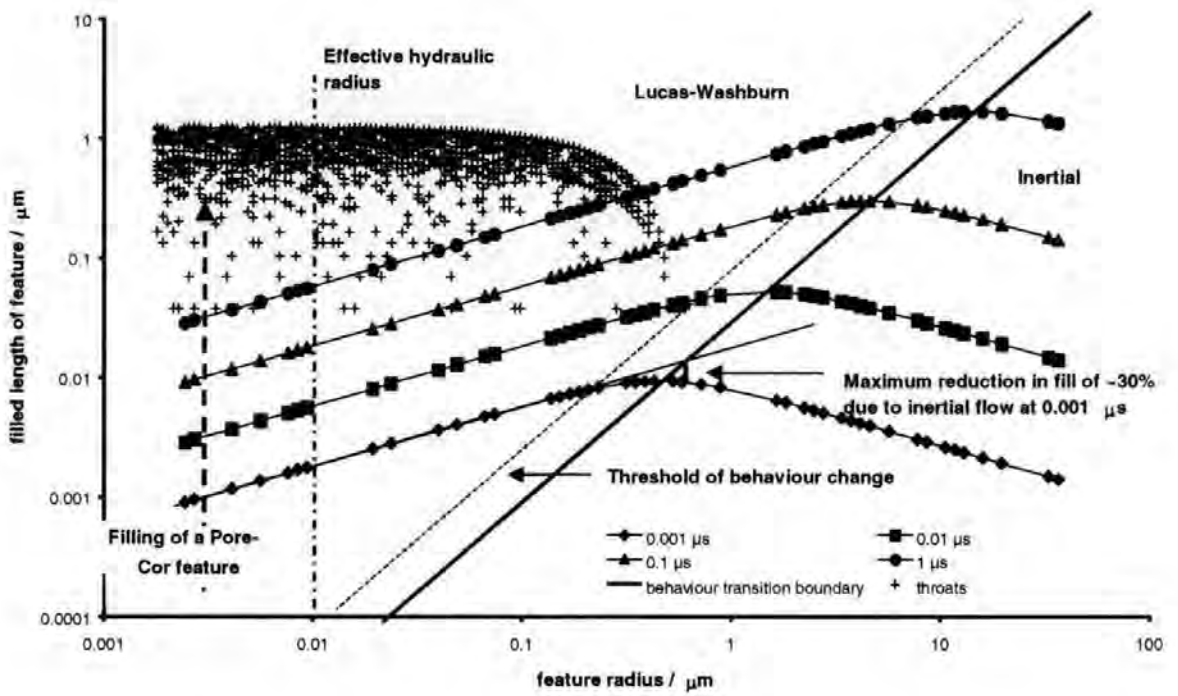


Fig. 53 Regions of behaviour of inertial and viscous dominated flow for 1,3-propanediol. The plot also shows the distribution of imbibition lengths for the array of throat diameters used in the modelling by the pore-level simulation in 9.7

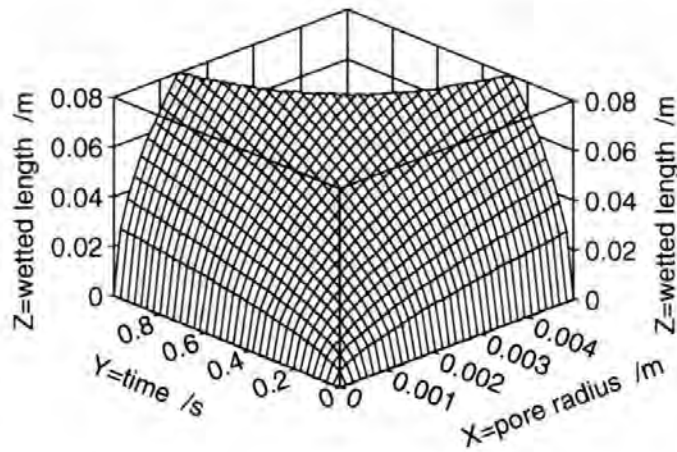


Fig. 54 Methyleneiodide absorption length into a distribution of capillary sizes as described using the LW equation.

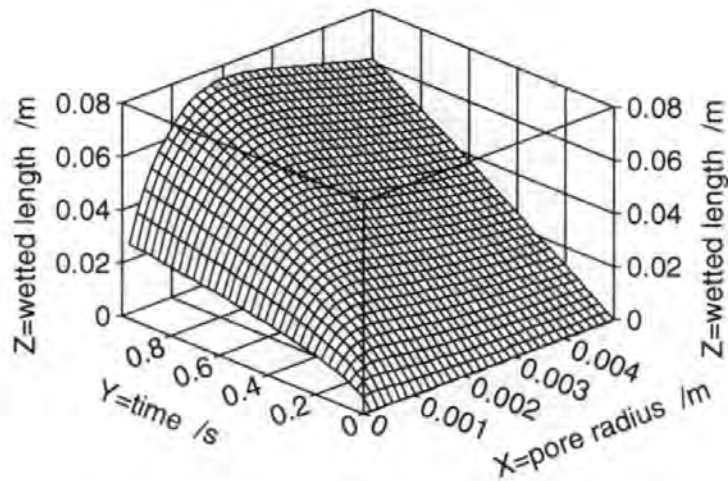


Fig. 55 *Methyleniodide absorption length into a distribution of capillary sizes as described using the Bosanquet relation.*

The comparison of Fig. 54 and Fig. 55 shows the difference in penetration depth, or filled wetting length in a capillary, predicted first by LW and secondly by Bosanquet for methyleniodide, and demonstrates the impact of a higher density liquid. Similarly, Fig. 56 and Fig. 57 depict the case comparing LW with Bosanquet for nonane as a typical representation of mineral oil. The pronounced influence of the liquid density in combination with growing pore radius promoting inertial retardation of uptake is clearly seen. The effect is even more strikingly visible when regarded as the predicted wetting front axial velocity as shown, for nonane, in Fig. 58 according to LW and in Fig. 59 according to Bosanquet.

Regarding velocity, we have to remember that neither equation strictly applies at time  $t = 0$  because the acceleration of the fluid is not accounted for but rather its momentum. This effectively results in infinite acceleration at the origin. Nevertheless, the velocities shown at  $t > 0$  are indicative.



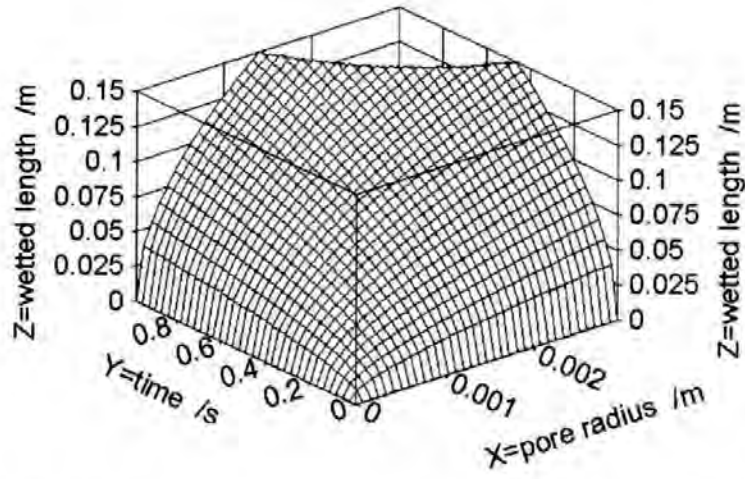


Fig. 56 Nonane absorption length into a distribution of capillary sizes as defined by the LW equation.

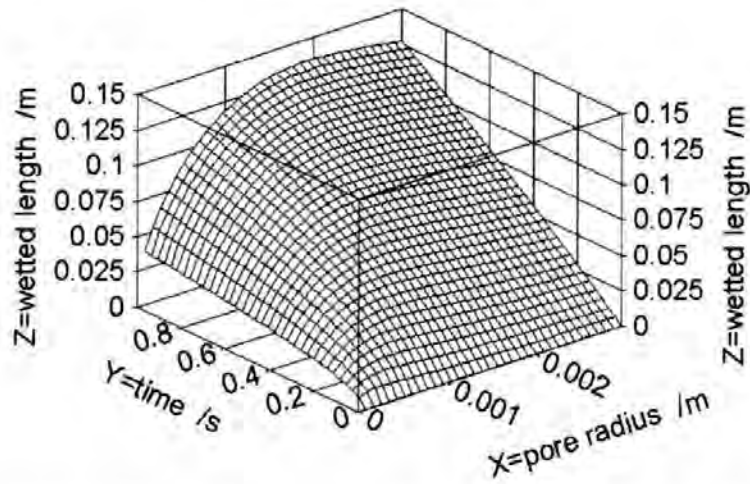


Fig. 57 Nonane absorption length into a distribution of capillary sizes as defined by the Bosanquet equation.

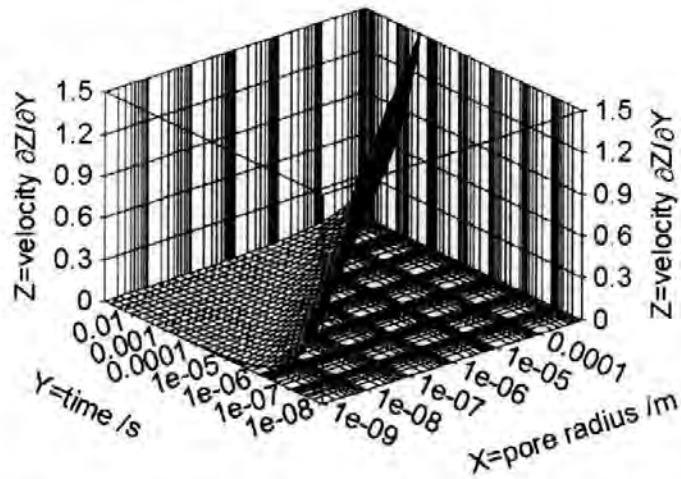


Fig. 58 Nonane wetting front velocity entering an array of capillary sizes depicted by the LW relation.

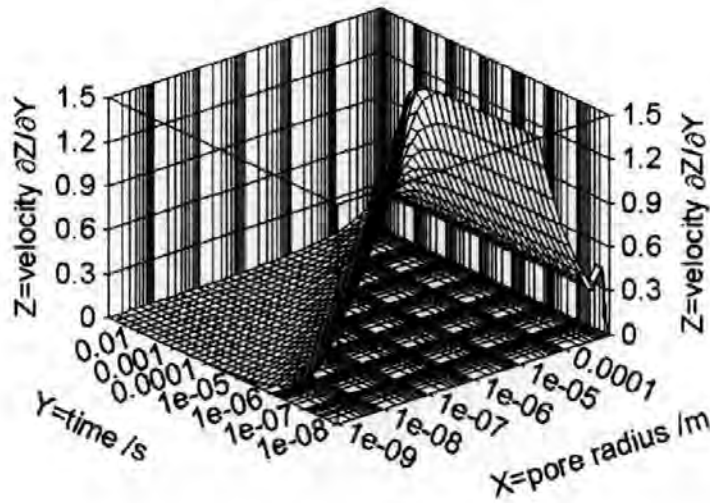


Fig. 59 Nonane wetting front velocity entering an array of capillary sizes calculated from the Bosanquet equation.

From the above plot (Fig. 59) it can be seen that on the left side of the maximum velocity ridge, the viscous-Poiseuille flow regime applies, while on the right side (towards larger pore radii) the inertial, linear "speed" regime dominates. Therefore, it is concluded that there exists a preferred capillary size which evolves as a function of time ranging from the finest at time  $t = 0$  up to a given preferred size after time  $t$  defined by the "Bosanquet ridge".

While these graphs demonstrate well the underlying physical effects, for practical printing situations maybe the most relevant form of these equations deals with liquid volume removal from the exposed surface. This case is depicted again for the low viscosity alkane (nonane) in Fig. 60 for LW and Fig. 61 for Bosanquet, respectively.

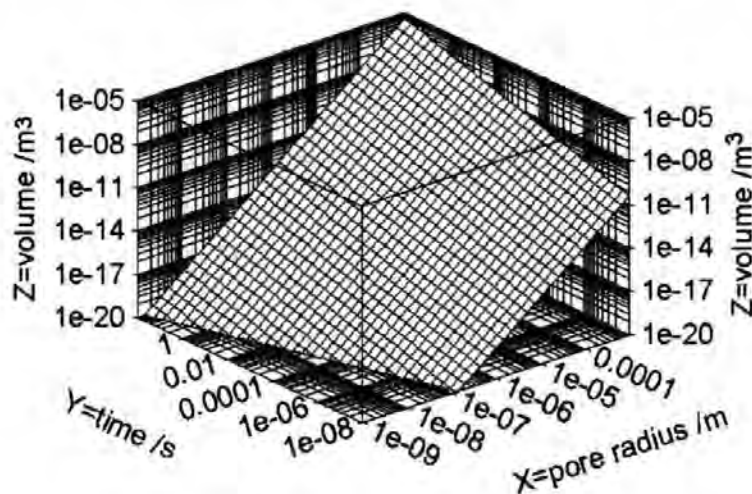


Fig. 60 Volume absorption distribution in capillaries defined under LW for nonane.

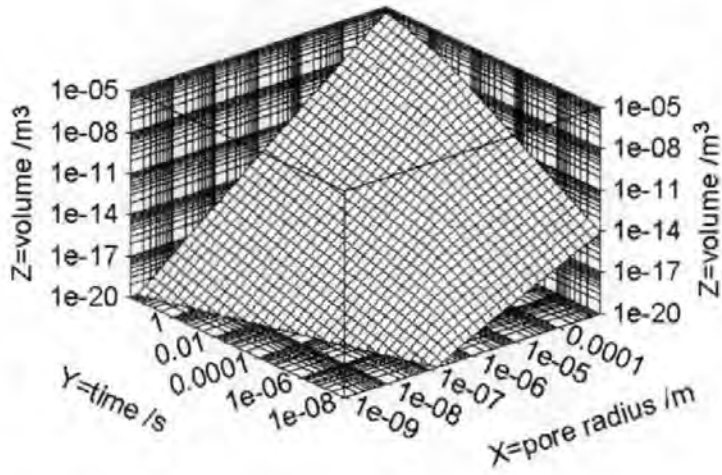


Fig. 61 Volume absorption distribution in capillaries as defined by the Bosanquet equation for nonane. Note the kink from the viscous regime on the left hand side to the retarded one on the right.

### 5.2.4 Reynolds numbers during imbibition

Following Seguin *et al.* (Seguin *et al.*, 1998b), the Reynolds number, as an indicator of the linearity of flow streamlines within a pore, can be written as :

$$Re = \frac{v_p 2r_p \rho}{\eta} \tag{Eq. 49}$$

where the condition of  $Re > 180$  indicates the breakdown of the laminar flow regime in a pore (Seguin *et al.*, 1998b). If the velocity of the liquid front in the pore  $v_p$ , following the LW equation, Eq. 27

$$v_p = \frac{dx}{dt} = \frac{r\gamma \cos \theta}{4\eta x} \tag{Eq. 50}$$

is inserted into Eq. 49 then the following expression is obtained

$$Re = \frac{r^2 \cos \theta \gamma \rho}{2\eta^2 x} \tag{Eq. 51}$$

as a measure of Reynolds number during viscous imbibition. It needs to be kept in mind that at  $t = 0$  there occurs the previously discussed singularity of infinite initial velocity. Eq. 51 is plotted using the parameters of the mineral oil "PKWF 6/9 af neu" (Table 11) in Fig. 62.

$$Z=Y^2*805*0.0274/(2*(0.00432^2)*X)$$

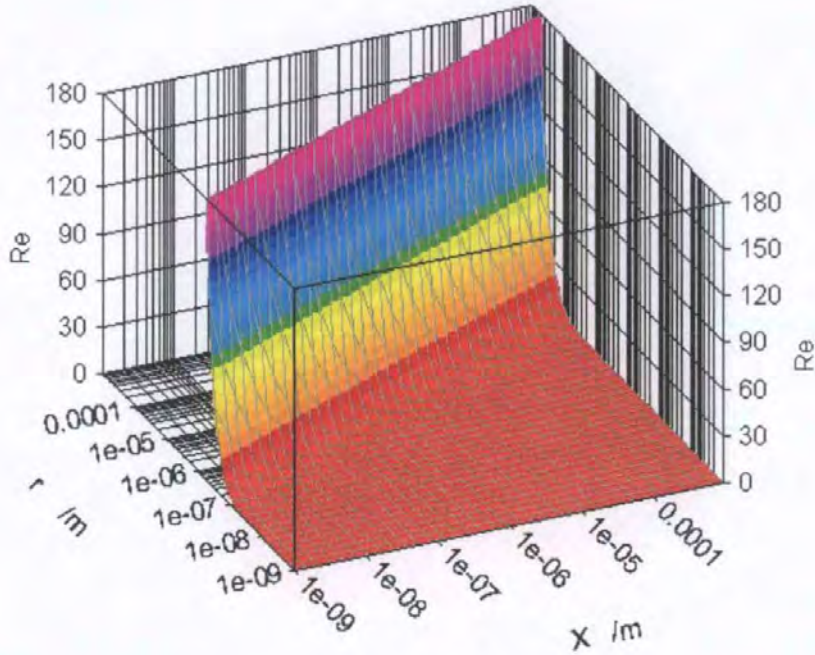


Fig. 62 The Reynolds number during viscous imbibition as function of the travelled distance by the liquid front,  $x$ , in a range of capillaries of radius parameter  $r$ .

Most of the flow occurs in the laminar regime. However, this plot, based on LW alone would suggest that there is a regime of flow at very short distances where laminar flow cannot be expected. Considering the earlier discussion it is known that flow in this domain is inertial according to the Bosanquet model and therefore constant in time with a velocity of  $(2\gamma\cos\theta/\rho r)^{0.5}$  (Eq. 48). Therefore the Reynolds number should be calculated based on the velocity of inertial flow as given in Eq. 48. Putting this value into Eq. 49 we obtain,

$$\text{Re} = \left( \frac{8\gamma \cos\theta r \rho}{\eta^2} \right)^{0.5}$$

Eq. 52

which is plotted in Fig. 63, and shows that the inertial flow regime is not complicated further by turbulent flow as also suggested by Pickett (Pickett, 1944).

$$Z = \text{SQRT}(8 * 0.0274 * Y * 855 / X^2)$$

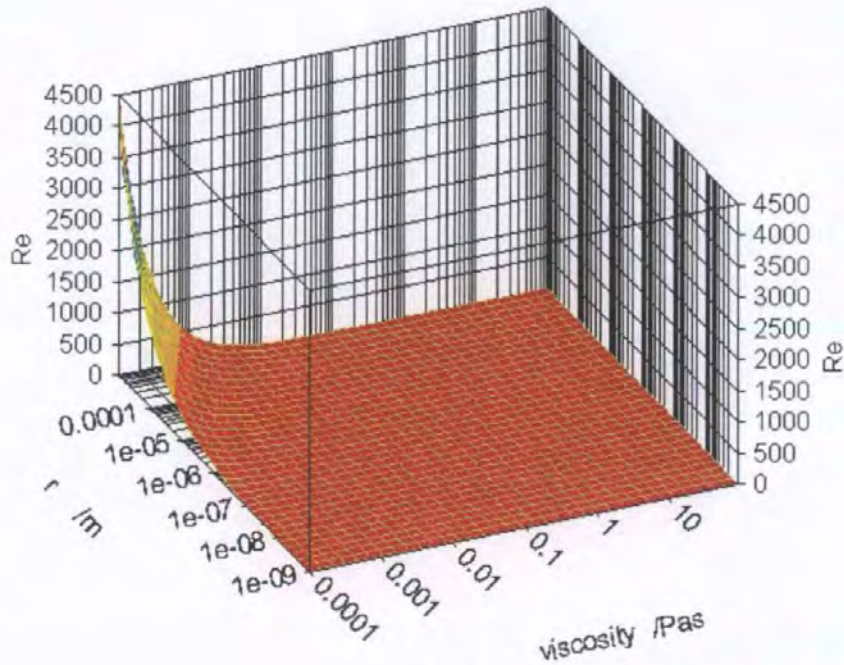


Fig. 63 Reynolds number over a range of viscosities and pore radii at an assumed liquid density of 855  $\text{kgm}^{-3}$ .

### 5.3 The next step to realism – the network model

Under these newly-defined conditions it is important to understand how the absorption behaviour of a network structure, such as a paper coating layer, could be better understood and therefore be made more controllable.

In most cases, the properties of the liquids contained in ink formulations are defined through the ongoing development of the various ink types. Absorption could be selectively controlled through using the inertial delay effect by moving to higher density liquids. In practice this effect could be realisable, for example, if halogenised solvents were used, but today these are deemed to make no sense environmentally.

The more accepted way to control what is identified here as inertia is by changing the size distribution and geometry (or chemistry) of the pore network. While the influence of spatial pore shape geometry is discussed elsewhere (Kent and Lyne, 1989), the retarding influence of inertia may be controlled by adjusting the pore diameter distribution and surface chemistry distribution of the coating which is increasingly being practised by introducing structured pigments and costructures between pigments into the formulation of the coating colour (Gane *et al.*, 1999).

### 5.3.1 The wetting algorithm

The solution to the Bosanquet equation Eq. 31 is now used by the network simulator to calculate the wetting flux in each pore and throat in the void network at every time step. It is assumed that inertial flow occurs when fluid begins to enter each throat, initially wetting the throat in the form of a monolithic block of fluid as described previously. Once a throat is full, the volumetric flow rate of the fluid leaving the throat is calculated and this fluid starts to fill the connected pore. The pore can be filled by fluid from more than one throat, which may start to flow into it at different times. Once a pore is full, it starts to fill the throats connected to it that are not already full and which are not already filling from other pores. If at any stage the outflow of a pore exceeds the inflow then a mass conservation restriction is applied which removes this imbalance and restricts the further fluid flow into the network.

To overcome the singularity at  $t = 0$ , a predictor-corrector method is used. The results of the predictor-corrector are verified for the boundary conditions  $\lim_{t \rightarrow 0} dx/dt$ , using the software package Maple as discussed in Ridgway and Gane (Ridgway and Gane, 2002).

At the start of the calculation for wetting into the unit cell, the total time length for the absorption is specified. The maximum length of a time step is 1 ns (nanosecond), its value being such that the maximum distance advanced by the fluid in one time step is never more than  $0.1 Q$ . There is also a further restriction on the length of the time step in order to prevent an oscillatory flow behaviour in the throats with the smaller radii as explained by Ridgway and Gane (Ridgway and Gane, 2002). This occurs if  $r^2\rho/4\eta$  is less than 1 ns, where  $r$  is the minimum throat radius in the structure. In this case the time step is set to  $r^2\rho/4\eta$ . The flow rate varies greatly with throat diameter, with the consequence that many millions of timesteps must be calculated. The absorption is quantified as the fraction of the total void volume in the unit cell which is filled with the fluid at time  $t$ .

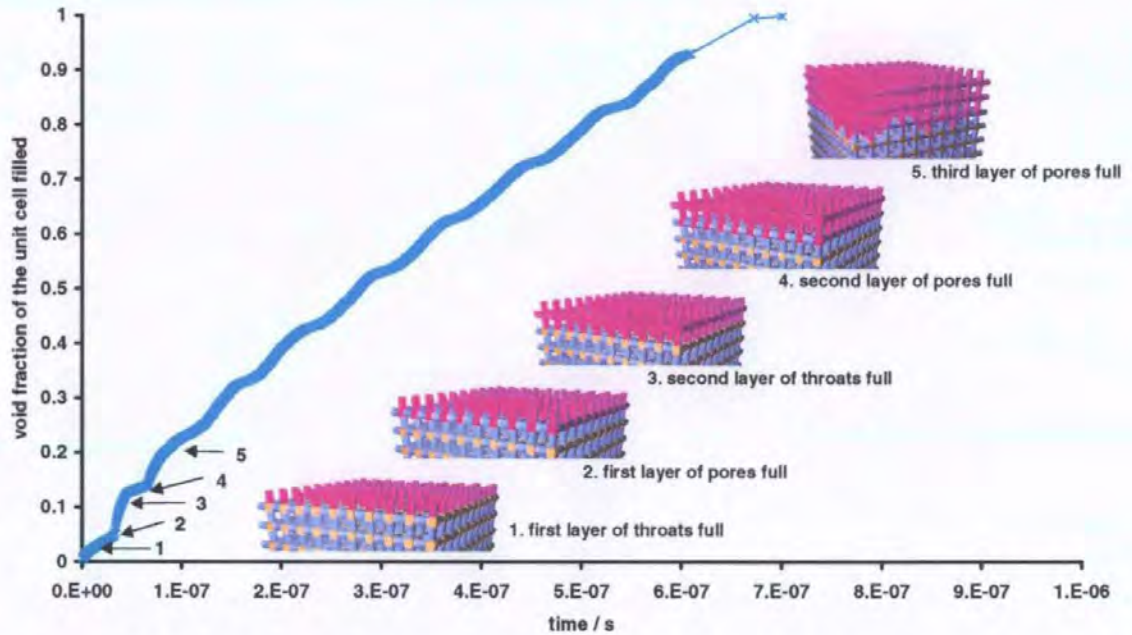


Fig. 64 *Artefact of artificially regular unit cell structure and the iterative way of stepping through the algorithm computing the flow rate through the unit cell in respect to the repeat boundary condition of its nearest neighbours. Fluid, shown purple, imbibes from the top surface of the unit cell.*

In the case of a mono sized distribution the simulated intrusion curve is not smooth, but has regular bumps. These bumps are an artefact of this particular artificially regular structure within the unit cell and the stepwise way in which the algorithm calculates the flow rate through the unit cell in respect to the repeat boundary condition of its nearest neighbours. This artefact is shown using a unit cell with a size distribution of  $0.099 - 0.101 \mu\text{m}$ , a connectivity of 6, a throat skew of 1 and a porosity of 30 %. The simulated imbibition curve for this structure is shown in Fig. 64. There is a smooth transition between the filling of the first layer of throats, position 1, and the first layer of pores, as the pores are designated to fill at the final flow rate exiting from the top layer of throats. The first bump occurs at  $3.2 \times 10^{-8}$  s, shown as position 2. At this point, both the first layer of throats and the first layer of pores are full. Once a layer of pores is full, the subroutine sequentially steps through each pore and starts to fill any empty throats adjoining it. For this reason there is an artificial sideways 'sweep' across the unit cell as it fills. As all these throats fill there is a significant increase in the fractional void volume filled over a short period of time, position 3. These steps in the curve occur each time the next layer of pores are full and the adjoining throats, both lateral and in the next layer, start to fill, positions 4 and 5.

Although the step-wise filling jump seen after every throat-pore layer pair is an artefact of the system, and only applies to the particularly regular arrays used here, it actually could be used to resemble the time delay associated with such other phenomena as Gibbs hinging described by Senden *et al.* (Senden *et al.*, 2000), in which it was shown by physical micro-modelling that as an imbibing fluid reaches a discontinuous boundary,

such as would be found in an artificial regular array of connecting rectangular tubes, there is a delay which occurs over an as yet mathematically undefinable time during which the meniscus front hinges about the discontinuity before proceeding rapidly once a wetting configuration is re-established. Because the mathematics of the phenomenon is so intractable, the sequential boundary condition and 'sweep' sequencing intrinsic to the computer network simulator wetting algorithm is in fact suited to modelling this effect.

Matching the pore size and throat size distribution parameters of the simulation to the percolation data obtained from mercury porosimetry provides for a small transition during absorption, as will be seen later in the application to real systems.

### **5.3.2 Limitation of imbibition model compared to reality**

It is worthwhile here to summarise the limitations of the model. Although the background has been discussed in detail, it is needed to understand the gap between the model and the realm of natural imbibition.

Work concerning the visualisation of the geometrical void structure demonstrates that the throats in packed pigment coating structures are mainly slits or crevices between the closest boundaries of adjacent particles and pores are formed between the largest distances of adjacent particle centres. The work of Toivakka and Nyfors (Toivakka and Nyfors, 2000) as reviewed in section 2.4.1.1 rendered the voids for the case of spherical particles. Structures formed of crystallite particles like calcite with a rhombohedral shape are shown in section 4.5. Triangular shapes in pore cross-section are common in any of the lateral directions. There is both theoretical and experimental evidence regarding the liquid behaviour in angular pores and their corners. It is obvious that in a void space with polygonal spatial geometry the actual viscous flow is more complicated than a simple Poiseuille approximation.

Micro-models have given some insight into the micro-mechanisms of liquid films and their transition to meniscus-driven flow. The influence of pre-viscous inertial flow in relation to pore dimension and liquid parameters and the resulting selectivity mechanism was discussed and has been involved in the previous section. Furthermore, it is known from observation under a microscope that the liquid front advances not in a steady motion at the pore scale level but jumpwise, a phenomenon known as the Haines jump. The roughness and microroughness contribute to the discontinuity of flow. Local temporary pinning of the wetting line may occur in some cases caused by local geometrical and/or surface chemical features leading to a slip/stick motion or



avalanche type movement. Putting these findings together it is postulated that imbibition into an interparticulate void structure would behave generally in the following way:

- Very fast absorption occurs first into narrow slits and crevices without a fully established viscous drag.
- Film flow processes act by coating exposed particles very fast with a film of subsequently growing thickness.

These two phenomena are not clearly divisible and they are accompanied (depending on the liquid) by an evaporation – recondensation/adsorption process forming a precursor film.

- When the films in the pore corners and crevices approach a state where a united meniscus can be formed, then the pore fills as a jump with an inertial and a viscous regime depending on the pore dimensions.

The potential implications, therefore, can now be summarised.

In some cases the range of mechanisms may act to prevent a pore from completely filling. The film flow sequence, as described by Bernadiner (Bernadiner, 1998), leads to air bubbles which tend to be entrapped in pores. Fast capillaries may by-pass slower ones so that the air has no way to escape. In the case of a limited liquid supply, as in many practical situations, like printing, there is simply not enough liquid around to fill the larger pores as all the liquid has been already "stolen" by small and fast capillaries. In a subsequent equilibrium liquid distribution regime all the interconnected menisci seek for mutual meniscus curvature equilibration, probably moving within the geometrical boundaries of a pore. Subsequently, much slower processes govern further liquid transport which are basically beyond the practical interest of this work, such as wicking in the microroughness of the solid surfaces and diffusion.

### **5.3.3 The permeability algorithm (Bodurtha *et al.*, 2002)**

The description of permeability with the Darcy equation, Eq. 33 and the permeability  $k$  can be linked to the fundamental Poiseuille flow.

In the Poiseuille equation, Eq. 24, the term  $r^4/l$  corresponds to the volumetric flow capacity  $\Xi$ . In using the Poiseuille equation, it should be recognised that it is only a first approximation to the resistive flow of a feature within the network.

Now it is assumed that Poiseuillian flow occurs across the whole cell:

$$\left(\frac{dV}{dt}\right)_{\text{cell}} = -\frac{\pi}{8\eta} \Omega_{\text{cell}}(\Xi_{\text{arcs}}) \Delta P_{\text{cell}} \quad \text{Eq. 53}$$

where  $\Omega_{\text{cell}}$  is an averaging operator over the whole unit cell, operating on the flow capacities of the arcs ( $\Xi_{\text{arcs}}$ ). Again, there is an approximation in doing this. The model implicitly assumes that Poiseuillian flow occurs at all points within the network. For the double-conical throats it is presently assumed that their flow capacities were the same as a cylinder with the same entry and exit sizes as the double-conical feature.

An arc represents a pore-throat-pore pathway and a node is sited at the centre of each pore algorithm (Matthews *et al.*, 1993). Each arc in the flow network is the flow channel between adjacent nodes, positioned at the centre of each pore. It generates a term which is related to the effective Poiseuillian capacity of the cell for flow in the  $-z$  direction (from the top to the bottom face), and in the  $\pm x$  and  $\pm y$  direction. Flow, however, is not allowed in the  $+z$  direction, thereby applying an implicit positive pressure gradient with respect to  $z$ . The combination of the Eq. 24 with the Darcy equation, Eq. 33, results in an expression for the absolute permeability independent of the pressure gradient imposed on the sample:

$$k = \frac{\pi}{8} \Omega_{\text{cell}}(\Xi_{\text{arcs}}) \frac{l_{\text{cell}}}{A_{\text{cell}}} \quad \text{Eq. 54}$$

A network analysis approach to this problem supplies a term  $\Omega_{\text{cell}}(\Xi_{\text{arcs}})$  as the maximal flow capacity through the network of pores and throats. It is calculated by means of the ‘Dinic’ network analysis algorithm (Bodurtha *et al.*, 2002). There is an overall conservation of flow, so that the entire volume of fluid entering the top of the unit cell emerges at the bottom, with no build-up through the network. The value obtained, as the maximal flow, is an average of the capacity values over only the channels found to carry flow.

## 5.4 Transition to experiment

To this point the author has prepared the theoretical and modelling basis for the later application and comparison with experiment. We now go on to view the experimental studies, beginning with the observed behaviour of droplets absorbed in to porous pigment composites. Their equilibrium distribution is noted and then compared with the distribution derived from supersource equilibrium absorption. Permeability provides the link between equilibrium saturation and flow. The dynamic supersource absorption then provides the data for comparison with

imbibition, modelling and the discussion of the prior equilibrium results. Finally, practical ink paper coating interaction is studied in the light of those findings.

## 6 Equilibrium distributions of imbibed droplets (Gane, Schoelkopf, et al. 2000)

### 6.1 Introduction

In the manufacture of paper, pigments for coating and filling hold one of the key functions in the processes of liquid adsorption, spreading and absorption into the porous structure. When a droplet of printing ink, e.g. from an office ink-jet printer, comes onto the paper surface, the final printing result, in terms of colour setting, intensity and detail accuracy, is strongly dependent on how far the droplet penetrates in relation to the spreading on the paper surface and where the ink pigment particles or dyes are deposited, and also in which order and timescales these occur (Zang and Aspler, 1998), (Sangl and Weigl, 1997). If the ink penetrates too deeply into the paper, the colours appear dull and weak. If they spread too much on the surface, effects akin to blurring of the image and bleeding between colours are seen. If they spread partially or, worse, directionally, e.g. wick along fibres which act as capillaries or form directional continuous wetting paths, so-called feathering is observed (Arnold *et al.*, 1995). An example of bad printing, taken from the case of ink-jet application, is shown in Fig. 65.

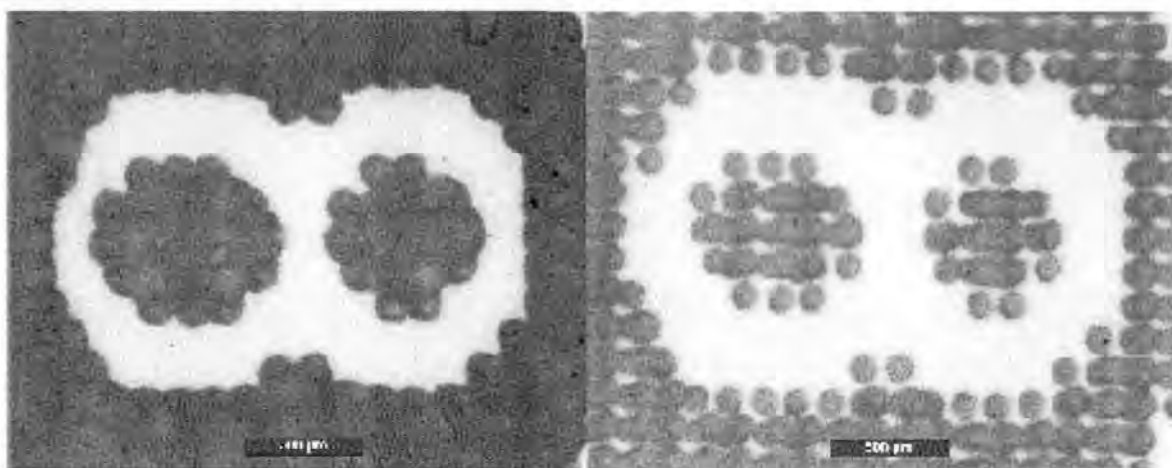


Fig. 65 The right ratio of surface spreading/bulk imbibition is important for ink-jet printing. The picture on the right shows insufficient spread, resulting in bad colour coverage.

The desired balance is therefore formed from an ink droplet that has the optimal spread/penetration ratio, sets fast within the runnability limits of the printing process, thereby depositing the colour particles close to the paper surface, giving a sharply defined colour intensive printing dot. A further important requirement is that the distribution of the absorption controlling parameters over the surface be uniform, otherwise a pattern of irregular print density or gloss becomes visible, known as print mottle.

The porosity of paper alone gives insufficient information about liquid uptake characteristics. A primary determining factor for non-pressure driven imbibition is the contact angle and, therefore, the interfacial energy relationships between the imbibed fluid and the microscopic surface continuity/discontinuity of the pore structure network. If the solid surface adhesion forces to the liquid are much weaker than the fluid cohesivity, resulting in a locally high contact angle, pore entry may be prevented even for very porous samples.

The aim in this part of the study is not to analyse in detail the dynamics of droplet spreading and imbibition but to focus initially on the final liquid equilibrium distribution within representative  $\text{CaCO}_3$  pigment structures. This method is a direct approach to simulate on a macro-scale what is happening when a limited amount of dyed liquid is contacted upon a porous surface, and, after surface spreading has acted in competition to the imbibition into the capillaries, to determine the equilibrium state. This is monitored by the use of an adequate dye which must show no adsorption to the solid so as to maintain independence of the surface chemistry while following the wetting front.

### **6.1.1 Spreading and absorption mechanisms**

Referring to the theoretical sections, we see that the distribution and wet adhesion of the fluid phase of an ink on the solid matrix material, at and within the porous structure surface, are determined by many factors, (Unertl, 1998). Any force that acts at the microscopic interface between fluid and solid will influence the characteristic behaviour of spreading on a microscopic surface. The geometrical arrangement of these microscopic surfaces combine to control the spreading seen on the macroscopic scale. The same forces also interact with the fluid on the capillary walls of the mutual pore system and determine the penetration micro mechanics which couple together with the geometrical parameters of the capillary network to determine the larger scale pore filling characteristics. The right balance between spreading and penetration/absorption influences whether the desired printing process will be successful or not (Picollet *et al.*, 1998).

## 6.2 Method development

### 6.2.1 Selecting a suitable dye

Different aqueous dyes have been investigated for their suitability as an indicator for the liquid front. For this reason an experiment was made applying drops of the different dyes onto the base surface of the sample block (formed as described in section 4.4), Fig. 66.

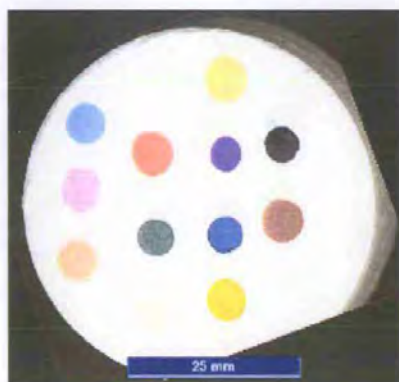


Fig. 66 Some of the dried dyed droplets seen as stains on the compressed pigment block.

After equilibration, the sample block, with the set drops on the base, was then used to check the aqueous chromatographic behaviour of different dye molecules and ions in relation to the slightly anionically dispersed  $\text{CaCO}_3$  surface network. This was made using a method, similar to that described later in the supersource experiment (section 7.3), where the block was brought into contact with the water. The separation of dye was then studied. Setacarb, the fine anionically dispersed  $\text{CaCO}_3$  pressed with 100 kN force, was used as the pigment block, Fig. 67.

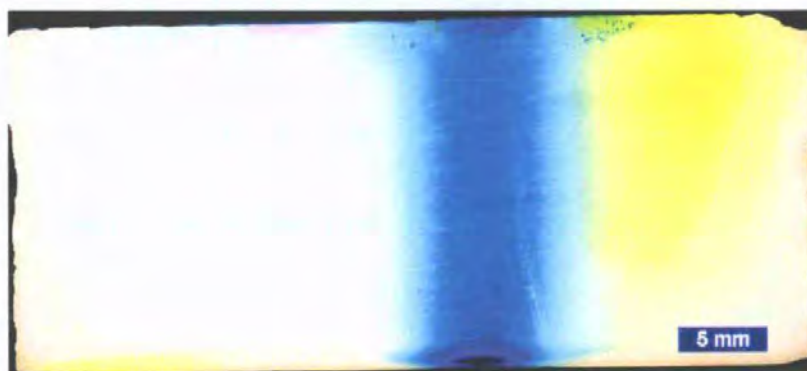
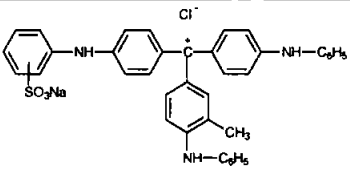
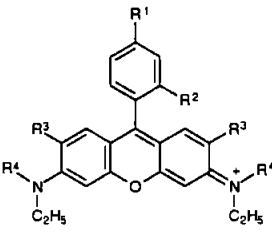
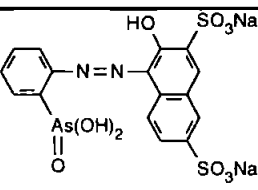
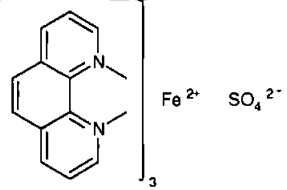
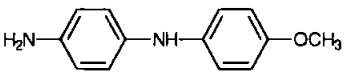
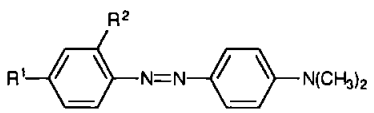
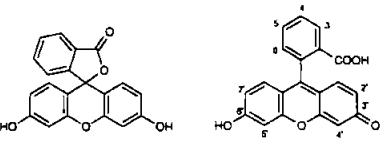


Fig. 67 Cross-sectional grinding through a tablet after a chromatographic experiment.

The range of dyes tested are summarised in Table 5.

Dye*	Chemical Structure	Chromatographic Behaviour: adsorption	Remarks
Alkali blue		yes	
Rhodamine B		medium	
Thorine		no	
Ferroine		yes	
Variamine blue		yes	
Methyl red Methylorange: R1=SO3Na, R2=H Methylred: R1=H, R2=COOH		no	
Fluoresceine used as the Na Salt of the acid form		no	
Irgalite M		yes	Commercial dyes without known composition
Tuerkisblau -	anionic	no	
Gelb 30L-	anionic	no	
Pergasol F2+	cationic	yes	
Gelb KGL+	cationic	yes	

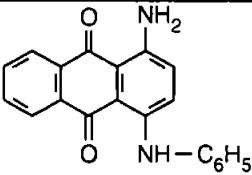
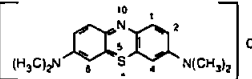
Oracet blue		medium	
Cibalux	anionic	no	Commercial dye without known composition but containing Aluminiumphthalocyaninesodiumsulphonate
Methylene blue		yes	

Table 5 Chromatographic behaviour of dyes. Adsorption: yes = little to no mobility of dye, medium = dye moved away from starting line, no = dye moved from starting line to endline.  
\* all the dyes except the commercial named dyes are available from Fluka<sup>9</sup>.

### 6.2.2 Findings

The results are also summarised in Table 5. All dyes with a cationic charge showed an expected strong adsorption to the anionically treated  $\text{CaCO}_3$  surface. This confirms that the ionic forces (Coulomb forces) contribute the strongest part of the adhesion force and is in agreement with findings covering ink-jet dye adsorbing mechanisms. Acid dye molecules have a significantly weaker adhesion mechanism in which it is assumed that the  $\text{COOH}$ -groups probably interact with free surface of the  $\text{CaCO}_3$ . Dyes with an anionic colorant revealed no adsorption onto the slightly anionically dispersed  $\text{CaCO}_3$  surface and so showed good mobility within the anionically dispersed matrix.

Aluminiumphthalocyanine-sodiumsulphonate was chosen as dye for the subsequent droplet tests. The surface tension of the 1 % solution used in the experiments was determined as  $63 \text{ mNm}^{-1}$ . An example of differential dye adsorption is shown in Fig. 68.





*Fig. 68 The picture displays the cross-section view under the fluorescence microscope of the dyed tablet space after imbibition of a blend of equal amounts of Rhodamine B (orange, retarded) and Aluminiumphthalocyanine-sodiumsulphonate (dark blue, advanced). This shows impressively the chromatographic effect. (Magnification 50x).*

Attempts to stain apolar solvents proved a major problem because the interaction of dye molecules with an organic solvent always seemed weaker than its affinity to a pigment surface which led immediately to adsorption and therefore to chromatographic separation of liquid and dye. For this reason investigation of absorption at this stage was confined to aqueous systems.

### **6.2.3 Droplet application method**

For the subsequent analysis of droplet behaviour on a range of tablet samples a droplet of 5  $\mu\text{l}$  of liquid was formed at the tip of a gas-chromatic syringe. The drop was then carefully brought near to the surface of the tablet. When the drop touched the surface it was pulled by adhesion forces toward and onto the tablet surface. Every tablet was tested with at least 3 droplets - most of the experiments were made in quintuplicate.

The tablet with the surface droplet stains was placed on a normal Desktop Publishing Scanner (UMAX Powerlook II<sup>21</sup>) and scanned with a resolution of 1 400 dpi (dots per inch). The spot shape or "roundness" was monitored and checked as a form-factor, which was calculated as the ratio of the minimum dimension to that of the maximum, i.e.  $\text{diameter}_{\text{min}}/\text{diameter}_{\text{max}}$ . This provided a cross-check of the sample surface spread uniformity.

---

<sup>21</sup> See [www.umax.com](http://www.umax.com) for local distributors

To study the imbibed distribution of droplets, the samples were allowed to equilibrate for 24 h. Each sample dot on the compressed pigment tablet was subsequently ground in such a way that the cross-section of the drop penetration at its largest lateral expansion could be scanned (Fig. 73). With the help of an image analysis software package (KS 400, Kontron Electronic GmbH<sup>22</sup>) the relevant parameters of surface spread area, shape, penetration cross-sectional area and penetration depth could be determined.

### 6.2.3.1 Obtaining a smooth surface and uniform spread

To check the influence of the sample surface roughness, a series of 4 tablets, each formed under a 100 kN press force, were surface ground in an automated grinding machine (Jean Wirtz, Phoenix 4000<sup>20</sup>) with 4 different grinding papers: 60, 320, 1 200, 2 400 grit. The following graph (Fig. 69) shows the influence of the coarser grind paper grades on directional wetting for a range of liquids and non-uniformity due to surface scratches, as illustrated by the visual example in Fig. 70.

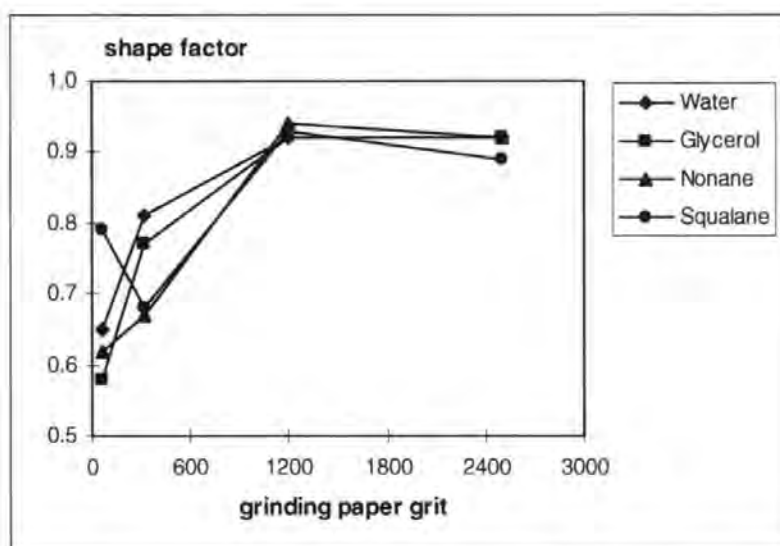


Fig. 69 Dot shape factor as a function of sand paper grit used for surface grinding/ polishing. 1 200, polished surfaces show maximum shape factor which means maximum roundness/uniformity of the droplet stain.

For all samples and all measured dots quoted here, the shape factor was  $0.93 \pm 0.01$  which indicated that directionality had been eliminated and that pore access distribution and surface energy continuity are within usable limits.

<sup>22</sup> See [www.kontron.com](http://www.kontron.com) for local distributors.

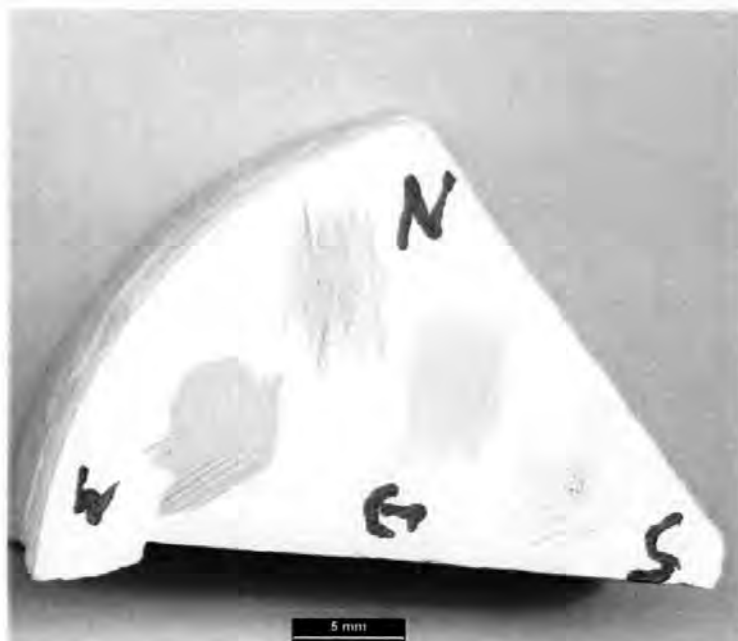


Fig. 70 Different stained liquids show strong influence of surface scratches (ground with 60 grit paper).

The humidity of the tablets also proved to be a very important factor. In the extreme case of a water-pre-soaked tablet, (Fig. 71), a drop of aqueous dye spreads to a large irregular dot (diameter > 10 mm) at very low penetration depth (< 0.5 mm). It is obvious that if the capillaries are already filled with water and the dye can absorb into the capillaries only in a diffusive way, surface spread is strongly favoured. On the contrary, an oven dried tablet (150 °C, 24 h) showed a higher surface wetting contact angle which resulted in a smaller dyed surface area and deeper fluid permeation. We might explain this by the amount of hygroscopically adsorbed water normally present on the polyacrylate-based dispersant. The dispersant polymer requires the water for sufficient hydration to be electrostatically active and thus hydrophilic. It is known that if the water is evaporated by the influence of heat, the polymer shrinks and protrudes much less from particle surface.

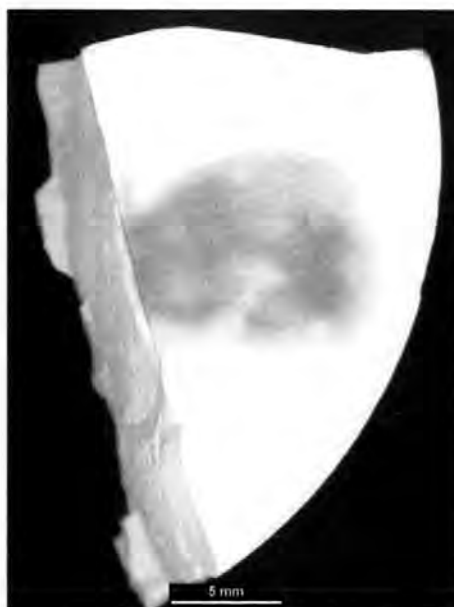


Fig. 71 Supersource water-soaked tablet shows a blurred dyed droplet front (distribution by diffusion rather than capillary absorption).

For this study it was decided to work under realistic climatic and humidity conditions such that, after consolidation, the tablets were equilibrated at 23 °C and 50 % relative humidity for more than 48 hours to a measured moisture content of 0.4 % to 0.8 %.

### 6.3 Sample structures

Porosimetry and simulated parameters of the experimental sample structures used in this section are given in Table 6.

sample no	pigment	$\phi_{lg}$ / %	$d_{min}$ / $\mu\text{m}$	$d_{max}$ / $\mu\text{m}$	$\psi$	$d_{50}$ exp / $\mu\text{m}$	$K_{sim}$ (liq) / mD
100 drop	coarse	28.70	0.004	1.22	3.2	0.214	1.56E-03
250 drop	coarse	28.02	0.004	1.22	3.4	0.129	3.74E-04
150 drop	coarse	26.77	0.004	1.22	3.4	0.116	1.25E-04
200 drop	coarse	24.31	0.004	1.22	3.3	0.141	1.72E-04
300 drop	coarse	22.14	0.004	1.22	3.2	0.132	9.57E-05
400 drop	coarse	21.69	0.004	1.22	3.4	0.095	5.60E-05
450 drop	coarse	19.26	0.004	1.22	3.5	0.081	2.46E-05

Table 6 Overview of the structures used for droplet experimentation. The porosities as given in the text allow for clear identification.  $K_{sim}$  is given for cylindrical throats. For an extended version and explanations refer to Appendix A, Table A1

### 6.4 Observations and results

The process of primary absorption was generally so fast that no contact angle measurement was made. A second outer area of sub-surface spread was subsequently observed caused by internal horizontal capillary forces within the volume of the structure. This led to a ring of lighter colour around the initial spreading area when observed from above (Fig. 72). This fundamental observation showed that, in general, the surface structure had not been altered chemically or physically to create spread without a corresponding quasi-isometric imbibition. The outer diameter of the lighter ring (in topview) is measured as a diameter which corresponds with the spreading regime seen in cross-section. The dark spot of intrinsic drop spreading is due to cumulative dye deposition during the transplanar drop infiltration process, with probably also some size exclusion separation of dye molecule clusters or degraded/insoluble dye components. The dark spot appearance with the lighter ring around it is also reported by Picollet *et al.* (Picollet *et al.*, 1998), using gravure ink and a paper surface.

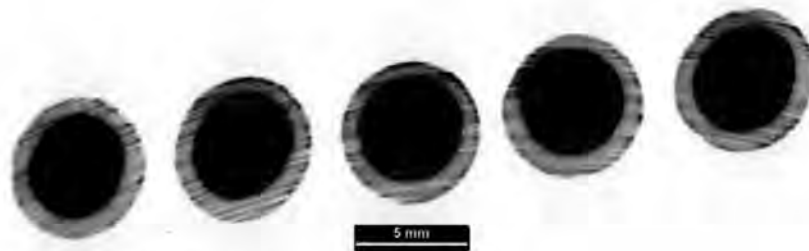


Fig. 72 Droplet dots on tablet surface.

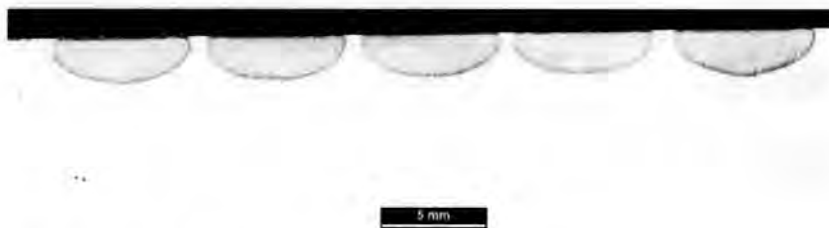


Fig. 73 Droplet dots viewed in cross-section after grinding.

The ratio between surface spread and absorption was calculated as the ratio of the mean surface diameter: maximum penetration depth (Fig. 72, Fig. 73). Therefore, a high ratio means surface spread is favoured over penetration, and vice versa.

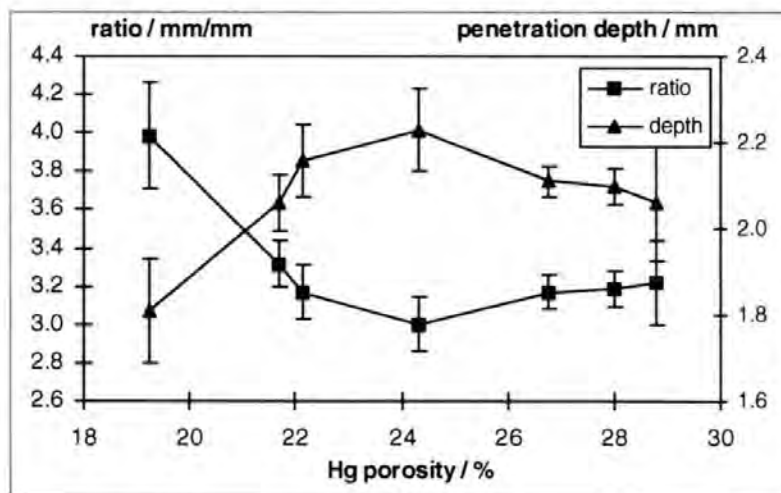


Fig. 74 Ratio of surface diameter to maximum penetration depth of a droplet shown as a function of the mercury porosity as measured from the identical series of compressed tablets. For comparison the depth of penetration is also shown.

Fig. 74 shows a transition in the spread to permeation ratio which can only be consistent with the presence of some unfilled voids. The individual penetration data indicate that there is an anomalously large penetration depth occurring as porosity increases. If all pores were filled (or remained filled) then the penetration depth of a highly porous structure should be less than that of a highly compressed structure. Since it is known from the supersource data that the liquid can access all pores, it must be assumed that any unfilled pores within the

network should at least be surface wetted either by filling and subsequent draining or by diffusional adsorption of the liquid front.

To model this deviation from complete pore filling/drainage, a simulation program was written calculating approximate dimensions of rotationally symmetrical spheroidal segment volumes,  $V_{\text{simdyed}}$ , using parameters obtained from the corresponding image analysis data of the droplet test and contrasting them to a theoretical dyed volume,  $V_{\text{theodyed}}$ , by considering the applied volume of ink and the tablet porosity. The degree of unfilled pores can be detected.

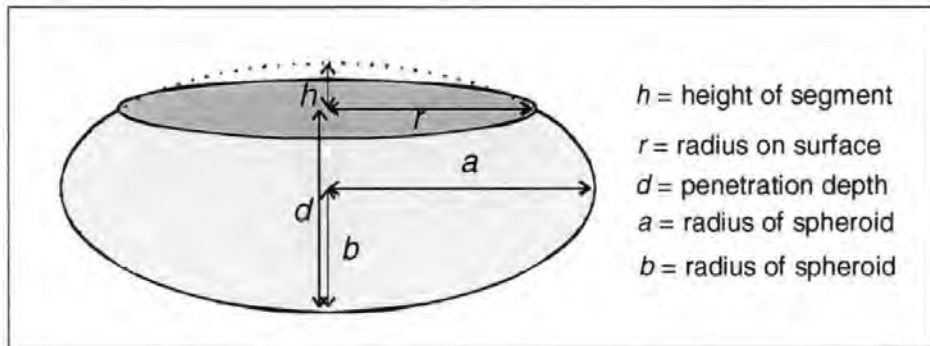


Fig. 75 Spheroidal approximation of the penetration volume.

The simulated penetration volume,  $V_{\text{simdyed}}$ , is calculated assuming the volume can be considered as part of a rotationally symmetrical spheroid having the two axes  $a$  and  $b$ , Fig. 75

$$V_{\text{simdyed}} = \frac{4\pi}{3} a^2 b - \frac{\pi h}{6} (3r^2 + h^2)$$

Eq. 55

where the volume,  $V_{\text{spheroid}}$ , for a complete spheroid would be

$$V_{\text{spheroid}} = \frac{4\pi}{3} a^2 b$$

Eq. 56

and the segment outside the penetration volume,  $V_{\text{simdyed}}$ , is subtracted as

$$V_{\text{segment}} = \frac{\pi h}{6} (3r^2 + h^2)$$

Eq. 57

The values for the spheroid radii,  $a$ ,  $b$ , the surface radius,  $r$ , and the total penetration depth,  $d$ , are provided by the image analysing system and the height of the outer segment,  $h$ , is calculated using

$$h = 2b - d$$

Eq. 58

Further, a theoretical volume,  $V_{\text{theoretical}}$ , for the applied droplet within the structure assuming complete filling is calculated as

$$V_{\text{theoretical}} = \frac{100V_{\text{applied ink}}}{\phi_{\text{Hg}}}$$

Eq. 59

Thus, comparing the two volumes  $V_{\text{simulated}}$  and  $V_{\text{theoretical}}$  we see that the observed value is always far greater than the range where pores would be simply filled with liquid (Fig. 76)

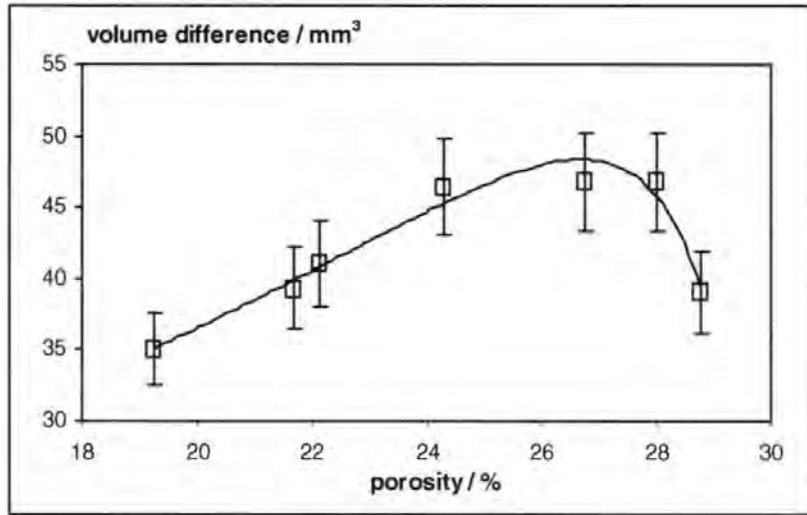


Fig. 76 The comparison of  $V_{\text{simulated}}$  and  $V_{\text{theoretical}}$ , expressed as difference ( $V_{\text{simulated}} - V_{\text{theoretical}}$ ), shows a marked transition as a function of the mercury porosity.

### 6.4.1 Discussion

In the first instant, after the droplet touches the surface, a competition takes place between surface spread and capillary absorption forces. During this period, supersource conditions are momentarily present. In this case, with the polar aqueous solution, it would be expected that nearly complete pore filling should occur near the surface at this stage displacing air in the pore network. Either these assumed saturation conditions do not prevail during the short timescale initial absorption dynamics or, later, there may be a distinction between either locally different pore-wall wetting or adhesion, or through draining of larger pores into smaller pores or throats replacing liquid once again with air (provided the access to air is still ensured), or a potential meniscus fracture/retreat associated with strong film flow/wall wetting in a divergent pore, or a combination of all these possibilities.

In a natural polydisperse pore network with a multiplicity of geometrical configurations and irregularities this transition would not manifest itself as a sharp discontinuity in the penetration parameters but rather as a softer trend (Fig. 77). However, it is possible to imagine that a complex combination of absolute pore diameter, pore-to-throat diameter ratio and connected throat void volume differential determines the competitive filling or drainage level of pores through connected throats.

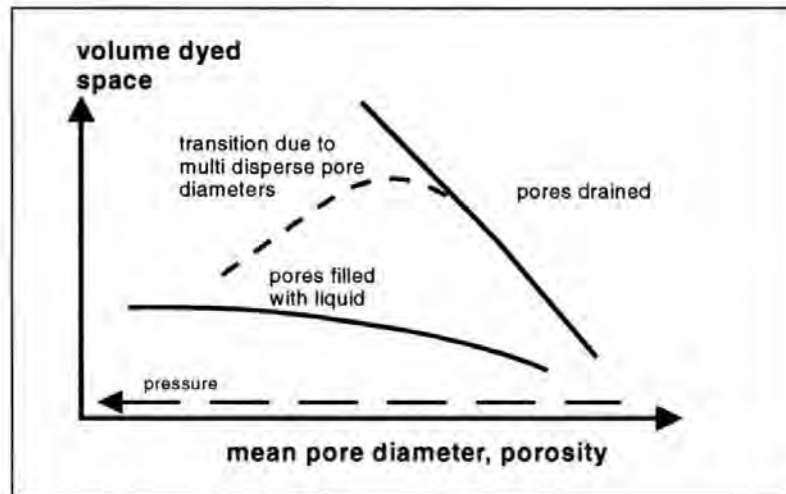


Fig. 77 Schematic showing the balance between total pore filling and either excluded pores or potential pore drainage/side-wall wetting.

#### 6.4.2 Intermediate conclusions

That a transition/discontinuity was seen in the case of *limited volume droplet* imbibition, where the ratio of droplet surface spread compared with absorption showed a marked deviation from complete pore filling as a function of porosity, means that under differential compressions, for example during calendering, a coating structure can create strongly varying absorption characteristics. These are likely to affect print gloss and density without there being any changes in coating composition. It is suggested that this may be one of the dominant causes for print mottle in modern coated papers and supports the previous analysis of coating distribution and correlatable roughness given by Gane (Gane, 1989).

Associated with this transitional spread phenomenon is a further second potential discontinuity in coating layer absorption, which may be related to the various stages of liquid content of pores. With increasing pore diameter, a transition involving a mechanism of pore structure differentiation either between large and fine pores on a short timescale and/or pore draining after longer times may occur. This condition is further dependent on the pore-to-throat diameter ratio and the available volume of the smaller voids. Conversely, strongly divergent pores associated with highly porous structures may lead to a potential imbibition termination and leave some pores



competitively unfilled. In the offset process, where different volumes of contrasting fluids are used, the discrepancy between the droplet volume exclusion case (limited volume) and the supersource saturation effect (abundant volume) may account for differential absorption of offset fountain solution compared with ink, in that, depending on the volume balance of the fluids and their properties, they may strongly compete for and access different pore volume.

A simple droplet absorption method has been used which allows for the study of absorption of limited volumes of fluid into bulk samples of controlled porosity determined by mercury porosimetry. Experimentally it has been shown that there exists unfilled volume within the pore network volume defined by the wetting front as it is absorbed into a compressed pigment structure (Gane *et al.*, 2000), and that this unfilled fraction increases as a function of porosity even when using a wetting fluid, i.e. the observed distance of absorption into a porous network of coating pigment is anomalously greater than would be expected if the total pore volume were to be filled. This is contradictory to the prediction made by the simple LW relationship which predicts that large pores fill faster than fine ones and that all the highly porous structure would be expected to fill as the fluid front progresses, especially at high porosity. Since the parameters of surface energy and wetting are unchanged as a function of porosity, both in these experiments and in the case of many paper coatings, pore diameter and geometry form the controlling factors. It is therefore confirmed here that it is necessary to search for a better imbibition model.

## **6.5 Modelling applications to droplet observations**

The observations made in the previous section can now be used as reference. The phenomenon of unfilled pores has been considered so far mainly on geometrical and surface chemical grounds. The potential influence of "inertial flow" has now to be considered further. The equation of Bosanquet, which includes an inertial term indicating that there is a retarding force at the entry to large capillaries, has been presented in the theoretical section and shown to act to differentiate strongly between large and fine capillaries. The following discussion shows how this approach has been chosen for the subsequent analysis.

## 6.6 Regimes of absorption

There are different theoretical approaches to how the phenomenon of unfilled pores within the imbibition area may be explained for limited fluid volumes. Two scenarios are possible and summarised in Table 7, where case 1 considers redistribution of fluid between different pores after uniform pore filling, and case 2 asks the question how initial differentiation of pore sizes/types might take place.

<b>Droplet application</b>	<b><i>initial regime</i> with local supersource conditions</b>	<b><i>later regime</i> of competitive liquid distribution</b>
Case 1	Uniform pore filling, liquid advancing according to viscous drag criteria.	Competitive redistribution due to Laplace pressure differences, drainage of larger pores, entry of air and filling of fine pores in surrounding area.
Case 2	Initial pore selective filling leaving some pores unfilled.	Only limited local redistribution in the confines of existing menisci Laplace pressures

Table 7 Proposed regimes of droplet imbibition and filling distribution.

"Unfilled" does not necessarily mean completely empty or dry. Some pore-wall wetting due to vapour adsorption or film flow is always to be expected. "Unfilled" can also be interpreted as entrapped air or vapour phase, where, again, entrapped does not necessarily mean immobile. The following considers possible explanations for each of these cases.

### 6.6.1 By-pass effect

The fluid in slow filling capillaries can be overtaken and by-passed by flow into faster ones. In this way, pores may remain unfilled as in case 2. What makes a pore "fast" or "slow" imbibing is of great interest to both the producer of designed porous structures and the science of natural sample imbibition. Inhomogeneous surface chemistry within the pore network must be considered at all stages. This could mean high local contact angles slowing down imbibition in the pore feature giving rise to the by-pass effect and entrapped air. Furthermore, geometrical divergence may have the same effect. Kent and Lyne (Kent and Lyne, 1989) discussed the action of so-called imbibition stoppers or terminators, as reviewed in section 2.3.13. These geometrical features would have the same end effect as chemical heterogeneity. Therefore, it is proposed here that the relevant controlling

parameters can be modelled through geometry and that contact angle heterogeneity can be encompassed within the concept of geometrical change. (This possibility of parameter reduction is considered in a computer network modelling approach and is briefly discussed later).

### **6.6.2 Film flow phenomena**

The physical relevance of film flow, as opposed to meniscus movement, has already been discussed in section 2.3.17. In the literature, some suggestions are given as to how the liquid really advances in a porous network. A recent approach (Bernadiner, 1998) monitors the sequence of film flow with associated liquid surface bulging, snap-off and meniscus movements. These, and more mechanisms are observable in a simple side wall wetting glass capillary using a dyed fluid as shown in Fig. 28. Many of these mechanisms lead to the forming of air (vapour) bubbles within the liquid phase. It is likely that these bubbles could become entrapped in pores. The relevant pores consequently stay unfilled and further flow is only possible for or through films - this falls again into case 2, Fig. 29.

### **6.6.3 Laplace competition**

This is sometimes called the redistribution effect (Marmur, 1992), occurring between fine and larger pores within the network until equilibrium of all the interconnected menisci is obtained (in the limits of air access, which may be restricted in printing processes where a solidifying ink layer forms) - case 1. However, some other dynamic effect, related to the wetting force, must be invoked if the situation in case 2 is to be physically explained.

### **6.6.4 Inertial flow**

Whilst not excluding any one of the already mentioned potential mechanisms, the probable effect of inertial retardation together with a defined regime of inertial filling into fine pore features of the structure network now forms the focus and explanation for the suggested case 2. The logic behind such an assumption is supported in terms of actual print observations, i.e. the commonly observed phenomenon that fine pore coatings absorb thin ink fluid layers faster than large pore coatings, emphasising the potential role of a short timescale effect rather than an equilibrium absorption dynamic. Inertial wetting is used as a model for pore size differentiation during

absorption and leads to the prediction of a preferential tracking of the fluid initially through a preferred network within the porous structure.

### 6.6.5 Discussion of the results in correlation with pore networks

The important distilled results from the droplet experiments, in respect to the excluded pore volume as a function of porosity, are shown in Fig. 78 and are then reviewed in the light of this model.

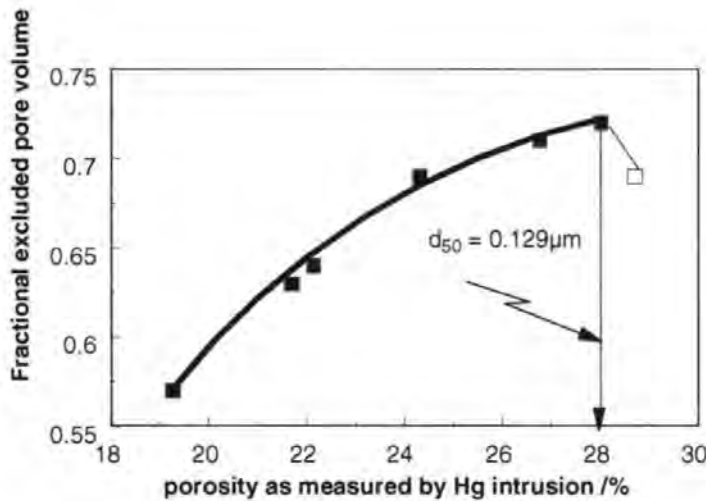


Fig. 78 Fractional excluded pore volume  $(V_{\text{unabsorbed}} - V_{\text{theoretical}}) / V_{\text{unabsorbed}}$  during droplet absorption as a function of measured porosity given in %. Highest porosity point is discussed in section 6.6.6.

It can be seen in Fig. 78 that the fractional excluded pore volume increases monotonically with increasing porosity until a maximum and then falls again. This indicates that if a competitive mechanism is to be proposed, that mechanism would have an increasing differential effect between pore sizes progressively favouring a given pore size or range of pore sizes until the proportion of that pore size once more decreased. Considering Fig. 79 and Fig. 80 below, the predicted pore radius differentiation for water (a low viscosity fluid), using the Bosanquet equation, as similarly generated previously for nonane (see section 5.2.3), has a maximum ridge on the 3D plot that runs from the finest pores at time zero to a pore size equivalent of  $d \approx 0.1 \mu\text{m}$  after time  $t \approx 10 \text{ ns}$  which acts progressively to favour a particular pore size region containing both the finest pores and all those pores up to a preferred equilibrium absorption pore size in competition with larger pores. This, in effect, is an integral of the available pores within a given pore size range which is determined by the fluid in question and the surface chemistry of the network solid.

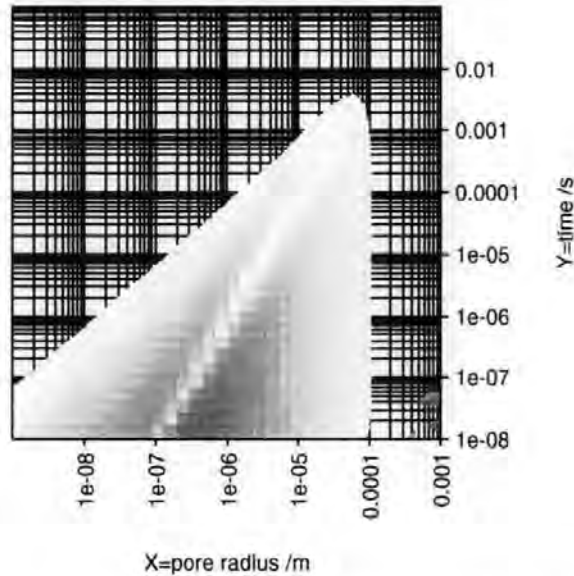


Fig. 79 The "ridge" of maximum absorption velocity for water ( $z$ -axis) as a shaded log/log/log plot, the base  $z$ -plane is  $1 \text{ ms}^{-1}$ . Fig. 80 shows the same data as a mesh plot.

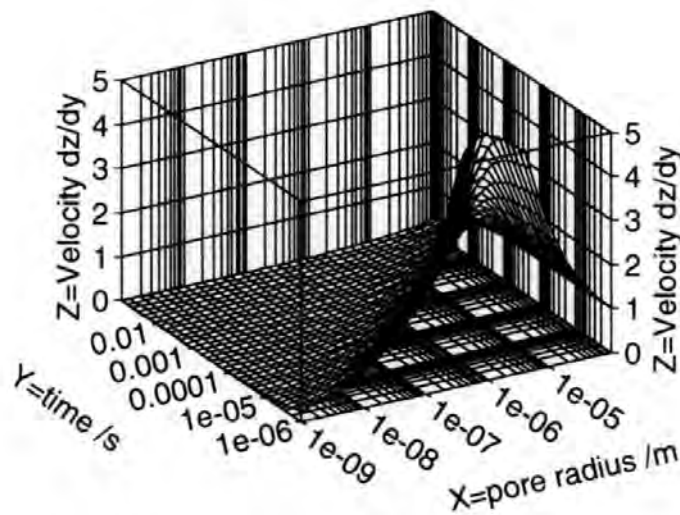


Fig. 80 Bosanquet pore size differentiation favours the pore size which corresponds to the maximum absorption velocity  $\partial z/\partial y$  in  $\text{ms}^{-1}$  for water as a function of time.

The choice of the time for absorption at  $t \approx 10 \text{ ns}$  as the cut off in the log axis of Fig. 79 is not arbitrary. If the Bosanquet plot for water imbibing into capillaries, as shown in Fig. 80, is considered, it can be seen that the effect of inertia is first of all directed toward the exclusion by retardation of all but the finest pores from the absorption process close to time  $t = 0$ . Then the effect of inertia is to favour absorption into those capillaries corresponding to the maximum in the three-dimensional surface which progresses away from the origin decaying in magnitude progressively with time. Now the maximum in observed exclusion as a function of porosity, from Fig. 78, can be correlated with a structure having a measured median pore size of  $0.129 \mu\text{m}$ . This is close to the predicted capillary size sampled preferably by inertial uptake after about  $10 \text{ ns}$  and this in turn corresponds to a

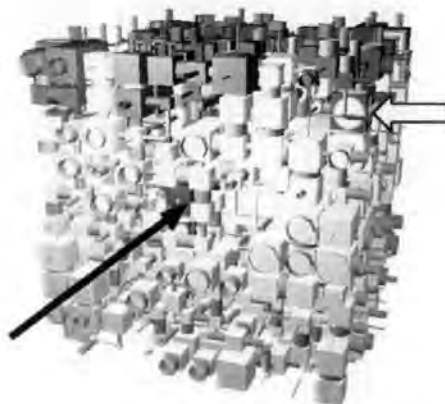
predicted absorbed length of  $\approx 0.1 \mu\text{m}$ . That is to say, the distance of absorption, if it were a capillary, is of the same order as the preferred capillary size. This in effect defines a predicted pore dimension of  $\approx 0.1 \mu\text{m}$  as being the maximum pore size (here in the case of water) into which the inertial imbibition regime exists. (This incidentally provides a self-consistent agreement with experiment and the supporting evidence for modelling a network imbibition by preferential absorption). This imbibition is into an integrated network volume consisting only of the finest pores up to and including a pore dimension of  $\approx 0.1 \mu\text{m}$  to the exclusion of the remaining pore volume. This (case 2, Table 7) is in stark contrast to the normally considered viscosity controlled regime (case 1, Table 7) which would only apply to structures of either much higher porosity with no pores equal to or finer than the Bosanquet optimum ( $\sim 0.1 \mu\text{m}$  for water) or progression toward saturation in supersource (unlimited fluid volume) conditions.

It can be seen from representations of water absorption into the computer network simulator, Fig. 81, defined at the critical porosity from Fig. 78, that there is a progressive filling of the finer pores first, followed by the larger pores. This can be observed directly in the graphical picture of the simulator itself as a function of time. Since there is a preferential distinction between pores up to a given preferred size, it can be seen that, with limited volumes of liquid, not all pores become filled within the volume defined by the penetrating front. Absorption progresses further into a wider range of pore sizes only after the initial inertial imbibition mechanism, which, in turn, then continues to occur at each accelerating feature in the network. Eventually, the energy is dissipated by viscous flow but still the front moves with the largest pores excluded even in this regime by the inertial retardation effect which continues to discriminate against the largest pores. The arrow in Fig. 81 highlights the furthest position of the liquid after an imbibition time of  $10 \mu\text{s}$  which, it can be seen clearly, does *not* form part of a uniform front of completely filled porosity.

From Fig. 82, it can be seen that a lower porosity structure (which also means a smaller mean pore diameter - see Table 6) does not show the preferred pathway effect to the same extent, primarily because there are not so many of the contrasting larger pores and throats present.

For higher viscosity fluids (such as propandiol, butanediol and butanetriol as used in section 9.8), the finest pores, although beginning to fill, are quickly retarded by the higher viscous drag of these fluids resulting in potential exclusion of both the very finest and the largest pores by viscosity and inertia, respectively. If saturation conditions were to apply then larger pores would have to be provided with fluid through a

combination of absorption and percolation throughout the network as they could not compete against the capillarity of the finer pores.



*Fig. 81 Schematic of a computer network simulator cell filling from the top surface under inertially controlled exclusion and wetting for water and a high porosity structure ( $\Phi = 28.02\%$ ,  $Q = 1.26\ \mu\text{m}$ , see Table 6). Note the non-uniform wetting front and the potential for a preferred wetting pathway. Dark grey indicates fluid filled features. The black arrow shows the most advanced pathway (after  $10\ \mu\text{s}$ ). The white arrow points on the representation of partially filled feature.*



*Fig. 82 Schematic of a computer network simulator cell filling under inertially controlled exclusion and wetting for water and a low porosity structure ( $\Phi = 19.26\%$ ,  $Q = 1.31\ \mu\text{m}$ , see Table 6). Note the relatively uniform wetting front (after  $10\ \mu\text{s}$ ).*

### 6.6.6 Implications

It has been shown how the inertial effects can be explained in terms of the structure of a particular porous material being situated within the zone of sensitivity to inertial wetting behaviour. The  $\text{CaCO}_3$  sample used in the present study was brought into the threshold of this zone by applied compression to cover a range of

porosities, and this was demonstrated using the model of Bosanquet applied to the computer network simulator corresponding to these measured porosities. This means that the effective absorbtivity falls off as pore size increases beyond a certain point. This may then lead ultimately to either surface wall wetting or meniscus retreat which might explain the as yet undefined mechanism for the repeatedly observed further reduction in excluded pore volume as porosity further increases beyond the maximum (see the last datum point "□" in Fig. 78). These effects are more applicable to uncoated papers with high porosity fibre networks and have been studied by Knackstedt *et al.*, (Knackstedt *et al.*, 2000). This would mean practically that the removal of oils, for example, from an offset ink would remain incomplete as the fine structure in the drying ink (Lepoutre, 1995) acts to withhold fluid from the coating. There is now insufficient remaining capillarity in the coating structure to complete the separation in competition with the fine pore structure and affinity remaining in the ink.

There is increasing practical evidence for the exclusion phenomenon today in commercial papers, for instance, in the case of coarse pore structures in matt paper, or gloss papers using very steep pigment particle size distributions. This effect can be visualised in the summarising schematic shown in Fig. 83. In conjunction with the excluded volume, the effect of the exclusion mechanism on the observed tack cycle response of an offset ink as measured on a fresh non-pre-split printed ink film can be predicted qualitatively as a function of time. The general features predicted by this method, using the techniques described and discussed by Gane and Seyler (Gane and Seyler, 1993), (Gane and Seyler, 1994), are in close agreement with this new model of absorption. Namely, the initial tack rise behaviour is controlled by the microstructure of the finest pores removing the low viscosity fluid phase, including inter-polymer absorption phenomena by latex (van Gilder and Purfeerst, 1994), involving inertial exclusion of larger pores and absorption into the finest network up to and including the relevant Bosanquet optimum. This is followed by a slowing toward the maximum under the control of LW absorption as viscous drag becomes increasingly dominant. Finally, absorption into the larger pores occurs during the longer time taken for surface tack to decay toward complete ink drying. The tack decay rate, therefore, represents the total pore volume as sampled by the ink. The larger pores acting in this region are at first excluded on the shorter timescale of the tack rise measurement by the inertial retardation effect, but some may also fail to be sampled at all by the ink as they often have insufficient capillarity to compete with the internal ink pore and polymer network forming in the concentrating ink layer during drying. The large pores may also be permanently excluded throughout the absorption as the volume of fluid available may itself be limited and be insufficient for saturation to occur. It remains to repeat that other features, such as geometry or inhomogeneous surface chemistry, may also lead to further excluded volume.



The problem of highly porous structures, or more particularly those with monosized pores, is seen by an almost endless surface tack effect indicating that some of the oil fractions remain in the ink. These circumstances of apparently "anomalously" insufficient pore volume, despite the use of highly porous coatings, are strongly implicated in poor post-tack ink-paper surface adhesion and the observation of poor ink rub resistance.

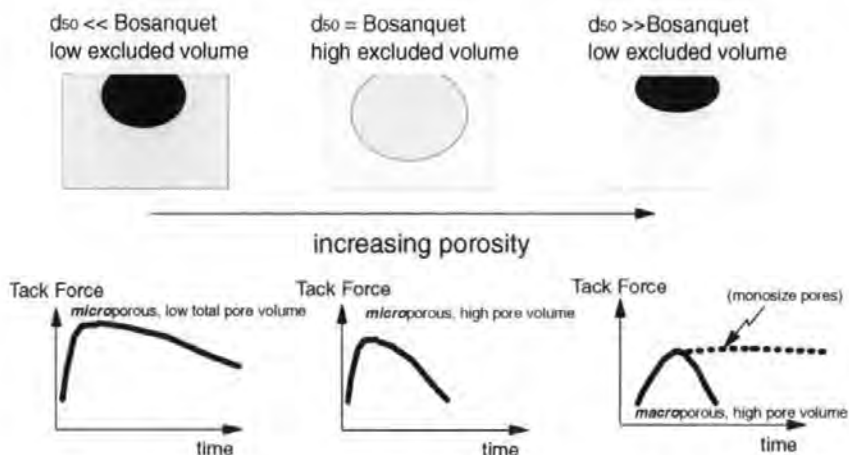


Fig. 83 Schematic representation of the absorption steps controlling the tackification and surface drying of an offset ink. "Bosanquet" refers to the optimum diameter for imbibition as described in section 6.6.5.

This approach gives a new insight into the absorption contrast between large and fine pores in a pigment structure network. The various exclusion mechanisms described here provide interesting new opportunities to understand better how competition between fluids on grounds of their properties such as density and viscosity, as well as wettability, allows for various parts of pore structures to be filled differentially by these fluids. Perhaps one may begin to explain why the apparently incompatible immiscibility of ink and water in the offset process works on a coated paper. The fluids can access either parts of the same void volume or differentiated pore volume, discriminated by wettability criteria, pore size and absorption rate, under the combined dynamics of network inertial imbibition, inertial retardation and viscous drag.

## **7 Equilibrium distributions of imbibed supersource liquids** (Gane, Schoelkopf, et al. 2000)

### **7.1 Introduction**

The supersource imbibition saturation method is a straightforward method for determining absorptive porosity, sampling the total available imbibition void volume. The amount of liquid which can be taken up by the capillarity of the porous system alone is measured without the influence of an external pressure, i.e. if a liquid were totally non-wetting then no liquid would be absorbed. The conception of a "supersource" means that liquid is present in abundance in a reservoir, and the sample is small enough so that the differential between gravity and capillary pressure is negligible. Similar methods are used in a wide range of industrial applications (Hsieh and Yu, 1992), (Pezron *et al.*, 1995), (Taylor *et al.*, 2000).

### **7.2 Liquids**

Many of the fluids used in ink formulations, shown in Table 2, are blends of various sub-components. Some of them contain dissolved or colloiddally dispersed solids. Of each family of liquids one typical representative in its chemically pure form was chosen. These are shown in Table 8 together with some additional liquids with typical values of surface tension, viscosity and polarity selected to cover the imaginable range of fluids likely to absorb into a pigmented paper coating layer. To complete the table, viscosity and surface tension of some of the relatively unknown fluids were measured in the laboratory (\*). Viscosity was determined with a StressTech<sup>15</sup> rheometer performing a small ramp of shear rates. Surface tension was measured with a Krüss Digital Tensiometer K10T<sup>8</sup>.

	Surface tension / $10^{-3} \text{ Nm}^{-1}$	Viscosity at room temperature / $10^{-3} \text{ Pas}$	Dielectric constant	Boiling point / $^{\circ}\text{C}$	Polarity
Water	72	1.056	80.18	100	high
Glycerol	63	1490	42.5	138-140	medium
Ethyleneglycol	48	19.9	37/25	195-197	medium
Linseed oil (*)	35	33.1	n.a.	n.a.	medium
Toluene	29	0.71	2.379/25	110-111	low
Squalane (*)	29	38.8	n.a.	350	very low
Nonane	22	0.59	1.972/20	150-151	negligible

Table 8 Properties of the test fluids for equilibrium supersource imbibition.

*Squalane* (2,6,10,15,19,23-Hexamethyltetracosan, Perhydrosqualane), a derivate of an extract from shark liver, was chosen because it is one of the few available long-chain liquid alkanes of medium viscosity which is chemically pure, Fig. 84.

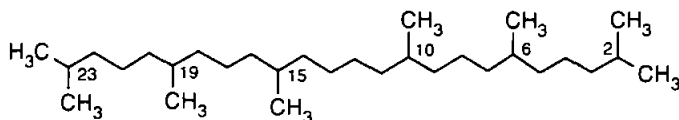


Fig. 84 Chemical structure of squalane.

*Linseed oil* was chosen to represent a vegetable oil relevant to the recent revival of the use of natural oils in printing ink formulations (Siegrist, 1994). It is also frequently used to solve alkyd resins, incorporated in inks to form a drying varnish. Because its main components, namely triglycerides of linolic-, linoleic- and oleic-acid, are uncommon in chemically pure form we chose to work with the natural oil. An important difference from typical aliphatic alkane-based mineral oil is its more polar (dipole) character due to the double bonds and carboxyl- groups (Fig. 85). In the context of this work, the term apolar is therefore only used for the aliphatic alkanes.

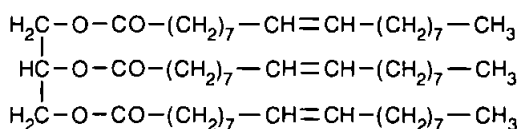


Fig. 85 Chemical structure of trioleine, triglyceride of oleic-acid.

*Toluene* is included representing the typical rotogravure solvent. *Ethyleneglycol*, as a component of flexographic inks, is one of the few liquids with a surface tension within the mid-range of  $\approx 40\text{-}50 \text{ mNm}^{-1}$ . The dipole moments of liquids can be measured over a specified range of oscillator frequencies. However, values are not generally available. The polarity of the bulk liquid, on the other hand, is a less well-defined term associated with dipole moment, but is also dependent on other properties such as molecular polarisability, intermolecular

hydrogen bonding and the entropy of the liquid (Kittel, 1999), (Goldschmidt A. *et al.*, 1984). A useful qualitative estimate of polarity can be made by inspection of the molecular structure. The small size and large dipole moment of water molecules give the liquid a high polarity. The substituent groups within glycerol, ethyleneglycol and linseed oil give these liquids a medium polarity. In squalane, the small local dipole moments of the methyl groups, together with the random C-C orientations within the backbone of the molecule, give it a very low but non-zero overall polarity. The polarity of nonane, which has no substituent groups, is caused only by distortions of the carbon backbone and is, therefore, considered negligible.

### 7.3 Sample structures

Porosimetry and simulated parameters of the experimental sample structures used in this section are given in Table 9.

sample no	pigment	$\phi_{Hg}$	$d_{min}$	$d_{max}$	$\psi$	$d_{50 exp}$	$K_{sim(liq)}$
		%	$\mu m$	$\mu m$		$\mu m$	mD
ss hc og 100	coarse	31.52	0.004	1.22	3.4	0.167	1.13E-03
ss hc og 200	coarse	28.75	0.004	1.22	4.4	0.137	6.33E-04
ss hc og 300	coarse	24.52	0.004	1.22	3.3	0.107	2.05E-05
ss hc og 400	coarse	22.12	0.004	1.22	3.2	0.095	2.48E-05
ss hc og 450	coarse	23.14	0.004	1.22	4.3	0.085	8.93E-05

Table 9 Overview of the structures used for equilibrium supersource experimentation. The porosities as given in the text allow for clear identification.  $K_{sim}$  is given for cylindrical throats. For an extended version and explanations refer to Appendix A, Table A1.

### 7.4 Method

Typically, a sample size of about 1 cm<sup>3</sup> is made by cleaving a pre-formed pigment tablet into a number of pieces with the help of a gentle tapping and cutting with a very sharp blade (a microtome blade was used in this work). The edges of the roughly formed samples are honed with a sample grinding machine and a medium grit paper at 200 min<sup>-1</sup>. This finishing technique effectively removes artefacts that might have arisen during the sample breaking. Dust is removed by gentle air blowing and an electrostatic pistol (Aldrich Zerostat 3). The samples are weighed, labelled and put in a shallow glass dish, which in turn is placed in a larger outer dish. The inner dish is filled with the fluid under investigation, taking care to avoid splashes and false wetting of the sample. The filling depth is just sufficient to ensure that every sample is in contact with the fluid - too high a fluid level can lead to trapped air in the samples and this must be stringently avoided. The dish is fitted with an overlap cover and the outer dish carefully filled with distilled water until it reaches the cover to give a complete vapour seal.

After complete soaking of the compressed sample block(s) - often accompanied by a colour/brightness intensity change because of the reduced light scattering at the inter-particle boundaries - each sample is removed, superficially dried with a tissue and immediately weighed. When using the highly volatile solvents a very fast action is needed to avoid evaporative losses.

The volume of the sample is also determined in its soaked condition by an Archimedes balance. It was seen that a strongly polar Archimedes displacement liquid led to a rapid disintegration of the sample. It is suspected that the polar displacement fluid is absorbed faster than the extrusion capability of the non-polar fluid. Therefore, to ensure that no further pore access is inadvertently sampled by the displacement fluid, only a non-polar liquid could be used. Kerosene (density  $\rho_{\text{kerosene}}$ ) was the chosen fluid.

The outer volume of the sample,  $V_{\text{sample}}$ , can be calculated from the Archimedes displacement:

$$V_{\text{sample}} = \frac{\text{apparent sample mass in kerosene}}{\rho_{\text{kerosene}}} \quad \text{Eq. 60}$$

To minimise the unavoidable errors due to evaporation and loss of small particles at the edges, every sample type (compaction level) was measured in triplicate.

By combining the Archimedes displacement of the soaked volume,  $V_{\text{sample}}$ , (the outer volume of the sample) and the preweighed ( $M_{\text{sample}}$ ) filled sample skeletal volume,  $V_{\text{skeleton}}$ , a measure of the internal pore volume,  $V_{\text{pore}}$ , can be calculated.

$$V_{\text{pore}} \% = \frac{100 \left( V_{\text{sample}} - V_{\text{skeleton}} \right)}{V_{\text{sample}}} = \phi_{\text{Archimedes}} \quad \text{Eq. 61}$$

where

$$V_{\text{skeleton}} = \frac{M_{\text{sample}}}{\rho_{\text{calcium carbonate}}} \quad \text{Eq. 62}$$

and  $\rho_{\text{calcium carbonate}}$  is the assumed density of solid crystalline  $\text{CaCO}_3$  pigment. The absorbed mass of fluid,  $M_{\text{fluid}}$ , further gives the volume of pores accessed by the fluid, of volume  $V_{\text{fluid}}$ , knowing the fluid density  $\rho_{\text{fluid}}$ .

$$V_{\text{absorbed}} \% = \frac{100 V_{\text{fluid}}}{V_{\text{sample}}} = \phi_{\text{absorbed}}$$

Eq. 63

## 7.5 Results and discussion

This last parameter,  $V_{\text{absorbed}}$ , is compared with the value of  $V_{\text{pore}}$  to determine the pore volume sampled by the imbibed fluid compared with the available pore volume. In general, the porosity  $\phi_{\text{Archimedes}}$  was found to be in good macroscopic accord with imbibition volume  $\phi_{\text{absorbed}}$  for the test liquids. Mercury porosity also matches these findings (Fig. 86). (Note that the deviation of the last data point is unexplained and is assumed to be an artefact of the mercury intrusion measurement. It could not be repeated due to limited sample quantities).

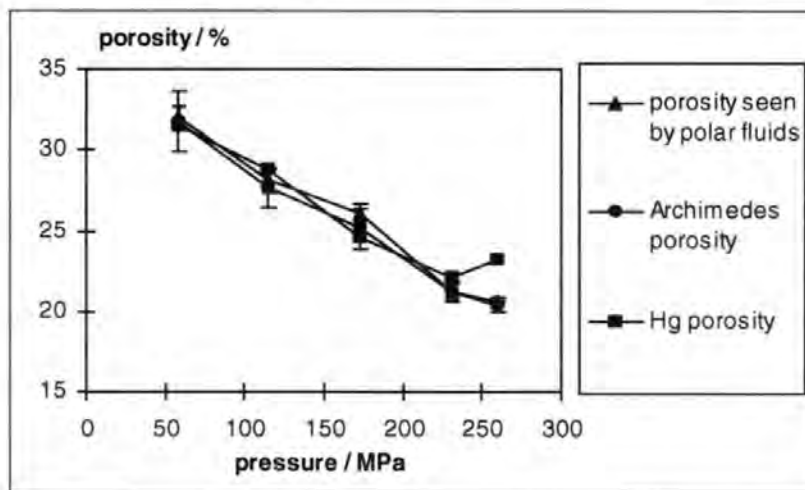


Fig. 86 Comparison of  $\phi_{\text{absorbed}}$  for some polar fluids,  $\phi_{\text{Archimedes}}$ , and mercury porosimetry  $\phi_{\text{Hg}}$  as a function of sample tablet compaction pressure.

The complete set of permeation (supersource imbibed) porosities for all the liquids tested, as shown in Fig. 87, including water at two arbitrarily chosen porosities, is in direct correlation with the experimentally derived porosities over the sample compression range. It is seen that in the case of supersource imbibition, therefore, there is little or no detectable differentiation between the case of apolar and polar liquids between the actual penetrated pore volume and the experimentally defined total available pore volumes. The limitations of this result are discussed in section 8.3 where permeation data give more insight.

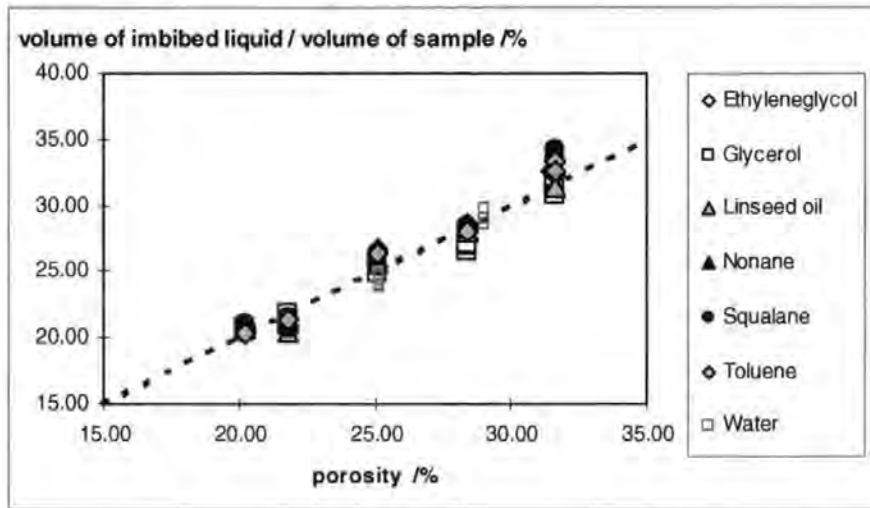


Fig. 87 One-to-one correlation of imbibed liquid volume with porosity for both the polar and apolar fluids as determined from the generalised correspondence shown in Fig. 86, including water at two arbitrarily chosen porosities.

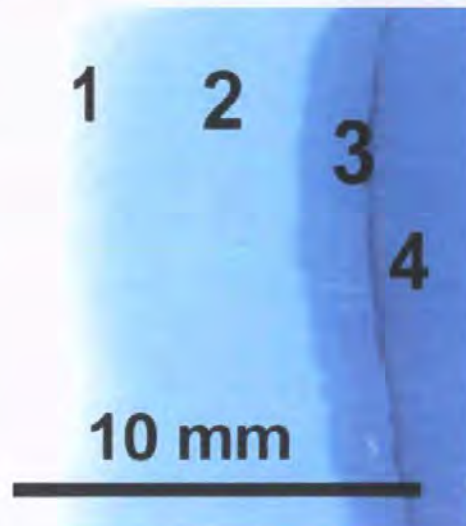
These results mirror the findings reported by other researchers, (Johnson *et al.*, 1998), (Leskinen, 1987), who found a good agreement between void volumes measured by oil absorption and mercury porosimetry. As was discussed earlier, this full saturation effect as seen by supersource is in marked contrast with the situation when the volume of liquid to be imbibed is limited in respect to the available pore volume of the sample, i.e. in the application of a droplet or where the layer of fluid, such as contained in an ink layer, has insufficient volume to lead to saturation equilibrium of the sample.

## 7.6 Visualisation of the imbibing liquid front on the sample-scale

A supersource imbibition experiment was carried out as described previously using dyed water as a liquid. The dye used was the same as in the droplet experimentation, namely Cibalex (section 6.2.1). The sample had a porosity of 28.56 %. (No silicone ring was used around the basal edges in order to have a undisturbed visualisation of the contact area with the fluid reservoir. See also section 9.2.1 where the use of such a barrier is explained). The usual linearity with respect to  $\sqrt{t}$  for pure liquid absorption was once again observed.

During the dynamic stage of the experiment the sample was removed from the liquid source, excess liquid was wiped away and the sample was immediately placed onto a digital image scanner (UMAX Powerlook II) with a resolution of 1 400 dpi. In general, after imbibition experimentation, fluids can be observed in the sample via the change in translucency. This effect has also been described by other researchers (Taylor *et al.*, 2000). The use of a dye, however, enhances the visibility. The liquid front is not a clearly defined line, but a fuzzy regime of transition, Fig. 88 (as previously discussed in the context of Darcy length, - see Fig. 107 for an illustration and

discussion of the effect). Behind it is the bulk fluid uptake, including liquid distribution and remaining pore filling. The meniscus boundary of the reservoir of freely held supersource liquid is visible, and, above it, a regime of surface wicking from the reservoir. The dark area is formed over the area where the dye influx takes place, as was also seen in the droplet experiments (section 6.3). It is a surface phenomenon, probably due to filtration, and quickly disappears if the surface layer is ground away.



*Fig. 88 A scan of the dyed liquid imbibition, view of sample from the side in the wet state, liquid imbibing from right to left (actual experiment performed vertically): (1) liquid front (fuzzy appearance), (2) regime of void filling and liquid distribution, (3) the line shows the meniscus boundary, above it a regime of surface wicking, (4) the dark area is the regime of liquid influx.*

In contrast, a similar experiment is shown with the same structure but a different dye, namely a Ni-(II) phthalocyanine-tetrasulphonic-acid tetrasodium salt. From droplet experiments it is known that the dye has a cationic charge and adsorbs onto the surface of the slightly anionic  $\text{CaCO}_3$ . This means that the solid surface is continuously covered with the dye molecules. This leads to a strong chromatographic effect, and the liquid front is composed of clear water. Fig. 89 shows the sample in the final state when the liquid has reached the top of the sample. The front of the dye represents the liquid distribution far behind the wetting front. Here the dye boundary is much more defined as obviously the dynamics of liquid flow in saturated pores are much more equilibrated.



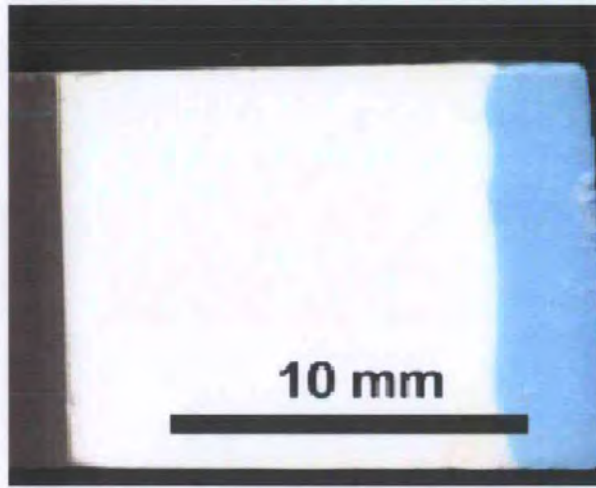


Fig. 89 *Imbibition of water into a  $\text{CaCO}_3$  porous compressed tablet. In this case the cationic dye is adsorbing onto the anionic carbonate surface.*

## 7.7 Conclusions

In *supersource* imbibition, corresponding to the situation of abundant fluid at all stages of absorption, the progress to complete saturation of the pore volume is independent of the range of fluid types studied and corresponds within the macroscopical limits of the method to the fully corrected mercury porosimetry values. (A limitation of the method in respect to the assumption of complete saturation is discussed later in section 8.3).

## 8 Equilibrium pressure-driven flow of liquid through saturated samples

### 8.1 Introduction

It has been shown that in imbibition there is a contribution to the pathway taken by the wetting front which is affected by the inertia of the liquid, and that the imbibition process is complicated by the presence of unfilled pores. Therefore, it was of interest to measure the absolute liquid permeabilities of the samples, using a pressure-driven permeameter, to compare the behaviour under these very different conditions. The measured liquid permeabilities could then also be compared with those predicted by the network simulator, providing for the first time a direct experimental challenge to the permeability model published by Matthews *et al.* (Matthews *et al.*, 1993).

Absolute liquid permeabilities are expressed in terms of the Darcy equation (Eq. 33). The derivation of this equation, and its applicability, have already been discussed in the Introduction.

In paper science and industrial quality control a permeability value is practically obtained by transplanar air permeation through a paper sheet. Although this method is widely used, the major drawbacks have been discussed earlier (see sections 2.1.5.1 and 2.5.4).

The method developed and introduced here is suitable for a magnitude of macroscopic materials which can be formed in a suitable way, preferably as a cuboid. These materials include consolidated pigment tablets, semi-friable porous media and multi-layers of planar substrates. In the latter case, the approach removes major uncertainties of measuring a single, somewhat inhomogeneous sheet of paper or other substance. However, it requires very careful sample preparation and handling, and the experiment itself takes much longer than the standard methods.

## 8.2 Experimental method development

### 8.2.1 Calculation of necessary pressures

Obviously the measurement of the absolute liquid permeability must be made using a differential pressure which is (i) of a magnitude which moves the fluid through the structure at a rate regime similar to that experienced during imbibition, while (ii) generating a flow regime which is laminar rather than turbulent, so that Darcy's law is valid. Condition (ii) may follow naturally from condition (i), but nevertheless both calculations are carried out as a check.

(i) During imbibition, the driving force is the pressure differential across the liquid menisci, which is acting against the viscous and inertial drag of the liquid. The movement of the wetting front becomes slower as the viscous drag in the system increases (hence the  $\sqrt{t}$  relationship). The viscous forces during the measurement of absolute liquid permeability approximately correspond to the imbibition conditions at  $t = \infty$ , when the viscous drag is at a maximum. Since the liquid is moving at a constant rate during the permeability experiment, the inertial forces can be taken as negligible. During the measurement of permeability, the sample is full of liquid, (apart from very small pockets of trapped air as discussed later). Therefore, there are no menisci driving the liquid and so inertial wetting can be eliminated. Instead, the external applied pressure drives the fluid. In imbibition, the resultant of the viscous, inertial and capillary forces cause the fluid to move through the structure. A similar rate of movement during the permeability experiment must be achieved by a balance between the viscous forces and the external pressure. Therefore, the external pressure to achieve usable fluid flow rates can be approximated as being the same as the capillary pressures during imbibition. Using the Laplace equation (Eq. 21) the pressure was computed using the surface tension of the used mineral oil "PKWF 6/9 af neu", in the following referred as "af 6/9" (Table A 4) and a typical throat radius of 100 nm. A value of  $\approx 548\,000$  Pa = 5.48 bar was obtained. Pressures in a range centred on this value should therefore cause fluid movement at rates comparable to those towards the end of the imbibition experiment.

(ii) The standard means of characterising the flow regime is by use of the Reynolds number,  $Re$  (Eq. 49). The flow rate through a feature within the void structure must have a similar order of magnitude to the rate of movement of the entire wetting front. The latter is expressed as a change in distance of the wetting front from the source, measured as a Darcy length, with time. As explained above, we need to consider the limiting rate of movement as  $t$  approaches infinity.

An experimental value for the limiting rate of movement, expressed as a Darcy velocity, is:

$$v_p = \frac{dm}{dt} \frac{1}{\rho \phi A}$$

Eq. 64

We take values of density  $\rho$  and viscosity  $\eta$  for the mineral oil at 6/9 (Table A 4), and substitute them into the Reynolds equation for a pore (Eq. 49), (Seguin *et al.*, 1998b) to give a relation between Reynolds number and void feature radius:

$$Re_p = \frac{dm}{dt} \frac{2r_p}{\eta \phi A}$$

Eq. 65

Solving Eq. 65 for  $dm/dt$  in order to reach Seguin's critical limit of laminar flow at  $Re_p = 180$ , mass flow rates in the magnitude of  $\gg 1 \text{ kg s}^{-1}$  would be needed. Therefore the experimentation with expected flow rates in the order of  $0.0001 \text{ kg s}^{-1}$  is well within the laminar regime of flow.

### 8.2.2 Construction of the pressure cell

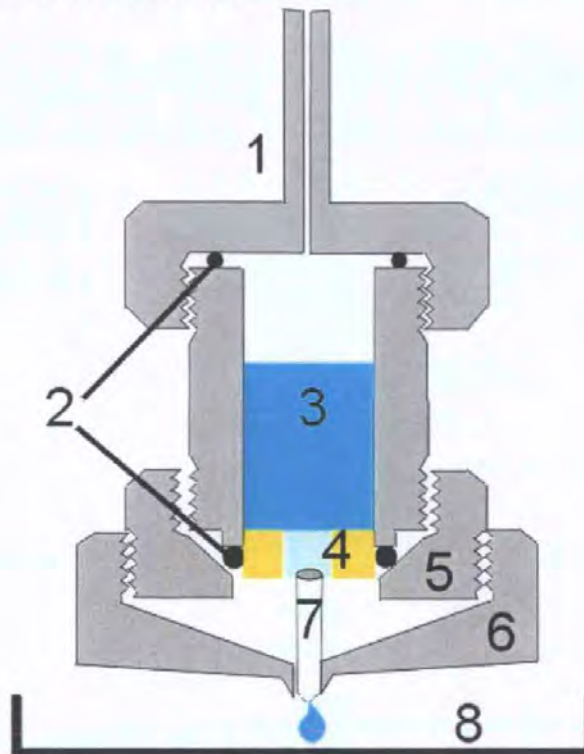


Fig. 90 Permeability measurement cell : (1) lid with pressure inlet, (2) sealing O-rings, (3) liquid cell; outer diameter = 40 mm, (4) porous sample embedded in resin disc of diameter = 30 mm, (5) fixing ring compresses the o-ring which seals the resin disc, (6) security shroud and drop collector, (7) drop captor (Teflon tubelet), (8) dish on micro-balance.

The cell design used for the permeability experiments is shown in Fig. 90. The individual parts of the cell are machined from aluminium and connect via large pitch threads to enable complete and easy disassembly.

The use of epoxy resin to embed the cuboid porous pigment samples (preparation described in section 9.2.1) allows for rigid clamping and sealing of the sample into the pressure cell.

Gas pressure is supplied from a nitrogen bottle and passes a precision pressure reduction valve (Messer FM 62<sup>23</sup>). A Y-piece connects a digital barometer (Eurolec<sup>24</sup> PR 205, 0 - 7 000 mbar) to the pressure line. This gauge was zeroed to atmospheric pressure daily, and therefore all pressures mentioned in this chapter are gauge - i.e. differential pressures  $\Delta P$  relative to one atmosphere.

The pressure cell is fixed on a tripod over a micro balance. A PC samples the balance data using the same software<sup>27</sup> as developed for the imbibition experimentation (shown also in Fig. 101), and records the flux of liquid through the sample.

### 8.2.3 Method optimising

The setup worked almost immediately as soon as it was realised that a drop captor was needed in the base of the cell to guide the permeated liquid drops to the outlet. An important point of practical technique is that the whole chamber below the position of the sample has to be pre-wetted with the liquid so that each drop leaving the sample causes a drop to fall into the dish. Once these precautions are taken the continuity of flow is ensured.

### 8.2.4 Embedding materials and sample preparation method

The epoxy resin was from Buehler Epothin<sup>25</sup>, the PTFE-moulds for the casting of the embedments from Prüfmaschinen AG<sup>26</sup> are circular having an inner diameter of 30 mm.

The cuboid compressed tablet samples were placed into the mould and the resin poured around it. The rapidly increasing viscosity of the curing resin permits only a small penetration at the outer boundaries of the sample (approximately 1 mm). This depth is easily visible because of the opacity change of the porous sample and the open area of the porous sample can be evaluated after the final sample preparation. After the complete curing of

---

<sup>23</sup> Messer Griesheim GmbH, Füttingsweg 34, 47805 Krefeld, Germany. worldwide see [www.messergroup.com](http://www.messergroup.com)

<sup>24</sup> Eurolec Instrumentation Ltd., Cluan Enda, Dundalk, Co. Louth, Ireland

<sup>25</sup> Epothin is a product name of Buehler Ltd., 41 Waukegan Road, Lake Bluff, IL 60044, USA

<sup>26</sup> Prüfmaschinen AG, Giessenstr. 15 CH-8953 Dietikon, Switzerland

the resin, the embeddings are removed from the moulds and dry ground on the two circular surfaces till the open porous structure is reached. (The grinding equipment described in section 4.4). Then compressed air is carefully blown over the sample to remove any dust. Now the dimensions of the free porous sample can be determined.

Subsequently, the sample discs are placed in a dish containing the probe liquid in order to saturate the void network of the sample with the liquid. A complete description of this saturation method is given earlier (7.3).

### 8.2.4.1 Sample structures

Porosimetry and simulated parameters of the experimental sample structures used in this section are given in Table 10.

sample no.	pigment	$\phi_{1g}$	throat type	$\psi$	$d_{50}$ exp	$d_{50}$ sim	$Q$	pore skew	throat skew	$K_{um}$ (liquid)
		%			$\mu\text{m}$	$\mu\text{m}$	$\mu\text{m}$			mD
61	coarse	0.2463	cyl.	3.4	0.098	0.060	1.39	1.4	0.99	6.27E-05
186	coarse	0.2634	cyl.	4.4	0.109	0.103	1.25	1.4	1.42	2.35E-04
177	coarse	0.2673	cyl.	3.4	0.118	0.105	1.23	1.1	0.87	1.67E-04
70	coarse	0.2704	cyl.	3.3	0.115	0.096	1.36	1.4	0.89	5.71E-05
35	coarse	0.3307	cyl.	3.3	0.164	0.137	1.25	1.2	0.60	4.09E-04
61	coarse	0.2463	con.	2.6	0.098	0.099	1.47	1	0.12	3.17E-05
186	coarse	0.2634	con.	3.2	0.109	0.129	1.62	1	0.14	6.29E-04
177	coarse	0.2673	con.	2.7	0.118	0.123	1.46	1	-0.03	1.91E-04
70	coarse	0.2704	con.	2.8	0.115	0.114	1.47	1	0.01	4.89E-04
35	coarse	0.3307	con.	2.9	0.164	0.152	1.35	1	-0.26	1.43E-03

Table 10 Overview of the structures used for permeability experimentation with oils. The porosities as given in the text, allow for clear identification. For an extended version and explanations refer to Appendix A, Table A1.

## 8.3 Results and discussion

The first results showed a strange behaviour. The flux at a constant pressure did not appear to be constant with time. An extreme example showed no flow at 3 bar differential pressure, significant flow when the differential pressure was increased to 7 bar, which then continued proportionally reducing when the pressure was again lowered to 3 bar.

Examples of less extreme behaviour are shown in the graphs below (Fig. 91).

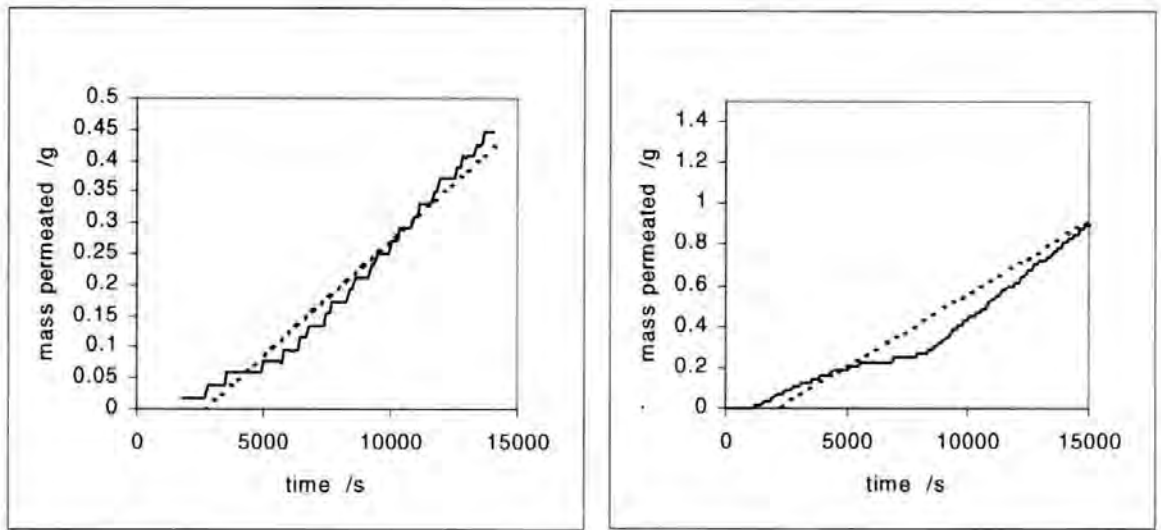


Fig. 91 Non-linear flow at constant pressure, left: 7.22 bar, 23.02 % porosity, right: 5.10 bar, 24.63 % porosity.

It was suspected that entrapped air bubbles could be the cause. If they start to move or become compressed, constant flow is only achieved when the air is displaced or moved into stable trapping positions consistent with the applied pressure and resulting flow. In order to investigate this issue further a hysteresis experiment was performed.

The handling of the sample was performed with the utmost care, making sure that no randomly introduced trapped air could arise from the sample pre-soaking handling and mounting into the measurement cell. A pressure hysteresis loop is shown in Fig. 92.

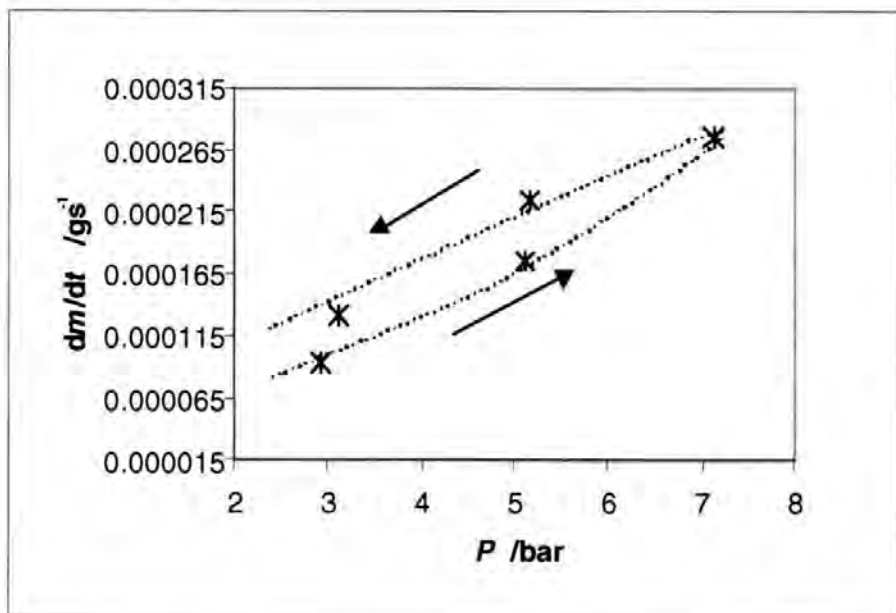


Fig. 92 Hysteresis of flow as a function of pressure: fractional porosity = 0.3298.

Clearly, the dependence of flow on sample history (applied pressure) is monitored. As we saw before, the flux is dependent on starting pressure. If the effect would be due to pore-scale eddies or similar phenomena hysteresis

would not necessarily be expected. So, the previous assumption of trapped air bubbles, which at a given pressure threshold value may start to move and are partly extruded, seems to be the most likely answer. The measurement routine above, starting with the highest pressure first, ensured at least no further bubble motion at lower pressures but the amount of remaining entrapped air is not yet known.

It has to be further assumed that the entrapped vapour bubbles do not have their origin in the sample handling after the supersource soaking, but occur in the supersource imbibition itself.

Therefore, cycles of measurement were subsequently performed first with the highest possible pressure ( $\approx 7$  bar) and then recorded in descending order of pressure. A decreasing series of pressure steps are used to record the permeation flow over a reasonable amount of time to achieve a curve with a usable gradient. Such an experimental data set is shown in Fig. 93. Each step in the recorded curve is caused by one drop falling into the weighing pan. By making a linear regression analysis using Microsoft Excel, a gradient is determined which represents a flow rate of mass per unit time. It is clearly visible that the flow is in the necessary steady state at a constant pressure.

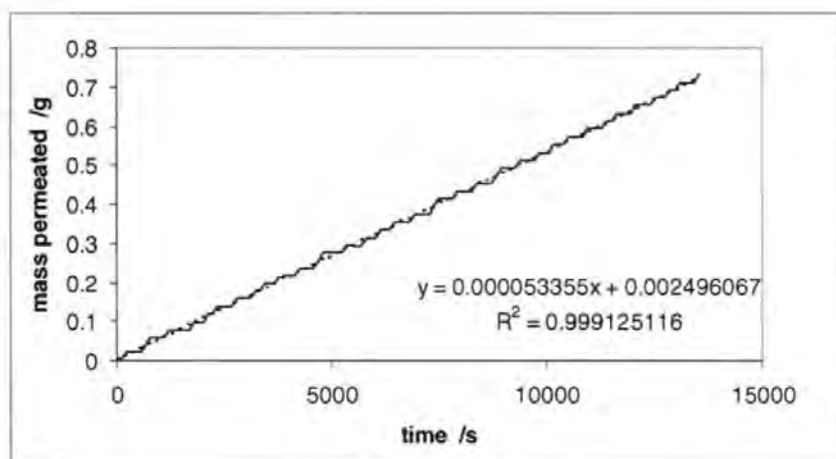


Fig. 93 Typical permeation curve, porosity = 26.34 %,  $P=4.82$  bar.

Determining gradients of further samples in this manner, gave the initial data in Fig. 94 and a more extended range of porosities shown in Fig. 95. Although these plots look reasonable in terms of pressure / flow rate ratios and seem also to track with the porosities, they do not yet contain the sample size parameters needed to derive a permeability.



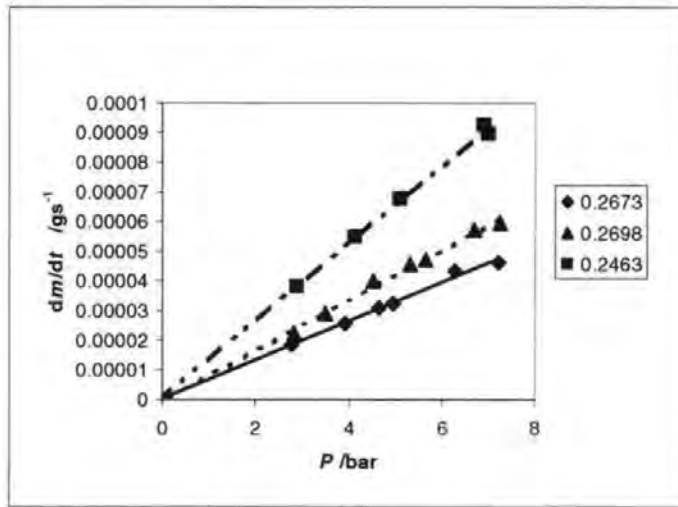


Fig. 94 Permeation gradients in a single sample as a function of applied pressure (legend shows fractional porosities as measured by mercury porosimetry).

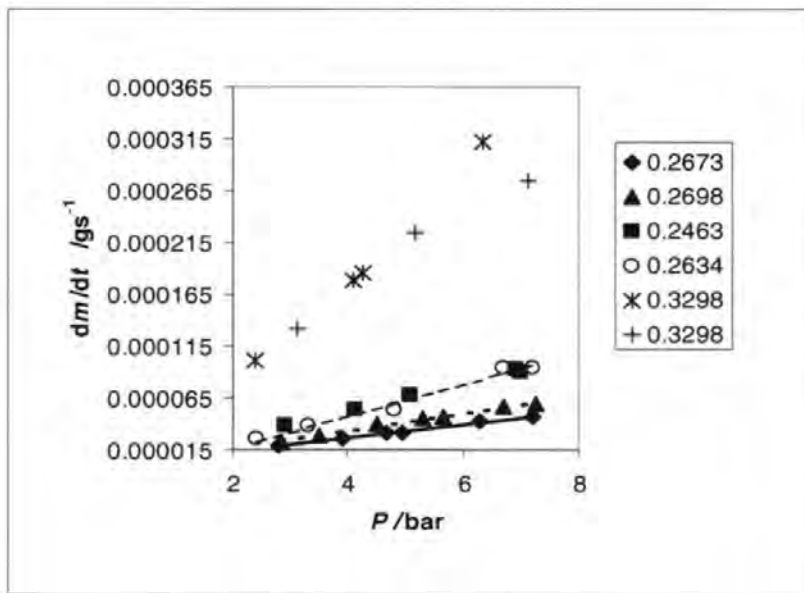


Fig. 95 Permeation gradients in a single sample as a function of applied pressure (legend shows fractional porosities as measured by mercury porosimetry).

As soon as a radius  $r_{\text{chcDarcy}}$  is calculated, by solving Eq. 33 and inputting the necessary dimensions of the sample, we see that  $r_{\text{chcDarcy}}$  falls out of correlation with porosity, Fig. 96. The consequence is that porosity seems not to be the linear controlling factor of permeability. We recall that this was also the case for the droplet imbibition.

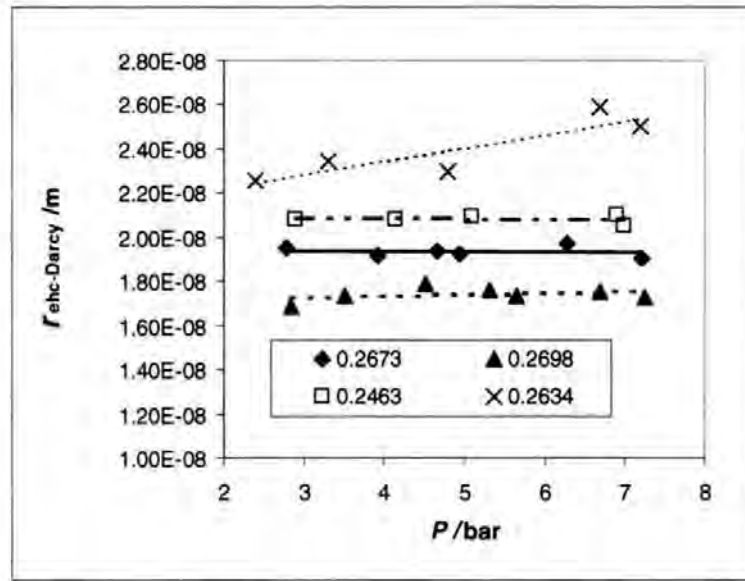


Fig. 96 Hydraulic radii not tracking with porosities (fractional porosities shown in legend).

### 8.3.1 Theory of entrapped bubbles

The finding that imbibition saturation leaves the sample with some entrapped air, is in contrast to earlier statements where it is described that a range of different liquids under supersource conditions imbibed into the whole pore structure present as determined by independent methods, i.e. by mercury porosimetry and Archimedes calculations. How can these apparent contradictions be explained, and can they contribute to a better understanding of flow mechanisms?

Let us approximate the dimensions of one of the porous pigment samples as having a cross-sectional area of  $1 \text{ cm}^2$  and a volume of  $1 \text{ cm}^3$ . It is known that the particles are in a size range of  $1 \mu\text{m}$ . It follows that a row of 10 000 particles in either kind of packing can line up along the sample edge, and in one in-planar layer of cubic packing there are  $10^8$  particles. Assume there is 1 pore between 2 particles and omit the boundary zones in order to get a rough estimate of 99 960 000 pores per layer and therefore  $9.99 \times 10^{11}$  pores in the sample. Suppose a mean pore size is such that a spherical bubble fits into it with a diameter of  $0.2 \mu\text{m}$  (this would be the case for particles with a radius of  $1 \mu\text{m}$  in tetraeder packing, (Spielmann, 2002), (German, 1989)). Such a bubble has a volume of  $0.00418 \mu\text{m}^3$ . So if one planar layer of pores is completely blocked by entrapped bubbles, the summation of the bubbles' volume is  $418 432.56 \mu\text{m}^3$ . This is equivalent to a mass of  $0.3368 \text{ ng}$  of displaced liquid as calculated using the mineral oil at 6/9 ( $\rho = 805 \text{ kgm}^{-3}$ ), which is far less than a microbalance can detect. Therefore, even with millions of entrapped bubbles in a sample they cannot be gravimetrically detected. So although the sample saturates as well as a sensitive balance can determine, there may well be a significant

number of pores remaining that contain vapour. This is a factor which has to be borne in mind in the interpretation of the equilibrium supersource saturation experiments described in chapter 7.

According to the size of an individual bubble, and the size and geometry of its host void, there are two distinct types of behaviour. The extreme behaviour mentioned above can be attributed to air bubbles which move and are flushed from the sample under pressure. The less extreme behaviour is due to air bubbles which move slightly or merely compress under increased pressure. The effect on permeability caused by both types of behaviour decreases with pressure, as compensated for in the experimental procedure.

The preferential wetting pathways, described from section 6.6 onwards, are likely to cause the formation of the bubbles, since wetting through fast pathways overtakes that in slow pathways, and the exit route of air from the slow pathway is cut off, thus producing a bubble.

Linked to this potential effect is the evidence of adsorbed layers of water on the inner surface of the porous network and the known phenomenon of capillary condensation. This results in micro-pores filled by water, which is not soluble in the mineral oil and may block the relevant ganglia. As this effect is expected only in micro-pores it does presumably not influence the permeation behaviour significantly, which is determined mostly by pathways of interconnected large voids.

### **8.3.2 Comparison of experimental and modelled permeabilities**

Fig. 97 shows the measured liquid permeabilities as a function of the porosity of each sample. It can be seen that there is a discontinuity in the permeability trend - i.e. the liquid permeability unexpectedly decreases between a porosity of 0.26 and 0.27. This accounts for the non-linear response to porosity shown in Fig. 96. The firstly unexpected behaviour tracks well with observations previously made with the droplet absorption experimentation, Fig. 76. The graph also shows the error bars which correspond to the scatter in behaviour from a straightforward Darcy proportionality of flow to differential pressure. This scatter is partly experimental, and partly attributable to entrapped bubbles as discussed above. It can be seen that despite these uncertainties the overall trend and its discontinuity are significant.

Also shown on the graph are the liquid permeabilities predicted by the network simulator. It can be seen that the simulated structures with cylindrical throats give a slightly more accurate absolute value of permeability and also match the trend a little more closely than the structures with conical throats.

An approximation is made in the conical model which adopts the diameter of the throat entry and equivalent exit over the whole throat length. We see that the throat skew values for the conical models are smaller than that of the cylindrical models. This results in an increased number of larger throats in the structure. This in turn generates an increased number of larger pores. Therefore to simulate the same experimental porosities,  $Q$  is increased. It is the increased number of larger throats which has a dominant effect in the permeability calculation. Further deviation may be due to the simplistic assumptions made in section 5.3.3 on the flow in double-conical features. Additional work is needed to understand the flow resistance in double-conical tubes in order to verify the suppositions made in the algorithm.

The matching of the simulated and experimental trends allows one to go a step further, and use the simulation to explain the discontinuity in the permeability trend.

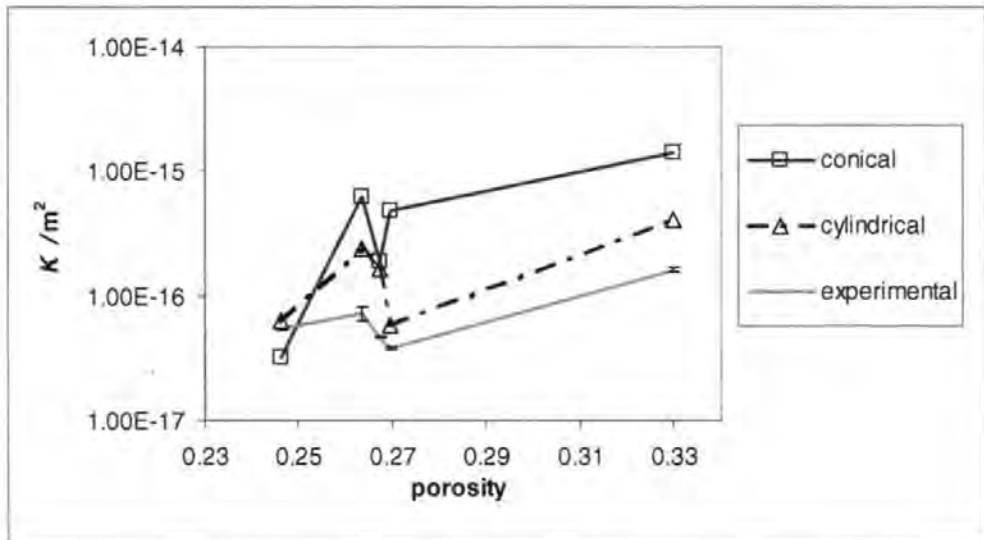


Fig. 97 Experimental permeability  $K$  calculated using Eq. 33 as function of fractional porosity. The errorbars indicate the variation under different experimental pressures as shown in Fig. 96 Comparison is given to two different network simulations involving conical and cylindrical throats.

## 8.4 Conclusions

A hysteresis in permeability was observed performing an up-down sweep of driving pressure. Taking into account the effects of earlier discussed mechanisms of preferred pathway flow and film flow during imbibition, it is postulated that some pores remain unfilled such that there is entrapped air or vapour phase in microscopic ganglia. This air may dissolve in polar liquids but does not dissolve in the aliphatic mineral oil used in the experiments. Structures without a delineated pore-throat structure, as shown for example in Fig. 21(b), will probably lead to an easier and complete extrusion of bubbles.

Even with millions of microscopic air bubbles in the sample they are however not detectable with the gravimetric possibilities offered by a modern microbalance.

The values obtained from these permeability measurements have, therefore to be evaluated with these boundary conditions in mind. It has to be stressed that the restrictions to the measurement procedures apply to the specific samples under study here. Experiments, for example, with paper samples as embedded porous material, yielded good consistent results, showing no hysteresis, (Ridgway *et al.*, in preparation).

The experimental permeability for the samples used in this study is not seen as a monotonic function of porosity. It passes through a local maximum at a fractional porosity of 0.263 with a decay at a porosity of  $\approx 0.27$ . This unexpected behaviour tracks well with observations previously made with the droplet absorption experimentation where the level of a mean liquid content in a pore in equilibrium condition goes through a minimum in the regime between porosities of 0.24 - 0.28. Minimum mean liquid content in a pore goes along with maximum droplet penetration depth.

Analysing the parameters of the computer network simulator it is found that there is no obvious discontinuity in the parameters - it looks like a combination of the throat skew (throat sizes) and connectivity which gives the "dip" in the curve. Comparing the unit cells of samples 186 and 70 (cyl.) (Appendix, Table A 3), we note a subtle difference in appearance. The mentioned combination of parameters being the cause could be explained by conformal changes in the compacting particles as mentioned by Toivakka and Nyfors (Toivakka and Nyfors, 2001), finding connectivities up to 9 for some packing modes. Another explanation would be that under the inter-particle stresses during compaction agglomerates break up. In the agglomerated stage the interstitial voids are smaller than in the de-agglomerated stage. Both proposals would lead to temporarily larger voids in the structure, thus influencing permeability.

This trend was also seen in the droplet experimentation. We now go on to see if permeability plays a role in supersource imbibition or whether the pathway flow at the wetting front is the main controlling factor.

## 9 Dynamic behaviour of imbibing supersource liquids

### 9.1 Introduction

The core of this thesis is represented here and concerns itself with the experimental study of the rate of imbibition as a function of the mutually antagonistic mechanisms of wetting force and resistive forces as reviewed in section 2.3.9 and thereafter. The condition "supersource" (chapter 7) represents the situation where the liquid interface with the sample pores is free from influence of the other bulk liquid interfaces, and the bulk liquid is present in abundance compared with the absorbed volume.

The experimental sample basis, once again, consists of the consolidated tablets compacted from calcite powder. These structures cover a range of different porosities while maintaining the chemical and overall geometrical similarity of the samples. The advantages of this consistent series have been discussed earlier in section 4.1.

The majority of liquids used show Newtonian behaviour. A more complex fluid, in the form of an offset ink in different states of dilution, is also studied. Experimentation starts with a mineral oil, as typically being involved in offset ink formulations as the main diluent. The oil is a blend of aliphatic alkanes and shows a zero contact angle to a freshly ground (and dispersant-treated)  $\text{CaCO}_3$  surface. Together with its low volatility, it is an ideal and practical model liquid which is used for experimentation with the many different pigment structures, each having a defined porosity and pore size distribution. This oil is also used in a blend with linseed oil which acts as a co-solvent for the ink resins (see section 2.2.4 for more details). Studies with these oils are described in sections 9.4 and 9.5.

Subsequently polar liquids are used, as they play a major role in modern ink formulations, such as in flexographic and ink-jet applications. An array of different alcohols, most of them bivalent, offer a wide range of testable viscosities, while changes in density and contact angle are minor. These liquids are used in imbibition studies with porous structures having approximately the same porosity and pore size distribution. An overview of the liquids used is given in Table 11, and the studies involving them are described in sections 9.4 to 9.8.

The stimulation of this portion of the work comes from the apparent paradox that many authors find a  $\sqrt{t}$  dependency for imbibition into many different porous substrates, and use therefore the LW equation with all its limitations to model the results, despite of the more complicated chemo-physical mechanisms which are the basis of imbibition (see section 2.3.11). The author and his co-workers were challenged to apply an equation

containing an inertial term. The classical equation of Bosanquet was uniquely applied into a computer network simulator as described in chapter 4. While the Bosanquet equation expands upon the dissipative viscous term by inclusion of the inertial resistance to liquid acceleration, the network simulator takes account for the fact that a practical interparticulate void network is a system of voids linked by interconnecting crevices or throats. Therefore, terms like tortuosity, permeability and connectivity gain a physical importance compared to any bundle of capillaries approach.

The answers which are expected from the following experimentation evolve around the following points:

- Does imbibition follow a  $\sqrt{t}$  relationship over a range of porous structures, all having the same surface chemistry and pore morphology?
- If yes, do the parameters in the LW equation hold across the range of porosities ?
- If no, is the predicted influence of inertia identifiable by the means of involving different liquid properties and/or structures with different mean pore diameters ?

The tackling of these questions benefits from the network simulator which replicates the percolation properties and structure of the porous tablets. It is found that using cubic pores and cylindrical throats in the simulation gives structures which are unable to replicate the porosity of the sample without invoking the rather unrealistic parameter known as 'pore skew', which bulks up the sizes of the pores, section 9.4. So for the simulations of a range of polar fluids, section 9.8 , the simulator is used in its more sophisticated form by the inclusion of double-conical throats. This modification makes also the throat geometry more realistic for the modelling of inter-particulate voids.

## **9.2 Materials**

### **9.2.1 Preparation of the porous samples**

The porous compressed tablet of finely pre-ground  $\text{CaCO}_3$  was cut and ground to form several 12 mm cuboid blocks, using the rotary disc grinder and the specially constructed, precisely adjustable jig (according to the method in section 4.4).



*Fig. 98 Samples for imbibition: cuboid blocks of compressed porous structures with wax barrier around basal edges to prevent surface wicking.*

To reduce artefacts caused by the wetting of their outer surfaces, the samples were coated with a thin barrier line of a silicone compound (Dow Corning, conformal coating P4-3117) for the oils and with a wax (Rotiplast, Carl Roth GmbH) for the polar liquids around the base of the vertical edges arising from the basal plane. The remainders of the outer planes were not coated, to allow for the free movement of displaced air during liquid imbibition, and to minimise any interaction between the wax/silicone and the absorbed liquid. Preliminary trials showed that the ring is efficient in preventing fluid from creeping up the outside of the sample as discussed later in section 9.3. The sample was consolidated, and therefore did not require a sample vessel surrounding it for the fluid imbibition experiments, thus eliminating uncertainties of fluid interactions with such a vessel. The properties of the individual samples are listed in the following relevant sections.

### **9.2.2 Calcite crystal surface**

To obtain approximate contact angles for use in the computer network simulator, measurements were carried out as described in section 3.3

As measurement surface, a macroscopic calcite crystal of "Iceland-spar" was used Fig. 33 . The crystal was wet ground under addition of a 5 % solution of Coatex GX, a commercial polyacrylate dispersant. The same dispersant chemistry is used in the production of the pre-ground  $\text{CaCO}_3$  powders. The grit of the grinding paper used to finish the surface was 1 200 (for details about the grinding procedure see 4.4). The microroughness of the surface was measured with a confocal laser scanning microscope (Lasertec 1LM21). The microscope scanned perpendicular to the surface at 4 780 points with a spacing of  $0.38 \mu\text{m}$ , and measured a variance of  $0.37 \mu\text{m}^2$ .



The contact angles were then measured on this surface. After a set of measurements, the surface was rinsed with water and re-ground,

One is aware that there is some discussion about the relation of static and dynamic contact angles where the dynamics of a spreading drop are completely different from the dynamics in capillary imbibition. Nevertheless the values obtained are usable for modelling, and in all cases the fluids used showed wetting behaviour.

### 9.2.3 Characterisation by mercury porosimetry

All the porous samples were characterised by mercury porosimetry. As an example, Fig. 99 shows the mercury intrusion and extrusion curves for sample 61. The observed intrusion is corrected for the expansion of the sample chamber under pressure, and the compression of the mercury, Eq. 34 , to give the corrected intrusion curve. Correction for the compression of the sample itself then gives the fully corrected intrusion and extrusion curves shown in Fig. 99.

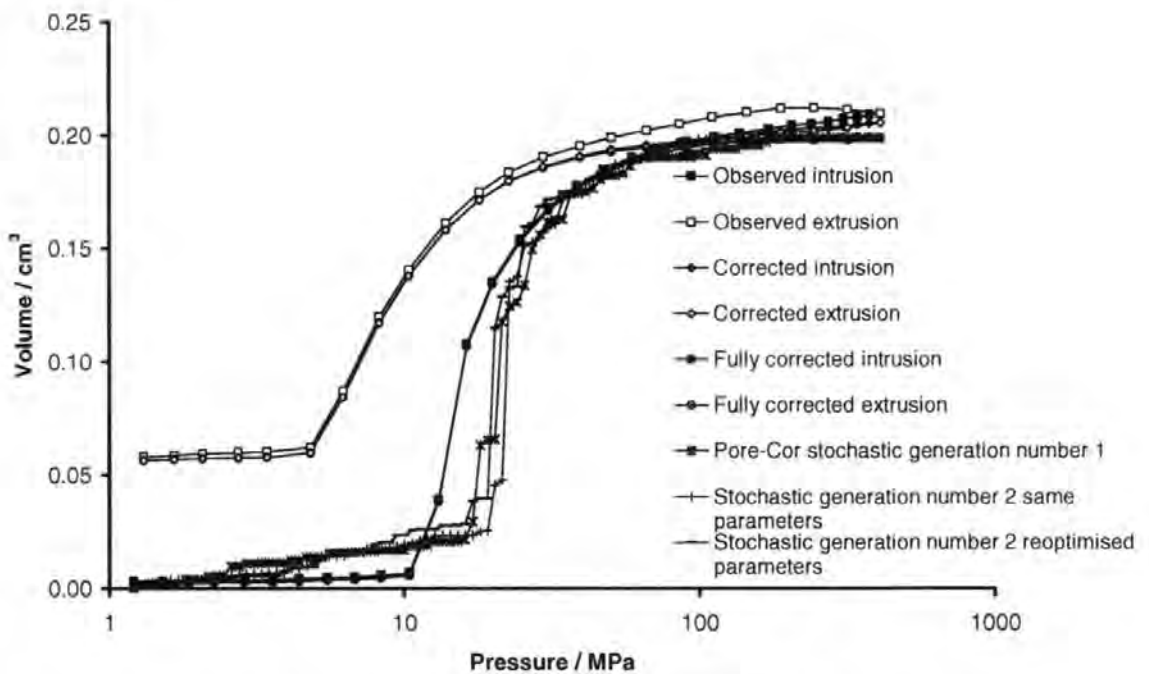


Fig. 99 Experimental and simulated mercury intrusion curves for sample 61.

### 9.2.4 Liquids

The liquids chosen represent, or are, components of commercial inks, Fig. 100, Table 11.

Liquid	Surface tension $\gamma$ / $\text{N m}^{-1}$	Density $\rho$ / $\text{kg m}^{-3}$	Viscosity $\eta$ / $\text{kg m}^{-1}\text{s}^{-1}$	Static contact angle $\theta$ $\clubsuit$ / degrees
Water*	0.07275	998	0.001	0, 10**
Ethanediol	0.048	1113	0.02	21.3
1,3-Propandiol	0.0458	1053	0.0571	34.5
1,3-Butanediol	0.0366	1004	0.135	39.7
1,2,4-Butanetriol	0.0559	1185	1.9	30
1-Octanol	0.0275	824	0.01064	20
PKWF oil 6/9 af neu	0.0274	805	0.0043	0

Table 11 Overview of the test liquids used for dynamic supersource experiments \* only used for simulation purposes, \*\* contact angle used in simulation,  $\clubsuit$  measured on a ground Calcite crystal in the presence of a dispersant as described in section 9.2.2.

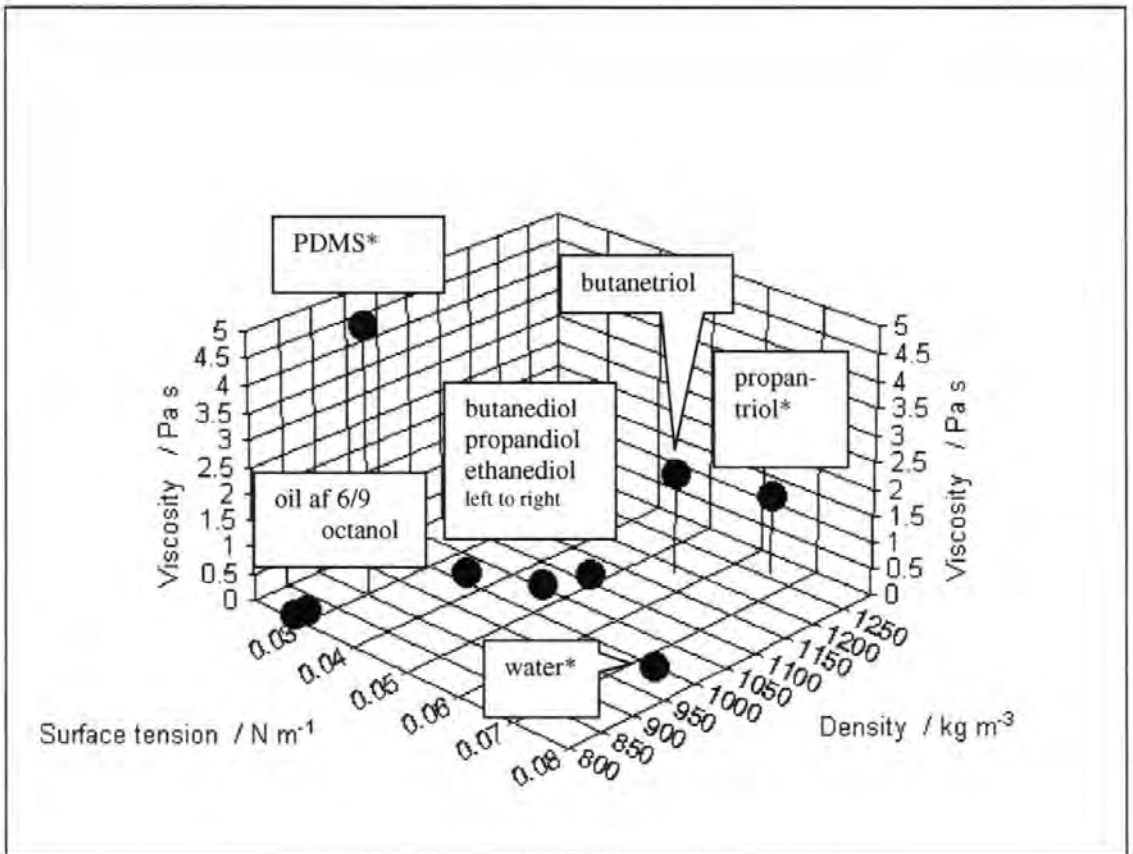


Fig. 100 3D plot overview of liquid properties \* for comparison only.

### 9.3 Experimental method development

The recording of the position of the liquid front within a compacted pigment sample by eye or camera is imprecise due to the fuzzy appearance of the wetting front. This is assumed to be due to the previously discussed suspected preferred pathway flow at the liquid front. Therefore, the rate of liquid mass uptake was measured instead using an automated microbalance. The decision was made to use existing electronic equipment where possible and to develop a custom designed sample/liquid cell which was then constructed in the Omya workshop.

#### 9.3.1 Wetting apparatus

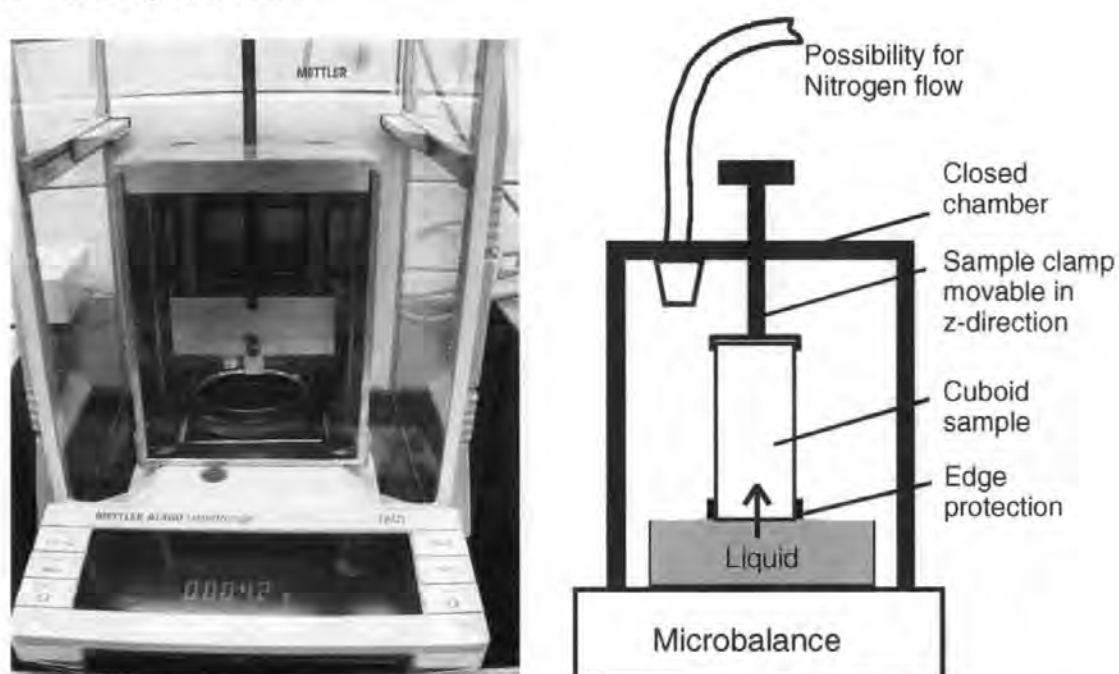


Fig. 101 Gravimetric wetting apparatus with the sample / liquid cell.

The balance used was a PC-linked Mettler Toledo AT460 with a precision of 0.1 mg, capable of 2.7 measurements per second. During the course of the study, the balance was updated to a new model from the same manufacturer, namely an AX 504 Delta Range, capable of 9 measurements per second. A software program was developed (Schoelkopf *et al.*, 2000) and improved further in the present work, interfacing with the balance for data sampling<sup>27</sup> (see Appendix D). To provide a sufficiently slow and precise approach of the sample down to the liquid surface, a special sample holder was constructed, Fig. 101. The chamber around the balance baseplate enabled a controlled atmosphere to be established, shielded from external air movement. The walls of the chamber included an array of gutters which could be filled with silica gel for working with hygroscopic

<sup>27</sup> Software available from the authors.

liquids, or with the liquid itself to allow the establishment of a saturated vapour. Additionally, there was a gas inlet which could be used to keep the cell under a steady stream of an inert gas, such as nitrogen.

### 9.3.2 Imbibition data treatment

The total force  $F_{\text{total}}$  acting on the solid-liquid interface during the imbibition of liquid into the  $\text{CaCO}_3$  is the sum of the wetting, gravity and buoyancy forces, all of which are functions of time  $t$  :

$$F_{\text{total}}(t) = F_{\text{wetting}}(t) + F_{\text{gravity}}(t) + F_{\text{buoyancy}}(t) \quad \text{Eq. 66}$$

The free liquid surface is always below the absorbing surface of the sample, so that  $F_{\text{buoyancy}} = 0$ .

It is necessary to evaluate the contribution of  $F_{\text{gravity}}$ . The largest void size in the sample, as detected by mercury porosimetry, was  $1.22 \mu\text{m}$ . If a capillary tube of this radius was lowered vertically into, say, 1,3-propandiol, the liquid would rise by 7.26 m according to Eq. 21, at which height

$$F_{\text{total}}(t) = F_{\text{wetting}}(t) + F_{\text{gravity}}(t) = 0 \quad \text{Eq. 67}$$

However, the maximum length of a feature in the simulated structure, which has the same order as the maximum length of a feature in the experimental sample, is only  $1.24 \mu\text{m}$ . Therefore, if such a feature was vertical and entirely full of fluid, the fluid column would be only 0.00002 % of the length of a vertical column in equilibrium with  $F_{\text{gravity}}$ . Therefore, it can be concluded that gravity has a negligible effect on the very short fluid columns within the modelled and actual features, and so  $F_{\text{gravity}} = 0$  to a very good approximation.

Another way to express the influence of gravity in relation to surface tension forces is by calculating the dimensionless Bond-number which is

$$Bo = \frac{P_{\text{gravity}}}{P_{\text{capillary}}} = \frac{\Delta\rho ghr}{2\gamma \cos\theta} \quad \text{Eq. 68}$$

where  $h$  is a ganglion length (or height), and balances the force per area induced by gravitational acceleration,  $P_{\text{gravity}}$ , with the capillary pressure,  $P_{\text{capillary}}$ . The smaller the Bond number, the less is the impact of gravity. At  $Bo > 1$ , gravity effects start to dominate. For all the systems used in this study,  $Bo$  is in the order of  $10^{-7}$ .

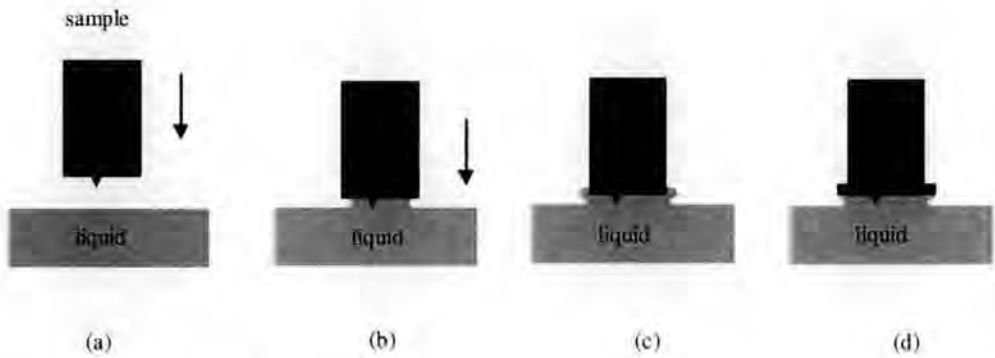


Fig. 102 Schematic of wetting.

In order to interpret the experimental data, it is necessary to understand the precise nature of the imbibition process which occurs. Initially, the liquid has a flat surface, Fig. 102(a). The sample is gradually lowered towards the fluid, with the flat sample surface parallel to that of the liquid. In practice, it is impossible to make the liquid and the microrough solid surface perfectly parallel to each other. Therefore, at some moment of the approach, the fluid touches some point on the solid surface, illustrated schematically by the point jutting downwards from the sample surface. When this point touches the liquid surface, fluid wets it and then the whole surface. A 'contact meniscus' rapidly forms which connects the entire surface of the liquid to that of the solid in a time  $t_1$ , Fig. 102(b). Not only does the liquid absorb into the sample, but also creeps up the outer vertical surface, Fig. 102(c). The rate of this creep is different from the rise of the fluid front inside the sample. If the rate outside is faster, then it will feed fluid back into the sample from the outer walls, and if slower, fluid will emerge from the sample and rise and fall on the outside. This process is unquantifiable, and is therefore minimised by a ring of wax, as described previously and illustrated in Fig. 102(d).

Following the notation of Miller and Tyomkin (Miller and Tyomkin, 1994b), the forces are split into 'inside' or wicking,  $F_{wi}$ , and 'outside'  $F_{wo}$ . The inside forces are those due to the wetting of the internal porous matrix of the block, in other words the forces exerted by the liquid lifted and not the sum of the wetting forces of all the menisci through the structure which would be in the order of  $F_{wi}(t=\infty)$  for a structure big enough to reach the equilibrium rise height. The outside forces are those arising from applied pressure of the fluid at the base of the sample  $F_{base}$ , the impulse when the contact meniscus forms  $F_{contact}$ , and the force caused by the sample side-wall wicking  $F_{side}$ :

$$F_{total}(t) = F_{wetting}(t) = F_{wi}(t) + F_{wo}(t) = F_{wi}(t) + F_{base}(t) + F_{contact}(t) + F_{side}(t)$$

Eq. 69

There has been controversy about this equation in the literature, in terms of the definition of  $F_{total}$  as the 'effective wetting force', and whether this should include just  $F_{contact}$ , or both  $F_{contact}$  and  $F_{side}$  (Hsieh and Yu, 1992), (Pezron *et al.*, 1995), (Hsieh, 1994), (Miller and Tyomkin, 1994b).

Experiments with solid marble blocks and propandiol as test liquid showed that the wax ring (for the apolar oil a ring of a silicone-rubber solution is applied) is efficient in preventing fluid from creeping up the outside of the sample, Fig. 103, so that, to a good approximation,  $F_{side} = 0$ .  $F_{contact}$ , caused by the force of attraction around the perimeter of the meniscus pulling the liquid up towards the fixed solid, is constant for  $t > t_1$ .

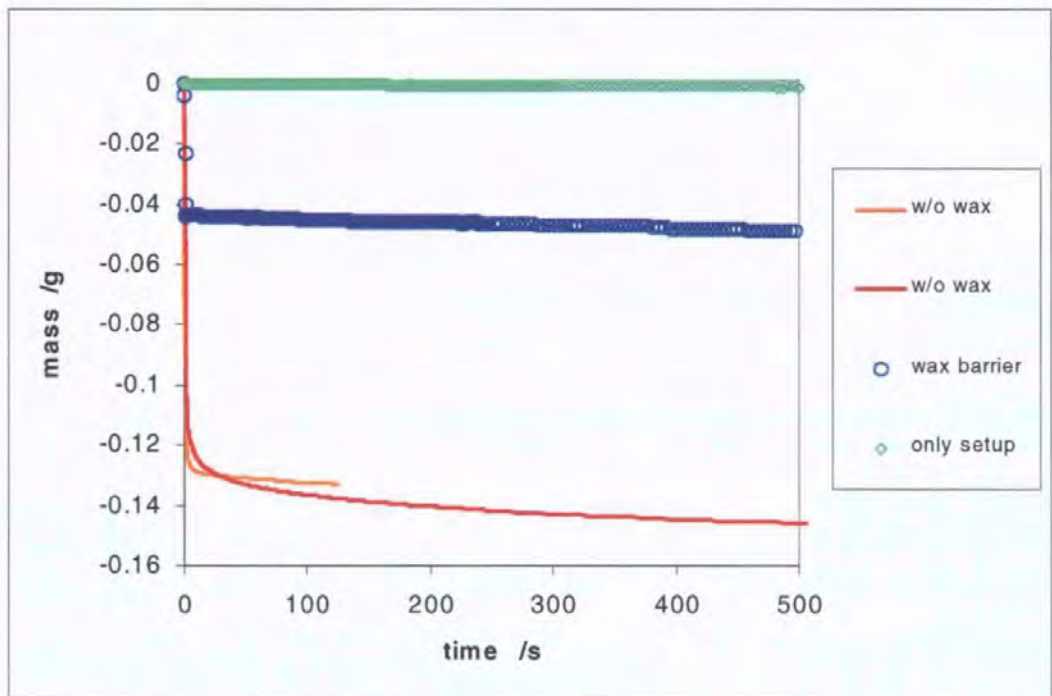


Fig. 103 Demonstration that the wax barrier strongly reduces the wetting jump [contrast the curve without wax ("w/o wax") to the curve with wax ("wax barrier")] and also the subsequent surface wicking. Moreover, the curve "wax barrier" shows a slight increase in lifted mass while the "only setup" (including liquid but no sample contact) curve shows a significant smaller change in mass. So it is unlikely that evaporation or balance drift are the main causes for fluid loss from the bulk. It is concluded that this is imbibition into the residual small porosity of the solid marble (liquid: propandiol).

$F_{base}$  is caused by the formation of the meniscus and the subsequent movement of fluid through the meniscus, the first effect is completed in time  $t_1$ , and the second is assumed negligible because the meniscus is thin and the curvature slight compared to the total cross-sectional area of the uptake. There is also inertia in the system which causes a lag and then an overshoot in the recorded weight. This effect is assumed to be completed in a time  $t_2$ , which is greater than  $t_1$ . Then to a good approximation,

$$F_{total}(t > t_2) = F_{wetting}(t > t_2) = F_{wi}(t > t_2) + F_{base}(t > t_2) + F_{contact}(t > t_2) + F_{side}(t > t_2) \\ = F_{wi}(t > t_2) + c$$

The constant term  $c$ , which is actually a measure of the wetting jump,  $c \approx F_{w0}$ , can be found by fitting the curve  $F_{\text{total}}(t > t_2)$  with a smoothing function, and extrapolating back to  $t = 0$ , at which point  $F_{wi} = 0$ . Then the constant term,  $c$ , can be subtracted from  $F_{\text{total}}$ , and  $F_{wi}$  calculated at all times. In practice, the forces were measured as apparent changes in liquid weight,  $m(t)$ , and a volume,  $V(t)$ , is calculated as  $V(t) = m(t)/\rho$ .

#### **9.4 Experimental imbibition of apolar liquid into samples of different porosities** **(Schoelkopf, Gane, et al. 2002)**

The following set of experiments involves the mineral oil "af 6/9". The same mineral oil is utilised in the accompanying independent study applying tack experimentation with diluted inks (chapter 10). This oil is ideally suited, having a low volatility (see Table 11 for properties).

For the first time (subject to the author's literature review) it is possible to show imbibition curves for a given fluid into pigment structures over a range of different porosities while maintaining the chemical and overall geometrical similarity of the samples. This is typical of paper coatings when keeping the pigment constant and changing calendering conditions.

The task is to analyse whether LW really applies for porous network structures with surface properties held constant. All parameters in the LW equation are tentatively known in this experimentation as they have been determined using independent methods. This gives us the opportunity to analyse the network contribution to the apparent pore-radius as if it would satisfy the LW equation and then to see if this correlates with observation.

##### **9.4.1 Imbibition into samples of different porosities and the same skeletal size distributions**

In a first set of experiments only structures made with the coarse  $\text{CaCO}_3$  powder are used. The changes in porosity are only due to powder compaction. The properties are listed in Table 12

###### **9.4.1.1 Sample structures**

Porosimetry and simulated parameters of the experimental sample structures used in this section are given in Table 12.

sample no.	pigment	$\phi_{Hg}$ / %	$d_{min}$ / $\mu\text{m}$	$d_{max}$ / $\mu\text{m}$	$\psi$	$d_{50}$ exp / $\mu\text{m}$	$d_{50}$ sim / $\mu\text{m}$
69	coarse	37.32	0.004	1.22	3.0	0.198	0.186
28	coarse	35.53	0.004	1.22	2.8	0.196	0.167
31	coarse	31.76	0.004	1.22	3.0	0.156	0.165
47	coarse	30.27	0.004	1.22	2.6	0.139	0.123
57	coarse	27.31	0.004	1.22	2.6	0.121	0.109
177	coarse	26.73	0.004	1.22	2.7	0.118	0.123
74	coarse	24.38	0.004	1.22	2.9	0.096	0.105
35	coarse	33.07	0.004	1.22	3.3	0.164	0.137

Table 12 Overview of the structures used for experimentation with oils. The porosities as given in the text allow for clear identification. For an extended version and explanations refer to A, Table A1.

### 9.4.2 Results and discussion

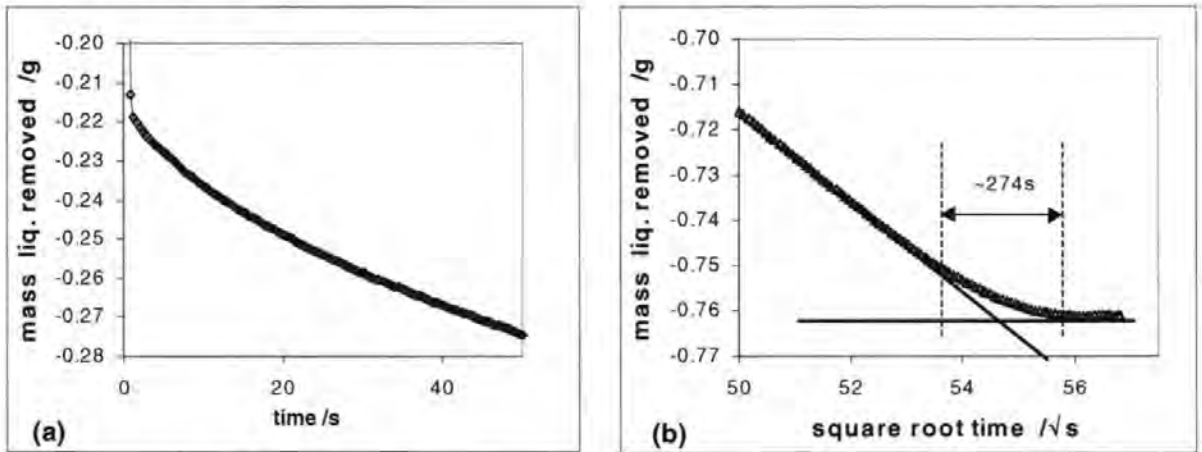


Fig. 104 (a) The absorption data for oil as detected by the balance, (b) the final stage of absorption, namely the saturation of the sample. The structure shown has a porosity of 32.26 %.

Fig. 104(a) shows a typical absorption curve for oil as sampled from the balance. At the very beginning, the last part of the wetting jump is visible with the subsequent regime being linear in respect to the square root of  $t$ . In Fig. 104(b) we see the sample in the final stage of saturation where the first imbibition pathways have already reached the top of the porous sample and there is subsequent filling of slower imbibing capillaries and liquid redistribution. This phenomenon is particularly relevant when we consider limited fluid volume, such as in the case of thin ink films or droplets, as it demonstrates clearly the preferred pathway filling of the sample.



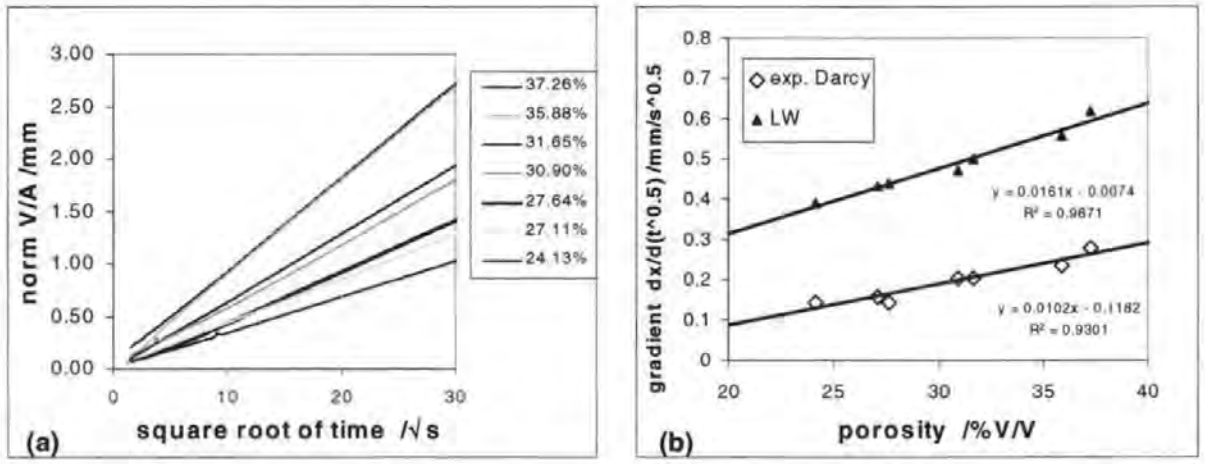


Fig. 105 (a) Imbibition curves for the different porosities translated to  $[V(t=0)/A]=0$ , (b) the slopes of  $x$ , described as (i)  $x =$  experimental Darcy length and (ii) as  $x =$  LW-calculated imbibition length, respectively, tracking with porosities.

In Fig. 105(a) we see the macroscopical uptake as a volume,  $V(t)$ , per unit area,  $A$ , with respect to the square root of  $t$ . For long times there is the expected linear relationship with  $\sqrt{t}$ , but at shorter times there is evidence of deviation, for example, as shown by the sample at 35.88 % porosity (Fig. 105(a)).

The constant term  $c$  in Eq. 70 can be found by fitting the function  $F_{\text{total}}(t > t_2)$  with a Cameron & Bell based equation (Eq. 26), and extrapolating back to  $t = 0$  at which point  $F_{w1} = 0$ .

The absorption mass (converted to volume by fluid density) data used in Fig. 105 have been translated as described above to remove the contribution of the other forces in order that at  $t = 0$ ,  $F_{w1} = 0$ . The uptake is analysed directly as a Darcy length  $x$ ,

$$x = \frac{m(t)}{\rho A \phi_{\text{Hg}}} \quad \text{Eq. 71}$$

where  $m(t)$  is the mass of liquid absorbed as a function of  $t$ ,  $\rho$  is its density,  $A$  is the area of transplanar uptake and  $\phi_{\text{Hg}}$  is the porosity found by mercury intrusion. A plot of  $x$  against the square root of time results in a similar picture as for  $V(t)/A$ . We compare the experimentally determined Darcy length with that predicted by the LW equation in the form of Eq. 72.

$$x = \sqrt{\frac{r_c \gamma_{\text{LV}} \cos \theta t}{2\eta}} \quad \text{Eq. 72}$$

where  $x$  again is the distance travelled by the liquid,  $\gamma_{\text{LV}}$  is the surface tension of the liquid,  $\theta$  is the contact angle,  $\eta$  is the dynamic viscosity and  $r_c$  is the capillary radius. An independent experimental value for  $r_c$  is derived by

halving of the  $d_{50}$ -diameter, which is the capillary diameter at 50 % intrusion volume of the corrected Hg-intrusion curves over the diameter range of 0.004  $\mu\text{m}$  to 1.22  $\mu\text{m}$ . These diameters are shown in Fig. 106.

To illustrate the deviation from true LW behaviour, we can follow the scaling of absorption as a function of porosity, comparing the experimental scaling with that predicted by LW. The experimental scaling is given by the application of Eq. 71, and the LW scaling is that predicted by Eq. 72. This comparison is conveniently shown in Fig. 105(b) where the respective scaling gradients have been formed in each case as  $dx/d\sqrt{t}$ , where  $x$  represents (i) the derived observed Darcy length and (ii) the  $r_{50}$ -based LW imbibition length, respectively. The correlations were determined by a linear regression analysis to obtain the relationships shown in Fig. 105(b).

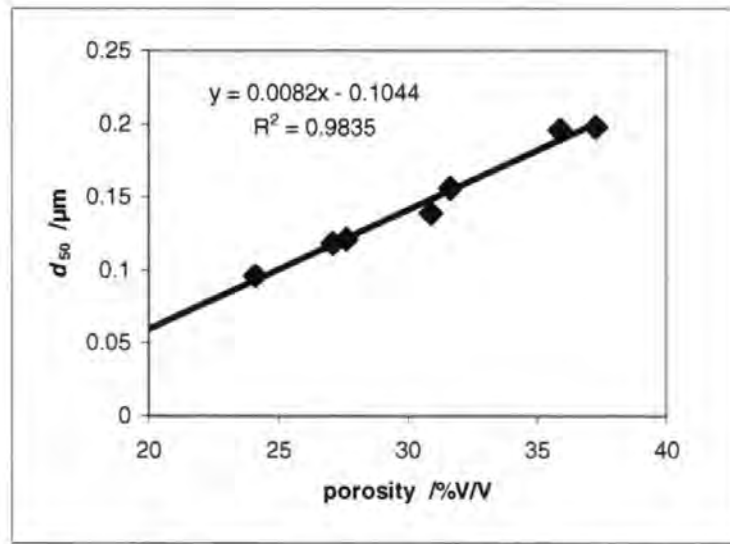


Fig. 106 The  $d_{50}$ -diameter, which is the capillary diameter at 50 % intrusion volume of the-corrected Hg-intrusion curves as a function of porosity.

The effect of inertial wetting and the proposed pathway phenomenon are in principle not detectable using the Darcy law. This is because Darcy describes a volume uptake only which does not account for liquid distribution micromechanisms between selective pore structures. The limitation of the Darcy assumption is shown schematically in Fig. 107.

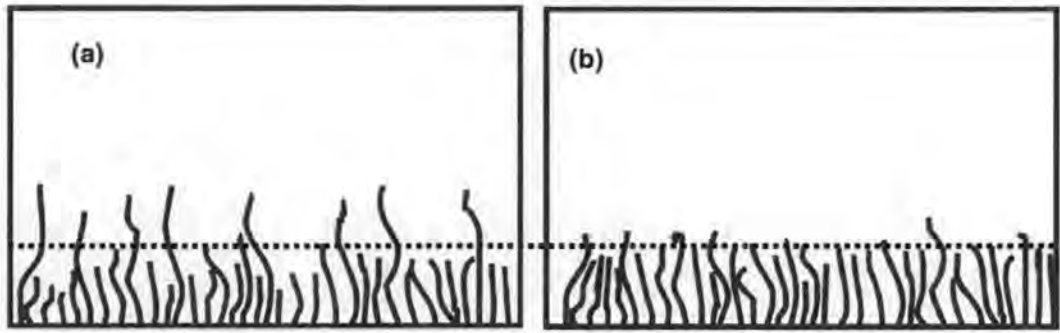


Fig. 107 A schematic drawing (omitting interconnectivity) showing (a) the preferred pathway effect and (b) an idealised more equilibrated uptake, both having the same Darcy length (dotted line) but clearly different wetting lines.

It is evident from Fig. 105(b) that there is a discrepancy between the experimental scaling gradients and the gradients based on calculations using the LW equation, Eq. 72. Similar discrepancy has been reported by other workers elsewhere (Yang and Zograf, 1986a), (Li *et al.*, 1994). Usually it is argued that the contact angle must be changing under dynamic imbibition (Marmur and Cohen, 1997). For this case, however, the argumentation of Chibowsky *et al.* is followed, (Holysz and Chibowski, 1994), who have demonstrated that a range of aliphatic alkanes completely wet a number of mineral surfaces, including  $\text{CaCO}_3$ . This is the basis of why these authors use alkanes to determine an effective pore radius. Only a small amount of work has been done confirming this effective radius using other methods. Li, *et al.* (Li *et al.*, 1994), however, used a variety of alkanes for wicking experiments into ceramic structures. They also assumed that the contact angle was zero, and found an effective radius which was smaller than that afforded by mercury porosimetry by a factor of about 2, which trends with the findings here (Fig. 105(b)). They questioned the mercury porosimetry result. The opinion of the author here is that mercury porosimetry has shown its reliability with many structures of high bulk moduli and was confirmed also in the previous work using pressureless liquid imbibition methods (chapter 7). There is, furthermore, no argument to question the surface tension and the viscosity of the liquid as the remaining influential parameters because they can be easily measured. In previous work other possible mechanisms are considered such as effects of geometry, inhomogeneous surface chemistry, meniscus retraction etc. In this context, while one has carefully maintained constant material properties, it is supposed that over small ranges of porosity basic geometrical changes are not likely to dominate, except perhaps in the case of connectivity, but rather the effective pore and throat size distributions. This is not meant to be an exclusive argument, but it allows us to move on to explore the potential validity of the model discussed above for polar fluids, (section 9.7) as an alternative to the LW model. The experimental evidence needed, and now provided, shows that an alternative is indeed necessary.

If we were to challenge the Poiseuille flow assumption and use an equation of purely inertial flow, as given in the short time solution of the Bosanquet effect,

$$x = t \sqrt{\frac{2\gamma_{LV} \cos \theta}{r_c \rho}}$$

Eq. 73

we would obtain non linear gradients with respect to  $\sqrt{t}$  for the liquid imbibition. Therefore, the proposal is made that the linear  $t$  absorption dynamic is indeed short lived within each acceleration regime within the network but acts to decide into which pores the fluid will flow such that the imbibing fluid can only "see" a fraction of the existing voidage of the porous sample as it selects the finer pores, but that it subsequently follows the viscous dynamic as  $t$  increases, as is predicted by the complete Bosanquet equation. The effective hydraulic radius therefore appears smaller than the one derived from mercury porosimetry. This will lead to a systematic error when applying this observed hydraulic radius to different liquids for calculations of surface free energy of the solid phase of a porous medium and brings into question the absolute values for surface energies derived from the methodology of Chibowski and others (Chibowski and Holysz, 1992), (Chibowski and Gonzalez-Caballero, 1993), (Holysz and Chibowski, 1994), (Chibowski and Holysz, 1997).

### 9.4.3 Imbibition into samples of different porosities and different skeletal size distributions

#### 9.4.3.1 Sample structures

The second part of the investigation using mineral oil is made on structures formed over a range of different porosities using two different skeletal size distributions forming a range of mean pore radii whilst maintaining the chemical and overall geometrical similarity of the samples. The data from the last section are now compared to structures achieved by using the "fine"  $\text{CaCO}_3$  powder as introduced in section 4.2.

sample no.	pigment	$\phi_{1g}$ %
15	fine	32.33
16	fine	29.90
253	fine	27.19
252	fine	25.65

Table 13 Overview of additional structures used for oil imbibition. The porosities as given in the text allow for clear identification. For an extended version and explanations refer to Appendix A, Table A1.

Experimentally, we see that the gradient of uptake volume as a function of  $\sqrt{t}$  follows a linear relationship with porosity and this describes typically the absorption dynamic of the samples, both coarse and fine (Fig. 108).

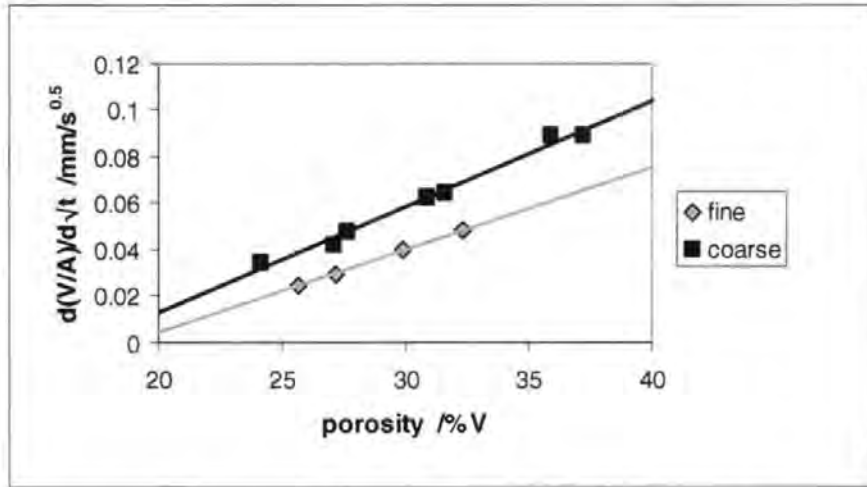


Fig. 108 Both structure series, differing in pore size distribution only, show slightly different volume rate imbibition as a function of porosity.

Assuming firstly the universality of the LW equation, the volume uptake per unit cross-sectional area of the sample should be expressed in terms of the basic interactional parameters between fluid and the solid surface making up the boundaries of the pores as

$$V_{LW}(t) / A = \pi r_{ehc}^2 \sqrt{\frac{r_{ehc} \gamma_{LV} \cos \theta t}{2\eta}} \quad \text{Eq. 74}$$

formed by balancing the Laplace pressure across a curved meniscus with the Poiseuille resistive laminar flow in the circular capillary, and letting the volume uptake per unit area equal the volume filled into our equivalent capillary which represents that unit area. This definition of  $r_{ehcV}$  no longer relates directly to the porosity of the sample and the incompatibility with a Darcy-length based  $ehc$ , discussed above, becomes a natural consequence.

Following the discussion in 5.1 we derive by equivalence from Eq. 74 the experimental  $r_{ehcV}$  for each structure by comparing the experimental uptake gradients with the assumed parameters of the LW equation acting over unit area, such that

$$\frac{d(V(t) / A)}{d\sqrt{t}} = \pi r_{ehcV}^2 \sqrt{\frac{r_{ehcV} \gamma_{LV} \cos \theta}{2\eta}} \quad \text{Eq. 75}$$

from which  $r_{ehcV}$  can be isolated as

$$r_{ehcV} = \sqrt[5]{\left(\frac{d(V(t)/A)}{d\sqrt{t}}\right)^2 \frac{2\eta}{\pi^2 \gamma_{LV} \cos\theta}}$$

Eq. 76

Comparing this volume-based  $ehcV$  value with the value we obtained for an  $ehc$  based on the Darcy length, we see that

$$r_{ehcV}^5 = r_{ehc} \left(\frac{\phi}{\pi}\right)^2$$

Eq. 77

If LW does in fact fail, in that there exists selective pore filling, then it is to be expected that the definition of an  $ehcV$  will not have the same dependency with the measured  $r_{50}$  between the two size distributions as it did with the measured porosity. The measured  $r_{50}$  values for the structures do not in fact fall on the same trend between pigments as a function of porosity, (Fig. 109).

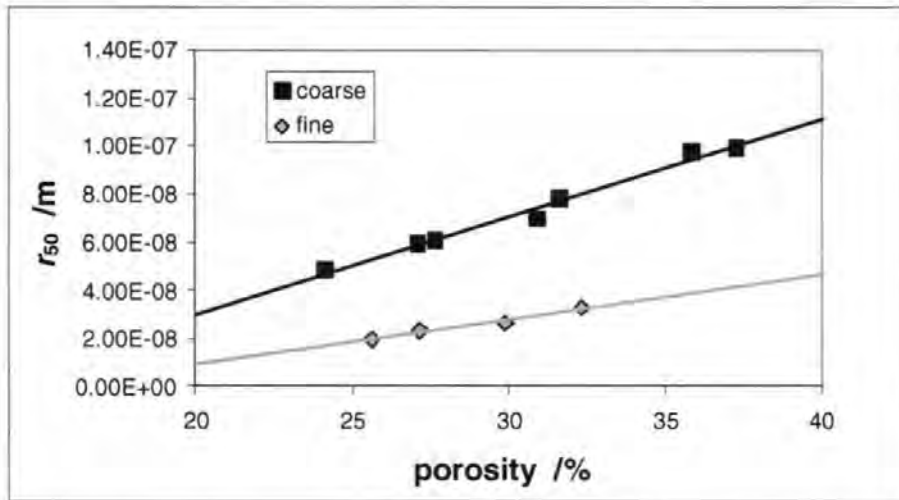


Fig. 109 The measured  $r_{50}$ -radius as a function of porosity for structures made from the two different skeletal particle size distributions.

If we compare the experimental observations with those according to LW as functions of porosity,  $\phi_{lig}$ , and pore size,  $r_{50}$ , we see that  $r_{ehcV}$  follows porosity but with a constant shift according to the skeletal size distribution, (Fig. 110) whereas there is a multiplicative scaling of  $r_{ehcV}$  between the two pigments as a function of pore size (Fig. 111).

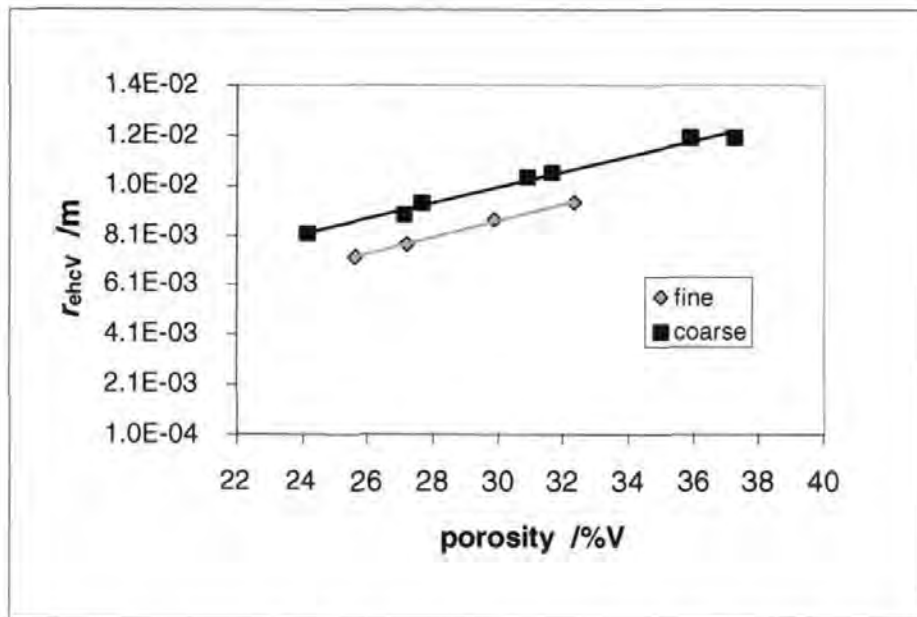


Fig. 110 LW-derived (volume based)  $r_{ohcV}$  as a function of porosity shows quite similar behaviour for the two structure series, but the difference in pore size distribution delivers a constant shift in the  $r_{ohcV}$  against porosity relationship.

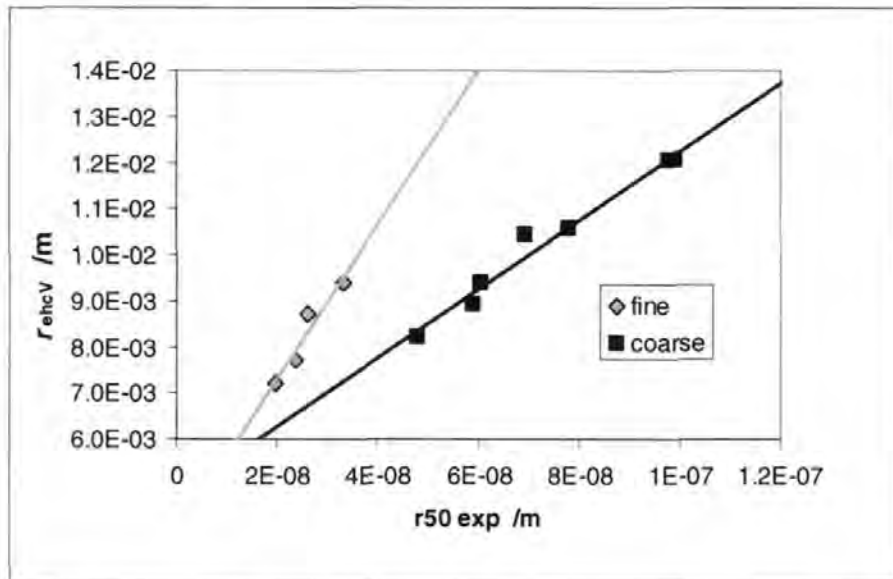


Fig. 111 LW-derived (volume based)  $r_{ohcV}$  as a function of  $r_{50}$ . Note the multiplicative scaling.

Since the absorption dynamic is shown experimentally to be linearly dependent on porosity, and since all the LW constants have been kept constant in these experiments, we must assume that the LW equation does not hold true for differing pore size distributions in a network structure due to the shift apparent in Fig. 110 and the multiplicative scaling in Fig. 111.

There must, therefore, be another factor involved in the dynamic of absorption which cannot be accounted for simply by the Poiseuille resistance to the flow developed under a Laplace pressure. This factor differentiates between pores of different dimensions other than by simple viscous drag, such that pores at the fine end of the pore size distribution behave under a different dynamic from those at the coarse end of the pore size distribution.

This dynamic is assumed here as a first approximation to be related to inertia as the fluid is accelerated at high rates into small pore sizes in the network structure. This is the basis and the reason for choosing an expression such as the Bosanquet equation which, including an inertial term, predicts this selectivity as shown in chapter 4.

#### **9.4.4 Conclusions with regard to apolar liquid imbibition**

Imbibition experiments have been performed using a range of structures with different measured porosity and pore size distributions while keeping all the other important parameters of surface chemistry and geometry of the skeletal material constant. These formed the basis to analyse the applicability of the LW equation for porous structures.

Definitions of the equivalent hydraulic radii derived from volume uptake rates and from calculated Darcy-length rates have been discussed. The implications arising from the use of an imbibed volume-defined equivalent hydraulic radius, thus removing the arbitrary dependency on porosity, have been illustrated.

Since all the LW constants have been maintained in these experiments, the lack of correlation between the measured pore radius and that of the derived porosity-independent equivalent hydraulic radius (based on volume uptake), for two similar but different pore size distributions, strongly supports the proposal that the LW equation does not hold true for differing pore size distributions in a network structure. To account for the discrepancy, models such as those provided by the inclusion of inertia are considered to provide a better solution, in which the individual fluid accelerations occurring within size-differentiated elements of a network structure lead to a deviation from straightforward Poiseuille flow simultaneously into every pore, such that pore selectivity occurs rendering the scaling of Darcy length with intrusion-measured porosity irrelevant.

### **9.5 Imbibition of a mineral/vegetable oil mixture**

Rousu *et al.* (Rousu *et al.*, 2000a), (Rousu *et al.*, 2001a), (Rousu *et al.*, 2001b), have shown that during imbibition into a paper coating pigment structure there occurs a chromatographic separation between mineral oil and vegetable oil components. At the wetting front in a binder free sample, mineral oil was found to have penetrated further than the vegetable oil. The tools used to monitor this included visual observation and FTIR microscopy of the transverse wetting front in thin layers of paper coating pigments and coating formulations.



A supersource dynamic imbibition test was therefore carried out with a 1:1 blend of mineral oil (af 6/9, Table 11) and linseed oil to test the dynamic of absorption under mixed oil conditions. The absorption was followed using the same compressed block technique as for the preceding discussions. The sample used was No 35 with a porosity of 32.98% (see Table 12). No deviation of volume uptake from the "macroscopic square root of  $t$ " linearity was observed. This leads to the suggestion that the wetting front consists of one oil only, i.e. mineral oil, right from the measurable beginning of the experiment. This single oil delivers a constant driving force, and the effect of the viscous drag of the concentrating linseed oil far behind the wetting front is continually integrated with the increasing mineral oil separation, which is less viscous. This conclusion is fully in accordance with the miscibility of the two oils shown by Rousu *et al.*

As a conclusion, it is clear that chromatographic separation of the mutually miscible liquid phase components of an offset ink cannot be used to account for observed deviation from LW behaviour during initial setting as seen by tack build.

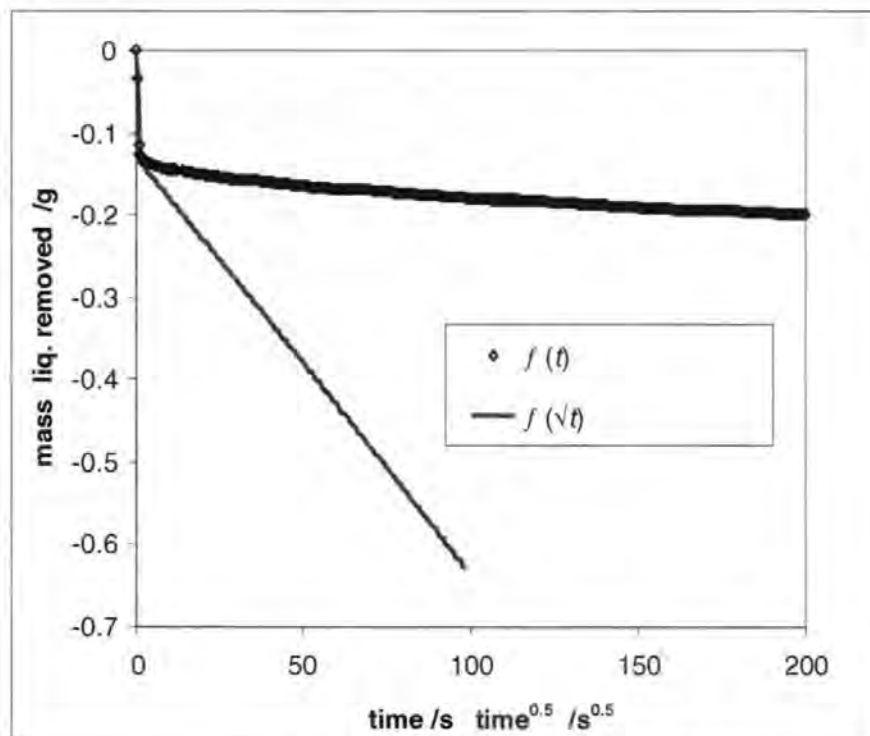


Fig. 112 Imbibition of a 1:1 blend of mineral oil af 6/9 and linseed oil. No deviation from  $\sqrt{t}$  linearity is observed, porosity = 32.98%.

## 9.6 Experimental imbibition of a polar liquid (Schoelkopf, Ridgway, *et al.* 2000)

The conclusions from the previous section showed the need for an algorithm more comprehensive than the LW equation for the capillary or pore-scale imbibition of a liquid. The Bosanquet equation was chosen because of its

historical priority in containing correctly an inertial term. The second goal, so far achieved, was to incorporate this equation into a computational simulator interconnecting capillary features to a 3-dimensional void network. The basic description of this work was briefly shown in chapter 4.

During the following experimentation, in-depth comparison is made with the network simulator results. To start with, 1,3-propandiol is used as the test liquid in order to adapt the experimental technique to the hygroscopic nature of the glycols. Tests showed that over a 16 hour period, due to the hygroscopic nature of the 1,3-propandiol, the balance recorded a weight increase of up to 0.6 g in the measurement cell containing the dish of liquid and a mounted 1.5 g sample block (not touching the liquid). The cause is ambient air leaking into the balance chamber. With silica gel in the chamber, the corresponding weight increase reduced to 0.2 g. Under nitrogen flowing at 1 litre per minute, there was a corresponding weight reduction of 0.003 g - the reduction being due to the absence of any hygroscopic effect, coupled with very slight evaporation, giving an overall weight change which was negligible on the scale of the experiment. The subsequent imbibition experiments with the polar fluids are performed under a steady stream of nitrogen flowing at 1 litre per minute in the balance chamber described above and all apparatus, gases and samples in this study were maintained at  $23.0 \pm 1.5^\circ\text{C}$ . Prior to the imbibition experiments, each sample was placed in a 5 litre ( $\text{dm}^3$ ) chamber. The chamber was then flushed through with dry nitrogen, and the sample left to equilibrate for 48 hours.

### 9.6.1.1 Sample structures

Porosimetry and simulated parameters of the experimental sample structures used in this section are given in Table 14.

sample no.	pigment	$\phi_{\text{Hg}}$ / %	$d_{\text{min}}$ / $\mu\text{m}$	$d_{\text{max}}$ / $\mu\text{m}$	$\psi$	$d_{50 \text{ exp}}$ / $\mu\text{m}$	$d_{50 \text{ sim}}$ / $\mu\text{m}$	used for liquid:
61	coarse	24.63	0.004	1.22	2.6	0.098	0.10	Propandiol
59	coarse	23.02	0.004	1.22	3.3	0.091	0.08	Butanetriol, Octanol, Propandiol
66	coarse	23.83	0.004	1.22	3.4	0.091	0.07	Butanediol, Ethanediol, Propandiol
67	coarse	23.35	0.004	1.22	3.4	0.091	0.07	Propandiol

Table 14 Overview of structures used for polar liquid imbibition. The porosities as given in the text allow for clear identification. For an extended version and explanations refer to Appendix A, Table A1.

## 9.7 Results, discussion and comparison to modelling

Fig. 113 shows the observed apparent weight of the liquid at the start of a typical experiment. The microbalance was tared so that the weight reading was close to zero, and the solid sample gradually lowered towards the liquid. At around 57.5 seconds, the apparent weight of the liquid is seen to decrease under the influence of the forces described previously. The experimental measurements occurred only every 0.4 seconds. The exact shape of the observed weight change curve at the start of the experiment was therefore unknown, but was likely to be approximately of the form shown as a solid curve on the graph, which estimates the lag and overshoot. A smoothing curve was fitted to all points at  $t > t_2$ , and extrapolated back in time to form the corrected line as shown by the dashed line with open data points. The time at which this extrapolation intersected the smoothed observed plot was assumed to be the moment internal wetting commenced,  $t = 0$ , shown as a vertical dashed line. The maximum estimated uncertainty in the estimate of the start time was  $\pm 0.2$  s as shown, and the imbibition curves corresponding to this maximum uncertainty are shown in Fig. 117. Experiments with four similar samples gave a repeatability as shown in Fig. 114.

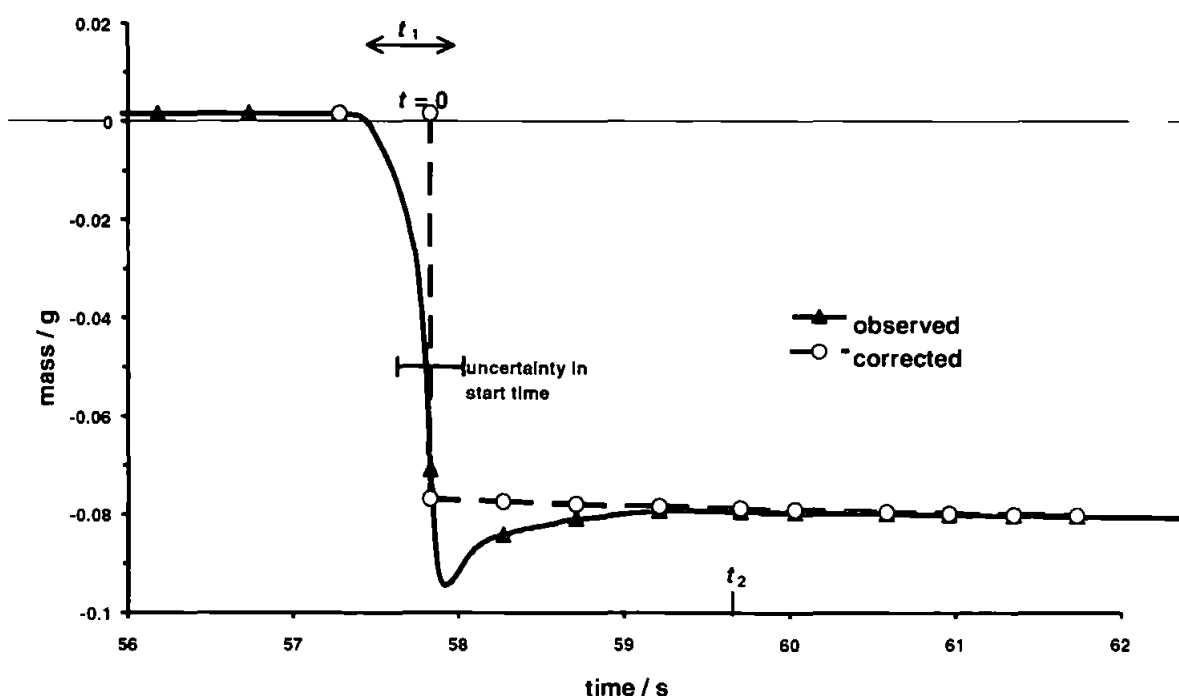


Fig. 113 Typical plot of observed and corrected mass change around the wetting jump.

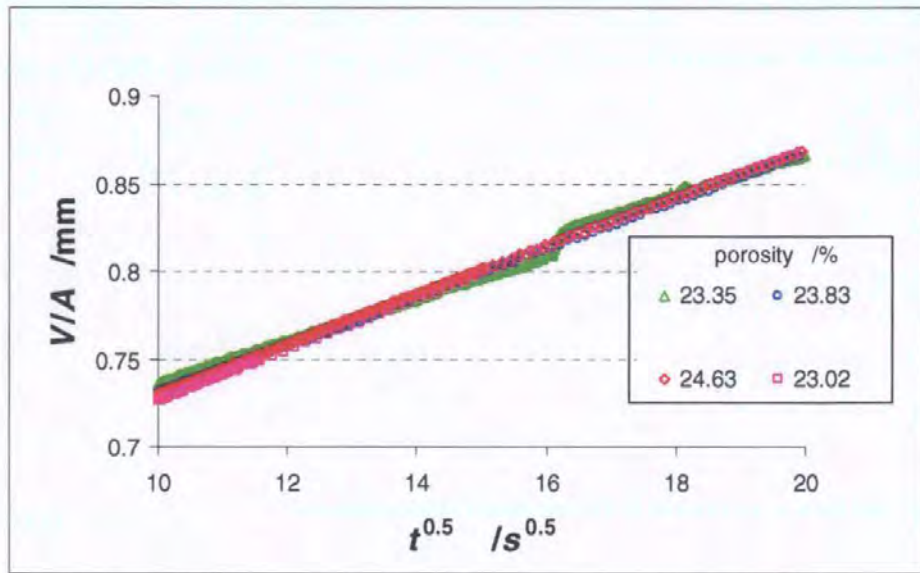


Fig. 114 Repeatability shown as gradients  $d(V/A)/d(\sqrt{t})$  for 1,3-propandiol for 4 similar samples.  $V/A$  is volume uptake per unit area of sample cross-section, (see Table 14 for sample details).

The lengths and radii of the throats in the first stochastic generation of the computer network simulator unit cell for structure 66 are shown in the top left of Fig. 53. Each of these features fills progressively as the computer network simulator time step increments, as exemplified by the dashed arrow. It can be seen that those features above  $0.2 \mu\text{m}$  radius will be initially in a region which is affected by inertial retardation. The largest features will have the filled distance reduced by around 30 % as shown in Fig. 53. From Eq. 29 it can be seen that the inertial term is directly dependent on the fluid density. Density does not affect other terms in the equation, and so the LW wetting part is unaffected by density changes. Therefore, another way of expressing the extent of inertial flow is to calculate the sensitivity of wetting to density, Fig. 118. Increasing the model fluid density from  $1\,053 \text{ kg m}^{-3}$  to  $10\,000 \text{ kg m}^{-3}$  reduces the Darcy length (Eq. 71) at 1 ns by 53 %, and at 10 ns by 21 %. Reducing the model liquid density from  $1\,053 \text{ kg m}^{-3}$  to  $100 \text{ kg m}^{-3}$  increases the Darcy length during the first nanosecond by 27 %, but by only 4 % at 10 ns. Above 10 ns, the wetting becomes insensitive to further reductions in density, which confirms that it follows the LW equation, as was also shown in Fig. 52. The imbibition does experience inertial effects above 10 ns because the liquid enters each new feature within the structure by inertial wetting. However the effects are masked by the greater imbibition volume occurring in a LW manner. This, however, does not mean that the liquid front is distributed according to LW criteria.

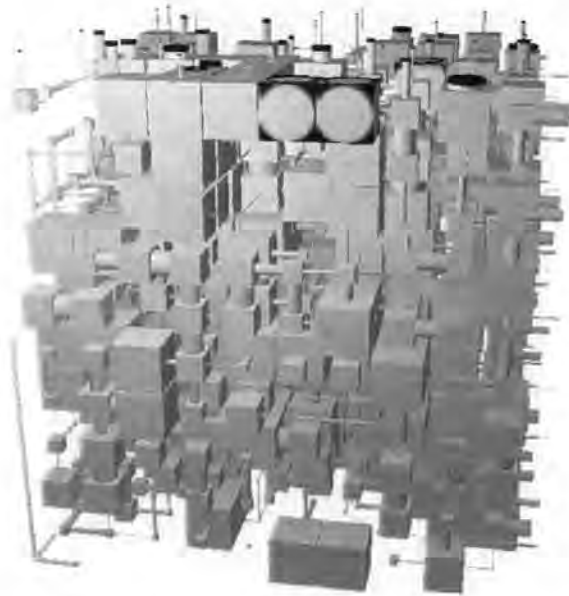
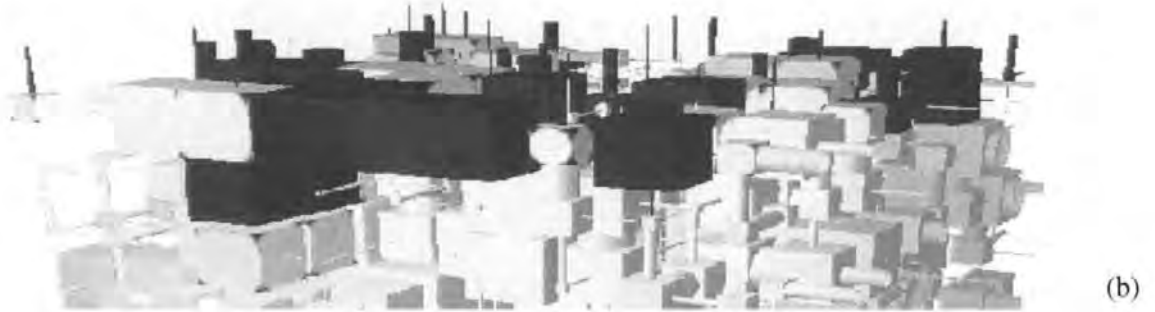
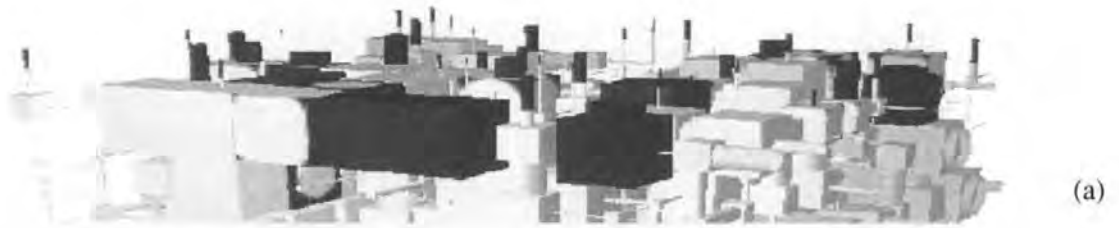


Fig. 115 The computer network simulator unit cell showing imbibition (dark shading) of 1,3-propanediol at 100 ns. Partial filling is shown by partial shading of the features, but this should not be interpreted as the absolute position of the fluid in such features, (sample 66).

Fig. 115 shows the imbibition of 1,3-propanediol, represented as dark shading, at a time of 100 ns. 1,3-propanediol, in the form of a model fluid, has been supplied from a supersource above the top surface of the diagram, and has wetted both the long narrow throats and the shortest wide throats. Inertial flow and the associated differential retardation has caused the fluid to enter the large pores slower than would be expected by the LW equation and favours the imbibition into the smaller throats. It can be seen that other, smaller vertical throats are only partially full. As time proceeds, the fluid in these smaller throats rapidly slows down as the viscosity of the fluid takes effect. Fig. 116(a) and Fig. 116(b) show the extent of wetting of the top of the unit cell at 10  $\mu$ s and 100  $\mu$ s, respectively. It can be seen that the fluid front advances very unevenly, and that by 100  $\mu$ s a large pore on the left of the diagram, which is near the surface but connected to it by only a narrow throat, is still empty and has been overtaken by the fluid (1,3-propanediol) further into the network of voids.

The imbibition was simulated for 0.1 seconds in total, which involved the calculation of all the wetting and mass balance equations for each of  $10^8$  timesteps. The entire curve is shown in Fig. 117. It can be seen that the imbibition of the first stochastic generation unit cell is not monotonic – it has two maxima in its first derivative. However, the second stochastic generation follows a different track with only one maximum, showing that the maxima are dependent on the variability of the structures of individual unit cells. The wetting between 0.01  $\mu$ s and 1  $\mu$ s is faster than predicted by the  $r_{ehc}$  (effective hydraulic radius) approximation described below, and has a  $t^{0.8}$  dependence rather than the  $\sqrt{t}$  dependence predicted by the  $r_{ehc}$  approximation based on the LW equation, Eq. 27.



*Fig. 116 Imbibition into the unit cell at (a) 10  $\mu$ s and (b) 100  $\mu$ s after fluid contact (sample 66).*

In order to compare the simulation with experiment, it was necessary to extrapolate it to the infinite time asymptote shown in Fig. 117. The extrapolation equation is given in Appendix B 1. The complete comparison with experiment, discussed below, under application of a sensitivity analysis, was insensitive to the exact form of this extrapolation.

### **9.7.1 Sensitivity analysis**

The sensitivity to uncertainties in experimental time measurement are shown in Fig. 117, 'shorter' and 'longer' referring to the boundaries of the uncertainty at 0.2 s. This level of uncertainty does not show on the graph at longer times, as it becomes negligible relative to the increasingly large total time.

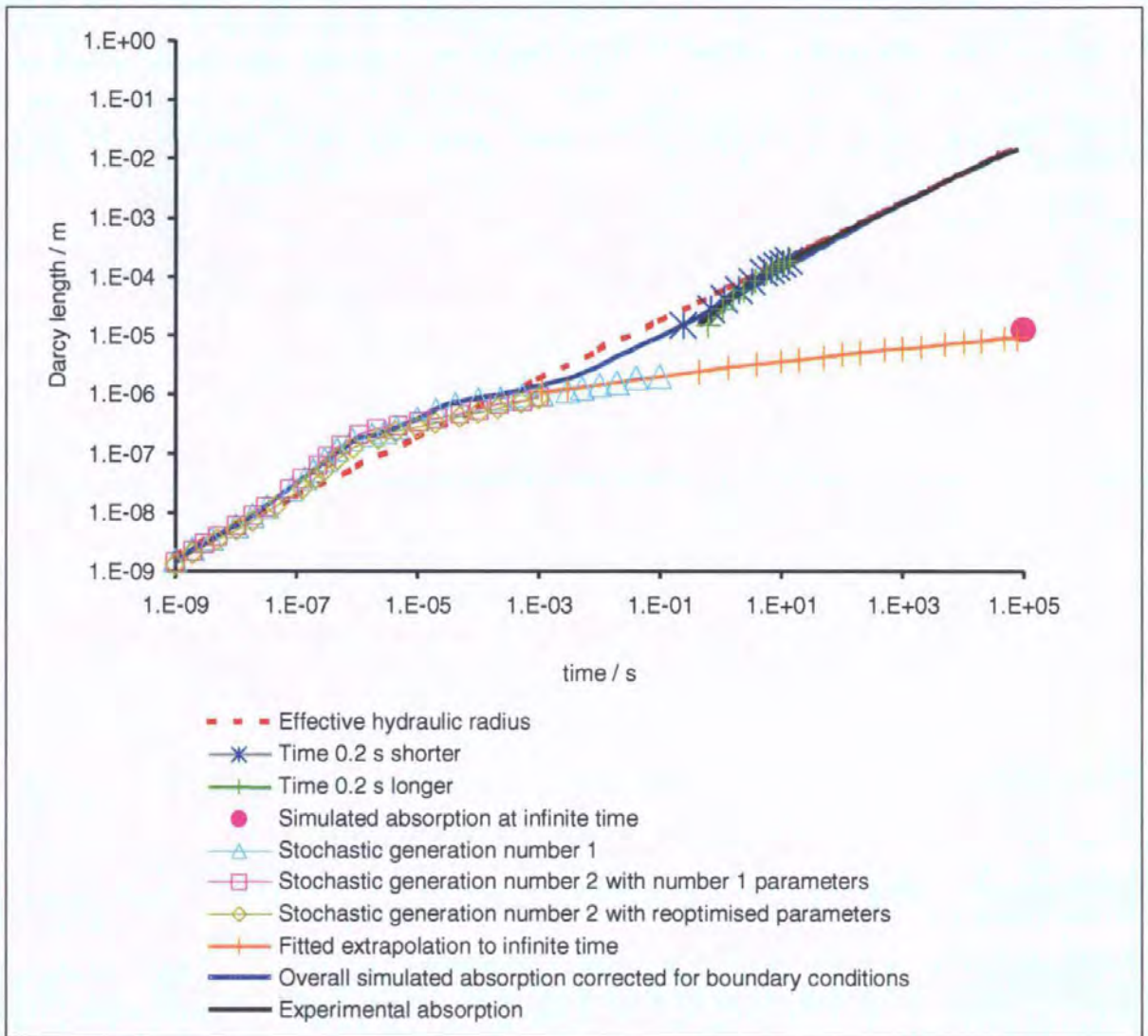


Fig. 117 Simulated (computer network simulator with cylindrical throats) and experimental imbibition expressed as Darcy length, together with sensitivity analysis as explained in the text (sample 66, see Table 14 for details).

With regard to simulated properties, Fig. 99 showed the modelled mercury intrusion curves resulting from various combinations of parameters from two different stochastic generations, (section 2.6.1.1) 'number 1' and 'number 2', of the simulated network. When the imbibition simulation was carried out using these different combinations, it yielded slightly different results, as shown in Fig. 117, but these uncertainties do not mask the overall trends. Fig. 118 shows the sensitivity of the simulated imbibition to liquid density, and hence inertial wetting effects. These are seen, as might be expected, to be most relevant in respect to absorption volume dynamic at the shortest times.

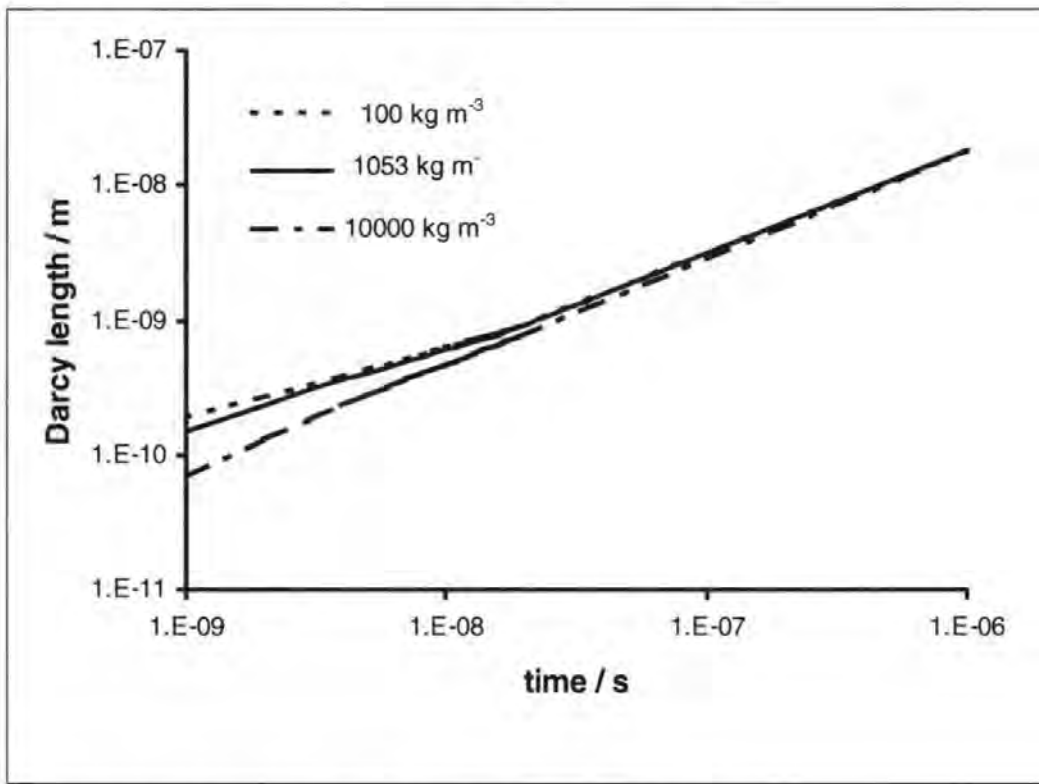


Fig. 118 Sensitivity of modelled absorption to change in liquid density.

### 9.7.2 Effective hydraulic radius ( $r_{ehc}$ ) approximation

The processes involved in the simulated and experimental imbibition are identical, in that both are concerned with uptake of the same fluid into a porous network. However, the time and length scales of the simulation are much smaller than those of the experiment. This does not invalidate the comparison, but it does mean that the simulated and experimental imbibition curves do not overlap when plotted graphically (Fig. 117). The boundary conditions for the simulation and experiment are also entirely different. The simplest way of overcoming this is to invoke the *ehc* approximation, using a radius  $r_{ehc}$  adjusted to mimic most closely the observed uptake. It follows directly from Eq. 27 that the slope of the imbibition, plotted using the logarithmic axes (Fig. 117), must be a straight line of gradient 0.5 with an intercept dependent on  $r_{ehc}$ ,  $\theta$  and  $\eta$ . The imbibition (Fig. 117) corresponds to an effective hydraulic radius  $r_{ehc}$  of  $0.01 \mu\text{m}$ , and both the simulated and experimental imbibition follow approximately this *ehc* imbibition curve. However, it can be seen from Fig. 53 that this radius is too small for inertial wetting delay effects to be relevant. Thus the *ehc* approximation loses information about both the effect of the three-dimensional void structure of the sample and any inertial flow within it.



### 9.7.3 Comparability of modelled and experimental processes

A potentially more informative, but more difficult approach, is to adjust the simulation such that its boundary conditions tend to the same asymptotes as the experiment at  $t = 0$  and  $t = \infty$ . The scales and boundary conditions can be most readily understood by reference to a schematic diagram, Fig. 119. The diagram shows the processes occurring, using circled numbers referred to in the text, and also the scale difference between the model and the sample, which is  $\sim 10 \times 10 \times 10 \mu\text{m}^3$  for the computer network simulator relative to  $\sim 10 \times 10 \times 10 \text{mm}^3$  for the experimental sample.

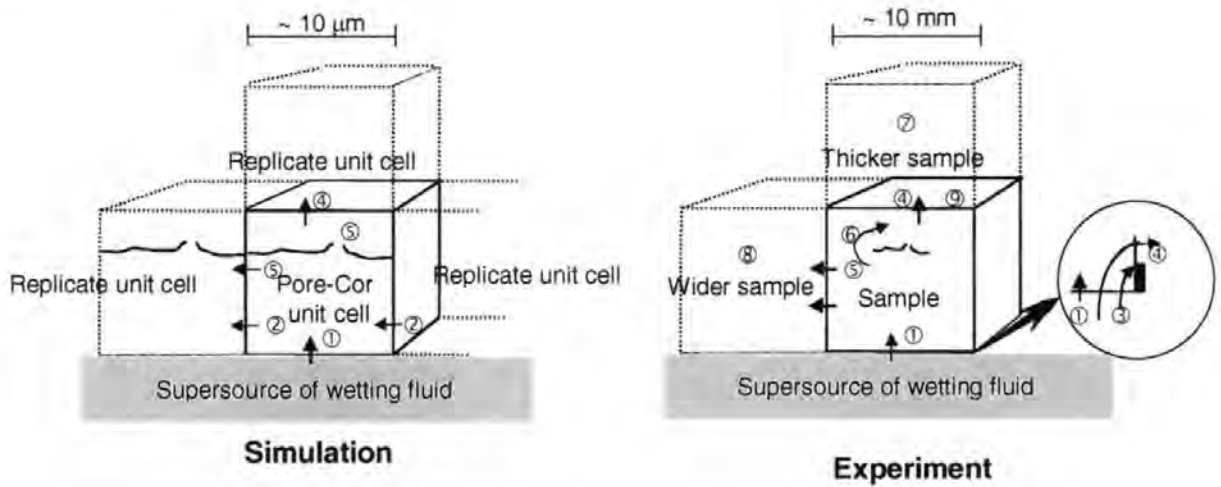


Fig. 119 Comparison of boundary condition of simulation and experiment.

Initially, both the simulated and experimental sample experience Bosanquet imbibition ①, which is inertially-influenced. The array of pores and throats in the simulation has been generated by the computer network simulator with the same percolation characteristics as the void structure of the experimental sample. Initially, therefore, the processes occurring in the simulation and experiment match each other closely. Soon, however, the boundary conditions of the simulation and the experiment diverge. After around  $1 \mu\text{s}$ , fluid has entered and filled the first array of pores within the simulated void structure, and can spread sideways. If the sideways throat is at the edge of the computer network simulator unit cell, then the flux periodic boundary condition causes it to enter the adjacent face of the replicate unit cell, i.e. the opposite face of the existing unit cell, and hence into the shown unit cell itself ②. Initially, this may not cause any restriction to flow, but if the void into which the fluid wishes to flow is full, the fluid will stop. This becomes more likely as the unit cell fills, and therefore incrementally the flux periodic boundary condition changes into an effectively periodic zero flow boundary condition imposed at the edges of the unit cell.

For the experimental sample, the situation after about  $1 \mu\text{s}$  is different. Most of the fluid will have no difficulty in moving sideways, due to the random nature of the structure, analogous to the initial freedom of sideways movement in the simulated structure allowed by the flux periodic boundary condition. Furthermore, since the wetting front is not uniform, due to the preferred pathway phenomenon, the likelihood of finding an adjacent empty pore is greater than would be expected from LW wetting, and this applies also in the case of the real sample. Small amounts of fluid will be blocked from sideways movement by the wax ring used to reduce the sample surface wetting force. After about 6 minutes, the fluid will reach the top of the wax ring, and can escape to the sample surface ④. Later, capillary forces on the fluid will cease as it reaches the top surface, and the fluid may creep down the side of the sample by gravity or enter further up the sample by preferential surface wetting.

Furthermore, as the fluid progresses through the computer network simulator unit cell, it may happen to find a geometric boundary across most of the unit cell ⑤. Under these circumstances, the replicate cells on all sides of the unit cell would also contain the replicates of the geometric boundary, and so the restriction would cause a severe hold-up. Any fluid passing through each replicated restriction would then provide the total supply of fluid for all the volume of each replicated unit cell beyond the barrier, thus also causing a major restriction in total flux. This situation contrasts with the situation in the experimental sample. A geometric restriction would be unlikely to form a barrier over the much larger array of throats and pores in the real sample, and the fluid could move round it and continue ⑥.

There is, thus, a series of major differences between the experimental sample, which can be regarded as an array of varying unit cells, and the simulated case of a replicated unit cell during the intermediate phase of imbibition.

Finally, one must consider the infinite time asymptote. For the computer network simulator, this corresponds to an entirely full unit cell. The Darcy length at the asymptote, therefore, depends on the size of the unit cell, which is in turn determined by the percolation characteristics of the sample. In the experimental sample, however, the infinite time limit is dependent on the sample thickness. Suppose a sample is used such that the internal wetting force  $F_{wi}$  is sufficient to wet the sample completely. Then, the experimentally observed wetting would be limited by the sample thickness, and if a thicker sample were to be used, the fluid would continue moving for longer ⑦. A wider sample ⑧ would not greatly alter the boundary conditions, but would simply make the edge effects less important since they are proportional to circumference over cross-sectioned area, and therefore decrease in importance linearly with sample diameter. Ultimately, the fluid reaches the top of the experimental sample ⑨, provided that  $F_{wi}$  is sufficient. When it does so, the capillary forces on the fluid cease and the fluid becomes only

subject to the ambient gravitational field. The fluid will then appear at the top surface of the sample, and develop a slight hydrostatic head which will progressively impede further flow of fluid out of the sample. The absence of capillary forces and imposition of the hydrostatic head retardation cause a sharp flux boundary at the sample surface. So, the question arises as to how to match the boundary conditions of the simulation and experiment for long times,  $t$ . Increasing the size of the computer network simulator unit cell is beyond current computational capability. One must therefore apply a scaling function,  $F$ , to the computer network simulator to upscale the Darcy lengths to those of the experimental sample. Some characteristics of this function follow directly from the discussion above. It must approach unity with zero gradient as  $t \rightarrow 0$ , and approach with zero gradient towards the ratio,  $F_\infty$ , of the extrapolated values of the simulation and experiment as  $t \rightarrow \infty$ . It must also begin to increase significantly from 1 at  $t \approx 1 \mu\text{s}$ . Inspection of Fig. 117 shows that the computer network simulator unit cell would still not have reached full saturation by an equivalent experimental time of 100 000 seconds. However, by this time, it would be very significantly full, and so the scaling function should have reached a significant fraction of the final asymptotic value. A polynomial in  $t$  and  $\ln(t)$  was found to have the correct characteristics, and is given in Appendix B 1. The resulting corrected curve is shown as the orange line in Fig. 117.

#### **9.7.4 Comparison between both the simulated and experimental imbibition, and the effective hydraulic radius prediction.**

It can be seen in Fig. 117 that all the simulated imbibition curves show wetting greater than that which would be expected according to the *ehc* approximation ( $r_{ehc} = 0.01 \mu\text{m}$ ) up to 0.1 ms. The fluid imbibition is not monotonic, but has various maxima in its first derivative, dependent on the stochastic computer network simulator generation. Above this time, both the simulated and experimental imbibition are less than that predicted by the *ehc* approximation.

Wetting would be expected to be slowed down by inertial flow, not speeded up. However, the computer network simulation predicted that the wetting occurred through many pathways into the unit cell, which could overtake some large voids, and therefore apparently wet more efficiently than predicted by a single, effective hydraulic stream tube. This, as we saw earlier, reproduces exactly the effect that was observed experimentally from droplet absorption tests.

### 9.7.5 Intermediate conclusions

The imbibition of the wetting fluid 1,3-propanediol into the computer network simulator model void structure has been simulated by repeated application of the Bosanquet equation and mass conservation requirements at intervals of 1 ns. Slight maxima in the slopes of the simulated imbibition curves appeared due to the structural features of the individual unit cells. The imbibition of all stochastic generations was greater than that expected by the *ehc* approximation ( $r_{ehc} = 0.01 \mu\text{m}$ ) at times up to 0.1 ms.

Fig. 116(a) and Fig. 116(b) revealed that the wetting occurred through many pathways into the unit cell. (This issue will be shown later in a more pronounced way). By following these pathways, the fluid could overtake some large voids, and therefore imbibe more efficiently than predicted by a single, effective hydraulic capillary. Above 0.1 ms, both the simulated and experimental imbibition was lower than predicted by the *ehc* approximation.

It has been demonstrated that inertial wetting decreases the Darcy length, i.e. the distance of travel of the wetting front assuming all pores within the porosity definition are filled, by 27 % at 1 ns, decreasing to 4 % at 10 ns. This leads to the observation that the actual position of the wetting front in a porous network does not relate consistently to the conceptual Darcy length. It was shown how the inertial effects can be explained in terms of the structure of a particular material being situated within the zone of inertial wetting behaviour. The  $\text{CaCO}_3$  sample used in the present study was on the threshold of this zone, and the effect in the *ehc* disappeared within 10 ns. However, this timescale and related fluid volume uptake can act to differentiate pores of contrasting size, especially in the case of denser fluids in wider and longer features which would show greater effects of inertially delayed wetting. Although inertial wetting delay slowed down the uptake of fluid in the first nanosecond into surface features of the structure, overall there was an increase in wetting up to 0.1 ms due to the connectivity of the void network, which increased the efficiency of the wetting above that predicted by the LW equation.

In all models or wetting equations that consider single (or bundles of) capillary(ies), the inertial delay acts only to slow volume imbibition. However, a sequence of linear  $t$  inertial short timescale wetting occurring within a network of pores of optimally-related aspect ratio, while the filling of larger pores remains delayed, results in a faster imbibition than would occur in a network of pores of non optimally-related aspect-ratios. This is the key to the original question which we may now modify slightly to: "Why does a paper coating consisting of low aspect-ratio pores absorb a liquid faster than a coating with large pores?" This shows the importance of considering a network rather than a bundle of capillaries and demonstrates the departure between the actual wetting front position and either a conceptual Darcy length or that predicted by an *ehc* obeying only LW absorption.

## 9.8 Experimental imbibition of different polar liquids (Ridgway, Schoelkopf, et al. 2001)

In this next step, different polar liquids related to the previously used 1,3-propanediol are involved. These are several alcohols which are found as components of waterborne inks, namely ethanediol, 1,3-butanediol, 1,2,4-butanetriol and 1-octanol (Fluka, research grade). The properties of these fluids are shown previously in Table 11. These experiments are used to compare experiment with extended computer network simulator models adopting a range of throat geometries. Water was used for simulation purposes only, because it was found that when used experimentally together with the carbonate tablets (without added binder) in some cases, it caused the samples to disintegrate.

The three porous  $\text{CaCO}_3$  tablet samples used in this section, namely samples 59, 61, 66, are described in Table 14. The porosities were chosen to be as similar to each other as could be achieved experimentally. So although the separate samples are identified in this work, for purposes of discussion they are considered equivalent.

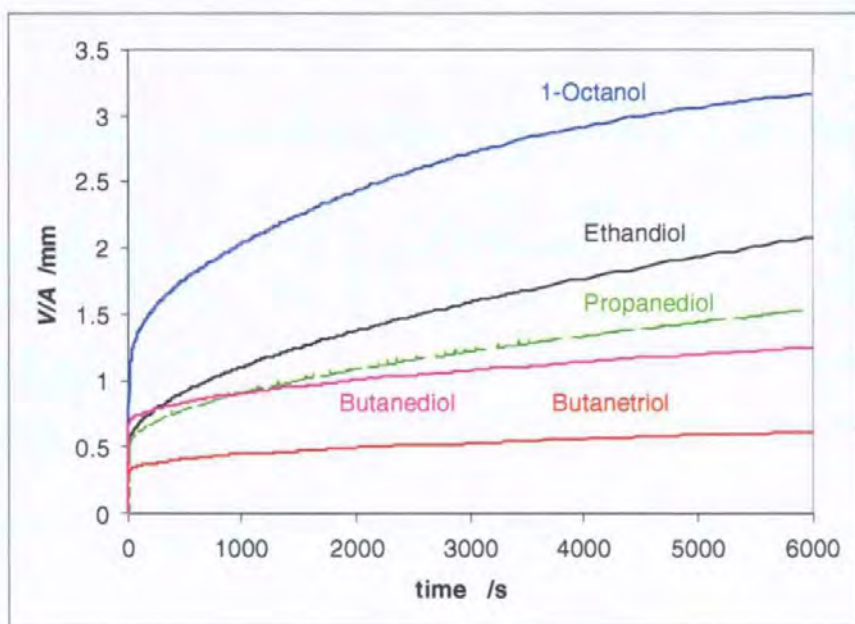


Fig. 120 Original experimental imbibition curves shown as volume uptake per unit cross-sectional area. At  $t = 0$ , note the wetting jump, (see Table 14 for details).

The experimental observations, obtained using the methodology of supersource imbibition described in section 9.3, are shown in Fig. 120, Fig. 121 and Fig. 122.

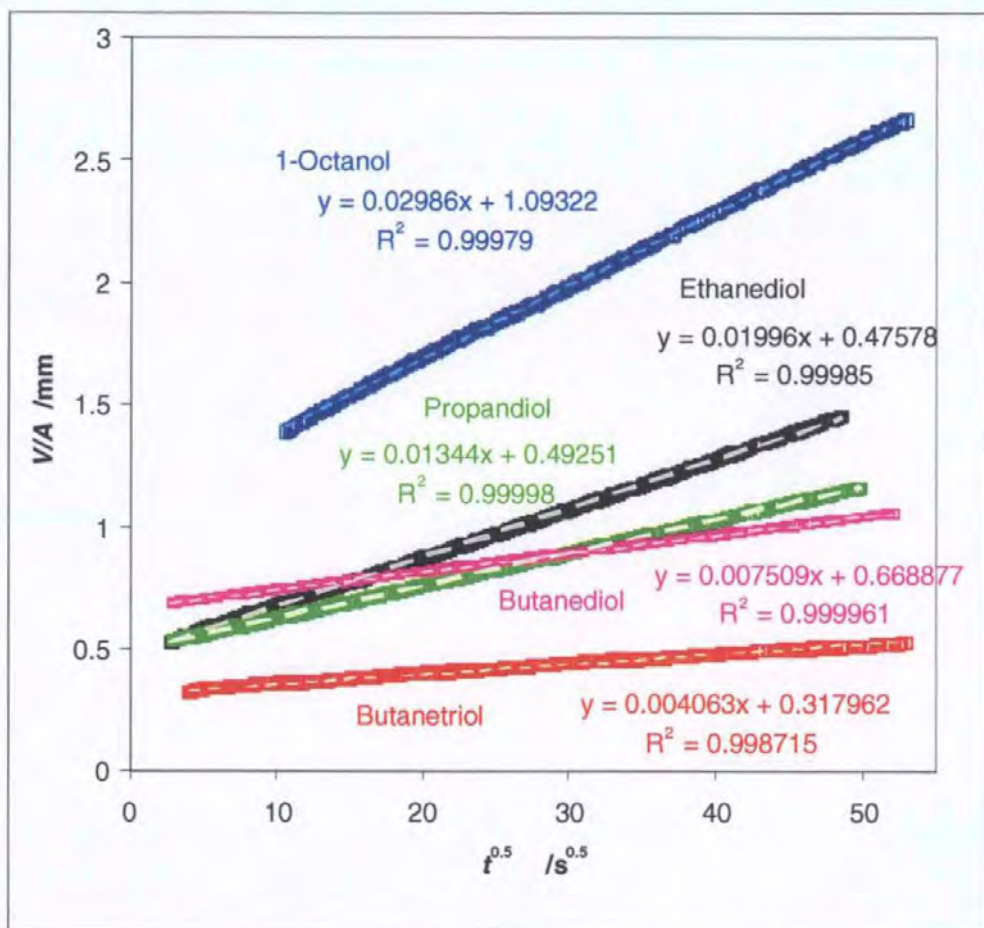


Fig. 121 Uptake curves plotted as a function of the square root of time and determinations of gradients as  $d(V/A)/d(\sqrt{t})$ , (see Table 14 for sample details).

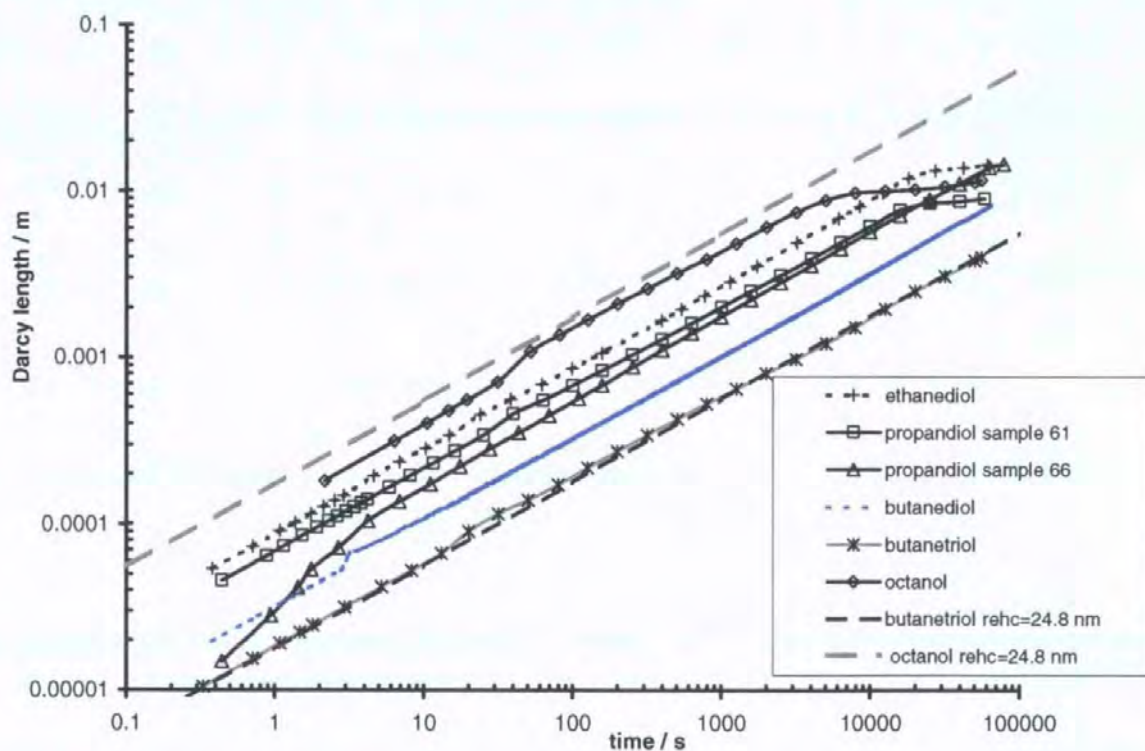


Fig. 122 Experimental absorption curves shown in comparison with  $r_{chc}$ , (see Table 14 for sample details).

exemplified by Fig. 127. They also mask the inertial effects which occur in each feature, and which make the wetting of larger features by denser liquids slower than expected, and the wetting via smaller features faster than would be expected based on viscous drag alone. Overall, the fluids, behaving inertially, will wet via preferential pathways, which are well-connected throughout the structure, and which follow tracks containing smaller features than would be predicted by Lucas-Washburn.

#### **9.8.1.2 Summary of simulation and comparison**

The geometry of the computer network simulator unit cell structure has been modified to represent more realistic void shapes within a porous material, in this case compacted  $\text{CaCO}_3$  powder. The shapes of the throats have been changed from cylindrical tubes to a double-conical shape incorporating a diverging and then converging geometry. In effecting this change one is clearly replacing one arbitrary parameter (pore skew) with another (conicality). However, the resulting structure assigns additional porosity in a manner which more closely resembles the void structures of particulate samples (Toivakka and Nyfors, 2000). It also incorporates an additional degree of heterogeneity within the sample, which again is a step closer to reality. This heterogeneity is in the form of geometric variations, which cause hold-up of not completely wetting fluids and differential acceleration and deceleration of fluids generally. Such effects could also be caused in reality by different surface interaction energies, and the increased heterogeneity in the simulated geometry can also be regarded as a representation of the heterogeneity of surface interactions within a real sample, i.e. geometry and surface interaction energy both affect the Laplace pressure by the contact boundary condition and so can be modelled interchangeably.

The effect of the change in throat shape has been shown for both wetting and non-wetting fluids. The structure of the unit cell was optimised so that its intruded porosity was identical with the experimental sample, so that the simulated non-wetting fluid (mercury) intrusion curve matched the experimental curve as closely as possible. Absorptions into this structure showed deviations from both the simulated and the experimentally derived *ehc* approximation as a function of time. The absorption rates of five alcohols were measured and the computational simulated network absorption curves were then compared to these. The beginnings of the simulation curves have similar gradients to the experimental curves and track in the same order for increasing viscosity. Plotting the results relative to the *ehc* approximation highlights the trends, and shows how the advancement of the wetting front, expressed as a Darcy length, differs very significantly from that which would occur in a single tube or bundle of tubes. Overall, the effect of inertia is to cause fluids to wet via preferential pathways, which follow

well-connected tracks containing smaller features than would be predicted by Lucas-Washburn. These effects show up on the very short timescales of the simulation, and are of great importance in industrial processes such as printing which involve fast absorption in initially short contact times.

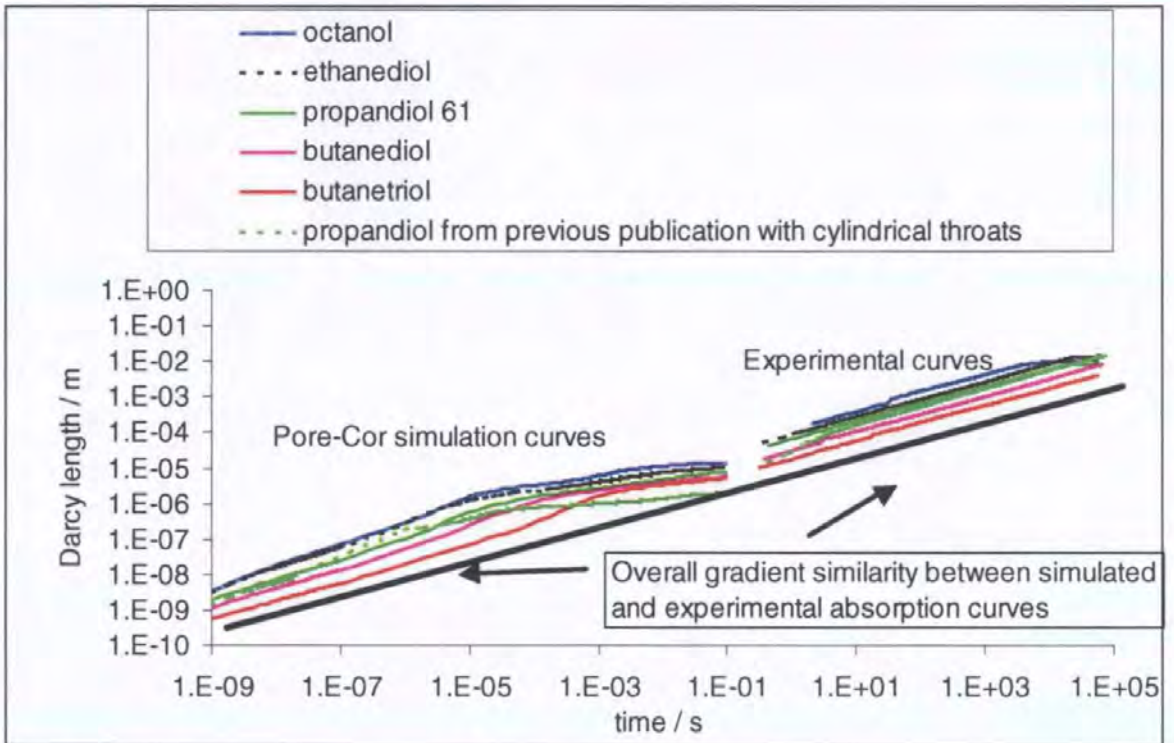


Fig. 128 Overview of experimental and simulated uptake curves (conical throats, if not otherwise indicated) for a range of different polar liquids, (see Table 14 for sample details).

### 9.9 Application to previous experiments with apolar oil

With the experimental method alone, no knowledge can be gained directly about the very initial regime of uptake due to the required equilibration of the contact forces and experimental resolution over this timescale. This, however, is the speciality of the absorption algorithm in the network simulator. As previously discussed, the size of the network simulator unit cell and the computer processing time still limit direct comparison with longer term experimentation. In the earlier analysis (section 9.7.3) a scaling function was used to extrapolate the initial regime of simulated imbibition of the unit cell where the slope of the uptake curve matches experimental data. During the later stages of the absorption simulations, the boundary conditions of the unit cell (size limitations) cause a delay of liquid imbibition. In Fig. 129, simulated absorption gradients of the Darcy length  $dx/d\sqrt{t}$  between 5.29 ns and 18.5 ns are chosen to compare with the experimental gradients and there is a good agreement between simulation and experimentation. Indeed it is astonishing that the mercury intrusion-based network model, including the Bosanquet absorption algorithm, reproduces many details of the curve-shape of the experimental absorption data-based slopes.



## 9.11 Conclusions from dynamic supersource imbibition

Summarising these and previous experimental findings, we observe for all involved liquids and structures macroscopically the behaviour as expressed in Eq. 26 ( $x^2 = kt$ ). Two cases were analysed, namely:

(a) similar structure, different liquids, i, where

$$x_i^2 = k_i t \quad \text{Eq. 79}$$

As  $\gamma_i$ ,  $\cos \theta_i$  and  $\eta_i$  have been measured independently, we can write:

$$k_i \propto \frac{\gamma_i \cos \theta_i}{2\eta_i} \quad \text{Eq. 80}$$

or

$$k_i = r_{\text{ehc}} \frac{\gamma_i \cos \theta_i}{2\eta_i} \quad \text{Eq. 81}$$

and

b) different structures, j, same liquid, where

$$x_j^2 = k_j t \quad \text{Eq. 82}$$

but now

$$k_j \neq r_j \frac{\gamma_i \cos \theta_i}{2\eta_i} \quad \text{Eq. 83}$$

i.e.

$$x_j \not\propto r_j \quad \text{Eq. 84}$$

We now have for all j a changing function of  $r_j$ . Therefore, changing structure introduces the failure to scale to LW. In this work this effect was shown for well-identified structures with similarity. The similarity is in respect to network features, connectivity and geometry, the surface chemistry being constant throughout.

Even greater divergence from LW scaling is to be expected comparing two structures with the same  $r_{50}$ , but different pore morphology. This study has not been made specifically here but forms part of the work of Bodurtha, (Bodurtha *et al.*, 2001).

The argument above now enables the questions put in the beginning of the chapter to be answered as follows:

- Yes, imbibition follows macroscopically a  $\sqrt{t}$  relationship over a range of porous structures, all having the same surface chemistry and pore morphology.
- No, the parameters in the LW equation do not hold true across the range of porosities. The radius used in the LW equation is not a realistic physical parameter for porous structures.
- An influence of inertia was not explicitly identifiable by the means of involving different liquid properties, but was identified by using different structures with different pore size distributions comparing their properties of permeation and imbibition.

The main implication of these findings is that manipulation of the pore structure is a flexible, and therefore convenient tool to steer imbibition processes outside the simplistic dependence on pore size. The study has shown that this structure manipulation is more effective than changing liquid properties. Liquid properties are generally connected with other physical properties. For example a decrease in viscosity is normally associated with an increase in volatility. To raise the liquid density would require, for example, compounds with halogen atoms within the molecule. The limitations for changes in fluid and surface energy properties are dictated by process usability, toxicity and industrial pricing. Additionally, the range to play experimentally with these properties covers only a few decades.

In contrast to the abovementioned experimental limitations in respect to practical surface energy and liquid properties, in the case of the pore structure design we have the possibilities ranging from the adoption of nano particles up to macroscopic sizes, covering an array of particles over 5 orders of magnitude influencing the effective  $r_{chc}$  of the structures. Furthermore, the possibility is given in paper coating of involving different geometries using platy, blocky or needle-shaped particles and a combination of these by controlled costructuring or agglomeration (Gane *et al.*, 1999).

### 9.8.1 Comparing cylindrical and convergent computer network simulator throat geometries with experiment

The experimental results in Fig. 120 and Fig. 121 provide the observed absorption data. In Fig. 122 the experimental absorption measurements have been corrected for the 'wetting force' jump of the liquid up onto the bottom surface of the sample. Appendix B 2 details the equations used for this correction, which involves an extrapolation of the apparent weight curve to time zero while ignoring the first few experimental points involved in the wetting jump. Although this extrapolation incorporates corrections for oscillations caused by the inertia of the meniscus as it jumped, there remained uncertainties in the exact start time of the experiment, estimated at  $\pm 0.2$  s, because of these effects. The experimental points up to 1 s were therefore considered to be of poor accuracy with respect to time. It is this uncertainty that is considered a major cause of the difference between the experimental absorption curves for 1,3-propanediol in samples 61 and 66, Fig. 122.

#### 9.8.1.1 Comparison between simulations and experiment

We begin by studying the absorption curves derived from the cylindrical model of the network simulator. Unfortunately but unavoidably, the experimental measurements are over a much longer timescale than the simulated absorption, and do not overlap the simulated values with respect to time. They also have different boundary conditions, as previously discussed. However, it can be seen that the initial rates of the simulated absorption exhibit a correspondence with the overall rates of the experimental absorption. The trends with different fluids are also similar between simulation and experiment. Fig. 122 and Fig. 123.

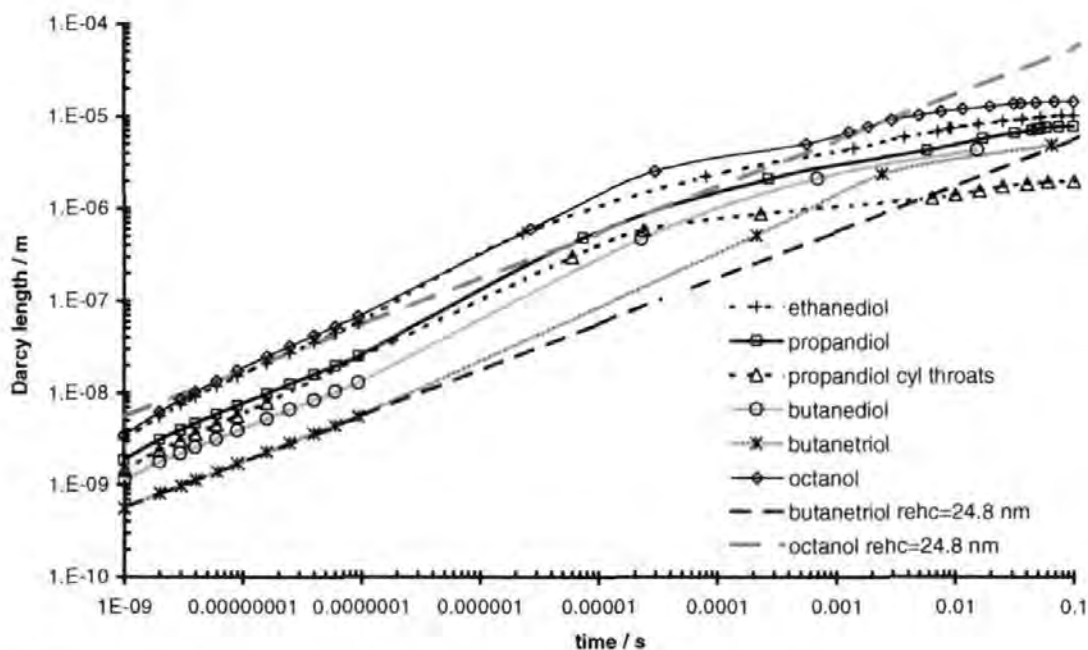


Fig. 123 Simulated absorption curves, (see Table 14 for sample details).

These previous computer networks simulations based on cylindrical throats are now used for comparison with the developed model of double-conical throats, as displayed here. It can be seen that there is less discrepancy between the simulated and experimental values in the case where double-conical throats are used in the simulator model, i.e. in the current simulations as clearly shown in Fig. 124, and discussed in more detail below.

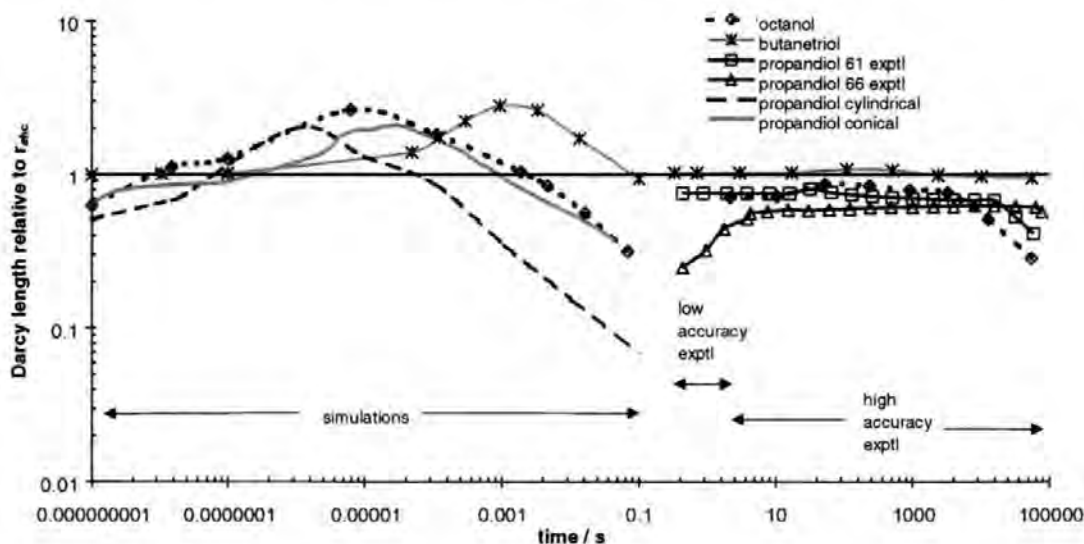


Fig. 124 Imbibition relative to the  $r_{ehc}$  approximation for octanol and butanetriol with  $r_{ehc} = 24.8$  nm, (see Table 14 for sample details).

Fig. 122 and Fig. 123 also show the absorption of octanol and butanetriol predicted by the *ehc* approximation with its radius  $r_{ehc}$ . An effective hydraulic radius  $r_{ehc}$  of 24.8 nm gives curves closest to those observed. Fig. 125 shows that the corresponding capillary diameter ( $= 2 r_{ehc}$ ) of 49.6 nm lies just below the geometric mean of the pore diameter size distributions, 65.9 nm, of the simulated voids.

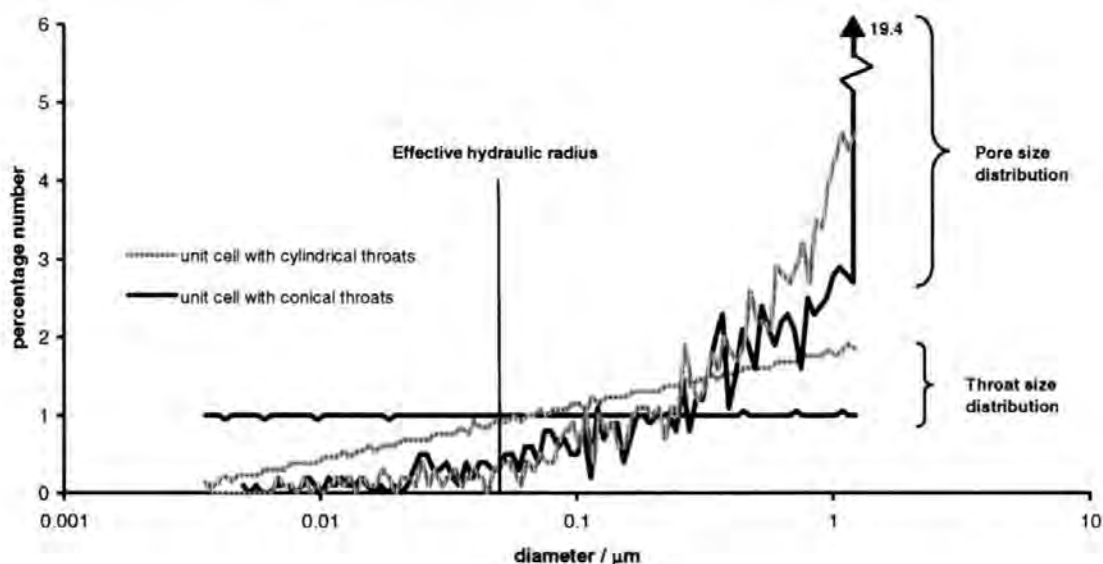


Fig. 125 Size distributions of pores and throats for the cylindrical throat computer network simulator structure and the conical throat structure, each for sample 61.

In Fig. 124, The *ehc* curves are plotted artificially as a horizontal straight line of value 1 and the effective deviations from the *ehc* line of both the simulated and experimental absorption of octanol and butanetriol are shown by plotting their absorption lines relative to this *ehc* standard. The data are simply another presentation of those already shown in Fig. 122 and Fig. 123.

It can also be seen in Fig. 124, that the simulated absorption at around 1 ms of butanetriol is nearly twice that expected from the *ehc* approximation. The simulated 1-octanol absorption varies between 0.6 and 1.9 times that of the *ehc* absorption. Fig. 126 and Fig. 127 show the simulated absorption of butanetriol (shown dark) into the unit cell for sample 59, both for 200  $\mu\text{s}$  and also for 8 ms - either side of the maximum in the absorption rate. It can be seen from the diagrams that the imbibition begins to slow down when lateral movement of fluid is restricted. At 200  $\mu\text{s}$ , the fluid has entered most of the top surface conical throats, and one or two pores connected to them, Fig. 126.

At 8 ms, the possibilities of lateral movement near the top of the unit cell have been exhausted, and lateral movement from one unit cell to its identical neighbours is also prevented, because the neighbours are also identically full, Fig. 127. The regions over which the simulated curves begin to show reduced absorption in Fig. 123, emphasised in Fig. 124, mark the times at which the periodic boundary condition begins to affect the absorption.

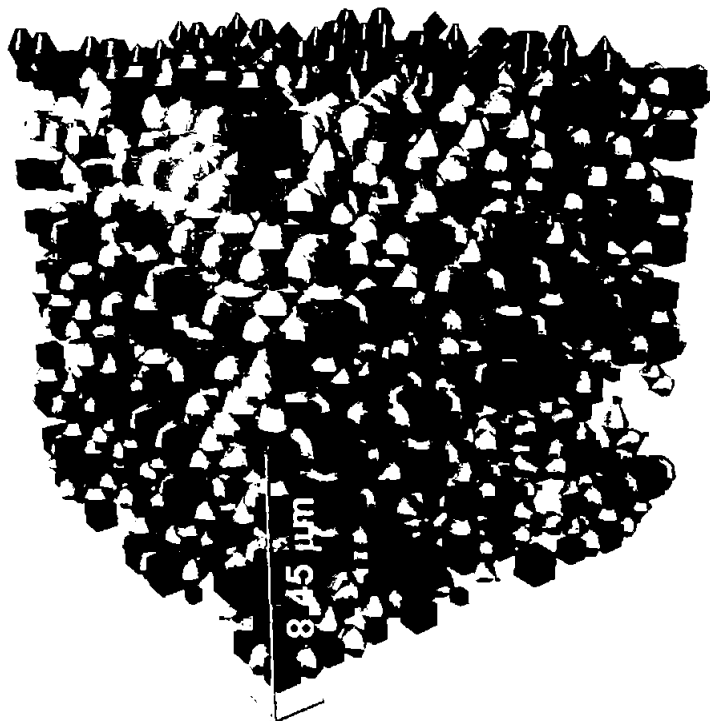


Fig. 126 *Imbibition of butanetriol, shown as dark shading, from top face of the unit cell for sample 59 at  $t = 200 \mu\text{s}$ .*

The longer time experimental curves shown in Fig. 122 and Fig. 124, demonstrated that butanetriol follows an *ehc* type of absorption, whereas 1-octanol absorbs considerably less than predicted by the *ehc* approximation at times greater than 1 000 s. The difference in behaviour arises from the difference in properties of butanetriol and octanol, the former being 100 times more viscous and 43 % denser (Table 11).

Comparing the experimental and simulated results for each alcohol shown in Fig. 124, we can conclude once again the practical value of the model when considering rapid absorption phenomena. Firstly that experimental measurements of butanetriol absorption suggest *ehc*-type absorption, whereas the simulation using the network shows much greater absorption around 1 ms than would be inferred from this experimental *ehc* behaviour. Secondly, the simulated network absorption of the less viscous and less dense 1-octanol shows positive deviations from *ehc* at much shorter times than butanetriol, which again could not be inferred from the experimental results which show initial *ehc* behaviour followed by a reduction relative to the  $r_{ehc}$ .

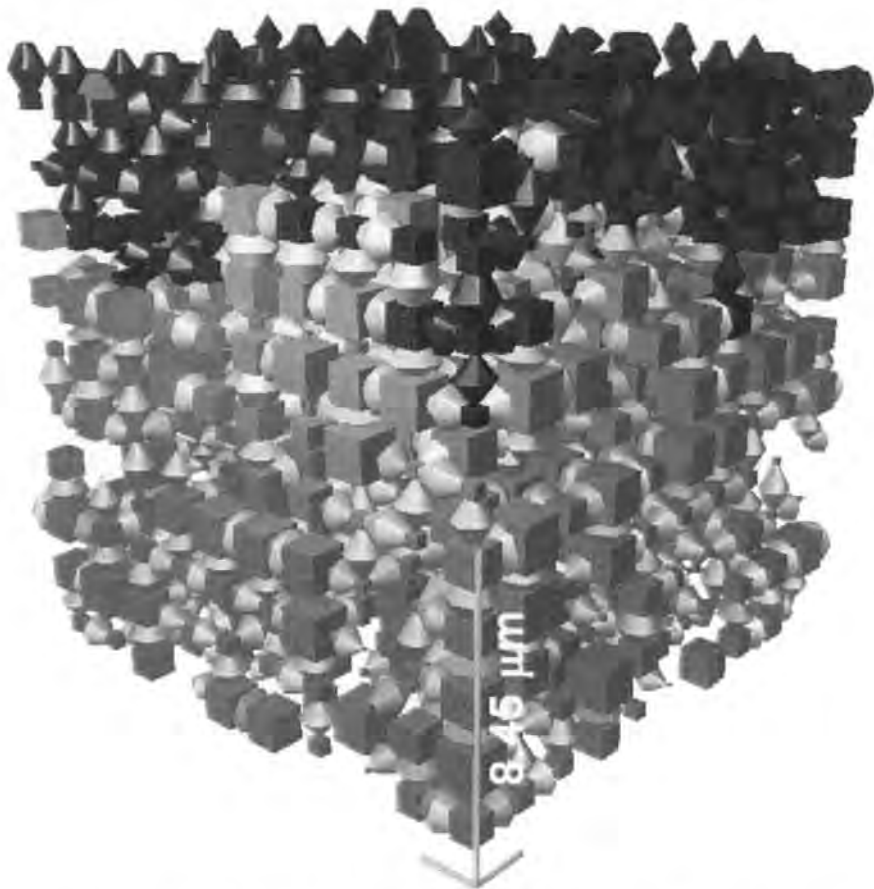


Fig. 127 The same as described in the legend to Fig. 126 but now at 8 ms after contact.

What must also be remembered is that the Darcy lengths shown in Fig. 124, are volume-averaged positions of the wetting front assuming complete filling of the available porosity. These averages mask the development of preferential pathways through the void structure, which lead to highly heterogeneous wetting fronts, as

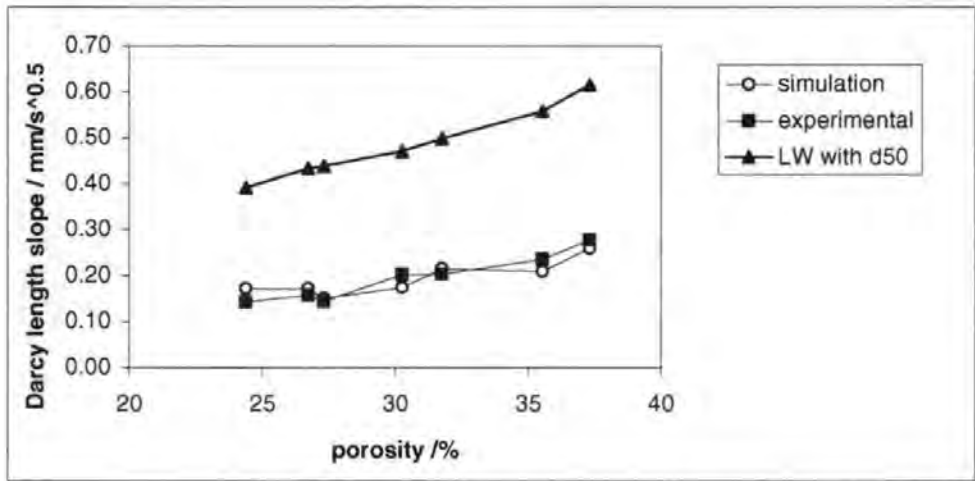


Fig. 129 Comparison of slopes  $dx/d\sqrt{t}$  show at some points a very good agreement between the absorption simulation in the porosimetry data-based structure and the experimental slopes of exactly the same structures. For comparison, included is the LW prediction from Fig. 105(b) based on  $r_c = d_{50}$ .

### 9.10 Overall comparison of hydraulic radii "ehc" and uptake gradients

Here we have an opportunity to review all the collected data generated so far for supersource imbibition. To make comparison, the data are arranged into a set relating to samples with similar porosity, (see Table 14 for details of the structures and Table 12, structure 74 for the oil datum point). The  $d_{50}$  diameters of these structures are also similar,  $0.093 \pm 0.004 \mu\text{m}$ . The liquid parameters were presented in Fig. 100.

The aim is to find an expression where the experimental gradients  $d(V/A)/d(\sqrt{t})$  of all the liquid imbibition experiments at constant porosity and pore size distribution can be plotted as a macroscopic property average function. It is found that the experimental gradients  $d(V/A)/d(\sqrt{t})$  in relation to the "effective" LW parameters reflect the first derivative of the LW equation with respect to square root of  $t$ , Eq. 78 ,

$$\frac{dx}{d\sqrt{t}} = \sqrt{\frac{r\gamma \cos \theta}{2\eta}}$$

Eq. 78

and show such a property averaging effect, as plotted in Fig. 130 with a constant "structure property" gradient ( $\sqrt{r}$ ).

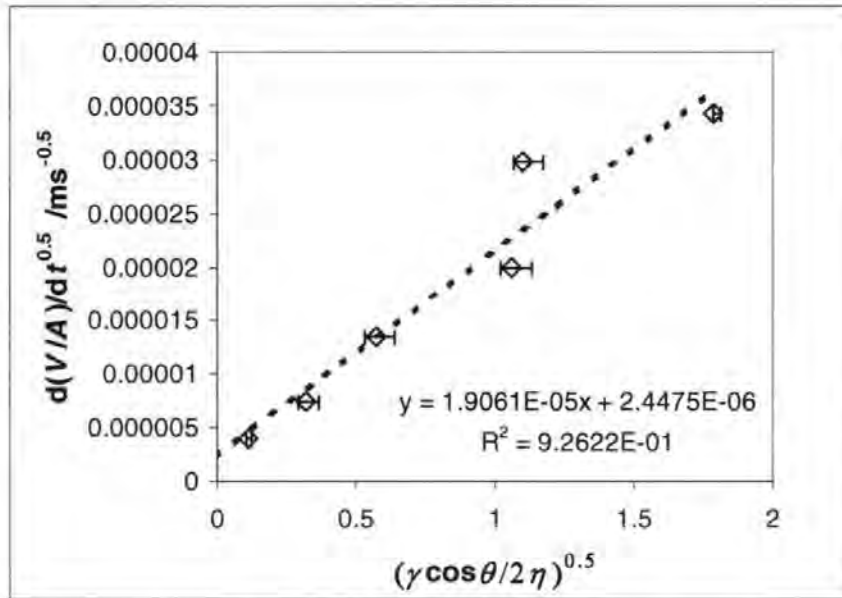


Fig. 130 Uptake gradients as a function of LW parameters. Points from left to right; butanetriol, butanediol, propandiol, ethanediol, octanol, mineral oil af 6-9. The error bars indicate the influence of  $\theta \pm 15^\circ$ .

The fact that the fitted line is linear means that all the fluids have seen the structure in the same way, i.e. the pore radius is a constant and confirms what we saw before. Porosity was previously shown to be a major controlling factor and by keeping the porosity constant one obtains constant parameters for the structure and the surface interactions.

Now we consider data from the various porosities. Fig. 131 shows the relationship between porosity and  $d_{50}$  diameter, both as measured by Hg-intrusion. The good correlation allows us to consider the relations in Fig. 132 between the various observed and derived radii and porosity.

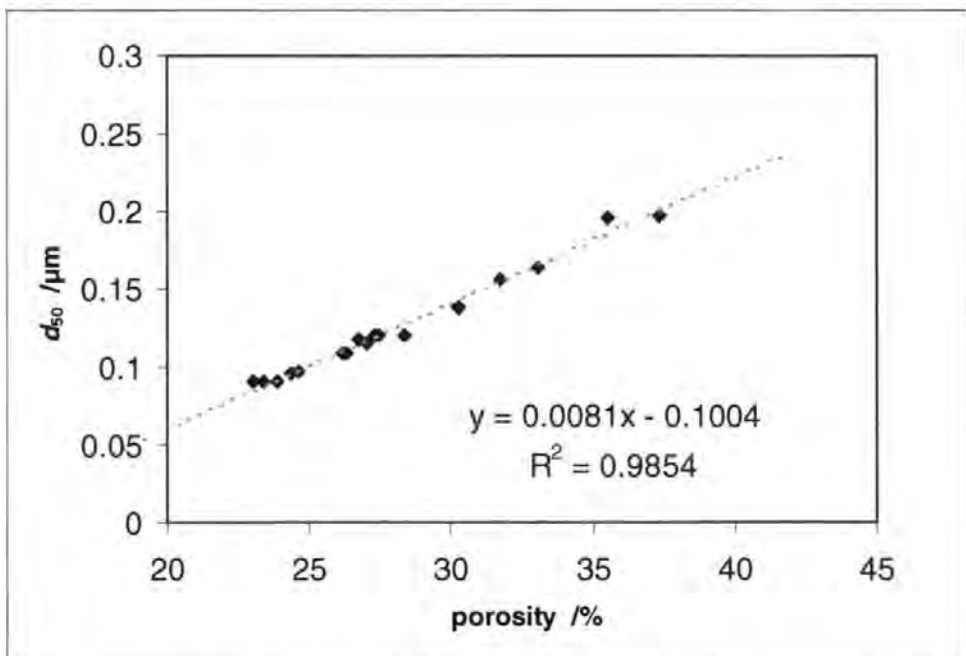


Fig. 131 The  $d_{50}$  diameters of all structures used, plotted as a function of structure porosity.



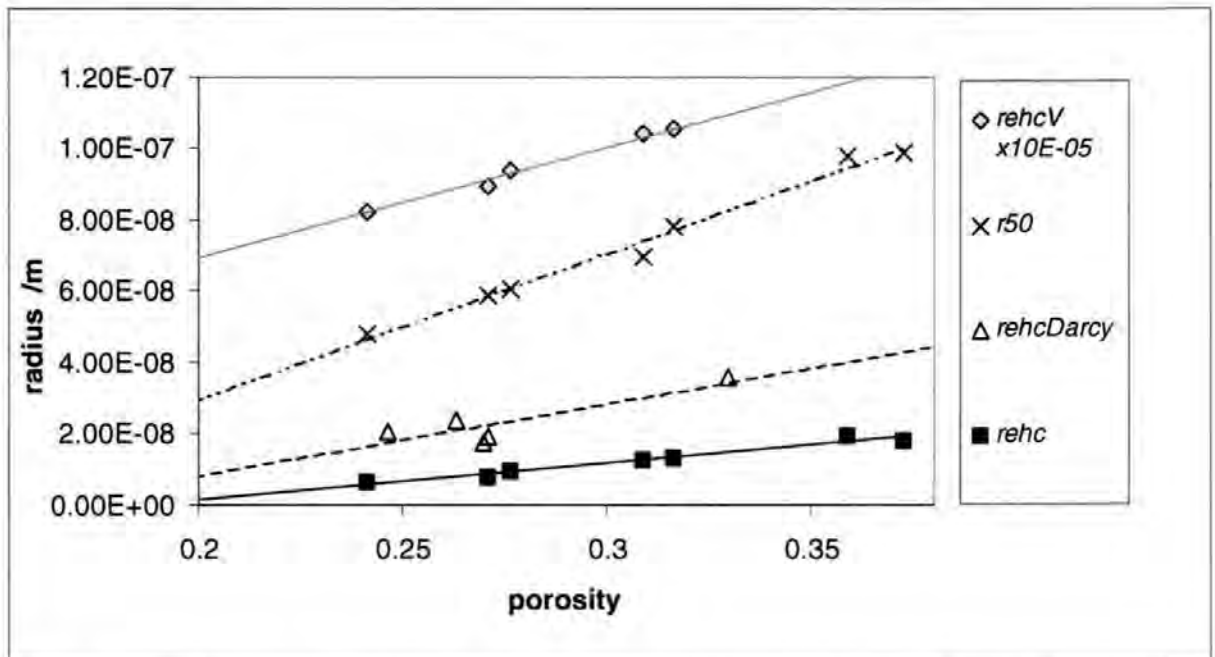


Fig. 132 Comparison of descriptive radii derived from different experimentations. All ehc values are for the mineral oil of 6/9.

Here we see that the  $r_{50}$  value is the larger than the descriptive imbibition/permeation defined radii. As it represents the pore size following the Laplace equation at the pressure of 50 % of intruded volume, it is obvious that this volume-related parameter represents more the large pores rather than the statistical numerical occurrence of fine pores. These large pores seem not to have the impact that would be expected on imbibition if we were to consider the LW equation alone. The classical  $r_{ehc}$  is at the lower end of the size-scale. The findings once more suggest that mechanisms of imbibition are different from simple LW behaviour. Porosity, however, is again confirmed to be the controlling factor of the imbibition in these structures.

The permeation-derived  $r_{ehcDarcy}$  is larger than the  $r_{ehc}$ , by a factor of  $\sim 2$ . Permeation represents the porous sample in the state closest to saturation which is the final stage of the supersource imbibition. Imbibition is postulated to occur with the preferred pathway flow at the wetting front, governed by small pores, up to and including the earlier defined Bosanquet optimum, and subsequent liquid redistribution behind the wetting front promoting the overall viscous drag. This gives rise to an envelope curve following a  $\sqrt{t}$  function. The difference between  $r_{ehcDarcy}$  and the  $r_{ehc}$  is therefore proposed to be due to the pathway flow and the subsequent redistribution process.

The  $r_{ehcV}$  is plotted in this context only for comparison. This term has its strength in the comparison of structures differing in pore size distributions independently of any pre-conceived absorption theory, (section 5.1).

## 9.12 Absorptive removal of oil from an offset ink (Schoelkopf, Gane, et al. 2001)

Having analysed the absorption of pure liquids including oils, the next step is to apply the technique to a commercial offset ink to detect the rate uptake of oil from the ink into the same structures using the same methodology. Porosimetry and simulated parameters of the experimental sample structures used in this section are given in Table 15.

### 9.12.1 Sample structures

The properties of the porous structures in the following study of oil removal from offset-ink are listed in Table 15.

sample no.	pigment	$\phi_{lg}$ / %	$d_{min}$ / $\mu\text{m}$	$d_{max}$ / $\mu\text{m}$	$d_{50}$ exp / $\mu\text{m}$
74	coarse	24.38	0.004	1.22	0.096
61	coarse	24.63	0.004	1.22	0.098
65	coarse	26.18	0.004	1.22	0.109
186	coarse	26.34	0.004	1.22	0.109
70	coarse	27.04	0.004	1.22	0.115
52	coarse	27.44	0.004	1.22	0.121
54	coarse	28.35	0.004	1.22	0.120
47	coarse	30.27	0.004	1.22	0.139
31	coarse	31.76	0.004	1.22	0.156
28	coarse	35.53	0.004	1.22	0.196
69	coarse	37.32	0.004	1.22	0.198

Table 15 Overview of structures for offset ink experimentation. The porosities as given in the text allow for clear identification.  $K_{sim}$  is given for cylindrical throats. For an extended version and explanations refer to Appendix A, Table A1.

### 9.12.2 Ink vehicle removal under supersource conditions

It was obvious that offset ink, showing one of the highest viscosities of all different sorts of inks, could cause some severe problems of experimentation due to its low fluidity/flowability. The high viscosity is seen to delay the hydrodynamic effects of wetting compared with the case of the pure liquids, and so the terms in Eq. 70 are ill-defined upon initial contact between the sample block and the ink. Special experimental techniques have to be developed to allow for the slow relaxation dynamic before the forces involved in establishing the wetting front reach equilibrium.

Conducting a first series of first experiments with the same procedure as for pure oils led to the confused plots shown in Fig. 133. The curves did not show any systematic behaviour and were not reproducible. This forced the analysis in some detail of the phenomena (arising from the high viscosity) which interfere with the contact regime of the gravimetric imbibition method.

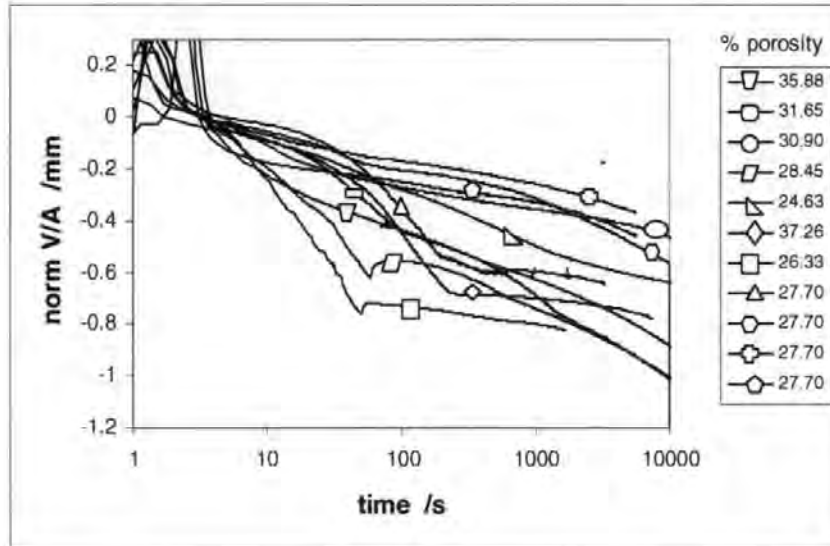


Fig. 133 Uptake curves from the ink shown as  $V(t)/A$  normalised to  $[V(t = 3 \text{ s})/A] = 0$ .

Fig. 134 shows in more detail one of the curves from Fig. 133, where we see an initial upwards peak which corresponds to the sample touching the highly visco-plastic liquid. Basically, it is a mass perturbation with a viscous decay. The time for that decay is seen to be  $2.5 \text{ s} \pm 0.2 \text{ s}$  for the normal contacting procedure where the sample is just brought into contact with the fluid. When forcing a deeper penetration of the sample into the liquid ( $> 0.5 \text{ mm}$ ) the decay time increases up to 3 s. After this peak we have a regime of relatively steep decrease of weight detected by the balance, including the progressive uptake of fluid which one wishes to measure, often quite abruptly going over into a regime of much lower slope. Sometimes even a short period of positive slope is observed after that point. So clearly, the regime where one would like to detect oil imbibition from the ink into the porous sample is perturbed by other phenomena which impart a force of unknown dynamics on the mass-detecting balance.

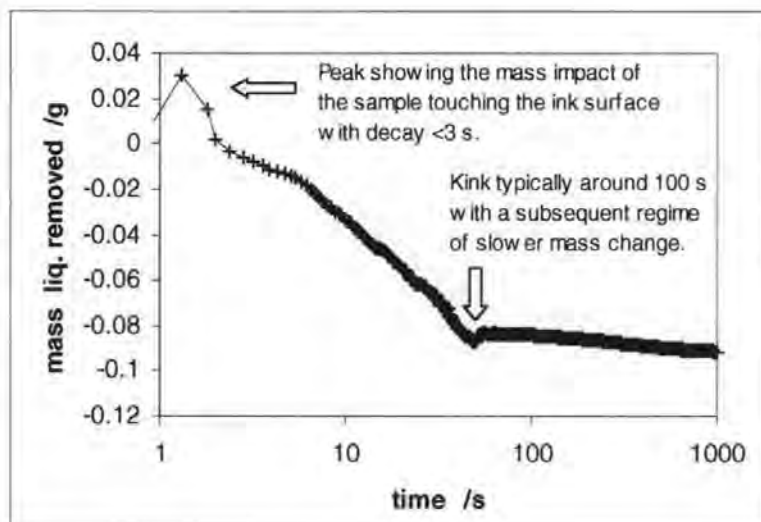


Fig. 134 Typical curve of mass change with characteristic perturbation phenomena due to the low fluidity of the offset ink.

By performing an experiment with a non absorbent cubic sample of Teflon<sup>®</sup> PTFE it was possible to analyse the pull force of the fluid meniscus wetting the basal plane. Even when the sample is macroscopically well aligned with the free surface of the ink (as perfectly as it can be with the help of the jig) there may remain some microscopical misalignment. This effect was observed earlier as a very short time phenomenon when using liquids of low and medium viscosity resulting in a constant "pull"-force. It appears to act over a period up to 200 s in the case of the viscous ink. This effect was well illustrated by an experiment highlighting the effect with the PTFE sample visibly slightly misaligned.

To overcome this misalignment effect the basal plane of the sample was rounded and a forced wetting was then performed, driving the sample approximately 1 mm into the fluid taking into account the strong but fast decaying pressure peak and the remaining constant buoyancy force. However, an ongoing decrease in the balance reading with the PTFE sample was still observed, which could not have been due to absorption. Close observation of the triple interface line showed that even on the low surface energy PTFE, and also to be expected on the low energy silicone used for edge protection of the pigmented blocks, the ink established a contact angle much smaller than 90°. Under a confocal laser scanning microscope a static advancing contact angle of approximately 45° was measured. The establishment of the contact angle toward an equilibrium force as seen on the balance lasts, in the case of PTFE, for times > 350 s. With higher energy surfaces we could expect even longer delays.

To try to solve this contact angle equilibrium problem a specially shaped resin cast was formed with a sharp edge embedding the sample as shown in Fig. 135, in order to make use of the Gibbs hinging inequality (Kent and Lyne, 1989). The sharp edge should act to pin the meniscus in an approximately approached equilibrium. In practice, the edge seemed to be microscopically too round, such that there is still a considerable time of apparent

mass change visible, which must still be the viscous delayed self-adjustment of the meniscus as shown in Fig. 135 to the left.

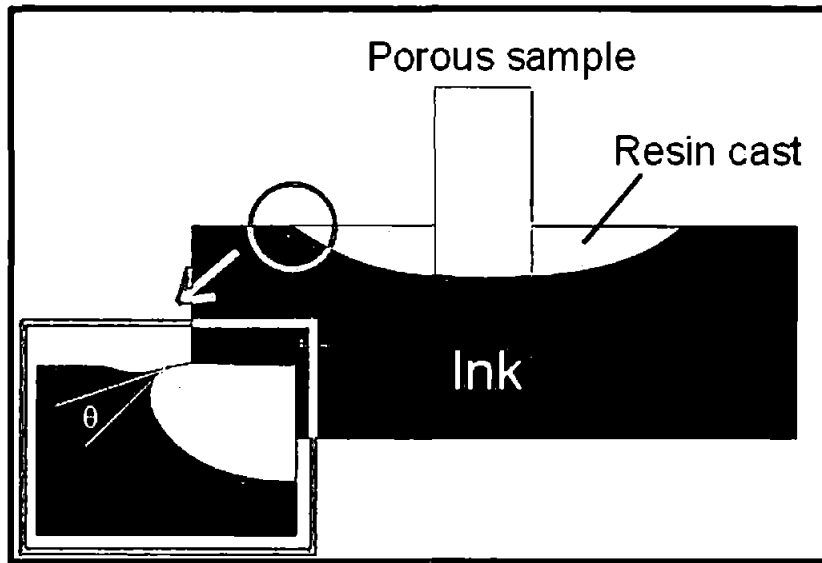


Fig. 135 Approach attempting to make use of the Gibbs hinging inequality to try to overcome delayed meniscus formation.

A further and final possible solution was considered by preadjusting mechanically the contact angle  $\theta$  by consecutive immersion and retraction of the sample basal plane, progressively reducing the amplitude to an approximated equilibrium position. This is a kind of predictor/corrector method and is shown in Fig. 136. This is carried out to the limit of mechanical resolution of the height adjustment screw of the sample holder used. This adjustment in its present form takes too long to capture short time effects ( $> 50$  s). However, it gives us reasonable data for the time after the pre-adjustment. Therefore, an absorption curve was finally derived from longer times.

Firstly, a test fit of a LW-based function: (compare with Eq. 27) was made, using

$$m_{\text{oil}}(t) = a - b\sqrt{t} \tag{Eq. 85}$$

Here  $m_{\text{oil}}(t)$  is the mass loss from the balance, as given by the experimental curve, and  $b$  is a fitting parameter containing the implicitly unknown parameters  $r_{\text{ehc}}$ ,  $\gamma$  and  $\theta$ . An equation of this type was discussed previously as given by Eq. 26, (Bell and Cameron, 1906).

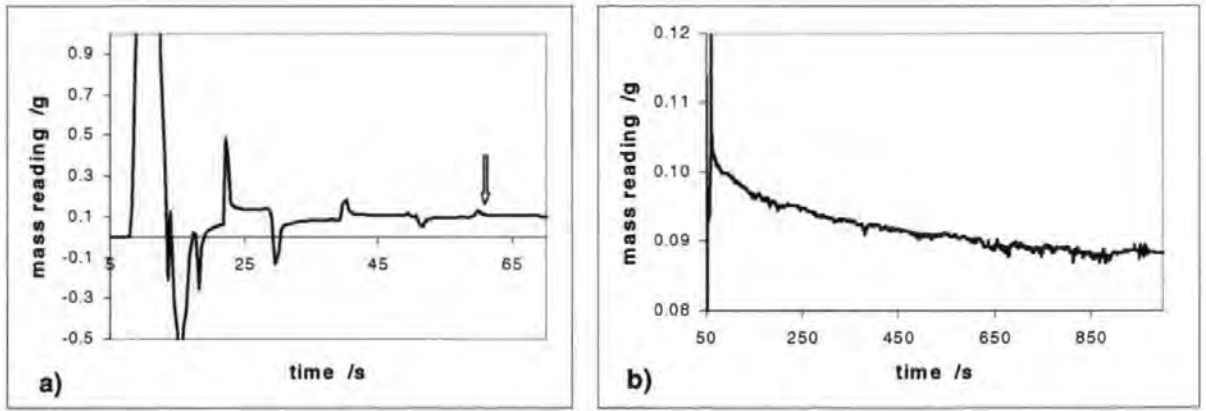


Fig. 136 a) The preadjustment of  $\theta$ , b) the regime of absorption after the indication arrow, which is used for the extrapolated fit back to shorter time. The porosity of the sample in this case was 27.04 %.

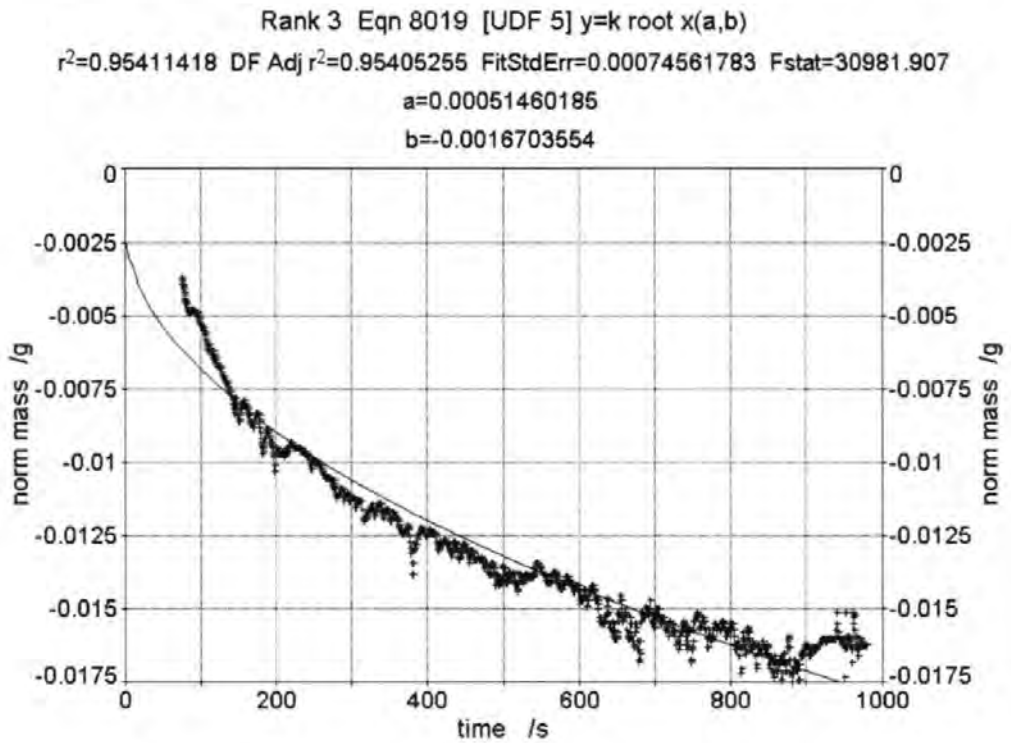


Fig. 137 Eq. 85 is fitted in the form of  $y = a + b\sqrt{t}$ . The fit is not satisfactory. Sample 70, porosity = 27.04 %

We see from Fig. 137, that such a  $\sqrt{t}$ -dependent function does not fit the data well.

The next chapter discusses a greatly improved function fit, derived directly from in-situ ink-on-paper tack measurement (section 3.6)

## 10 Extension to a complex system – dynamic behaviour of ink on coated paper

(Gane, Schoelkopf, et al. 2000)

### 10.1 Introduction

We now consider a comparison of the rheological structure relaxation of a presheared offset ink with observed ink tack development on both non-absorbent substrates, of different smoothness and surface free energy, and on a representative absorbent multi-coated paper. The structure relaxation is determined as a function of time using oscillatory and shear rheometry. The ink tack is measured with the SeGan Ink Surface Interaction Tester<sup>2</sup> (ISIT). By incorporating the extrapolated viscosity properties of the ink toward increasing concentration, a mutual relation is sought and developed to establish the viscosity character of the ink on the substrate such that ink-on-paper viscosity and solids content can be derived from the tack force measurement.

The experimental determination of viscosity extrapolation is derived from viscosity data obtained initially under progressive dilution with mineral oil. The comparison with ink tack is made via the individual force-time integrals of the ISIT, ink tack pull-off curves during tack rise (Gane *et al.*, 1994) to obtain a predicted volume loss of fluid from the ink.

The role of intrinsic ink/rubber blanket adhesion (section 2.1.6) is assumed inherently as a continuous boundary condition, but the "sealing" effect at the substrate surface, which is dependent on ink amount, roughness and ink mobility, strongly influences the evidence of cavitation, which contributes an important component to the observed tack force especially on very smooth and non-absorbent substrates. The findings are linked to measurements of printed ink tack force development on different non absorbent substrates to analyse the contribution from mechanisms of ink split, structural rebuild and cavitation.

An earlier proposed model for the separation of ink blanket from a printed ink layer adopted a geometry of parallel plate separation in a fluid medium (Xiang and Bousfield, 1998). This model is compared here with tack results and a considerable mismatch is found for the method under study. Better agreement is found using an analysis of the tack force-time integrals, footprint area and an uniaxial extensional viscous term from which an improved model of the tack-force mechanism is presented. This novel approach allows the solids and viscous parameters of the ink to be analysed as the initial ink setting actually occurs on real papers.

Furthermore, it is possible to analyse on the same device the influence of the mobile ink layer thickness as a function of time between printing and subsequent backsplitting on a typical offset paper.

## 10.2 Materials and methods

In order to study the behaviour of ink, it is of preliminary importance to examine some of the ink's relevant flow properties. For this purpose a StressTech controlled stress rheometer with a plate-plate system (UP40) was used. The plate-plate system permits the measurement of a wide range of viscosities due to its adjustable gap (a gap of 0.25 mm is used throughout this work). The decision was made not to invoke model inks, but to use a commercial ink, Skinnex cyan 4x73<sup>28</sup>.

Offset-ink is a liquid-polymer-solid blend of complex rheological behaviour. The main interest was to analyse the viscosity of the ink as a function of oil loss as experienced in the post-print regime on an absorbent substrate. As concentrating an ink is almost impossible to perform uniformly, ink dilution was investigated. By progressively expanding (diluting) the ink with a standard mineral oil, as used in the formulation of offset-inks (Haltermann PKWF 6/9 af (section 2.1.6.1)), the influence on steady state shear and subsequent structure rebuild was monitored as a complex viscosity  $\eta^*$  as discussed in section 3.5.1.

## 10.3 Rheological study of oil "loss" from ink

The ink and the oil were mixed thoroughly first by hand using a spatula, then under ultrasonic for 5 minutes, and finally homogenised on the rheometer device itself. For the rheological measurements, a steady shear rate of  $360 \text{ s}^{-1}$  was used for 180 s, and for the tack measurements, a time of 180 s on the IGT distributor was also used for comparative consistency. With the measurement system, high shear rates ( $> 50 \text{ s}^{-1}$ ) showed an unstable rheological behaviour, probably due to centrifugal loss of fluid/measuring system contact. Therefore, a shear rate of  $30 \text{ s}^{-1}$  was applied, a value which produced reasonable flow curves.

The requirement is to obtain data to model the tack rise as measured with the ISIT device. During the ISIT test procedure, as explained later in some detail, and also in a real printing process, the ink is sheared moderately in the nips of the distributing rollers, then split onto the paper where the "sheared-out" ink structure subsequently

---

<sup>28</sup> Skinnex is a product name of K+E Inks, Stuttgart, Germany.



starts to relax. During the on-going relaxation the tack is measured as a function of time after printing while oil is lost from the ink into the paper surface.

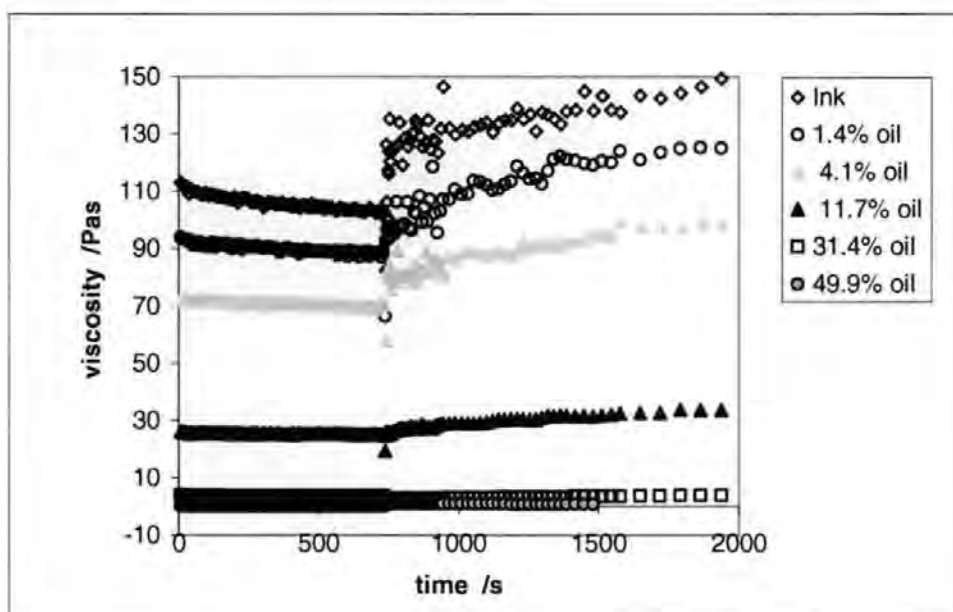


Fig. 138 Overview of shear viscosity at  $30 \text{ s}^{-1}$  and subsequent relaxation monitored by stress oscillation in the linear visco-elastic (LVE) regime as a complex viscosity,  $\eta^*$ . The dilution of the ink with the mineral oil is shown in % w/w.

Fig. 138 shows an overview of the rheology experiment. The data from the initial range represents the steady shear experiment. We see the shear thinning of the original undiluted ink over an extended period of time. The shear thinning is progressively less pronounced with increasing added oil content. After relief of the shear stress a structure rebuild occurs, as monitored by sinusoidal oscillations of the lowest possible shear or strain (0.5 Pa) in order to remain in the linear visco-elastic (LVE) domain. The phenomena underlying the sheared ink relaxation are polymer chain rearrangement and re-establishment of interactions of the solid ink particles and the fluid phase. It has to be noted that in the structure relaxation, in contrast to the steady shear experiment, a complex viscosity is measured which contains an elastic contribution.

The relaxation is seen to obey approximately the relation:

$$\eta^*(t) = (\eta^*(\infty) - \eta^*(0)) \cdot (1 - e^{-t/\tau_0}) + \eta^*(0)$$

Eq. 86

where  $\tau_0$  represents the characteristic relaxation time. Eq. 86 was entered into TableCurve 2D<sup>29</sup> which fits  $\tau_0$ ,  $\eta^*(0)$  and  $\eta^*(\infty)$  to achieve the smallest residue, here as  $r^2$ , (this software is used for all curve fittings in the following work). The equation applies well to the measured curves except for the first few data-points where a much faster relaxation process overlays. This initial relaxation may be sample or instrument related as there is

<sup>29</sup> TableCurve is a product name of SPSS Inc.

evidence of a viscosity drop before recovery and this could be an inertial effect. However, the first regime lasts only a few seconds. The characteristic relaxation times trend towards shorter values as the ink oil content decreases. As an example, the blend containing 11.7 w/w% oil is shown in Fig. 139 with a  $\tau_0 \approx 500$  s.

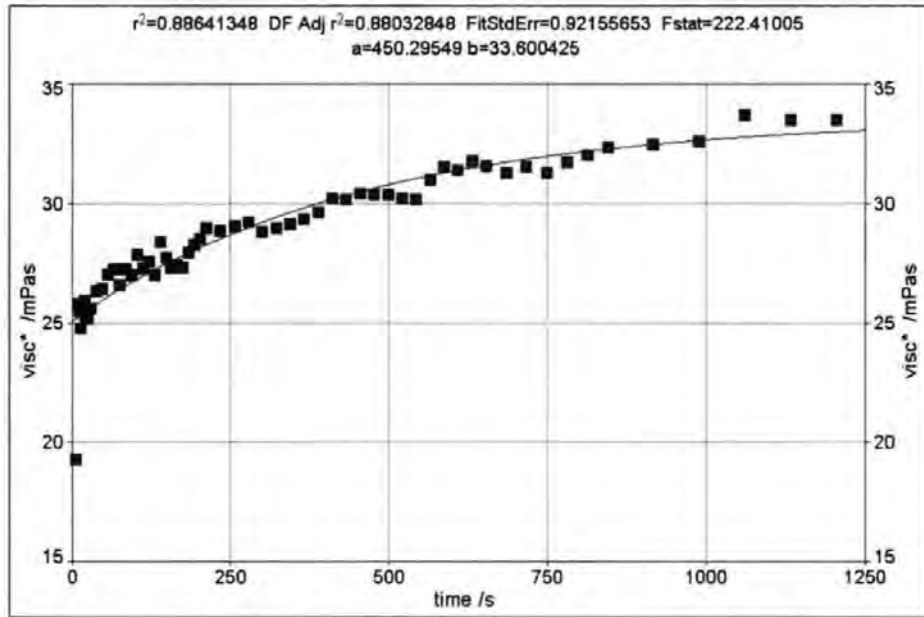


Fig. 139 Ink structure recovery regime fitted with Eq. 86 (11.7 w/w % added oil).

The viscosity data for  $\eta^*(0)$  are then used as representative values for the subsequent extrapolation to increasing ink solids content, i.e. the regime of oil loss by capillary absorption into the substrate, using an exponential fitting function.

$$\ln \eta^* = a + b\Delta\Phi_{oil}$$

Eq. 87

where  $a$  and  $b$  are fitting parameters and  $\Delta\Phi_{oil}$  is the added oil content in w/w% with respect to the sum of the undiluted ink plus the added oil. The resulting curve is displayed in Fig. 140 with the parameters  $a$  and  $b$  shown, and the proposed values are used later to compare with the ISIT findings.

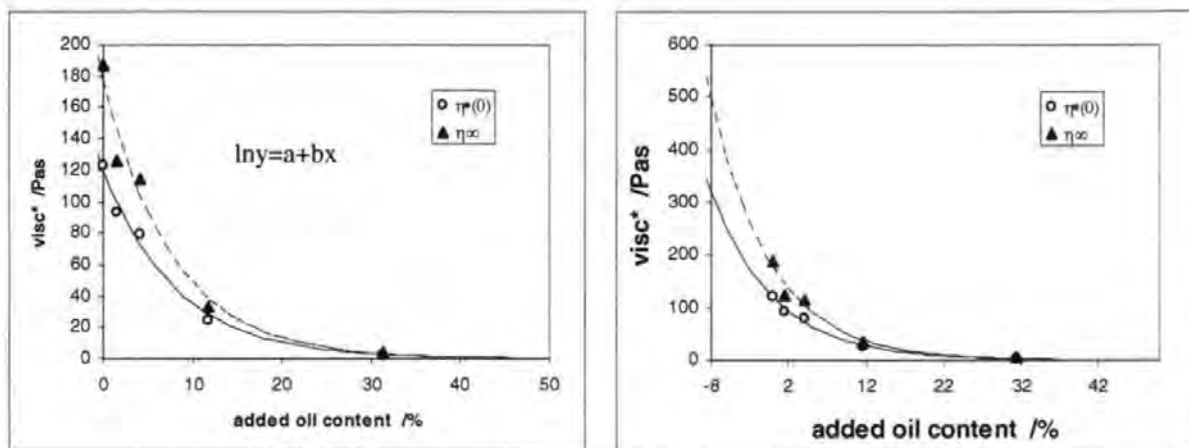


Fig. 140 Comparison of  $\eta^*(0)$  and  $\eta^*(\infty)$  as a function of added oil content of the ink  $\Delta\Phi_{oil}$  (w/w%) - the extrapolation of  $\eta^*(0)$  ( $a=4.78$ ,  $b=-0.122$ ), on the right, to reduced oil content, is used as the basis for the viscosity comparison with ink tack measurements.

## 10.4 A new approach using the ISIT force-time integral

### 10.4.1 The tack force development of an ink film on a substrate

The basic physics behind the tack force has been previously described (Gane and Seyler, 1994). The classical interpretation involving optical examination of the pull-off areas on the printed paper stripe and the tack force curve over time proposes a rupture at the weakest point of the adhesion/cohesion chain (Gane *et al.*, 1994).

In respect of ink wetting and adhesion, it has to be mentioned that the surface tension of an ink is not easy to measure because of the reduced mobility. Although the surface tension of the included mineral oil is quite low, the ink itself has a strong contribution from the more polar binders, their solvating agents, e.g. linseed oil, and the relatively high surface energy of the contained solid particles.

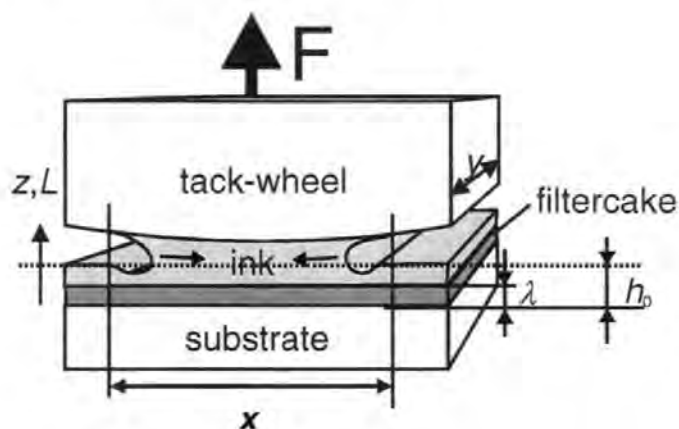


Fig. 141 Schematic view of tack set-up under the assumed formation of a filtercake with thickness  $\lambda$ .

Corresponding to Fig. 141, a more comprehensive model is introduced here as follows in a general form of:

$$F = F_{ad} + F_m + F_L + F_{cav} + F_\eta + F_i \quad \text{Eq. 88}$$

where  $F$  is the force measured on one single pull-off and  $F_{ad}$  is the static force due to interfacial tension and, according to Adamson (Adamson, 1990), is approximated by:

$$F_{ad} \cong (\gamma_S + \gamma_L - \gamma_{SL})\sqrt{xy} \quad \text{Eq. 89}$$

This is the force, for example, which holds a water drop on a vertical glass surface, where  $\gamma_S$  is the surface energy of the solid,  $\gamma_L$  the surface tension of the liquid and  $\gamma_{SL}$  is the interfacial tension. In the case of two smooth, flat solids, adhesional forces can become appreciable. However, it is recognised here that pure solid surfaces do not exist in nature. Even a clean crystal immediately after cleavage is covered by adsorbed molecules from the surrounding atmosphere. If this can be prevented, solid surfaces of the same material, which are absolutely smooth and plain, grow together, a process known as "ansprengen" in the optical industry, and in the case of two different crystals as "wafer-bonding". In contrast, for the case of a setting ink, the continuity of the adhesional boundary condition contains an additional factor due to the adsorptive nature of the coating pigment surface for ink polymers.

If there is only liquid between the two solid surfaces, the volume is given by  $xyh_0$ . (Fig. 141). There is then the additional effect of meniscus formation and retreat exerting two forces, the tension of the meniscus which is

$$F_m = 2\pi\gamma \sin\theta \sqrt{\frac{xyh_0}{z\pi}} \quad \text{Eq. 90}$$

and  $F_L$  which is due to the Laplace underpressure given by Adamson (Adamson, 1990):

$$F_L = \frac{2\gamma_{LV}xyh_0 \cos\theta}{z^2} \quad \text{Eq. 91}$$

for a given value of  $z$ , and furthermore the cavitation phenomenon will exert the force  $F_{cav}$  which is discussed further in the following section (10.4.3).

The macroscopic adhesion effect, which is, for example, observed while separating two large glass plates has a strong contribution from the underpressure between them, which can be heard and felt in the form of the subsequent airflow into the gap forming between. If in the above case a fluid with a higher viscosity than air is between, e.g. if the glass plates are immersed in water, then viscosity and inertia of the fluid seem virtually to glue the plates together.

Xiang and Bousfield (Xiang and Bousfield, 1998) developed a model based on the separation of parallel plates in a fluid, relating ink viscosity and other dimensional parameters to the force of separation occurring in the remaining fluid layer assuming that a filtercake forms a definable boundary between immobilised ink and that remaining fluid ink layer, Fig. 8.

Keiter (Keiter, 1998) solved the Navier-Stokes equation for circular and elliptical plate-plate systems for the viscous contribution and arrived at a fairly similar equation to that used by Xiang and Bousfield (Xiang and Bousfield, 1998), who quote a form of "Stefan's law" which, however, seems to be dimensionally inconsistent ( $r^2/2$  is missing comparing with Eq. 93). Keiter's derivation is

$$F_{\eta} = A \eta u r^2 / 2h^3 \quad \text{Eq. 92}$$

where,  $r$  is the radius of the circular plate,  $A$  the basal contact area,  $\eta$  the viscosity of the fluid,  $u$ , the velocity of separation and,  $h$  the separation distance. In the course of this work the application of this equation to the results is tried. The viscous term, here  $F_{\eta}$ , is noted to be of elongational nature.

Finally, the whole process is explicitly dependent on the velocity of separation, or more particularly the acceleration. At sufficiently slow separation no cavitation occurs at all, only menisci form (provided the ink is mobile enough) which retreats with growing distance  $z$  and coherent growing radius of the menisci, i.e. one single large filament forms which stretches till it breaks. For faster separation, inertia of the liquid in between becomes important, represented in Eq. 3 as  $F_i$ , resisting flow and giving rise to cavitation. The most general form of this force may be expressed as Newton's second law of motion acting on a mass,  $m$ :

$$F_i = \frac{d^2 z}{dt^2} m \quad \text{Eq. 93}$$

not taking into account the real flow field in a separating plate process.

#### 10.4.2 Relevant parameters for the ink film separation

Some relevant data for the physical characterisation of the tack experiments are given in Table 16.

	Symbol	Value	Unit
Ink density	$\rho$	$1.01 \times 10^3$	$\text{kg m}^{-3}$
Printed area	$A_p$	$46.62 \times 10^{-4}$	$\text{m}^2$
Pull-off or footprint area	$A_F$	$51.7 \times 10^{-6}$	$\text{m}^2$
Ink mass	$m_i$		kg
Ink layer thickness	$h_0$	$0.99 \times 10^{-6}$ (n = 37, st.dev. = 0.12)	m
Filtercake thickness	$\lambda$		m
Remaining ink layer under tack measurement	$h_T$		m
Mobile ink layer thickness	$(h_0 - \lambda)$		m

Table 16 Symbols, abbreviations and values used in the relevant calculations. Number of measurements for film thickness = n, (section 10.4.5).

### 10.4.3 Tack measurements on non-absorbent substrates

The ISIT device provides an easy means to study some of the above-mentioned phenomena using the geometry shown in Fig. 141. A standard procedure was followed of applying 0.3 ml of ink to the IGT distributor which results in a theoretical  $2.4 \mu\text{m}$  ink layer on the print roller. To start with, performing tack experiments on different non-absorbing substrates with different surface free energies should give us information about the influence and relevance of the first term  $F_{ad}$  assuming that the split is slow enough to ignore inertial terms.

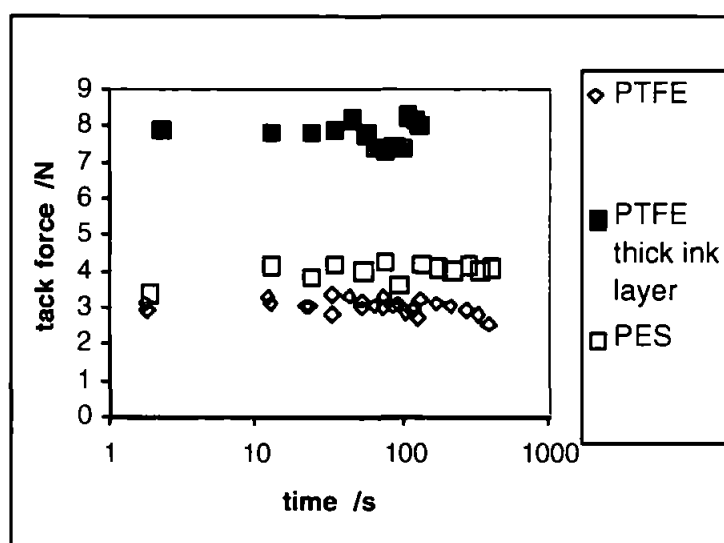


Fig. 142 Tack curve on smooth substrates.

Fig. 142 shows polyester (PES) and polytetrafluoroethylene (PTFE) as substrates, the latter having one of the lowest surface free energies ( $\approx 18.5 \text{ mN m}^{-1}$ , (Adamson, 1990)) of all available technical surfaces. Therefore,  $F_{ad}$  is at the lowest possible value. Indeed, a microphotograph shows non-wetting, with reticulated (spinoidal

dewetting) droplets of ink on the PTFE after printing, Fig. 143. From Fig. 142 a time dependent continuous decrease of the tack value is seen, probably due to the droplets receding from their initially forced lower contact angles to higher ones, resulting in less covered surface.

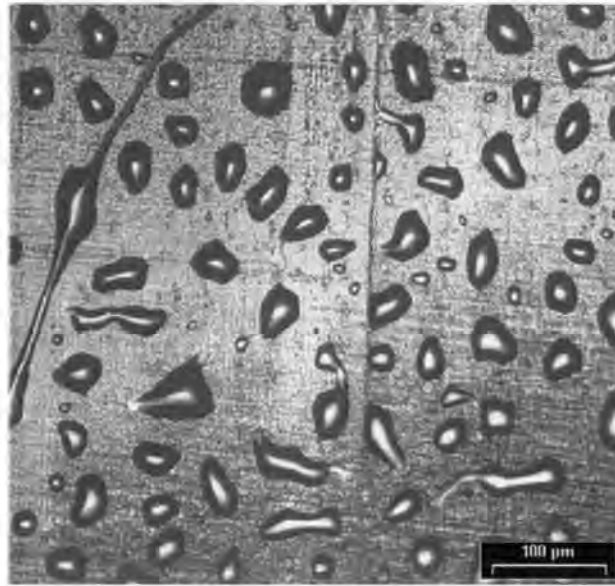


Fig. 143 Receding ink droplets on PTFE (spinoidal or nucleated dewetting) as seen using confocal laser scanning microscopy in reflected light mode.

It is interesting to see that there is a measurable tack value at all. Following Eq. 89, the value for the interfacial adhesion would be zero or even negative, therefore the interface PTFE/ink would be the weakest point. Nevertheless, it is seen that for a very thick coating of ink ( $\approx 50 \mu\text{m}$ , obtained from a PTFE strip blade coated with ink) that there is a very high tack reading. This shows clearly that there is no rupture at the weakest point of the adhesion chain but different mechanisms play a dominating role in the case of this very smooth substrate where the continuity of cohesion dominates. It is proposed that the liquid covering the solid has solely a sealing effect.

A forced separation in combination with a liquid of high viscosity causes cavitation while viscoelastic and inertial forces of the ink, denoted as  $F_{\eta}$  and  $F_i$ , withstand the meniscus equilibrium formation and the retreat. Cavitation means a vacuum forms within the nucleating voids, while the liquid and above-mentioned effects seal this vacuum for a short time period. This "sucker-effect" acts as a very strong force giving a steep rise in the pull-off force curve while a second regime of smaller gradient indicates the contribution of the subsequent filamentation under uniaxial elongational viscosity, which in turn is dependent on the amount of stretchable ink available.

A further experiment on PTFE includes samples which have been mechanically roughened by grinding them with different grit sand papers. Fig. 144 shows the mean tack as a function of "roughness". The effect of the

introduction of roughness is evident. The ink sits within the scratches constituting the roughness, consequently less ink is in contact with the tack test roller and the sealing effect is reduced (Fig. 145). Therefore, a direct relation of roughness and ink layer thickness is evident. If the ink layer is thinner than the average roughness of the substrate a step down in observed tack behaviour may be expected.

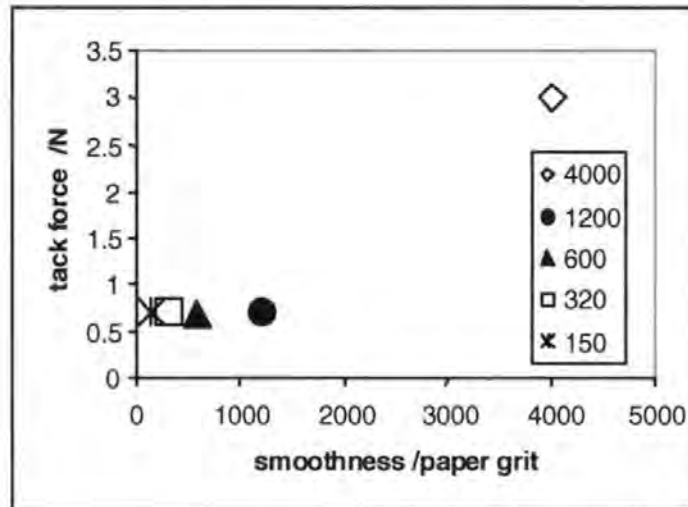


Fig. 144 Tack force on PTFE in relation to roughness/smoothness. The x-axis shows the sandpaper grit. The value of 4 000 is arbitrarily attributed to the untreated smooth surface.

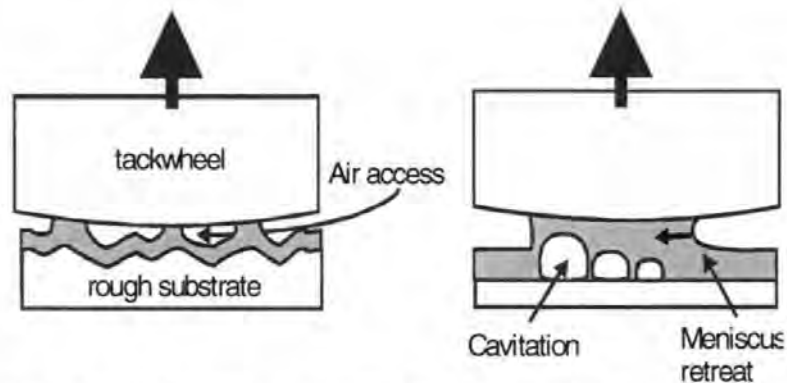


Fig. 145 Cavitation: on the left, a rough substrate means less ink contact and enables air access: on the right, cavitation at initial fast separation with meniscus retreat as extension progresses (dependent on  $\eta$ ).

#### 10.4.4 Tack measurements on paper

A "real" commercial offset paper (Ikonofix<sup>30</sup> 150 gm<sup>-2</sup>) is now considered. This paper is a multicoated gloss grade with two layers of CaCO<sub>3</sub> based coating formulation on each side. Ink is applied to the paper in the standard way (section 3.6). The long timescale tack curve cycle shown in Fig. 146 is averaged from more than 30 single tack curves.

<sup>30</sup> Ikonofix is a product name of Zanders Feinpapiere AG, D51439 Bergisch Gladbach, Deutschland



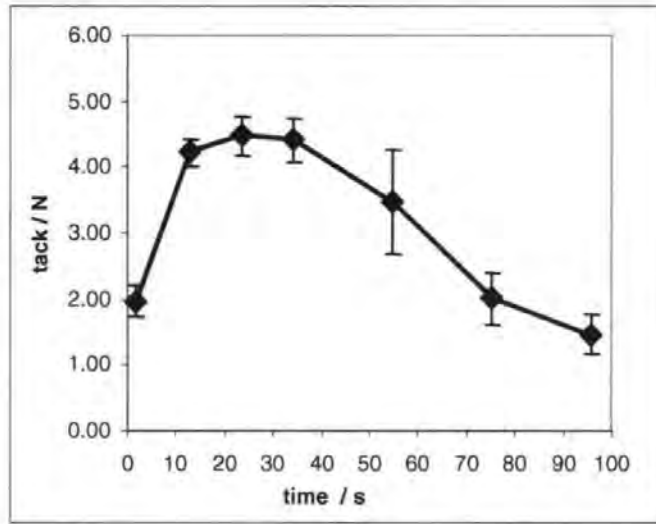


Fig. 146 Overall mean tack curve for test paper.

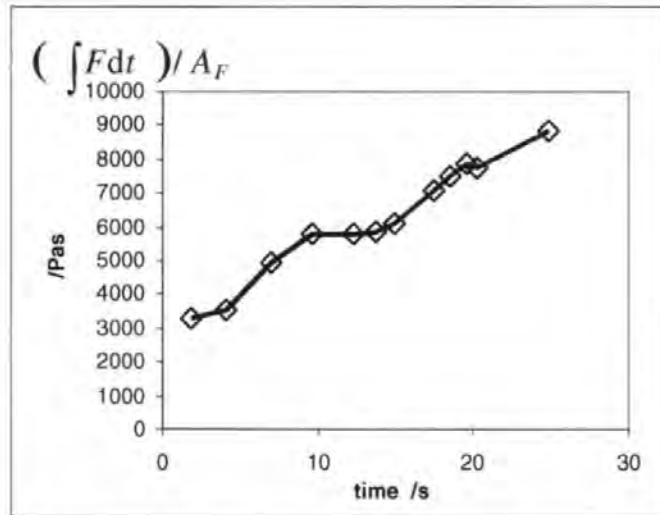


Fig. 147 The tack rise in the form of a "process viscosity", values are shown in Table 17.

It is seen that the tack rise is completed for this paper and ink in the order of 30 s. This is the regime of interest with respect to capillary oil imbibition from the initially viscosifying ink layer into the paper. Instead of plotting the force values at the relative coarse time steps shown in Fig. 146, the force-time integral was analysed, as suggested intuitively by Gane *et al.* (Gane *et al.*, 1994) for the single pull-off curves illustrated in Fig. 148, within the tack rise region, given by,

$$\eta_p = \frac{\int F dt}{A_F}$$

Eq. 94

where  $A_F$  is the footprint area formed by the contact of the tack wheel with the paper surface. The obtained expression has the units of viscosity (a "process" viscosity,  $\eta_p$ ) and is plotted in Fig. 147.

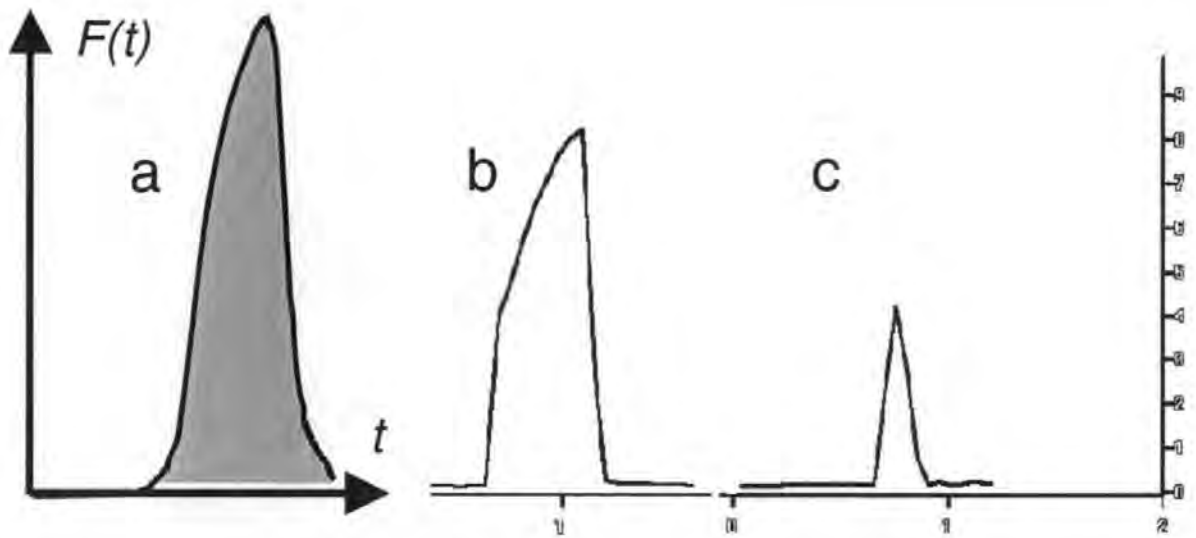


Fig. 148 (a) schematic pull-off curve with integrated area, (b) typical curve from a point of Fig. 142 showing 2 regimes: probably cavitation and viscous ones, (c) typical pull-off curve from a point of Fig. 147.

#### 10.4.5 Invoking the filtercake model

In the next step we invoke Eq. 92 to analyse the pull-off integral series in Fig. 147, for the proposed phenomenon of filtercake formation which is expected to lead to a decreasing layer of mobile ink.

In order to distinguish the potential effect of viscosity in relation to the mobile ink layer a test was performed to determine the mobile ink layer thickness as follows.

An ink roller was tared on a microbalance with a resolution of 0.1 mg. The ink roller was covered with ink on the IGT distributor device for 60 s. The roller was weighed to determine the applied mass of ink and then transferred to the ISIT device. The test paper strip was printed with one revolution (time  $t = 0$ ) at a speed of 0.5  $\text{ms}^{-1}$ . By measuring the weight of ink left on the print roller it was seen that a split ratio of 2 ( $\approx 50:50$ ) was obtained and a mass of printed ink,  $m_p$ , was applied onto the paper strip. The value of the starting ink film thickness,  $h_0$ , was obtained knowing the ink density and the complete area of the print,  $A_p$ , using Eq. 95, in which the distribution of the ink layer is assumed uniform.

$$h_0 = \frac{m_p}{\rho_i A_p}$$

Eq. 95

After  $t = \Delta t$  seconds, a fresh, uninked, also pre-weighed roller was used to split the ink layer back from the paper and the roller was weighed again. Using Eq. 96, the mass difference,  $m_{bs}$ , representing the back-split ink, yielded a mobile ink layer thickness, of mass  $m_{wet}$ , ( $h_0 - \lambda(t)$ ). The split ratio,  $R_{split} = m_{wet}/m_{bs}$ , for the back splitting was

determined from measurements at the shortest times (before the filtercake forms, i.e. when the wet layer thickness approximates to the applied ink film thickness). It was found to be 1.18, where a value of 1 would mean all the ink would be removed back onto the roller – this value is assumed to be constant over time as the filtercake grows.

$$(h_0 - \lambda(t)) = \frac{m_{bs} R_{split}}{\rho_i A_p}$$

Eq. 96

The values obtained are plotted in Fig. 149 and a fitting was applied providing a value of  $(h_0 - \lambda(t))$  as a function of time using the applied boundary condition of  $h_0 = 0.99 \mu\text{m}$ , given by the initial 50:50 printing application split, as follows:

$$\ln(h_0 - \lambda(t)) = a + bt$$

Eq. 97

where, once again,  $a$  and  $b$  are fitted constants. This expression was used as the universal mobile wet film thickness curve for the subsequent calculations.

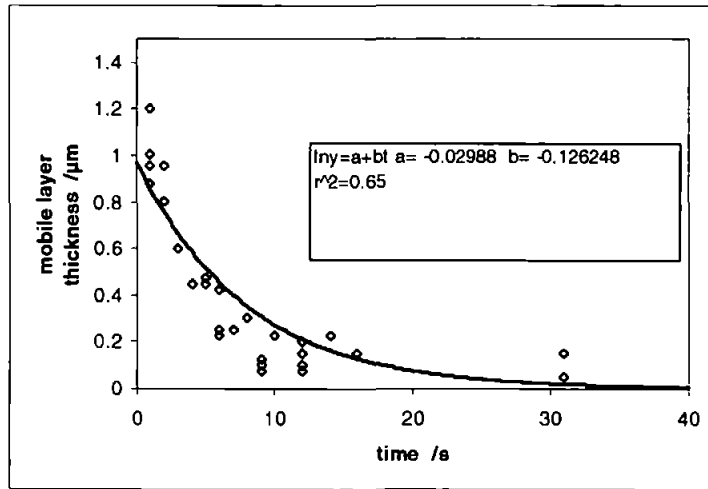


Fig. 149 Mobile ink layer thickness as a function of time obtained from gravimetric ink splitting experiments.

Invoking the separation of parallel plates, as given in Eq. 92, in an attempt to model the tack response, gives, however, a decreasing viscosity of the ink as tack increases because the reduction in mobile film thickness from the back split occurs so fast ( $h^{-3}$ ) that it disallows a response from the viscous term. This is considered practically unrealistic and, furthermore, it is many orders of magnitude away from measured shear viscosities. The results are shown in Table 17.

Balancing the tack-force/footprint area ratio with a process viscous term,  $\eta_p$ , and a dimensionless strain expression,  $\gamma(t)$  [ $\approx x/(h_0-\lambda(t))$ ], based on the schematic view of the parameters in Fig. 141, a different relation is obtained which is not so strongly depending on the mobile film thickness decay, following:

$$\frac{F(t)}{A_F} = \eta_p \frac{d\gamma(t)}{d t},$$

$$\text{where } \frac{d\gamma(t)}{d t} = \frac{u(t)}{(h_0 - \lambda(t))}$$

$$\text{and, therefore } \int \frac{F(t)d t}{A_F} = \eta_p \gamma(t) = \frac{\eta_p x}{(h_0 - \lambda(t))}$$

Eq. 98

Nonetheless, even if this equation is solved for  $\eta_p$ , a decreasing viscosity as a function of time is still obtained. This could be explained by invoking other dominant phenomena as discussed in the introduction of this section or by questioning the reliability of the obtained values of  $(h_0-\lambda(t))$ . The film-splitting technique must assume an immobilised layer which has a distinct boundary condition with the mobile fluid layer under the dynamics of the split. Oil loss is occurring within the region above the proposed filtercake as well as from the truly mobile layer above this interface. It must be concluded, therefore, that there is no well-defined delineation or boundary between the filtercake and the continuously concentrating mobile layer under the conditions of the test. The back split ratio deviating strongly from the 50:50 assumption is already an indication that wet adhesion close to the paper surface boundary, probably affected by air intake into the split from the underlying substrate roughness, is not strong enough to maintain the continuity of a filtercake with that surface. The static pull-off technique offered by the ISIT apparently, therefore, maintains the continuity between mobile and immobilised ink, thus probing the continuous tackification of the ink throughout the cohesive ink layer, and not identifying a filtercake as such but a continuous concentrating of the ink layer. A delineated filtercake model does not satisfy the observed tackification of offset ink.

A different method was therefore tried, measuring the print optical densities on the papers from the splitting test to find a correlation of remaining ink layer thickness and print density. The print densities are measured directly on the tack pull-off footprint areas of the tack tested samples used in the short time tack tests (see Fig. 39). By comparing the ink film thickness remaining on the paper after backsplitting as a function of print density, it is possible to determine the thickness of the layer extended during the independent pull-off measurement of the ISIT, i.e. via Fig. 150 to obtain Fig. 151.

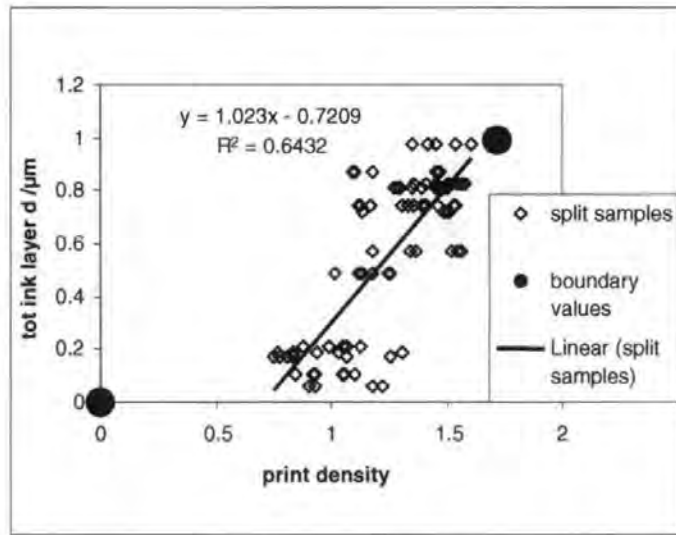


Fig. 150 Total remaining ink layer thickness.

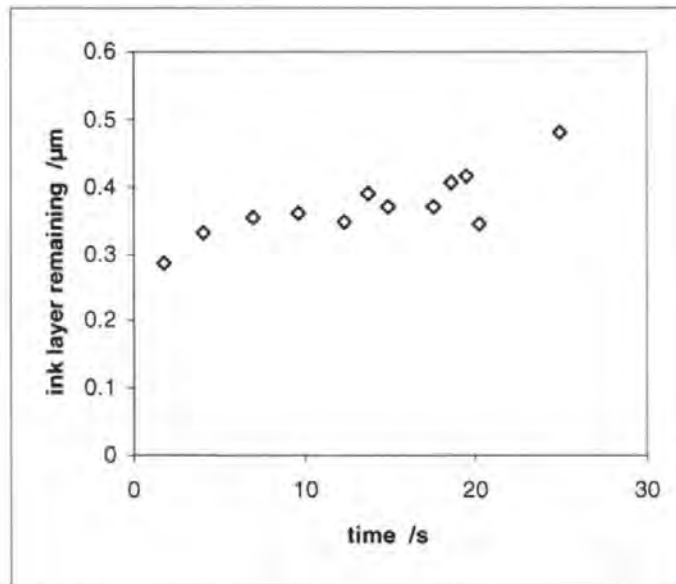


Fig. 151 Ink layer remaining on paper as a function of print density after tack test as a function of time.

Using the values in Fig. 151 in Eq. 98 there is a rising viscosity prediction (see Table 17) which confirms that the pull-off test leaves a thinner ink layer than is predicted from a simple filtercake back split model. But this viscosity is still 3 orders of magnitude away from a measured shear viscosity. This causes a question regarding the validity of both Stefan's law approximation or similar planar shear expressions involving a distance of separation for typical tack measurements involving very small layer thicknesses and fairly high velocities of separation.

### 10.4.6 Using an extensional model

The static pull-off mode of the ISIT provides a close approximation to a constant acceleration extensional regime. This feature is part of the machine design and is confirmed independently later by direct observation (section 10.10). Going back to Fig. 146, Fig. 141 and Eq. 94, we now consider an uniaxial extensional term as, for example, given by the strain expression (Macosko, 1994) in which the extension to a dimension of  $L$  occurs from a start dimension of  $L_0$ :

$$\varepsilon = \ln(L/L_0) \tag{Eq. 99}$$

such that the uniaxial extensional viscosity,  $\eta_u$ , can be expressed via the stress tensor,  $T_{ij}$ ,

$$\eta_u = (T_{zz} - T_{yy}) / \dot{\varepsilon} = F(t)e^{\dot{\varepsilon}t} / (A_F \dot{\varepsilon}) \tag{Eq. 100}$$

where  $\varepsilon$  is the Hencky strain. To obtain an expression without the unknown rate of change of strain, Eq. 100 is integrated with respect to time over the complete single pull-off curve using  $F(t)$  as the measured separating force to obtain a process extensional viscosity,  $\eta_{pu}$ .

$$\frac{\int_0^\infty F(t)dt}{A_F} = \int_0^\infty \eta_{pu} \dot{\varepsilon} e^{-\dot{\varepsilon}t} dt = \left[ -\eta_{pu} e^{-\dot{\varepsilon}t} \right]_0^\infty = \eta_{pu} \tag{Eq. 101}$$

The ISIT software provides directly the force-time integrals, so  $\eta_{pu}$ , can be obtained directly confirming the intuitively proposed Eq. 94. The values can now be matched with the extrapolated independently determined  $\eta^*(0)$  from the relaxation measurements using a scaling via the Trouton ratio,

$$\eta_{pu}(t) = 3\eta_1(t) \tag{Eq. 102}$$

which relates the extensional viscosity to the shear viscosity and normalising  $\eta_1(0)$  with  $\eta^*(0)$  by a simple scaling factor,  $k$ .

The assumptions implicit in the integration made in Eq. 101 are that the effect of changing  $L_0$  is ignored and that  $L$  is large when  $T_s$  represents the time at the end of the pull-off, i.e. that  $d\varepsilon/dt$  is large as the tack wheel finally extends the ink to fracture point, and therefore separation. This allows the boundary of the integral in  $t$  to be considered as  $t \approx \infty$ . If this were not the case then Eq. 101 would become,

$$\frac{\int_0^{T_s} F(t) dt}{A_F} = \int_0^{T_s} \eta_{pu} \dot{\varepsilon} e^{-\dot{\varepsilon} t} dt = \left[ -\eta_{pu} e^{-\dot{\varepsilon} t} \right]_0^{T_s} = \eta_{pu} \left( 1 - e^{-\dot{\varepsilon} T_s} \right)$$

Eq. 103

Practically,  $L_0$  is related to the reduced wet or effective mobile layer. However, the extension of the film is so great, leading in fact to a final fracture of the film, that the ratio  $L/L_0$  is always assumed large over the extent of the pull-off action such that conditions of strong flow only are considered. For thicker layers and slower separation times the change to weak flow might be a complicating factor. However, if one regime is considered, the scaling factor  $k$  can be expected to make a good compensation for this assumption. Development of the instrument to obtain position-sensitive data during the pull-off would allow evaluation of  $\varepsilon$  and  $d\varepsilon/dt$ . This is demonstrated later in section 10.7. Meanwhile, the information is already present in terms of the value of the experimental separation time,  $T_s$ , such that the scaling factor,  $k$ , could be related to already known parameters by,

$$k = \left( 1 - e^{-\dot{\varepsilon} T_s} \right)$$

Eq. 104

to obtain an estimate for  $d\varepsilon/dt \approx 0.6 \text{ s}^{-1}$ , for a pull-off time of  $T_s \approx 0.2 \text{ s}$  and  $k \approx 0.11$  (Table 17). This we go on to consider in section 10.7

Col.1	2	3	4	5	6	7	8	9	10	11
Data point	Time /s	Pull-off integral $\int F dt$ /Ns	Eq. 94 solved for $\eta_{pu}$ /Pas	mobile layer* after split / $\mu m$	Stefan's law $\ddagger$ solved for $\eta$ (as given by Xiang and Bousfield) /Pas	Eq. 98 solved for $\eta_p$ using col.5 /Pas	Eq. 98 solved for $\eta_p$ using col.9 /Pas	$h_T$ ** / $\mu m$	Eq. 94 / Eq. 101 and Eq. 102 solved for $\eta$ /Pas	Same Eq.'s as in col. 10, normalised $\dagger$ to $\eta^*(0)$ /Pas
1	1.8	0.28	3294.12	0.77	1.52356E-15	509497.89	464437.65	0.29	1098.04	122.65
2	4.1	0.30	3529.41	0.58	6.83356E-16	408363.86	466320.00	0.33	1176.47	131.41
3	7.0	0.42	4941.18	0.40	3.19114E-16	396490.00	629258.82	0.35	1647.06	183.97
4	9.7	0.49	5764.71	0.29	1.33952E-16	329001.23	726272.24	0.36	1921.57	214.63
5	12.3	0.49	5764.71	0.21	5.00549E-17	236971.88	741998.35	0.35	1921.57	214.63
6	13.7	0.5	5882.35	0.17	3.00626E-17	202646.73	704988.24	0.39	1960.78	219.01
7	14.9	0.52	6117.65	0.15	1.98496E-17	181135.42	760307.29	0.37	2039.22	227.78
8	17.5	0.60	7058.82	0.11	8.55849E-18	150539.54	873667.06	0.37	2352.94	262.82
9	18.5	0.64	7529.41	0.09	6.25175E-18	141537.44	877993.41	0.41	2509.80	280.34
10	19.5	0.67	7882.35	0.08	4.48201E-18	130604.52	907053.88	0.41	2627.45	293.48
11	20.2	0.66	7764.71	0.08	3.38723E-18	117777.35	1004721.88	0.34	2588.24	289.10
12	24.9	0.75	8823.53	0.04	6.49487E-19	73957.40	898014.71	0.48	2941.18	328.52

Table 17 Comparison of viscosity values obtained from different approaches. \* Mobile layer is determined from splitting experiments. \*\* $h_T$  is the remaining ink layer determined from print densities,  $\dagger$  normalising constant  $k = 0.1117$ ,  $\ddagger$  Keiter's expression gives results of similar dimensions.

#### 10.4.7 The ink rheology as it sets – obtaining the solids content as a function of time on the paper

Combining Eq. 87, Eq. 100 and Eq. 101 an approximation for the oil content in the system as a function of the tack force-time integrals and the footprint area is obtained,

$$\Delta\Phi_{oil} \approx \frac{\ln\left(\frac{\int F(t)dt}{3A_F} k\right) - a}{b}$$

Eq. 105

where  $k$  is the scaling factor used in Table 17,  $a$  and  $b$  are the fitting parameters from the  $\eta^*(0)$  as a function of oil dilution given in Fig. 140.

The values are plotted in Fig. 152 for the tack data of Fig. 147 showing the time dependent decrease in oil content of the ink. Recent work from Rousu *et al.* (Rousu *et al.*, 2001a) has shown the precursory absorption of mineral oils while the removal of linseed oil is more retarded. Not knowing the formulation of the ink and the total oil makeup, it may be assumed that at the time of 30 s, which is on the tack force plateau, the largest amount of oil removed from the setting ink is mineral-based.



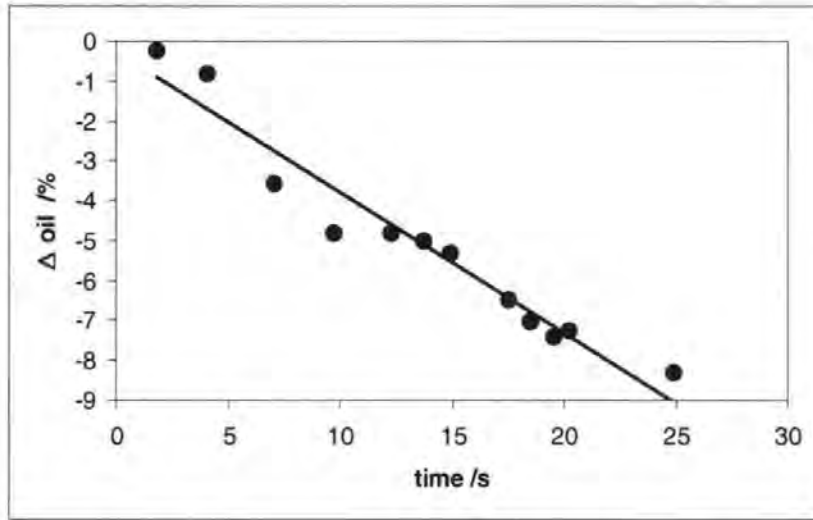


Fig. 152 The proposed differential oil content of the ink from Eq. 105 as a function of time in contact with the paper surface.

The fraction of oil content being absorbed by the paper is decreasing linearly with time over the timescale of tack increase (Fig. 152). If we assume the following linearity,

$$\Delta\Phi_{\text{oil}}(t) = \Phi_{\text{oil}}(t) - \Phi_{\text{oil}}(0) = -ct \quad \text{Eq. 106}$$

where

$$1/\Phi_{\text{oil}}(t) = \frac{m_{\text{oil}}(t) + m_{\text{solid}}}{m_{\text{oil}}(t)} = 1 + \frac{m_{\text{solid}}}{m_{\text{oil}}(t)} \quad \text{Eq. 107}$$

such that, rearranging, the mass of oil in the ink expressed as a function of time,  $m_{\text{oil}}(t)$ , in terms of the unchanging mass of solids,  $m_{\text{solid}}$ , and the original volume fraction of oil,  $\Delta\Phi_{\text{oil}}(0)$  in the ink, respectively.

$$m_{\text{oil}}(t) = \frac{m_{\text{solid}}}{1/\Phi_{\text{oil}}(t) - 1} = \frac{m_{\text{solid}}\Phi_{\text{oil}}(t)}{1 - \Phi_{\text{oil}}(t)} = \frac{m_{\text{solid}}(\Phi_{\text{oil}}(0) - ct)}{1 - (\Phi_{\text{oil}}(0) - ct)} \quad \text{Eq. 108}$$

This is an interesting finding, in that absorption of free fluid over such timescales would normally be expected to follow a  $\sqrt{t}$  relationship.

The rate of mass loss of oil is determined by differentiation,

$$\frac{dm_{\text{oil}}(t)}{dt} = \frac{-cm_{\text{solid}}}{[(1 - \Phi_{\text{oil}}(0)) + ct]^2} \propto -1/t^2 \quad \text{Eq. 109}$$

to find that this rate falls off as  $t^{-2}$  as a first approximation.

In this case, the existence of a resistive factor forming as the ink becomes more viscous is the likely explanation, although, as already shown, this is unlikely to be a filtercake in the accepted sense. This will need to be tested further independently and will be the subject of future work.

#### **10.4.8 Conclusions**

The balance between adhesive and cohesive aspects of a fluid layer in contact with surfaces of differing surface energy and roughness has been illustrated using an offset ink and a variety of substrates. It was found that for a non-absorbent smooth surface, the cohesion of the mobile ink film plays the dominant role in respect to the force required to separate a second contacting surface such as might occur between two parallel plates in the case where the basal area of one surface is much larger than the other. The ink film can, therefore, be considered infinite and continuous. This, it is concluded, differs in the case of a rough or a porous, permeable surface which would allow the influx of air and rupture at surface discontinuities, in which case the separation force is dominated by viscous, cavitation (adhesive when occurring at the boundary layer) and, if rapid, inertial forces.

It has been shown that it is possible to use tack measurements based on the pull-off technique, as used by the ISIT tester, to determine a model for the viscosity and solids content of an offset ink as the ink begins to set on a paper surface. Under these conditions, the separation force is related predominantly to the viscous properties of the cohesive ink layer. This technique is proven to maintain the cohesion between the wet mobile ink layer and the immobilising interface, between the ink and paper surface, and precludes the concept of splitting within a distinct mobile layer above that of a delineated forming filtercake. The continuity between the mobile ink and the upconcentrating interface is thus maintained and the increase in measured tack is related to the fluid loss and viscosity increase as defined through a uniaxial extensional viscosity model.

This method and description provides a tool for future workers to study the solids and viscosity properties of a wide variety of polymer and particulate suspensions as they interact with the surface of a substrate and follow the progressive change in their properties either through evaporation, absorption, catalysis or external curing.

#### **10.5 Comparing LW and the tack-based absorption equation**

Now the prediction expressed in (Eq. 108) can be used to fit to the earlier shown imbibition data of fluid removal from an ink, which are plotted in Fig. 153. If this new fit is compared to the previous fit based on the LW

expression Eq. 85, Fig. 137, it is clearly seen that the curve based on Eq. 108 gives a better correlation. This confirms that the supersource observation of offset ink vehicle absorption follows the dynamic of the thin layer absorption as measured directly on coated paper via the tack force-time integral. The correlation of the two measurements provides conclusive evidence for a dynamic other than LW for ink setting based on fluid absorption into a porous paper coating network.

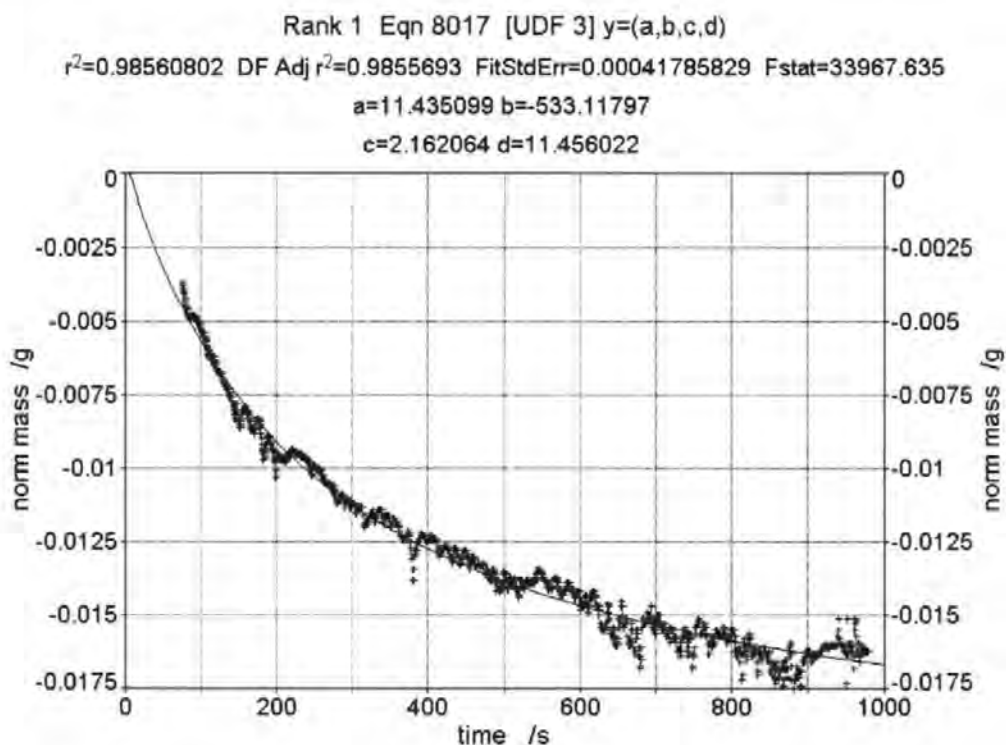


Fig. 153 A fit based on the prediction (Eq. 108) to compare with Fig. 137 which is based on a LW expression Eq. 85, The fitting parameters are given in the Appendix B 3. Sample 70, porosity = 27.04 %

The dependent mass axis in Fig. 153, which was based on a relative starting absorption mass, was shifted to fulfil the boundary condition  $m_{oil}(0) = 0$ , stating that no oil was lost at time  $t = 0$  (where  $t = 0$  is the start of the experiment at the first point of contact between sample and ink). It is not possible with this experimentation to get data for the initial regime after contact, but the target was achieved in that it was wished to test the proposed general rate behaviour in section 10.4.7 from Eq. 108.

For further confirmation, the offset ink was diluted to increase the fluidity. 2 parts (by weight) of ink were blended with 1 part of the previously used mineral oil, af 6/9. With lowered viscosity it was now possible to carry out a further supersource imbibition, in the same way as the oil itself had been tested, using the same compressed pigment tablet form (Table 15, sample 186). The viscosity of the blend was in the order of 1 Pas, so that for the wetting jump a timescale of  $\approx 3$  s could be expected. The raw imbibition data are shown in Fig. 154.

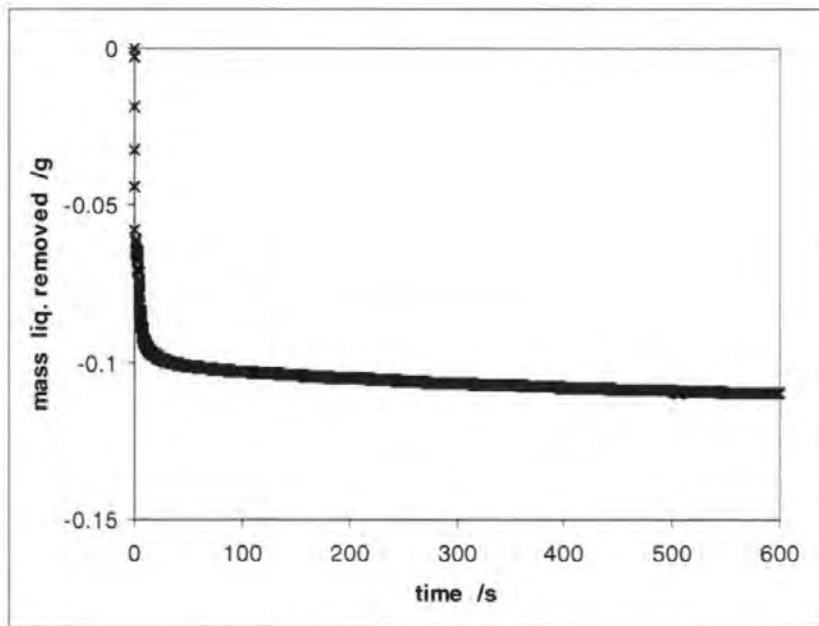


Fig. 154 Diluted ink mass removal curve for sample 186, porosity = 26.34 %.

Again the two equations used before are shown to compare their fitting potential. First the comparison is shown for a fit over the whole measured range of absorption covering 600 s, Fig. 155 and Fig. 156.

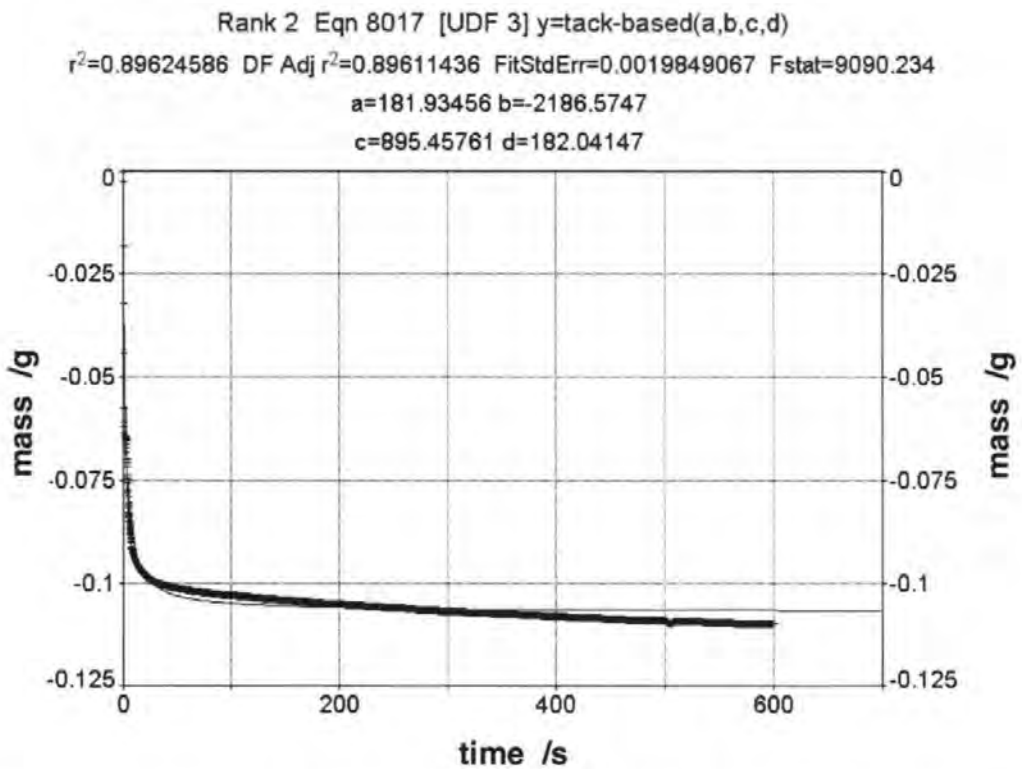


Fig. 155 Fit of the prediction (Eq. 108), i.e. prediction from ink tack force-time integral applied to supersource diluted ink. In this case, shorter timescales can be encompassed by the use of the more fluid ink, matching the timescale of tackification with that of supersource. Sample 186, porosity = 26.34 %.

Rank 4 Eqn 8019 [UDF 5]  $y=k \text{ root } x(a,b)$   
 $r^2=0.50373498$  DF Adj  $r^2=0.50342069$  FitStdErr=0.0043396699 Fstat=3206.5504  
 $a=0.00075508836$   
 $b=-0.093443882$

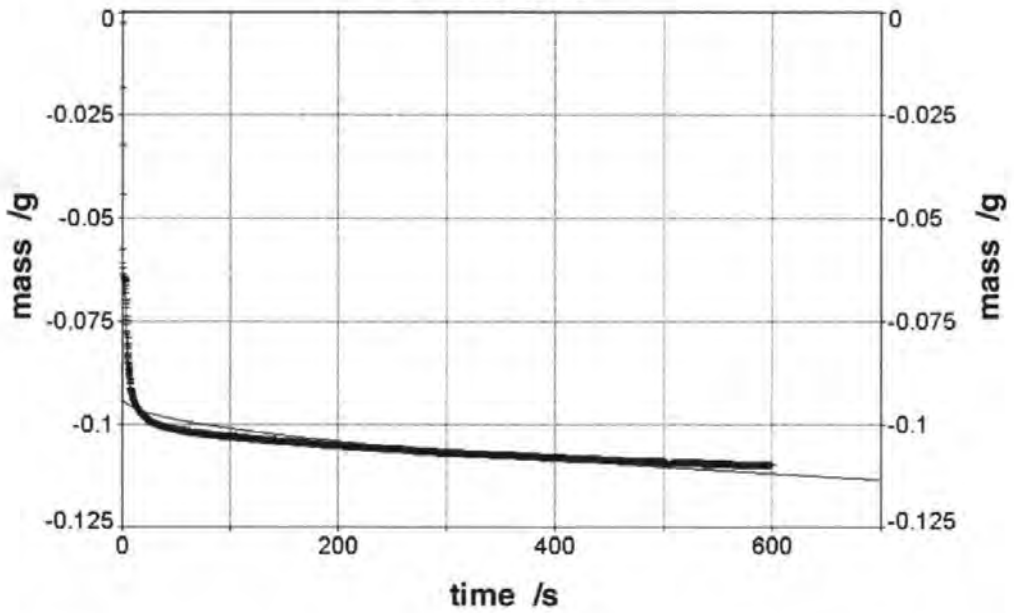


Fig. 156 *LW type fit applied to supersource imbibition of diluted ink (Eq. 85). We see a similar deviation from observations as for the undiluted ink. Sample 186, porosity = 26.34 %.*

Again, the better applicability of Eq. 108 with an  $r^2$  of 0.896 in contrast to the LW-type Eq. 85 with an  $r^2$  of 0.504 can be seen. Taking into account that Eq. 108 was derived from medium timescale tack measurements, focus should be made on the regime where it is expected that the equations will generally be more applicable. This is now carried out in Fig. 157 and Fig. 158 allowing the fitting software TableCurve 2D to re-optimize the fitting parameters for the new overlap time range.

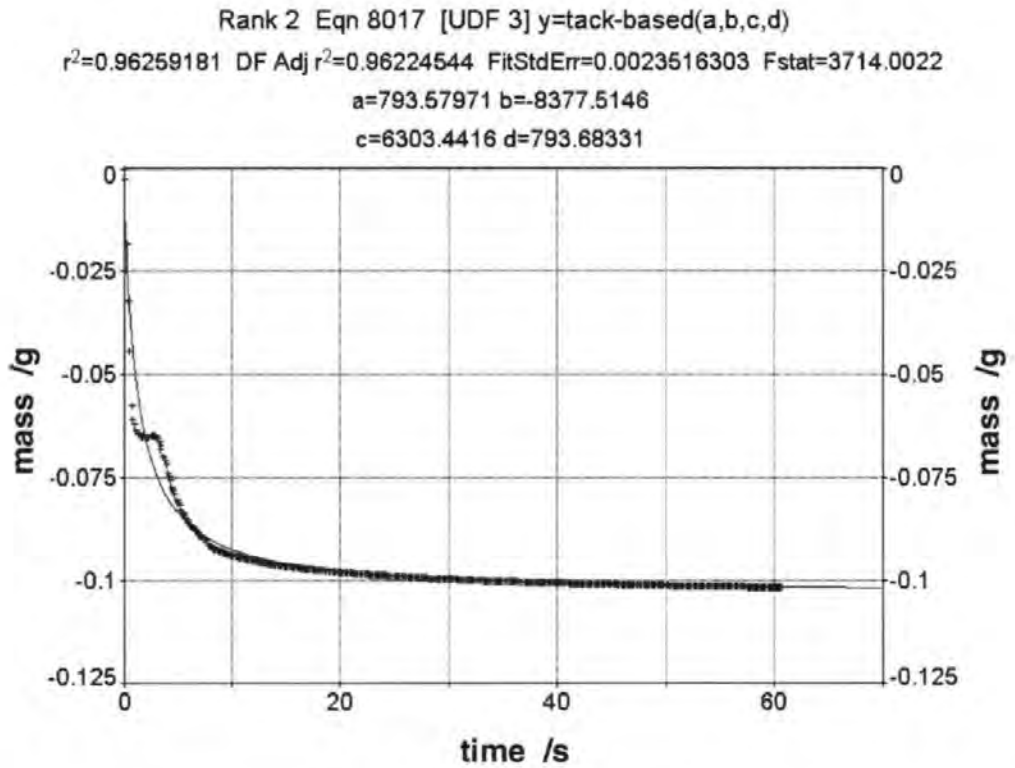


Fig. 157 The fit of the prediction (Eq. 108) over shorter timescales. Sample 186, porosity = 26.34 %.

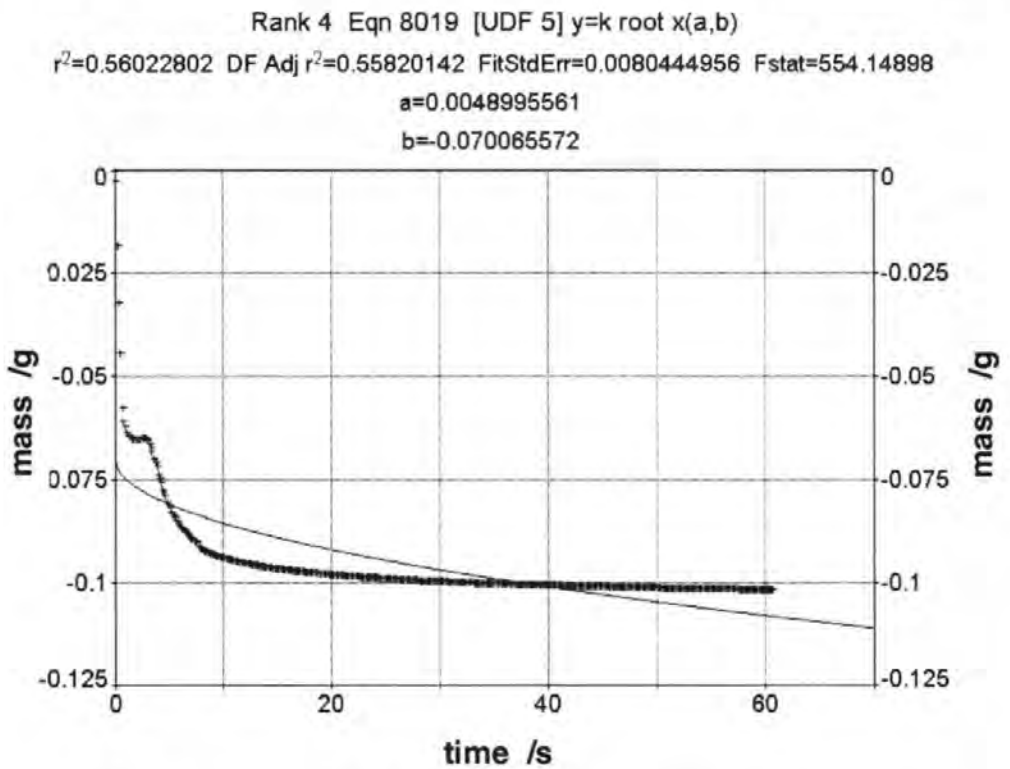


Fig. 158 The poor fit of the LW approach (Eq. 85). Sample 186, porosity = 26.34 %.

Here, at shorter timescales, the difference is even more pronounced. The step in the measured data at around 4 s, which is now visible in the curve, is probably an air bubble or a stick/slip behaviour of the outer wetting line. However, one could argue that the first steep part of the curve should be neglected anyway because the wetting jump can not be clearly separated from imbibition uptake.

Finally a third optimised fit is tried, namely a fit for  $t > 10$  s, avoiding the short timescale experimental artefacts.

This fit is shown in, Fig. 159 and the comparable poor LW fitting is shown in Fig. 160.

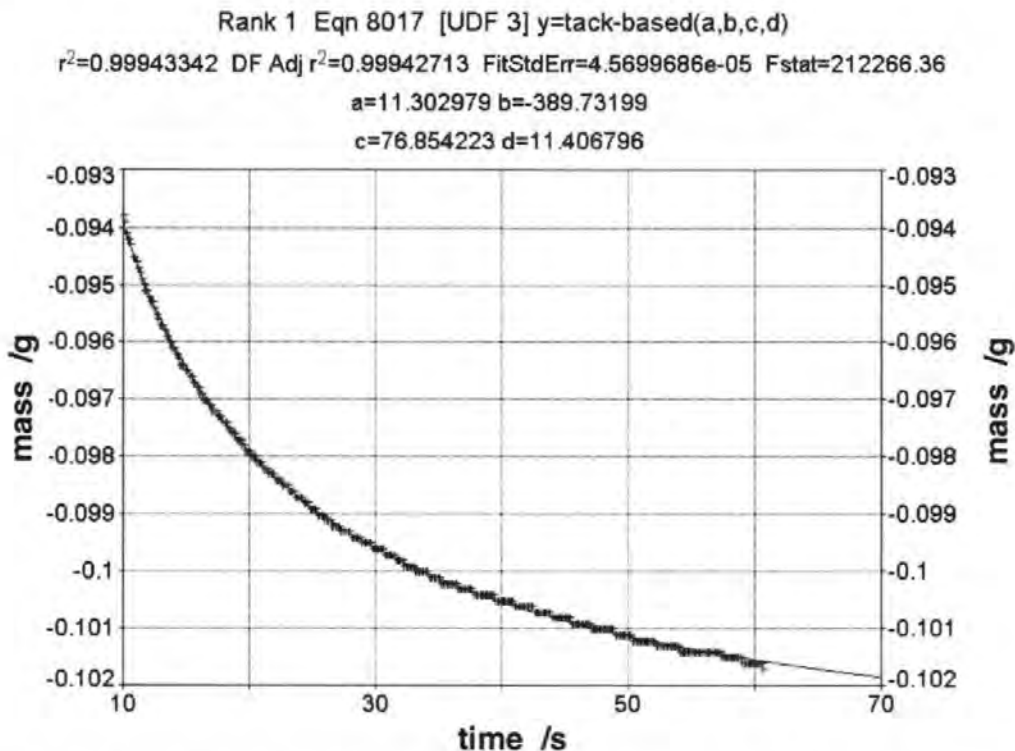


Fig. 159 Fit of the prediction (Eq. 108) with now an excellent  $r^2$  of  $> 0.999$ . Sample 186, porosity = 26.34 %.

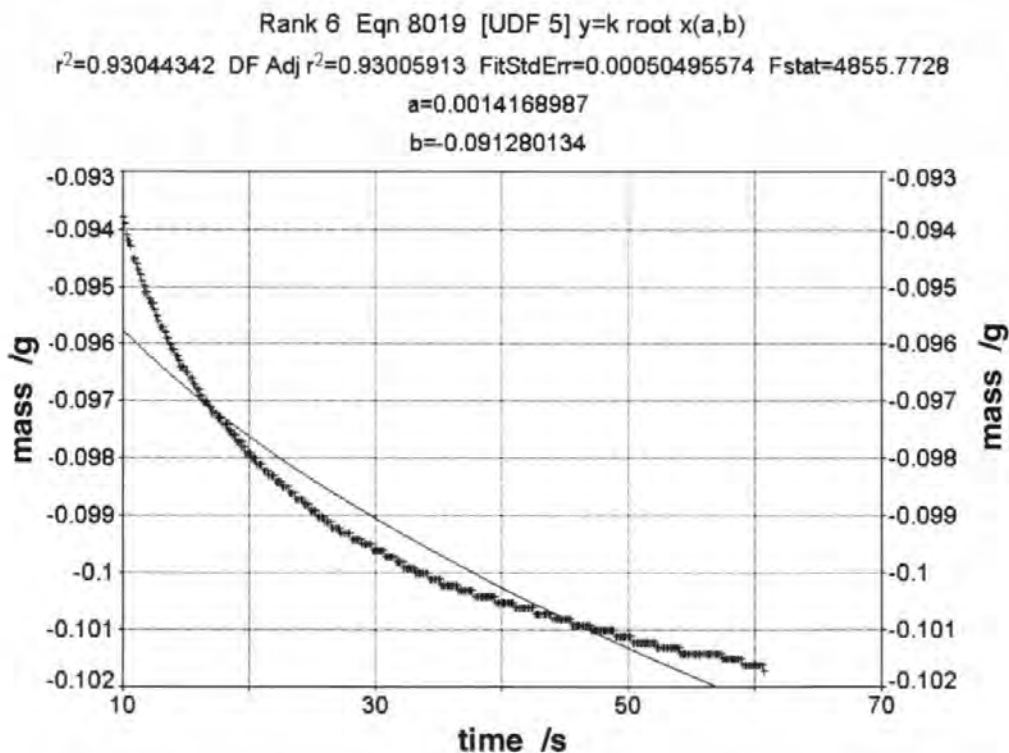


Fig. 160 Showing the poor fit of the LW approach (Eq. 85). Sample 186, porosity = 26.34 %.

This comparison strongly fortifies the previously found relationships between supersource imbibition and real time ink setting on a paper. Both methods of imbibition, namely a) with the undiluted ink, a pre-adjusted meniscus and data only for  $t \gg 0$ , and b) the direct method including the wetting jump with the diluted ink, have shown the better applicability of the prediction based on ISIT tack force-time integrals (Eq. 108) and leaves little room to argue for a LW based behaviour of fluid removal from an ink. That supersource conditions apply for viscous offset ink during imbibition in excellent correlation with thin film absorption in real time and under realistic application conditions is perhaps surprising.

### **10.5.1 Conclusions of the tack-based absorption prediction compared with the gravimetric approach**

The result of this comparative analysis means, in physical terms, that the absorption relationship for the removal of the fluid phase of an offset ink in contact with a paper coating, unlike that of pure oil or oil mixtures, is *not* dependent on a square root time law. It is seen that the supersource imbibition dynamic for offset ink, reported in section 9.10, corresponds to the thin film application of the ISIT, as measured during tack rise. Therefore, the continuity of the fluid in contact with the porous network must be maintained similarly in both cases. The concept of a delineated filtercake action was seen as unlikely during this time period at least. rather the observation supports a continuous increasing concentration gradient toward the sample or paper boundary in the case of an offset ink.

It is confirmed here that the ISIT, during tack rise, samples the viscosity and solids content of the complete ink layer irrespective of any effective longer term boundary structure formation. One has, therefore, not to correct for the effect of buoyancy of a distinctly forming filtercake (immobilised ink) in the gravimetric experiment. (This is in contrast to the approach used when considering a much more mobile flexographic ink (Gane and Ridgway, 2000) where a filtercake structure had been clearly observed).

### **10.6 Conclusions: offset ink imbibition**

The dynamic of oil absorption from an ink has been shown to be different from that of pure oil. The dynamic absorption of oil from an offset ink into a porous paper coating structure from a supersource (the case of abundant ink in contact with a porous block of coating pigment) is shown to be the same as in thin layer application (printing) during the early stages of absorption from that layer. This was confirmed by fitting the



dynamic equation derived directly from tack and ink viscosity measurements, applying to thin films, to that of experimental supersource imbibition. The determination, therefore, of ink solids and viscosity, made using the static position ink tack force-time integral of the ISIT method, has now been supported in terms of supersource rate predictions. The concentration gradient continuity of the fluid ink in contact with the porous substrate is therefore expected to be maintained in both cases. The *mass fraction of oil* lost from the ink follows a linear  $t$  absorption rate. The *absolute mass absorption* of the oil into the coating is *not* linear  $t$  related but decays according to  $\sim 1/t^2$ . The initial ink tack rise dynamic cannot, therefore, be predicted by LW.

Unlike the case of the droplet studies with low viscosity dyed fluids, in which the supersource imbibition results were dependent on porosity and  $\sqrt{t}$ , and the droplet penetration depth was dependent on permeability, we have here, in the use of high viscous suspensions of ink, a very different imbibition dynamic which applies equally well to supersource conditions as to the absorption from a thin film. The formulation of the ink is therefore critical. It has already been shown that mixed (miscible) oils is not the reason for the difference in dynamic. Therefore, the suspension characteristics of ink pigment and the solving of resins must be the key factors. These act as resistive components and allow oil loss only into the strongly acting pores exerting high capillarity. These are by definition the finer pores. We can conclude, therefore, that offset inks exaggerate the effects of fine pores, thus compounding the impact of those pores acting in the linear  $t$  regime, while the larger pores are excluded not only on inertial grounds but also on grounds of insufficient capillarity.

The previous statement is justified as follows: It is misleading to refer to a Darcy absorption length in a porous medium containing a distribution of interconnecting pore sizes, due to the previously observed phenomenon of selectively unfilled pores. The absorption dynamic is rather modelled as being related to a sequential inertial imbibition selection acting initially to exclude portions within a porous network structure, favouring the progress of fluid through the finer pores which then subsequently follow the expected viscous retardation.

By extending this theory to a computer network simulator, it has been shown that absorption into a porous network proceeds preferentially by the finer pores in that network, at first by initial inertial imbibition together with exclusion of larger pores by inertial retardation, followed by viscosity-controlled LW absorption dynamics but with the remaining inertial retardational exclusion of the largest pores. This inertially-driven selectivity leads to the establishment of a preferred pathway.

Practically, for the papermaker and printer, this means that ink drying is predicted to be retarded before full equilibrium of complete pore filling of the coating structure is established. The formation in the remaining

surface ink layer of a fine structure with high affinity will act to retain fluids within the ink once the selective "preferred" network in the coating is filled. This results in an apparently anomalous "insufficient" pore volume as "seen" by the ink as its fluid phase enters the coating structure, often observed as problems of print rub, incomplete ink setting and even sweat back and can be related to a lack of fine structure or an observed low affinity for absorption in the coating structure.

## 10.7 Development of a laser-based strain sensor for ISIT

In section 10.4.6 a scaling factor  $k$  was used to relate viscosity to the tack force-time integral terms as measured on the ISIT. It was stated that this factor could be related to already known parameters, namely  $k = (1 - e^{-d\sigma/dt T_s})$  (Eq. 104), to obtain an estimate for  $d\sigma/dt \approx 0.6 \text{ s}^{-1}$ , for a pull-off time of  $T_s \approx 0.2 \text{ s}$  and  $k \approx 0.11$  (Table 17). This is now the subject for further confirmation and the first attempt made to obtain experimental data from the ISIT for  $d\sigma/dt$ . Such data would furthermore allow an estimation of the work of tack.

To pursue this confirmation required a displacement sensor to monitor the position of the tack wheel as a function of time. A limiting factor was the mechanical tolerances of the ISIT components involved in the tack wheel motion. Conformation to an uneven substrate demands that the "play" in the tack wheel transverse mounting must be sufficient to ensure even deformation of the rubber offset blanket-like material on the tack wheel. This prevented a quantitative absolute analysis of position, but a relative semi-quantitative assessment was possible.

The requirements for the sensor were that it should work in a non-contact mode, it should fit dimensionally into the apparatus setup, and have a practically achievable resolution of approximately  $1 \mu\text{m}$ . The easiest and most economic approach was identified based on a laser cantilever method. The principle is shown in Fig. 161. The motion of the tack wheel is transferred via its extended axis to a thin connected mirror pivoting around a fixed base-point.

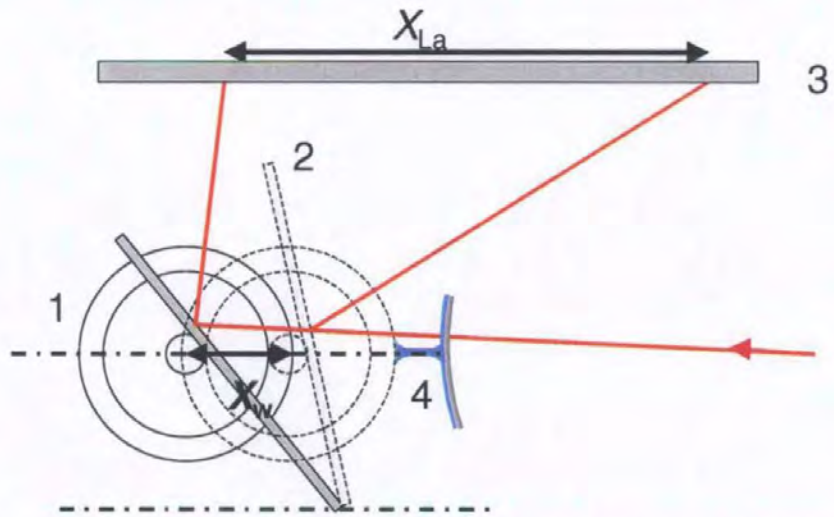


Fig. 161 Schematic of the laser cantilever: (1) tack wheel moving a distance  $x_w$ , (2) thin pivoting mirror guided by the extended axis of the tack wheel. The red lines indicate the laser beam, (3) is the plane on which the projected laser dot motion is monitored by means of a high-speed camera, (4) represents the printed paper stripe with the ink-film (blue) and the elongated ink filament (greatly exaggerated for clarity).

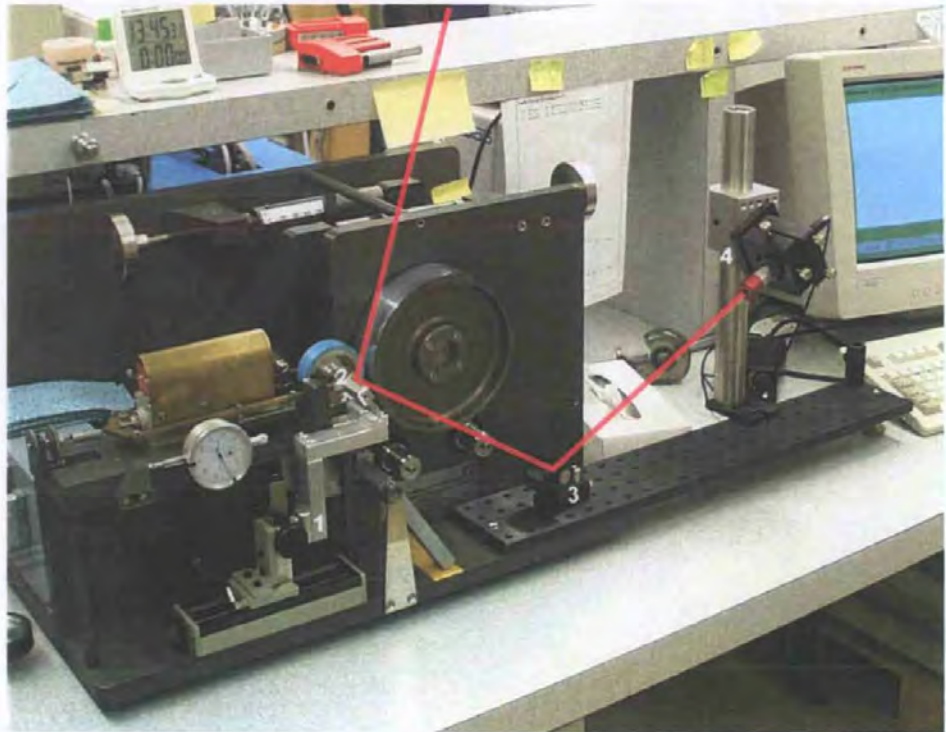


Fig. 162 The laser setup on the ISIT device (no ink or paper applied): (1) the  $xz$ -table holding the mirror, (2) tack wheel with extended axis pivoting the mirror, (3) beam steering unit, (4) diode laser. The laser beam is drawn schematically into the image.

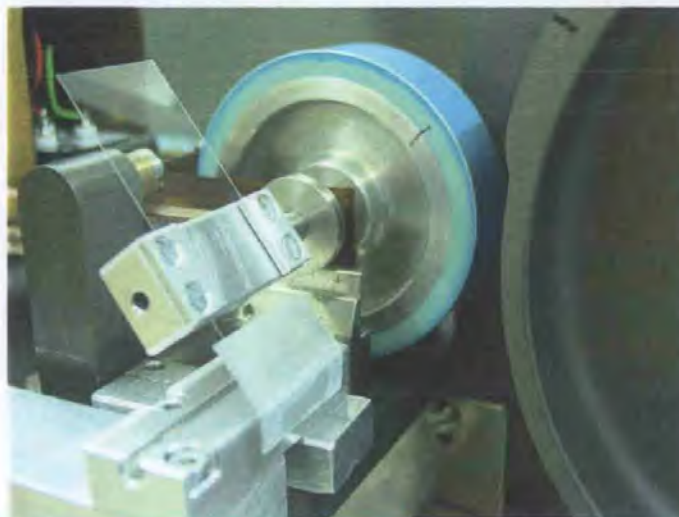


Fig. 163 Detail view of the mirror (glass slide) and the tack wheel, Nr.(2) in the previous figure.

## 10.8 Devices

The setup is shown in Fig. 162. All the parts used from Edmund Industrial Optics<sup>31</sup> and Coherent<sup>32</sup> are detailed in Appendix D. The  $xz$ -table (1) consists of a precision 6.5" screw travel movement with an L-bracket mount. The mirror consists of a microscope slide with a thickness of approximately 0.05 mm and a weight of 0.53g. At first a gold-plated slide was used but an uncoated slide shows sufficient reflection and further provides a transmitted reference beam helpful in controlling the alignment of the system. The mirror is fixed via a sliding holder/adapter which was machined from aluminium, Fig. 163. The adapter has a clearance which permits the mirror a sliding motion, where friction was minimised by applying a thin layer of graphite. The most practical way to provide a pivoting point fulcrum was to use a household self-adhesive tape.

The laser diode was mounted on a bench plate using a mounting rod with carrier and an angle bracket. A beam steering unit, consisting of a mirror which is freely positionable in 3 dimensions, was used to reflect and guide the laser beam to the mounted mirror as shown in Fig. 162. The laser diode had a circular beam diameter of 1.2 mm, a wavelength of 635 nm and a power of 4 mW, and was held by a 4-axis laser mount. The laser was powered by a LabLaser universal power supply.

The laser beam, reflected by the pivoting mirror, projected a path upwards toward the laboratory ceiling where a millimetre-scale graph paper was fixed upon which the laser dot or point was observable. The motion of the laser

<sup>31</sup> Edmund Industrial Optics, 101 East Gloucester Pike, Barrington, NJ 08007-1380 USA

<sup>32</sup> Coherent Auburn Group, Lindbergh Street, Auburn, CA 95602-9295 USA

dot was recorded with a high-speed camera, namely a MotionScope PCI 500 from Redlake MASD Inc.<sup>33</sup> A rate of 250 frames per second was used.

The recorded frames were analysed with the automated software package WINanalyse Motion Analysis<sup>34</sup>. This program detects the position of the marked features (here the laser point) in all of the captured frames, and provides for both 2D and 3D analyses on the sequence of images to derive the velocity and acceleration of the dot, providing the angles of deflection between defined (marked) points of reference are known. The analysis was effectively calibrated in this case directly by referring to the millimetre grid on the projection plane, without the need for the more generalised reference points.

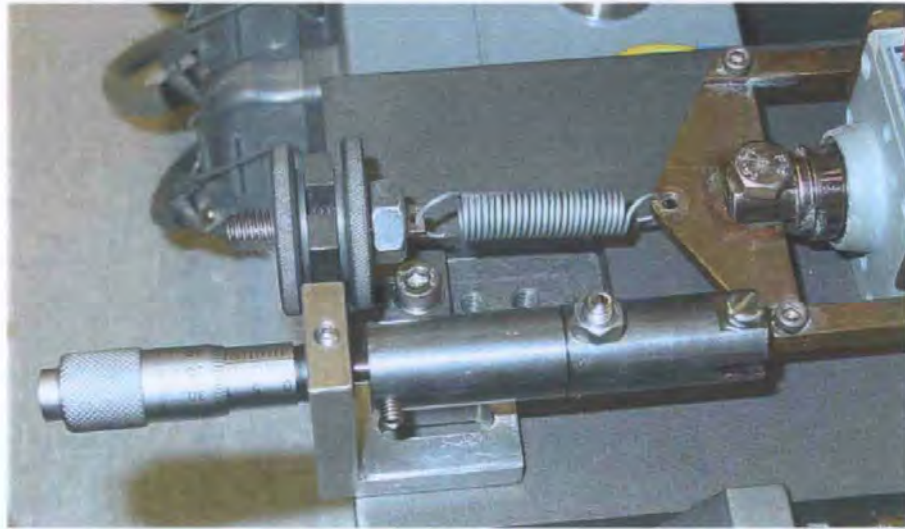


Fig. 164 *Micrometer screw with adapter. For the calibration of the ISIT tack wheel motion it is mounted in place of the coil spring in the picture.*

The ratio of magnification from the micrometer displacement of the tack wheel to the recorded motion of the laser point was performed by direct mechanical calibration. A micrometer screw gauge (Mitutoyo, range 1 000  $\mu\text{m}$ , precision 2  $\mu\text{m}$ ) was used to displace the tack wheel in increments of 50  $\mu\text{m}$  (see Fig. 164). After each increment, the position of the laser point was marked on the millimetre graph paper. The marks were then measured manually using a vernier caliper, the results from which are shown in Fig. 165. It is shown that an empirical linear function, as plotted and written in Fig. 165, gives us a reasonable fit of the data points. Therefore, the transformation of the data between observed displacement on the millimetre scale and the actual tack wheel axis displacement can be made as follows:

$$6.5922 x_{La} + 2.4389 = x_w$$

Eq. 110

<sup>33</sup> Redlake MASD Inc. San Diego, CA 92121-1097 [www.redlake.com](http://www.redlake.com)

<sup>34</sup> Mikromak GmbH, am Wolfsmantel 18, D-91058 Erlangen, Germany, [www.mikromak.com](http://www.mikromak.com)

where  $x_{L_d}$  is the distance moved by the laser point in mm and  $x_w$  is the displacement of the tack wheel in  $\mu\text{m}$ .

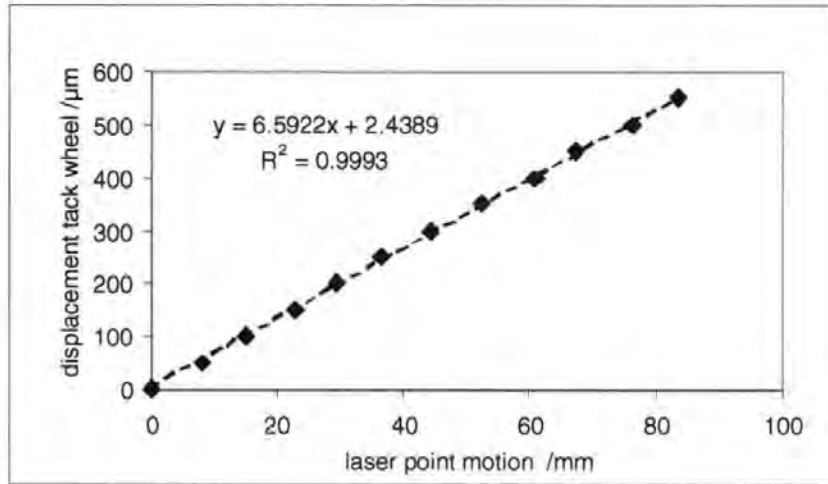


Fig. 165 Calibration of laser point to tack wheel displacement. 0 on the x-axis represents the point where the tack wheel touches the roll of the ISIT device.  $\text{StdErr} = 4.92 \mu\text{m}$ .

## 10.9 Measurement procedure

The same commercial offset paper (Ikonofix<sup>35</sup>  $150 \text{ gm}^{-2}$ ) was used as in the previous tack experiments together with exactly the same instrumental settings and the same ink (section 10.4.4). The first pull-off point was used for the analysis where the time of the pull-off,  $T_p$ , as shown schematically in Fig. 148b, was recorded as 0.15 s from the individual force-time integral. The position of the laser point was recorded as a function of time and described in the previous section. The captured motion/time data were transferred from WINanalyse to MS Excel. The data for the distance displaced by the laser point during the pull-off are shown in Fig. 166.

<sup>35</sup> Ikonofix is a product name of Zanders Feinpapiere AG, D51439 Bergisch Gladbach, Deutschland

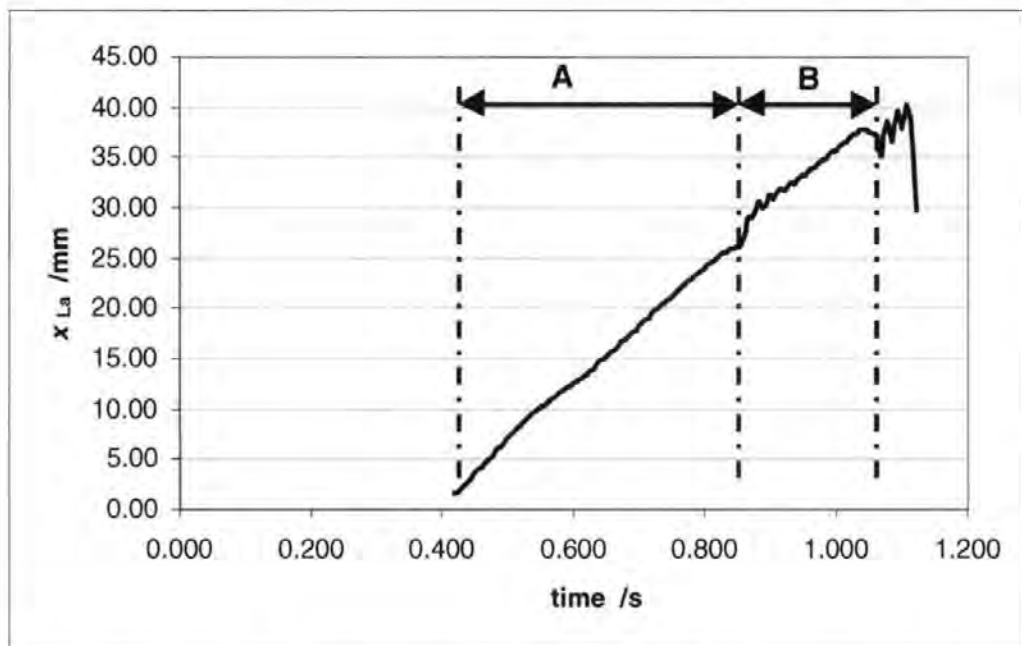


Fig. 166 The displacement,  $X_{La}$ , of the laser point on the projection plane as recorded by the high-speed camera.

Clearly, at least two different regimes are seen, denoted as A and B in Fig. 166. Careful observation of the tack wheel, and a short sequence recorded with the high-speed camera focussing on the wheel itself revealed that the quasi-linear regime A is a manifestation of the decompression of the system (paper, adhesive tape and rubber of the tack wheel, confirmed by recording the action of the tack wheel separation in the absence of ink). Subsequently, the second regime, initiated by a short transitional acceleration, shows also linear displacement in time which means a regime of overall constant velocity with some small superimposed oscillations, as shown magnified in Fig. 167. This is the effective range where the tack wheel is pulled-off combating the cohesive force of the ink layer, and thereby probing the tack-force of the viscosifying ink layer. The observed time span of  $\approx 0.2$  s in this second region of pull-off matches quite well the time span of 0.15 s as recorded by the ISIT for the same event (compare Fig. 148b).

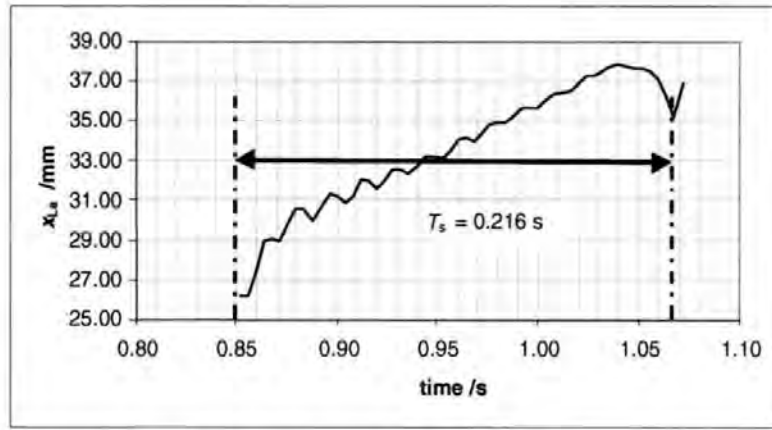


Fig. 167 Magnification of regime B, the effective pull-off in Fig. 166.

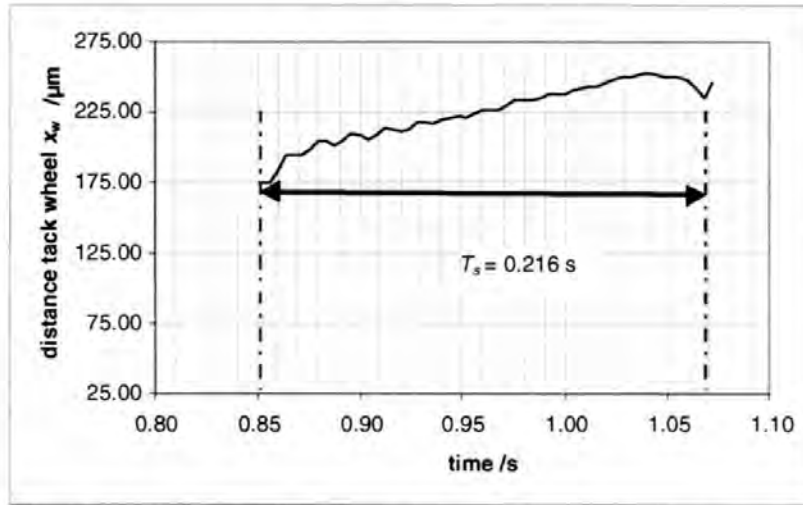


Fig. 168 The regime B, the effective pull-off transformed to the tack wheel displacement using Eq. 110.

In Fig. 168, the motion of the laser point is transformed to the displacement of the tack wheel using Eq. 110 which reads from the graph as  $x_w = 76 \pm 5 \mu\text{m}$ .

## 10.10 Results and discussion

We can now go back to the proposals for elongational flow made earlier and verify the assumptions made in Eq. 99 - Eq. 104. We want to obtain a value for  $d\varepsilon/dt$ . From Eq. 99 we differentiate

$$\frac{d\varepsilon}{dt} = \frac{d[\ln(L/L_0)]}{dt} = \frac{1}{L} \frac{dL}{dt}$$

Eq. 111

The expression, Eq. 111, describes the condition that a fluid sample is extended to length  $L(t)$  with a rate of extension of  $dL(t)/dt$ . In this experiment,  $dL(t)/dt$  is represented at the end point of the extension by  $dx_w(T_s)/dt$ .

However, at the point of fracture we reach a discontinuity at  $L(T_s)$ . In fact, the observed value of  $x_w = 76 \mu\text{m}$  is



likely to err on the small side for  $L(T_s)$  as it marks the point at the catastrophic failure of the ink and not a value during the final filamentation. The result is, therefore, highly likely to yield a slightly too high value for  $\varepsilon$ .

By applying the present displacement notation, using  $x_w = 76 \mu\text{m}$  for  $L(T_s)$ , and an extension rate of  $dx_w/dt = 242 \pm 158 \mu\text{ms}^{-1}$  as derived by WINanalyse and averaged (arithmetic mean) over 55 datapoints, we arrive at the final solution of

$$\frac{d\varepsilon}{dt} = \left\langle \frac{dx_w}{dt} \right\rangle \frac{1}{x_w} = 3.18 \text{ s}^{-1} (\pm 2.08)$$

Eq. 112

The large error is due to the uncertainty of the displacement co-ordinates allied with the mechanical oscillations derived from the coupling between the mirror and the tack wheel axis. Despite the crudity of the experiment we see that the lower extreme,  $1.1 \text{ s}^{-1}$  lays close to the earlier prediction of  $0.6 \text{ s}^{-1}$ . Furthermore the scaling factor  $k$  could contain also a minor contribution from other forces, as proposed in Eq. 88.

We also cannot be sure that the use of the Trouton ratio is in fact wholly applicable. The work of tack measurement/separation,  $W_s$ , can be calculated as the tack force multiplied by the displacement. To do this, since the separation force and displacement change with time, the tack force must be plotted against the corresponding displacement at each time point of the observation, i.e. the area under the curve of  $F(t)$ , defined during each single pull-off, against  $x_w(t)$  must be obtained:

$$W_s = \int_0^{T_s} F(t) \dot{x}_w(t) dt$$

Eq. 113

Actually since the velocity is constant, so it is possible to take the force-time integral and multiply it directly by the velocity such that

$$W_s = \frac{dx_w}{dt} \int_0^{T_s} F(t) dt$$

Eq. 114

The work of tack at the first pull-off point can now be calculated to be  $0.152 \text{ mJ}$ .

## 10.11 Summary and conclusions ISIT strain measurements

A first confirmation was achieved that the proposed extensional model describes reasonably well the tack force in terms of uniaxial viscous extension. It is difficult to obtain an absolute measurement of  $\dot{\epsilon}$  (the strain rate) due to the discontinuity at the point of filamentation, although the observed value is not far from that predicted via the  $T_s$ .

A further consequence is that out of the many proposed components of the tack force (10.4), the viscous term is the most important, given the boundary conditions of a thin layer of ink and a microrough, permeable paper. The small deviation of  $d\delta/dt$  from the predicted value based on the scaling factor  $k$  and separation pull-off time  $T_s$ , suggests perhaps that a minor contribution from other forces, as proposed in Eq. 88, cannot be completely ruled out.

These conclusions would also mean that a device like the ISIT, which is based on uniaxial separation of two adjacent surfaces, one of which is a permeable porous network, under constant velocity or acceleration conditions, could be used after refinement as a simple extensional rheometer for thin films of fluids/materials on such porous surfaces.

## 11 Conclusions

The main conclusions are summarised following the same division as used in the background theory chapter.

In the summary that follows the conclusions, the findings are listed following the initial hypotheses of the thesis.

### 11.1 Environmental

Vegetable oil derivatives cannot match totally the properties of aliphatic mineral oils in terms of surface tension, density and viscosity. This fact is now, however, to a great extent emasculated as a result of the main finding that manipulation of the mineral-based pore structure of a paper coating is a flexible and therefore convenient tool to steer imbibition processes. This is arguably easier and more effective than changing liquid properties as any one liquid property is invariably connected with other physical properties. For example, a decrease in viscosity is generally accompanied by an increase in volatility. To raise the liquid density would require, for example, compounds with halogen atoms within the molecule. The limitations for changes in fluid and surface energy properties are dictated by process usability, toxicity and industrial pricing. Additionally, the range to adjust these properties covers only a few decades.

In pore structure design the possibilities range from the adoption of nano particles up to macroscopic sizes, covering an array of particles over 5 orders of magnitude influencing the effective equivalent hydraulic capillary of the structures. Furthermore, the possibility is given in paper coating of involving different geometries using platy, blocky or needle-shaped particles and a combination of these by controlled costructuring or agglomeration, (Gane *et al.*, 1999).  $\text{CaCO}_3$  was shown to meet environmental criteria as well as the structural demands and the provision of fine pores of low aspect ratio extends the range of absorption equivalent radii beyond that previously suspected based on traditional imbibition theory as described by LW. The environmental advantage of using such a high geologically renewable resource as ground  $\text{CaCO}_3$  is now compatible with industrial application.

### 11.2 Scientific

A simple *droplet absorption* method has been used which permits the study of absorption of limited volumes of fluid into bulk samples of controlled porosity. Experimentally it has been shown that there exists unfilled volume

within a pore network, defined by the selective action of the wetting front as it progresses during imbibition into compressed pigment structures. This unfilled fraction passes through a maximum as a function of porosity, i.e. the observed distance of absorption into a porous network of coating pigment is anomalously greater than would be expected if the total pore volume were to be filled even when using a wetting fluid. This is contradictory to the prediction made by the simple LW relationship, which predicts that large pores fill faster than fine ones and that a porous structure would be expected to fill as the fluid front progresses, especially at high porosity. Since the parameters of surface energy and wetting have been kept unchanged, in this study as a function of porosity (applicable also in the case of many paper coatings), pore diameter and geometry have been identified as the controlling factors.

The maximum in unfilled volume was seen as a transition/discontinuity during *limited volume droplet* imbibition, where the ratio of droplet surface spread compared with absorption followed this transition. The practical implication is that, under differential compressions, for example during calendering, a coating structure can create strongly varying absorption characteristics, leading in offset printing to undesirable print unevenness (mottle) and problems of differential ink setting, resulting in set-off and print rub, both related to poor ink drying.

Associated with this transitional spread phenomenon is a potential transition in the coating layer absorption mechanism which may be related to the various pore sizes in a network structure. With increasing breadth of pore diameter distribution a mechanism of pore structure differentiation between large and fine pores on a short timescale, and/or pore draining after longer times, may occur. This effect is further dependent on the pore-to-throat diameter ratio and the available volume of the smaller voids. Additionally, the presence of a strongly diverging pore entry geometry may lead to a potential imbibition termination and result in some pores being competitively unfilled.

In equilibrium *supersource* imbibition, corresponding to the situation of abundant fluid at all stages of absorption, the progress to complete saturation of the pore volume is fulfilled independent of the range of fluid types studied, and corresponds in porosity value, within the macroscopic limits of the method, to the fully corrected mercury porosimetry porosity. The rate of imbibition under supersource conditioning for pure fluids was seen to be controlled mainly by porosity (for the structures under study).

In dynamic *supersource* imbibition a  $\sqrt{t}$  behaviour was observed for the equilibrium timescales considered. But on comparing structures with different skeletal particle size but having the same mercury intrusion derived  $r_{50}$

values, a failure to scale to consistent LW parameters was observed. In this work, the failure to scale was demonstrated for well-defined structures with geometrical similarity and constant surface chemistry. Even greater divergence from LW scaling is therefore to be expected comparing structures having different pore morphology despite having a similar pore size. [This study has not been made specifically here but forms part of the research by Bodurtha and co-workers, (Bodurtha *et al.*, 2000)].

The *mass fraction of oil* lost from an offset ink was seen to follow a linear  $t$  absorption rate in both supersource and real time printing experiments. The *absolute mass absorption* of the oil into the coating decays to a first approximation according to  $\sim 1/t^2$ . The initial ink tack rise dynamic in offset printing cannot, therefore, be predicted by LW.

It is found misleading to refer to a Darcy absorption length in a porous medium containing a distribution of interconnecting pore sizes, due to the selectivity of the wetting pathway. The absorption dynamic is advantageously modelled as a sequential inertial imbibition selection acting initially to exclude portions within a porous network structure favouring the progress of fluid through the finer pores which then subsequently follow the expected viscous retardation.

By extending the inertial selection theory to a computer network simulator, it has been shown schematically that absorption into a porous network indeed proceeds preferentially by the finer pores in that network, at first by initial inertial linear  $t$  imbibition in fine pores together with exclusion of larger pores by inertial retardation. This is then followed by viscosity-controlled LW absorption dynamics in those finer pores but with the remaining inertial retardational exclusion of the largest pores. This inertially-driven selectivity within the network, leads, subject to fluid availability, to the establishment of a preferred pathway.

A hysteresis in *permeability* was observed when performing an up-down sweep in driving pressure. Taking into account the effects of preferred pathway flow (and the potential for film flow) during imbibition, it is postulated that some proportion of pores remain unfilled despite the appearance of saturation in mass terms. This leads to entrapped air or vapour phase in microscopic ganglia. Residual air may dissolve in polar liquids but does not dissolve in the aliphatic mineral oil used in the experiments and typical of the oils in offset printing inks. Structures without a delineated pore-throat structure, will probably lead to a more complete elimination of bubbles. The experimental permeability when air is effectively removed is shown not to be a function of porosity. This is in contrast to supersource imbibition. The observed permeability of the pigment compacts passes through a local maximum at a fractional porosity of 0.263 with a subsequent decay at a porosity of  $\sim 0.27$ .

This behaviour tracks well with the observations made with the droplet absorption where the level of liquid content in the pore network behind the wetting front goes through a minimum in the porosity regime between 0.24 - 0.28.

### 11.3 Paper technology

Analysing the Bosanquet equation and applying a wetting algorithm in a pore-throat network computer model made it possible for the first time to give a plausible explanation as to why in some cases coarse paper coating structures with large pores absorb pure liquid slower in the short timescale than a coating with finer pores, each having the same porosity.

Combining this finding with further results from the computer network simulator it was possible to show that imbibition is slowed down when monomodal pore size distributions are used. The imbibition behaviour becomes increasingly dependent on viscous retardation and hence follows the Hagen-Poiseuille prediction. This limits the use of so-called steep curve pigments (narrow particle size distributions), which though they may have desirable optical properties, display unfavourable liquid absorption behaviour in respect to the setting of inks.

It has been shown that it is possible to use in-situ ink-on-paper tack measurements based on the pull-off technique, as used by the ISIT tester, to determine a model for the viscosity and solids content of an offset ink as the ink begins to set on a paper surface. Under these conditions, the separation force is related predominantly to the viscous properties of the cohesive ink layer. This technique is proven to maintain the cohesion between the wet mobile ink layer and the immobilising interface between the ink and paper surface, and precludes the concept of splitting within a distinct mobile layer above that of a delineated forming filtercake. The continuity between the mobile ink and the upconcentrating interface is thus maintained, and the increase in measured tack is related to the fluid loss and viscosity increase as defined through a uniaxial extensional viscosity model. The rate of oil loss is shown to match that of the oil uptake under supersource conditions and diverges strongly from LW.

Practically, for the papermaker and printer, this means that ink drying is predicted to be retarded before full equilibrium of complete pore filling of the coating structure is established. The formation in the remaining surface ink layer of a fine structure with high affinity will act to retain fluids within the ink once the selective "preferred" network in the coating is filled. This results in an apparently anomalous "insufficient" pore volume

as "seen" by the ink as its fluid phase enters the coating structure, often observed as problems of print rub, incomplete ink setting and even sweat back and can be related to a lack of fine structure or an observed low affinity for absorption in the coating structure. To enhance print performance, the paper coating technologist must seek to optimise the distribution between coarse and fine pores, and their geometry, within the limits set for optimal coverage and gloss/mattness.

## 11.4 Summary

It was shown in this thesis that:

- ◆ The description of the extent of imbibition as dependent on the square root of time, and hence describable by the Lucas Washburn equation, is simplistic and misleading, and masks interesting and useful details of the imbibition process. These have been identified by:
  - Application of the Bosanquet equation in a network simulator showing why, in some cases, large pores associated with coarse pigmented paper coatings absorb pure liquid slower than coatings with finer pores, having the same porosity.
  - Using a simple *droplet absorption* method, showing that there is
    - unfilled pore volume behind the wetting front, the degree of which is not a monotonic function of porosity
    - surface spread liquid relative to absorption which exhibits a marked deviation from a consistent ratio as a function of porosity, following the effect of selectively unfilled pore volume.
  - Observing *equilibrium supersource* imbibition: the equilibrium saturation is independent of the range of fluid types studied, and trends with porosity as measured by mercury porosimetry
  - Recording *dynamic supersource* imbibition, which shows an overall  $\sqrt{time}$  dependence of the uptake volume and a monotonic dependency on porosity; however
    - at shorter times and at greater precision, deviations from this behaviour are evident

- the volume-based effective hydraulic radius values ( $r_{chcV}$ ) derived from the  $\sqrt{time}$  dependence for coarse and fine samples with the same solid and fluid, trend differently for the intrusion measured radii ( $r_{50}$ ) values derived from mercury porosimetry, the trend lines are different in both slope and value, demonstrating that the Lucas Washburn equation provides only relative fitting parameters for surface interactions rather than realistic structurally based parameters,
  - when the structure is nearly full, the absorption volume increases asymptotically toward effective saturation, rather than maintaining proportionality to  $\sqrt{time}$ , which may imply transient unfilled pore volume.
  - Hysteresis was observed when the liquid permeability of blocks was measured at increasing and then decreasing pressures, suggesting unfilled pore volumes despite mass-determined saturation. Calculations showed these volumes to be smaller than detectable by the supersource gravimetric experiments.
- ◆ Additional information can be gained about imbibition into network structures of porous media by using improved and novel experimental methods applied to specifically prepared experimental samples. This was achieved by preparing and using:
- A set of variously compressed porous tablets, unique in having different porosities and pore size distributions but the same surface chemistry and particle shapes.
  - A study of droplet equilibrium distribution within the porous samples, analysed by sectioning the samples and applying image analysis of the dyed area.
  - A dynamic imbibition technique based on a time dependent gravimetric determination of supersource imbibition. This method provided fast and precise data which overcome the limitations of the traditional optical evaluation of wetting front or reservoir level position. A further advantage was that it provided independent assessment of volume imbibition without having to assume a uniform wetting front.
  - A permeability technique employing resin-embedding to mount the porous tablets into a specially constructed liquid permeameter.



- ◆ That novel experimental methods, coupled with the knowledge gained about imbibition, can give useful insights into the process of printing, specifically the setting of ink.
  - Tack measurements, using an ISIT tester, have led to the development of a model for the viscosity and solids content of an offset ink as the ink begins to set on a paper surface.
  - The *mass fraction of oil* lost from the ink is seen to follow a linear  $t$  absorption rate.
  - The *absolute mass absorption* of the oil into the coating decays according to  $\sim 1/t^2$ , therefore the initial rate of increase in ink tack cannot be predicted by use of the Lucas Washburn equation.
  
- ◆ Insights into the fine structure of the imbibition process can be gained by the use of a computer model of a pore-throat interconnected 3-D network
  - The inclusion of inertia into the equation of imbibition within the network simulator caused behaviour different from Lucas-Washburn, with imbibition rates exhibiting maxima with respect to individual selected throat size
  - A demonstration that preferential imbibition is observed within the entire simulated network. which, on the basis of the observed general behaviour, was shown to be significantly different from that predicted by the Lucas-Washburn equation
  - Use of a liquid permeater to reveal that the liquid permeability of the porous tablets is not a monotonic function of porosity. This unexpected behaviour is analogous to that found in the droplet absorption experiments. Excellent agreement was found between this behaviour and the trend in liquid permeabilites calculated by the network simulator.
  
- A consideration of ink setting behaviour in the context of the previous experiments and simulations suggests that ink drying is retarded before the pore filling has reached equilibrium, and that imbibition will be significantly limited to preferential pathways. Particles solved in resins within the surface ink layer can form a fine structure which can itself retain fluids. This competitive situation can result in an apparently anomalous insufficient pore volume as sampled by the ink despite the use of highly porous coatings, as its fluid phase enters the coating structure, often observed as problems of incomplete ink setting especially on matt papers.

- ◆ An improved knowledge of imbibition processes will allow the more effective use of a wider choice of environmentally friendly ink and coating materials, such as vegetable oils and  $\text{CaCO}_3$  as a coating pigment respectively.
- Manipulation of the pore structure is a flexible and therefore convenient tool to steer imbibition processes, and has been facilitated by the present studies which show that the opportunities are greater than predicted by traditional theory. The improved engineering of pore structures will enable enhanced use of optimised inks based on a variety of liquids, imbibing vegetable oils, their derivatives and ultimately aqueous systems.

## 11.5 Future Work

The methodology developed during the work presented in this thesis enables future study to be readily undertaken into the imbibition and permeation behaviour of a wide variety of porous network structures, including a variety of pigmented structures (using also pigments other than calcium carbonate), in paper and coatings, such as micro-permeable paints, as well as geological and powder-based technologies. Work is presently underway at Omya AG to implement specific pigment designs and mixtures for digital and ink-jet printing applications. These involve novel pigments, which have been especially developed, incorporating many of the principles built-upon in the thesis, for obtaining the optimal imbibition properties.

Taking the study of permeability in real samples further, it would be of value to study various liquids, especially focusing on the relationship of their vapour pressure in relation to application conditions, in order to understand and to take possible advantage of micro-bubbles of vapour within the structure after initial liquid imbibition. Uses might include catalysis, micro-emulsion reactions and the formation of nano-composites. Liquids, such as water, which can dissolve air easily, should show interesting behaviour through their permeation hysteresis and contrast against that shown for oil in this study. Extension to other porous materials that do not display a delineated pore-throat structure (e.g. woods and rigid foams) might be considered as a valuable extension, especially when considering environmentally friendly coatings for materials protection.

In terms of a more fundamental understanding of dynamic liquid imbibition, there is still a need to study the microscopic and molecular dynamic-driven shape of a fast moving meniscus under various flow and boundary conditions. The properties of the liquid, local "capillary" radii, and, most importantly of all, the definition or otherwise of a contact angle in the presence of adsorption phenomena (liquid layers) at the material walls, are all

critical issues. In porous media it would be valuable, for example, to have experimental evidence concerning the velocity and rate of the Haines' jump and Gibbs' hinging phenomena. In both cases, high speed cameras provide now the means to perform such measurements at reasonable costs. Tomography is also a useful tool for investigating liquid behaviour within porous media, and the needed resolution is continually improving.

The novel experimental determination of the rheological behaviour of viscous inks and pastes, introduced in the thesis via the application of the strain sensor technique applied to ink-on-paper tack measurement (ISIT), will enable a wider study of the extensional behaviour of a variety of thin films, which hitherto has been curtailed for the need of a suitable measurement system. Once again, this would not only be of value to the paper and printing industry but also to the application of thin polymer and pigment-filled coatings on a variety of permeable and non-permeable substrates. The issue of extensional viscosity and visco-elasticity in comparison with empirical value parameters, like "shortness" (the feel) of a liquid or suspension, is of further interest beyond the printing and coatings technologies, perhaps entering the varied fields of food technology, texture engineering and cosmetics.

## List of used symbols and abbreviations

$a, b$	Fitting constants
$A$	Area
$A_F$	Footprint area in tack measurement
$A_p$	Printed area
$Bo$	Bond number
$Ca$	Capillary number
$d$	Diameter
$d_{50}$	Diameter of 50% of the features having fulfilled a condition (Hg intrusion, particle size)
$ehc$	equivalent hydraulic capillary based on a Darcy length
$ehcDarcy$	equivalent hydraulic capillary based on permeation match.
$ehcV$	equivalent hydraulic capillary based explicit on a volume uptake
EHR	used in the authors earlier publications for $ehc$
$F$	Force
$F_{ad}$	Adhesion force
$F_{base}$	Force due to the impulse when the sample base is wetted
$F_{ca}$	Force due to cavitation voids
$F_{contact}$	Force caused by the wetting line around the sample
$F_i$	Force due to inertia
$F_L$	Force due to Laplacian "underpressure in the liquid
$F_m$	Force due to meniscus tension
$F_{side}$	The force exerted by side-wall wicking
$F_{total}$	The effective wetting force
$F_{vd}$	Force due to viscous dissipation
$F_w$	Wetting force
$F_{wi}$	The wetting forces exerted by the liquid lifted inside the structure
$F_{wo}$	The wetting forces exerted by the liquid lifted on the outer surfaces of the structure
$F_\eta$	Force due to (elongational) viscous friction
$g$	Acceleration due to gravity
$G$	Gibbs free energy
$h$	Height
$h_0$	Initial ink layer thickness
$h_T$	Remaining ink layer under tack measurement
$k$	Scaling factor used in extensional viscosity applications
$K$	Permeability
$L, l$	Length
LW	Lucas - Washburn
LvW	Lifshitz- van der Waals
$m$	Mass
$m_{bs}$	Mass of back split ink
$m_i$	Mass of ink
$m_{oil}$	Mass of oil
$m_p$	Mass of printed ink
$m_{solid}$	Mass of solids
$P$	Pressure
$P_e$	External Pressure
$q$	Volumetric flow rate
$Q$	Pore row spacing
$r$	Radius
$r_{50}$	$d_{50}/2$
$r_{ehc}$	Equivalent hydraulic radius based on a Darcy-length approximation including porosity
$r_{ehcDarcy}$	Equivalent hydraulic radius, based on steady flow liquid permeation
$r_{ehcV}$	Equivalent hydraulic radius based on imbibition volume
$Re$	Reynolds number

$R_{\text{split}}$	Split ratio between inked and contacted surfaces
STC	Surface tension component
$t$	Time
$T_s$	Separation time during tack pull-off
$u$	Velocity of separation during tack measurement
$V$	Volume
$V_{\text{absorbed}}$	Internal pore volume as probed by imbibed liquid
$V_{\text{sample}}$	The outer volume of the sample
$V_{\text{simdyed}}$	Rotationally symmetrical spheroidal segment volumes representing a model of the droplet spatial distribution
$V_{\text{skeleton}}$	The volume of the skeleton of a porous sample
$V_{\text{thoodyed}}$	Theoretical dyed volume assuming complete liquid saturation in pores
$W$	Work
w/w	weight/weight
$x$	Distance, mostly position of liquid front
$x_{\text{La}}$	Distance of laser point motion
$x_w$	Displacement of tackwheel
$y, z$	Co-ordinate position
$\Phi_{\text{oil}}$	Added oil content
$K$	Permeability
$\varepsilon$	Extensional strain
$\phi_{\text{absorbed}}$	Porosity as probed by imbibed liquid
$\phi_{\text{Archimedes}}$	Porosity measured by Archimedes balance
$\phi_{\text{Hg}}$	Porosity determined by mercury intrusion
$\gamma$	Surface free energy or surface tension, strain in rheology context
$\gamma^{\text{AB}}$	Acid-base components of surface free energy
$\gamma_{\text{LS}}$	Liquid solid interfacial tension
$\gamma_{\text{L.V}}$	Liquid-vapour interfacial tension
$\gamma^{\text{L.VW}}$	Lifshitz- van der Waals components of surface free energy
$\gamma_{\text{SV}}$	Solid vapour interfacial tension
$\eta$	Viscosity
$\eta_p$	Process viscosity
$\eta_{\text{pu}}$	Uniaxial extensional process viscosity
$\lambda$	Filter cake thickness
$\theta$	Contact angle
$\rho$	Density
$\rho_{\text{I}}$	Ink density
$\Xi$	Flow capacity
$\tau$	Stress
$\tau_0$	Characteristic relaxation time
$\psi$	Connectivity
$v_p$	Liquid velocity in a pore

## **Appendices**

### **Appendix A , tables**

next page: **Table A1 Overview of pigment tablets used as porous structures**

Sample number/name	Pigment type	$\phi$ %	Throat type	$d_{min}$ $\mu m$	$d_{max}$ $\mu m$	Throat skew	Pore skew	$\psi$	$d_{50exp}$ $\mu m$	$d_{50sim}$ $\mu m$	$Q$	$K$ (methane) mD	$K$ (nitrogen) mD	$K$ (liquid) mD	Skeletal density g/cm <sup>3</sup>	Bulk density g/cm <sup>3</sup>	Intruded volume cm <sup>3</sup> /g	Bulk modulus MPa
69	coarse	37.32	con	0.004	1.22	-0.5	1	3.0	0.198	0.186	1.28	1.48E-02	1.44E-02	2.75E-03	2.84	1.71	0.2218	44258
28	coarse	35.53	con	0.004	1.22	-0.44	1	2.8	0.196	0.167	1.27	1.51E-02	1.47E-02	3.33E-03	2.76	1.73	0.2075	82547
31	coarse	31.76	con	0.004	1.22	-0.28	1	3.0	0.156	0.165	1.41	7.69E-03	7.45E-03	1.36E-03	2.78	1.86	0.1726	73089
47	coarse	30.27	con	0.004	1.22	-0.13	1	2.6	0.139	0.123	1.33	1.42E-03	1.37E-03	1.61E-04	2.87	1.90	0.1629	26622
57	coarse	27.31	con	0.004	1.22	-0.04	1	2.6	0.121	0.109	1.41	8.68E-04	8.38E-04	9.26E-05	2.79	1.95	0.1419	76746
177	coarse	26.73	cyl	0.001	1.22	0.87	1.1	3.4	0.118	0.105	1.23	1.47E-03	1.42E-03	1.67E-04	2.77	1.97	0.1377	80768
177	coarse	26.73	con	0.004	1.22	-0.03	1	2.7	0.118	0.123	1.46	1.15E-03	1.11E-03	1.91E-04	2.77	1.97	0.1377	80768
74	coarse	24.38	con	0.004	1.22	0.14	1	2.9	0.096	0.105	1.60	1.23E-03	1.19E-03	1.79E-04	2.85	2.07	0.1188	31661
15	fine	32.33													2.63	1.77	0.1827	37522
16	fine	29.90													2.64	1.85	0.1612	40982
253	fine	27.19													2.67	1.94	0.14	36157
252	fine	25.65													2.64	1.97	0.13	61975
NOT USED FOR MODELLING																		
70	coarse	27.04	cyl	0.004	1.22	0.89	1.4	3.3	0.115	0.096	1.36	6.74E-04	6.49E-04	5.71E-05	2.81	1.97	0.137	22123
70	coarse	27.04	con	0.004	1.22	0.01	1	2.8	0.115	0.114	1.47	2.81E-03	2.72E-03	4.89E-04	2.81	1.97	0.137	22123
52	coarse	27.44	cyl	0.004	1.22	0.46	1.1	2.8	0.121	0.094	1.24	8.00E-04	7.72E-04	9.53E-05	2.77	1.96	0.1415	38275
52	coarse	27.44	con	0.004	1.22	-0.03	1	2.9	0.121	0.126	1.51	2.93E-03	2.83E-03	4.90E-04	2.77	1.96	0.1415	38275
65	coarse	26.18	con	0.004	1.22	0.04	1	2.8	0.109	0.114	1.50	2.52E-03	2.44E-03	4.42E-04	2.82	2.00	0.1317	63926
61	coarse	24.63	cyl	0.004	1.22	0.99	1.4	3.4	0.098	0.060	1.39	6.384E-04	6.15E-04	6.27E-05	2.78	2.03	0.1211	66045
61	coarse	24.63	con	0.004	1.22	0.12	1	2.6	0.098	0.099	1.47	3.59E-04	3.46E-04	3.17E-05	2.78	2.03	0.1211	66045
54	coarse	28.35	con	0.004	1.22	0.01	1	2.6	0.120	0.104	1.37	7.58E-04	7.31E-04	7.68E-05	2.86	1.96	0.1482	42313
186	coarse	26.34	cyl	0.004	1.22	1.42	1.4	4.4	0.109	0.103	1.25	1.81E-03	1.75E-03	2.35E-04	2.75	1.99	0.1321	40704
186	coarse	26.34	con	0.004	1.22	0.14	1	3.2	0.109	0.129	1.62	4.06E-03	3.93E-03	6.29E-04	2.75	1.99	0.1321	40704
35	coarse	33.07	cyl	0.004	1.22	0.6	1.2	3.3	0.164	0.137	1.25	3.32E-03	3.21E-03	4.09E-04	2.84	1.83	0.1809	42012
35	coarse	33.07	con	0.004	1.22	-0.26	1	2.9	0.164	0.152	1.35	7.72E-03	7.47E-03	1.43E-03	2.84	1.83	0.1809	42012
59	coarse	23.02	cyl	0.004	1.22	1.05	1.2	3.3	0.091	0.076	1.29	3.39E-04	3.27E-04	2.33E-05	2.83	2.09	0.1105	28126
66	coarse	23.83	cyl	0.004	1.22	1.15	1.2	3.4	0.091	0.070	1.25	3.94E-04	3.80E-04	3.01E-05	2.79	2.08	0.1161	49452
67	coarse	23.35	cyl	0.004	1.22	1.15	1.2	3.4	0.091	0.070	1.26	3.80E-04	3.66E-04	2.91E-05	2.76	2.05	0.1164	27906
100 drop	coarse	28.70	cyl	0.004	1.22	0.11	1	3.2	0.214	0.201	1.28	9.15E-03	9.15E-03	1.56E-03	2.72	1.87	0.1534	52399
250 drop	coarse	28.02	cyl	0.004	1.22	0.71	1.1	3.4	0.129	0.133	1.26	2.77E-03	2.76E-03	3.74E-04	2.80	1.97	0.142	93244
150 drop	coarse	26.77	cyl	0.004	1.22	0.89	1.2	3.4	0.116	0.102	1.29	1.22E-03	1.21E-03	1.25E-04	2.76	2.00	0.1341	87460
200 drop	coarse	24.31	cyl	0.004	1.22	0.73	1	3.3	0.141	0.115	1.23	1.56E-03	1.56E-03	1.72E-04	2.72	2.02	0.1204	51130
300 drop	coarse	22.14	cyl	0.004	1.22	0.59	1	3.2	0.132	0.112	1.31	1.45E-03	9.79E-04	9.57E-05	2.72	2.07	0.1064	74433
400 drop	coarse	21.69	cyl	0.004	1.22	1.01	1.1	3.4	0.095	0.086	1.29	5.86E-04	5.86E-04	5.60E-05	2.81	2.14	0.1034	191515
450 drop	coarse	19.26	cyl	0.004	1.22	1.10	1.1	3.5	0.081	0.078	1.32	3.07E-04	3.20E-04	2.46E-05	2.74	2.18	0.0886	42918
ss hc og 100	coarse	31.52	cyl	0.004	1.22	0.53	1.1	3.4	0.167	0.177	1.25	7.11E-01	6.88E-03	1.13E-03	2.62	1.76	0.177	110104
ss hc og 200	coarse	28.75	cyl	0.004	1.22	1.26	1.3	4.4	0.137	0.130	1.24	3.98E-03	3.85E-03	6.33E-04	2.75	1.91	0.1443	57695
ss hc og 300	coarse	24.52	cyl	0.004	1.22	0.94	1.1	3.3	0.107	0.087	1.24	6.29E-04	6.07E-04	2.05E-05	2.76	2.06	0.1195	161914
ss hc og 400	coarse	22.12	cyl	0.004	1.22	0.81	1.1	3.2	0.095	0.083	1.32	3.63E-04	3.49E-04	2.48E-05	2.73	2.09	0.104	99694
ss hc og 450	coarse	23.14	cyl	0.004	1.22	1.61	1.5	4.3	0.085	0.065	1.23	8.43E-04	8.14E-04	8.93E-05	2.75	2.10	0.1046	35118

Table A 1 Overview of pigment tablets used as porous structures, for definition see next page.

**Table A2 Definition of parameters listed in Table A1**

Pigment type	coarse = Hydrocarb OG, 60 % w/w < 2 $\mu$ m fine = Setacarb OG (otherwise known as Hydrocarb 95), 95 % w/w < 2 $\mu$ m
$\phi$	Porosity, % volume/volume as measured by Hg-intrusion
Throat type	cylindrical or conical
$d_{min}$	minimum throat diameter
$d_{max}$	maximum throat diameter
Throat skew	percentage number of throats of minimum throat diameter
Pore skew	factor which the pore size distribution is multiplied by
$\psi$	Connectivity, average number of throats per pore
$d_{50exp}$	diameter at 50% of the experimental intruded volume
$d_{50sim}$	diameter at 50% of the simulated intruded volume
$Q$	Pore row spacing, distance from the centre of one pore to the centre of an adjacent pore
$K$	Permeability, Darcian flow conductivity calculated for nitrogen, methane and a liquid..
Skeletal density	Density of the solid phase of the sample as measured by Hg-intrusion
Bulk density	Density of the sample
Intruded volume	Total intruded volume after Pore-Comp correction
Bulk modulus	The reciprocal of the compressibility of a sample

A 2 Definition of parameters listed in Table A 1



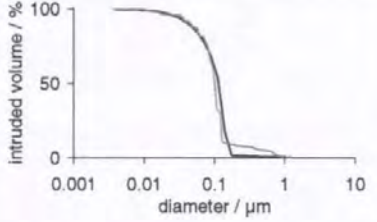
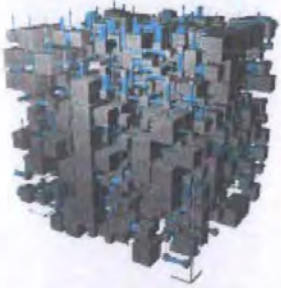
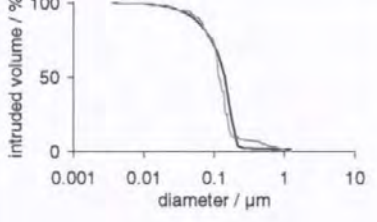
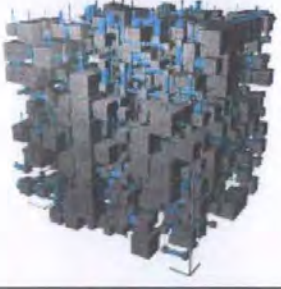
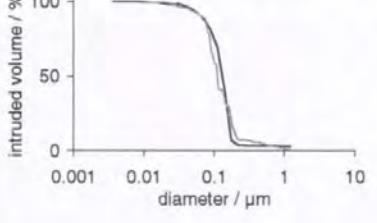

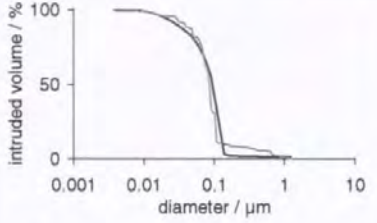

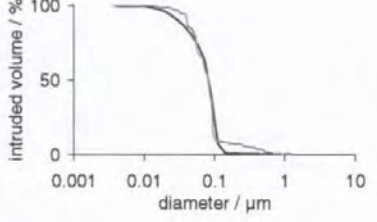
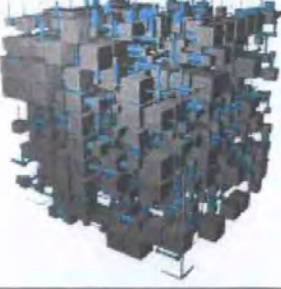
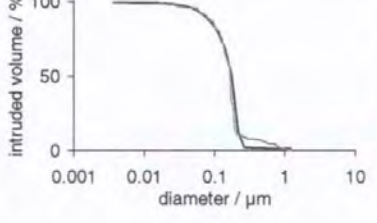

**Table A3 Overview Hg-intrusion curves and Pore-Cor unit cells of all structures used**

Number or label as used in the text	Hg - Intrusion curves, black line = experimental, grey line = simulated	Unit cell Depending on the relevant context the structures are either shown with cylindrical or conical throats (blue)
69		
28		
31		
47		
57		
177 (cyl)		

177 (con)		
74		
70 (cyl)		
70 (con)		
52 (cyl)		
52 (con)		
65		

61 (cyl)		
61 (con)		
54		
186 (cyl)		
186 (con)		
35 (cyl)		

35 (con)		
59		
66		
67		
100 drop 28.7		
250 drop 28.02		

150 drop 26.77		
200 drop 24.31		
300 drop 22.14		
400 drop 21.69		
450 drop 19.26		
Ss hc og 100		

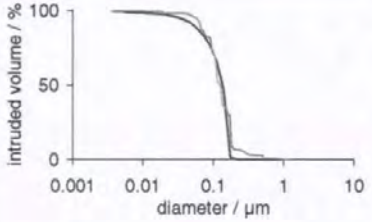

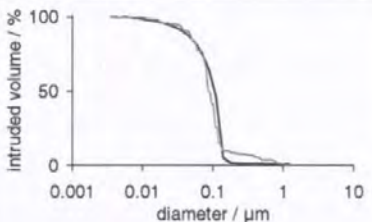

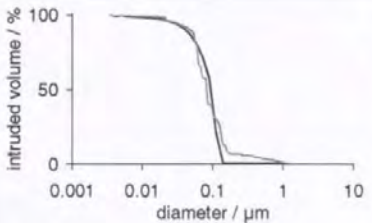

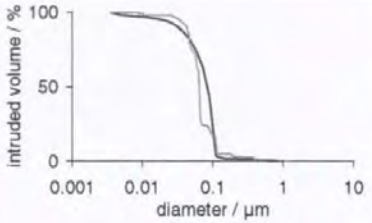
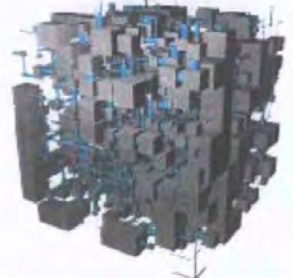
Ss hc og 200		
Ss hc og 300		
Ss hc og 400		
Ss hc og 450		

Table A 3 Overview used pigment tablets, intrusion curves and simulated unit cell

**Table A4 Overview liquid properties**

	Viscosity	Surface tension	Density	boiling point	Comments
	/ Pa s x10 <sup>-3</sup>	/ Nm <sup>-1</sup> x10 <sup>-3</sup>	/ gm <sup>-3</sup> x10 <sup>6</sup>	/ °C	
PKWF 4/7 af neu	2.5	n.a.	0.800	240 - 270	mixtures of aliphatic alkanes
<b>PKWF 6/9 af neu</b>	<b>4.3</b>	<b>27.4</b>	<b>0.805</b>	<b>160 - 290</b>	
PKWF 28/31 af neu	5.8	n.a.	0.808	280 - 300	
Linseed oil	33.1	35	0.921-0.933	decomposition when strongly heated	
Water	1.056	72.75	0.998	100	
<b>1-Octanol</b>	<b>10.64</b>	<b>27.53</b>	<b>0.824</b>	<b>194</b>	
<b>Ethandiol</b>	<b>20.0</b>	<b>48.4</b>	<b>1.113</b>	<b>&gt;300</b>	hygroscopic
<b>1,3-Propandiol</b>	<b>57.1</b>	<b>45.8</b>	<b>1.053</b>	<b>215</b>	
<b>1,3-Butanediol</b>	<b>135.0</b>	<b>36.6</b>	<b>1.004</b>	<b>205</b>	
<b>1,2,4-Butanetriol</b>	<b>1185.0</b>	<b>55.9</b>	<b>1.185</b>	<b>167</b>	
Squalane (*)	38.8	2929	0.81	350	
Nonane	0.59	22.85	0.718	150	
Methyleniodide	3.78	50.76	3.32	n.a	
Hexadecane	3.34	n.a.	0.7733	287	
n-Undecane	1.17	n.a.	0.7402	195	for comparison only

Table A-4 Overview liquid properties

**Table A5 Pigments used to improve paper properties**

Pigments	Crystal chemical formula	Symmetry	Particle shape	Brightness R457 %	Refractive index	Hardness (Mohs)	Density gcm <sup>-3</sup>
<i>Aluminium silicate</i> Clay Clay calcined	Al <sub>2</sub> O <sub>3</sub> 2 SiO <sub>2</sub> 2H <sub>2</sub> O Al <sub>2</sub> Si <sub>2</sub> O <sub>7</sub>	Triclinic Amorphous	Hexagonal platelets	80-90 90-92	1.57 1.60	1-2 2-3	2.6 2.4-2.5
<i>Calcium carbonat</i> Chalk, limestone, marble precipitated	CaCO <sub>3</sub> CaCO <sub>3</sub>	Trigonal Rhombic Orthorhombic	Spherical structures Prisms, needles	80-97 90-98	1.48/1.66 1.53/1.68	3-4 3-4	2.6-2.8 2.6-2.9
<i>Magnesium silicate</i> Talc	3MgO 4SiO <sub>2</sub> H <sub>2</sub> O	Monoclinic	Platelets, flakes	70-94	1.58	1	2.7-2.8
<i>Calcium sulfoaluminat</i> Satin white	Ca <sub>6</sub> Al <sub>2</sub> [(OH) <sub>4</sub> SO <sub>4</sub> ] <sub>3</sub> 24 H <sub>2</sub> O	Hexagonal	Needle shaped agglomerates	90-97	1.47	2-3	1.5-1.8
<i>Aluminium hydroxide</i>	Al(OH) <sub>3</sub>	Monoclinic	Hexagonal platelets	96-98	1.57/1.59	2-3	2.4
<i>Calcium sulphate</i> Gypsum	CaSO <sub>4</sub> 2 H <sub>2</sub> O	Monoclinic	Prisms, plates, needles	89-92	1.52/1.53	2	2.3-2.4
<i>Titanium dioxide</i> Anatas Rutil	TiO <sub>2</sub> TiO <sub>2</sub>	Tetragonal Tetragonal	Pyramids, spheres Rounded prisms	92-99 92-99	2.49/2.56 2.61/2.90	5-6 6	3.8-3.9 4.2-4.3
Plastic pigments	Polystyrene and others		spheres	>96	1.59	-	1.0-1.1

*Table A 5 Pigments used to improve paper properties*



## Appendix B : Fitting equations

### Appendix B1

Equation for extrapolating Pore-Cor model:

$$x = \frac{(a + c \ln t)}{(1 + b \ln t + d(\ln t)^2)}$$

where  $a = 2.68 \times 10^{-6}$ ,  $b = -0.07$ ,  $c = 1.42 \times 10^{-7}$ , and  $d = 2.23 \times 10^{-3}$

where  $x$  is the Darcy length in metres and  $t$  is the time in seconds.

Equation for scaling model data to experimental data

$$\Gamma = a + bt + cx \ln t + dt^{2.5} + et^{\frac{1}{2}},$$

where  $a = 0.99$ ,  $b = -0.18$ ,  $c = 0.01$ ,  $d = 3.40 \times 10^{-10}$ , and  $e = 11.80$ .

B 1 Extrapolation equation for simulation to infinite time

### Appendix B2

Smoothing equations for the apparent weight change with time during the absorption of different fluids, where  $m$  is the apparent weight (g),  $t$  the time (s), and  $r^2$  is the standard measure of goodness of fit. Equation types are the simplest in each case with  $r^2 > 0.997$ .

#### Ethanediol

$$m = (a + ct^{0.5} + et + gt^{1.5}) / (1 + bt^{0.5} + dt + ft^{1.5})$$

$a = 4.3561153$ ,  $b = -0.009256348$ ,  $c = -0.043688281$ ,  $d = 1.7126548e-5$ ,  $e = 0.000110932669$ ,  $f = 8.6388785e-8$ ,  
 $g = 2.5185248e-7$ ,  $r^2 = 0.9997$

#### 1,3-Propandiol

$$m = (a + ct^{0.5} + et) / (1 + bt^{0.5} + dt + ft^{1.5})$$

$a = 2.0413123$ ,  $b = -0.008960098$ ,  $c = -0.020493998$ ,  $d = 2.2832422e-5$ ,  $e = 6.6193272e-5$ ,  $f = 2.7494107e-8$ ,  
 $r^2 = 0.9994$

#### 1,3-Butanediol

$$m^2 = a + bt^{0.5}$$

$a = 54.483527$ ,  $b = -0.018292355$ ,  $r^2 = 0.9992$

#### 1,2,4-Butanetriol

$$m^{-1} = a + bt^{0.5}$$

$a = 0.49226177$ ,  $b = 0.00016415427$ ,  $R^2 = 0.9988$

#### 1-Octanol

$$m = (a + ct^{0.5} + et) / (1 + bt^{0.5} + dt + ft^{1.5})$$

$a = 23.01395$ ,  $b = -0.0095973436$ ,  $c = -0.22418864$ ,  $d = 0.00012091329$ ,  $e = 0.0027948089$ ,  
 $f = 5.3889712e-9$ ,  $r^2 = 0.9978$

B 2 Smoothing equations for short time mass correction

### Appendix B3

Equations for absorptive oil removal from offset ink

Eq. 108 is reduced to the form  $\Rightarrow y = a + \left( \frac{b(c-dx)}{1-(c-dx)} \right)$ , and the fit to the absorption curve provides values of,  $a = 11.435$ ,  $b = 11.456$ ,  $c = -533.113$ ,  $d = 2.162$ ,  $r^2 = 0.986$ ,  $FitStdErr = 0.000417$

Eq. 85 is reduced to the form  $\Rightarrow y = a + b\sqrt{x}$ , and the fit to the absorption curve provides values of,

$$a = 0.0005327, b = -0.0005528, r^2 = 0.966, FitStdErr = 0.000637$$

B 3 Equations for absorptive oil removal from offset ink

## Appendix C : Compilation of footnotes

1. Pore-Cor is a software package developed by the Environmental and Fluid Modelling Group of the University of Plymouth, Devon PL4 8AA, U.K.
2. ISIT is a product name of SeGan Ltd., Perrose, Lostwithiel, Cornwall PL22 0JJ, U.K.
- ™ PTFE (polytetrafluorethylene)
3. Encyclopaedia Britannica.
4. Royalex is a trademark from Uniroyal ([www.uniroyal.com](http://www.uniroyal.com)) and is made of a hard foam core "sandwiched between layers of polyvinylchloride and acrylbutadienstyrene and has an excellent ratio of weight to mechanical properties like e.g. stiffness and impact strength
5. Synteape is a registered trade mark of Arjo Wiggins Limited, Gateway House, Basing View, Basingstoke, Hampshire, RG21 4EE United Kingdom.
6. Pore-Comp is a software developed by the Environmental and Fluid Modelling Group of the University of Plymouth, Devon PL4 8AA, U.K.
7. Lasertec ILM21 is a product name of Lasertec Corporation, Unit 4, Wendell Court, 16/20 Wendell Road, London W12 9RT, UK.
8. Krüss GmbH, Borsteler Chaussee 85-99a, D 22453 Hamburg, Germany
9. Fluka products are available world-wide through Sigma-Aldrich. (see [www. sigma-aldrich.com](http://www.sigma-aldrich.com))
10. see [www.philips.com](http://www.philips.com) for local distributors
11. Phoenix-meccano Phoenix Electronics Distribution Ltd., Castlehill Industrial Estate, Carlisle ML8 5UF. [www.phoenix1.co.uk](http://www.phoenix1.co.uk)
12. GrabBit is a trademark of Soft Imaging System GmbH, Hammer Str. 89, 48153 Münster, Germany
13. Image Access is a product of Imagic Bildverarbeitung AG, CH-8152 Glattbrugg, Switzerland
14. Micromeritics, One Micromeritics Drive, Norcross, GA 30093-1877, U.S.A., [www.micromeritics.com](http://www.micromeritics.com)
15. StressTech® is a product name of ReoLogica Instruments AB, Lund, Sweden
16. IGT Reptest B.V,P.O.Box 4672, 1009AR Amsterdam, The Netherlands, [www.igt.nl](http://www.igt.nl)
17. Measurements made on a Sedigraph 5100 from Micromeritics Instrument Corporation, one Micromeritics Drive, Norcross, GA 30093-1877, U.S.A.
18. The pressing of pigments into tablets showed also, beyond the topic of this work, potential for AFM (atomic force microscope) sample preparation and for the evaluation of pigment hydrophobising quality.
19. Cymax AG, Studbachstrasse 12, CH-8340 Hinwil, [www.cymax.ch](http://www.cymax.ch)
  
20. Jean Wirtz is a subsidiary company of of Buehler Ltd., 41 Waukegan Road, Lake Bluff, IL 60044, USA
21. See [www.umax.com](http://www.umax.com) for local distributors
22. See [www.kontron.com](http://www.kontron.com) for local distributors.
23. Messer Griesheim GmbH, Fütingsweg 34, 47805 Krefeld, Germany, worldwide see [www.messergroup.com](http://www.messergroup.com)
24. Eurolec Instrumentation Ltd., Cluan Enda, Dundalk, Co. Louth, Ireland
25. Epothin is a product name of Buehler Ltd., 41 Waukegan Road, Lake Bluff, IL 60044, USA
26. Prüfmaschinen AG, Giessenstr. 15 CH-8953 Dietikon, Switzerland
27. Software available from the authors.
28. Skinnex is a product name of K+E Inks, Stuttgart, Germany.
29. TableCurve is a product name of SPSS Inc.
30. Ikonofix is a product name of Zanders Feinpapiere AG, D51439 Bergisch Gladbach, Deutschland
31. Edmund Industrial Optics, 101 East Gloucester Pike, Barrington, NJ 08007-1380 USA
32. Coherent Auburn Group, Lindbergh Street, Auburn, CA 95602-9295 USA
  
33. Redlake MASD Inc. San Diego, CA 92121-1097 [www.redlake.com](http://www.redlake.com)
34. Mikromak GmbH, am Wolfsmantel 18, D-91058 Erlangen, Germany, [www.mikromak.com](http://www.mikromak.com)
35. Ikonofix is a product name of Zanders Feinpapiere AG, D51439 Bergisch Gladbach, Deutschland
36. Edmund Industrial Optics, 101 East Gloucester Pike, Barrington, NJ 08007-1380 USA
37. Coherent Auburn Group, Lindbergh Street, Auburn, CA 95602-9295 USA

## Appendix D : Miscellaneous

### Manufacturers and part numbers for the laser based strain sensor

#### **Edmund Industrial Optics<sup>36</sup>.**

precision 6.5" screw travel movement L03-601  
bench plate, L03-638

#### **Coherent<sup>37</sup>.**

mounting rod, 61-1236,  
carrier, 61-1509,  
angle bracket, 61-1376,  
beam steering unit, 22-8882,  
laser diode, circular beam with a diameter of 1.2 mm, a wavelength of 635 nm and a power of 4 mW

The software (for MS Windows™) used for the balance data sampling was developed by Dr. D.C. Spielmann of Omya AG and may be requested at [daniel.spielmann@omya.com](mailto:daniel.spielmann@omya.com).

---

<sup>36</sup> Edmund Industrial Optics, 101 East Gloucester Pike, Barrington, NJ 08007-1380 USA

<sup>37</sup> Coherent Auburn Group, Lindbergh Street, Auburn, CA 95602-9295 USA

## References

- Gurley Paper Testing Instruments, 2001, Bulletin 1400, Teledyne Gurley.
- L&W Bendtsen Messgerät Bedienungsanleitung, 2001, 2. Ausgabe. AB Lorentzen & Wettre, Kista, Sweden.
- Abrams, L., Favorite Charles W., Capano, P. J. and Johnson, R. W., *Tappi Coating Conference*, Tappi Press, Atlanta, 1996a, 185.
- Adamson, A. W., *Physical Chemistry of Surfaces*, A. Wiley Interscience Publication, New York, 1990.
- Apel, M. and Marmur, A., *Colloids and Surfaces*, 1999.
- Arnold, H., Eisenschmid, K. and Kleemann, St. G., *Wochenblatt für Papierfabrikation*, 1995, **21**, 945.
- Auslander, J., Cordery, R. and Zeller, C., *Pan-Pacific and International Printing and Graphic Arts Conference, October 6-8, 1998. Québec Canada*, Pulp and Paper Technical Association of Canada, 1998, 175.
- Baldwin, C. A., Sederman, A. J., Mantle, M. D., Alexander, P. and Gladden, L. F., *Journal of Colloid and Interface Science*, 1996, **181**, 79.
- Barthlott, W., *Clarendon Press*, 1990, 69.
- Barthlott, W., *Nachrichten aus der Chemie*, 2000, **48**+
- Batten, G. L., *Journal of Colloid and Interface Science*, 1984, **102**, 513.
- Bell, J. M. and Cameron, F. K., *Journal Of Physical Chemistry*, 1906, **10**, 658.
- Bernadiner, M. G., *Transport in Porous Media*, 1998, **30**, 251.
- Beuleke, E. and Burri, P., *Wochenblatt für Papierfabrikation*, 1999, **127**, 1482.
- Bodurtha, P. A., Matthews, G. P., Kettle, J. P., Lohmander, S. and James, P. W., *2001 Advanced Coating Fundamentals Symposium Proceedings*, Tappi, San Diego, California USA, 2001.
- Bodurtha, P. A., Matthews, G. P., Kettle, J. P. Roy I., *Colloids and Surfaces*, Accepted, July 2002.
- Borhan, A. and Rungta, K. K., *Journal of Colloid and Interface Science*, 1993, **155**, 438.
- Bosanquet, C. H., *Philosophical Magazine, Series 6*, 1923, **45**, 525.
- Briscoe, B. J. and Rough, S. L., *Colloids and Surfaces A-Physicochemical And Engineering Aspects*, 1998, **137**, 103.
- Brittin, W. E., *Journal of Applied Physics*, 1946, **17**, 37.
- Chebbi, R. and Selim, M. S., *Journal of Colloid and Interface Science*, 1997, 66.
- Chiarello, R. P., Wogelius, R. A. and Sturchio, N. C., *Geochimica et Cosmochimica Acta*, 1993, **57**, 4103.
- Chibowski, E. and Gonzalez-Caballero, F., *American Chemical Society Langmuir*, 1993, **9**, 330.

- Chibowski, E. and Holysz, L., *American Chemical Society Langmuir*, 1992, **8**, 710.
- Chibowski, E. and Holysz, L., *Journal of Adhesion Science and Technology*, 1997, 1289.
- Chibowski, E. and Gonzáles, F., *Langmuir*, 1993, **9**, 330
- Danino, D. and Marmur, A., *Journal of Colloid and Interface Science*, 1994, **166**, 245.
- Darcy, H., *Les Fontaines publiques de la Ville de Dijon*, Libraire des corps imperiaux des ports et chaussees et des mines, Paris, 1856. Appendice D
- Davis, H. T., *Statistical mechanics of phases, interfaces and thin films*, VHC Publishers Inc. New York, 1996.
- del Rio, O. I., Kwok, D. Y., Wu, R., Alvarez, J. M. and Neumann, A. W., *Colloids and Surfaces A: Physicochemical and Engineering Aspects*, 1998, **143**, 197.
- Dempewolf, E., *Polygraph, Treffpunkt Druckindustrie*, 1994, **15/16**.
- Desjumaux, D., Bousfield, D. W., Glatter, T. P., Donigian, D. W., Ishley, J. N. and Wise, K. J., *Journal of Pulp and Paper Science*, 1998, **24**, 150.
- Dixit, A. B., Buckley, J. S., McDougall, S. R. and Sorbie, K. S., *Transport in Porous Media*, 2000, **40**, 27.
- Dong, M. and Chatzis, I., *Journal of Colloid and Interface Science*, 1995, **172**, 278.
- Donigian, D. W., Wise, K. J. and Ishley, J. N., *Tappi Coating Conference*, Tappi Press, Atlanta., 1996, 39.
- Dubé, M., Rost, M. and Alava, M., *The European Physical Journal B*, 2000, **15**, 691.
- Dullien, F. A. L., *Porous Media: Fluid Transport and Pore Structure*, Academic Press, Inc. New York, 1992.
- Einset, E. O., *Journal of American Ceramic Society*, 1996, **79**, 333.
- Einstein, A., *Annalen der Physik*, 1902, **4**, 513.
- Ellis, M. K. and Fripiat, J., *Tappi Proceedings: International Printing & Graphic Arts Conference*, 1996, 149.
- Fadeev, A. Y. and Eroshenko, V. A., *Journal of Colloid and Interface Science*, 1997, **187**, 275.
- Finley, C., *Printing Paper and Ink*, Delmar Publishers, New York, 288, 1997.
- Fisher, L. R. and Lark, P. D., *Journal of Colloid and Interface Science*, 1979, **69**, 486.
- Furo, I. and Daicic, J., *Nordic Pulp and Paper Research Journal. Paper presented at XXIII EUCEPA Conference*, 1999, **14**, 221.
- Gabriel, G., PhD Thesis, Technische Universität Graz, 1999.
- Gane, P. A. C., *Paper Technology, PITA*, 1989, 34.
- Gane, P. A. C., *Tappi Advanced Coating Fundamentals Symposium, Philadelphia*, Tappi Press, Atlanta, 1997, 73.
- Gane, P. A. C., *Wochenblatt für Papierfabrikation*, 2001, 110.

- Gane, P. A. C., Buri, M. and Blum, R., *International Symposium on Paper Coating Coverage*, Training Center of Finnish Forest Industries, 1999.
- Gane, P. A. C. and Coggon, L., *Tappi Journal*, 1987, **70**, 87.
- Gane, P. A. C., Kettle, J. P., Matthews, G. P. and Ridgway, C. J., *Industrial and Engineering Chemistry Research*, 1996, **35**, 1753.
- Gane, P. A. C. and Ridgway, C. J., *27th IARIGAI Research Conference, Advances in Paper and Board Performance*, Graz, Austria. , 2000.
- Gane, P. A. C. and Ridgway, C. J., *Advances in Printing Science and Technology Volume 27*, Pira International, Leatherhead, Surrey, **59**, 2001.
- Gane, P. A. C., Schoelkopf, J., Spielmann, D. C., Matthews, G. P. and Ridgway, C. J., *Tappi Journal*, 2000, **83**, 77.
- Gane, P. A. C. and Seyler, E. N., *PTS Coating Symposium, Munich*, 1993.
- Gane, P. A. C. and Seyler, E. N., *Tappi Coating Conference Proceedings*, 1994.
- Gane, P. A. C., Seyler, E. N. and Swan, A., *International Printing and Graphic Arts Conference, Halifax, Nova Scotia*, Tappi Press, Atlanta, 1994, 209.
- Gane, P. A. C., Watters, P. and McGenity, P. M., *PTS Coating Symposium, Munich*, 1991.
- Gao, C., Dai, P., Homola, A. and Weiss, J., *Journal of Tribology*, 1998, **120**, 358.
- Gate, L. F. and Windle, W., *The Adsorption of Oil in Porous Coatings*, Ernest Benn Ltd., London, UK, 1973.
- Gerdes, S., PhD Thesis, Institute for Surface Chemistry and Lund University, 1998.
- German, R. M., *Particle packing characteristics*, Metal Powder Industries Federation, Princeton, 1989.
- Goel, A., Tzanakakis, M., Huang, S., Ramaswamy, S., Choi, D. and Ramarao, B. V., *Tappi Journal*, 2001, **84**, 1.
- Goldschmidt A., Hantschke B., Knappe E. and Vock G-F., *Glasurit Handbuch, Lacke und Farben*, Curt R. Vincentz Verlag, Hannover, 1984.
- Good, R. J., *Chemistry and Industry*, 1971, 05, 600.
- Good, R. J. and van Oss, C. J., *Modern Approach to Wettability*, Plenum Press, New York. 1992, 1.
- Grattoni, C. A., Chiotis, E. D. and Dawe, R. A., *J. Chem. Tech. Biotechnol.*, 1995, **64**, 17.
- Grundke, K., Boerner, M. and Jacobasch, H.-J., *Colloids And Surfaces*, 1991, **58**, 47.
- Grundke, K., Bogumil, T., Gietzelt, T., Jacobasch, H.-J., Kwok, D. Y. and Neumann, A. W., *Prog. Colloid Polym. Sci.*, 1996, **101**, 58.
- Hadjiiski, A., Dimova, R., Denkov, N. D., Ivanov, I. B. and Borwankar, R., *Langmuir*, 1996, **26**, 6665.
- Hanke, K., *Deutscher Drucker*, 1996, **12/28**, 30.

- Havlinova, B., Cicak, V., Brezova, V. and Hornakova, L., *Journal Of Materials Science*, 1999, **34**, 2081.
- Heerjtes, P. M. and Witvoet, W. C., *Powder Technology*, 1970, **3**, 339.
- Heinemann, S., *Das Papier*, 1996, 233.
- Hilfer, R., *Advances in Chemical Physics, Volume XCII*, 1996, 301.
- Holysz, L. and Chibowski, E., *Journal of Colloid and Interface Science*, 1994, **164**, 245.
- Horvath, V. K. and Stanley, H. E., *Physical review*, 1995, **52**, 5166.
- Hsieh, Y.-L., *Textile Research Journal*, 1994, **64**, 57.
- Hsieh, Y.-L. and Yu, B., *Textile Research Journal*, 1992, **62**, 677.
- Huang, Y., Ringrose, P. S. and Sorbie, K. S., *SPE Reservoir Engineering*, 1995, 287.
- Ichikawa, N. and Satoda, Y., *Journal of Colloid and Interface Science*, 1994, 350.
- ISO, *International Standards Organisation*, 1994, 1.
- Janczuk, B., Bialopiotrowicz, T. and Chibowski, E., *Materials, Chemistry and Physics*, 1986, **16**, 489.
- Johnson, R. W., Abrams, L., Maynard, R. B. and Amick, T. J., *Tappi Journal*, 1999, **82**, 239.
- Johnson, R. W., Abrams, L., Maynard, R. B. and Amick, T. J., *TAPPI Coating Conference*, Tappi Press, Atlanta, 1998.
- Karathanasis, M., Carne, T., Dahlvik, P., Haugwitz, B. and Ström, G., *Wochenblatt für Papierfabrikation*, 2001, 426.
- Keiter, S., Master Thesis, Universität Dortmund, 1998.
- Keller, A. A., Blunt, M. J. and Roberts, P. V., *Transport in Porous Media*, 1997, **26**, 277.
- Keller, D. S. and Luner, P., *Colloids and Surfaces*, 2000, **161**, 401.
- Kent, H. J. and Lyne, M. B., *Fundamentals of Paper Making*, Mechanical Engineering Publications Limited, London, 1989.
- Kettle, J. P. and Matthews, G. P., *Advanced Coating Fundamentals Symposium*, Tappi Press, Atlanta, 1993, 121.
- Kettle, J. P., Matthews, G. P., Ridgway, C. J. and Wagberg, L., *The Fundamentals of Papermaking Materials: Transaction of the 11th Fundamental Research Symposium, Cambridge, Sep 1997*, Pira International, Surrey, 1997, 1355.
- Kissa, E., *Textile Research Journal*, 1996, **66**, 660.
- Kittel, H., *Lehrbuch der Lacke und Beschichtungen*, Verlag W.A. Colomb, Berlin, 1999.
- Klemm, K.-W., *Wochenblatt für Papierfabrikation*, 1999, 397.
- Klemm, K. W., *PRINT*, 1994.



- Knackstedt, M., *Wetting and Flow in Porous Media - Fundamental Concepts and Industrial Perspectives*, September 10-12, 1998, Uto, Sweden, Institute for Surface Chemistry, 1998.
- Knackstedt, M. A., Senden, T. J. and Lyne, M. B., *Nordic Pulp and Paper Research Journal*, **15**, 554
- Koehler, H. J., PhD Thesis, Eig.technische Hochschule in Zürich, 1970.
- Kwok, D. Y., Lam, C. N. C., Li, A., Leung, A., Wu, R., Mok, E. and Neumann, A. W., *Colloids and Surfaces A: Physicochemical and Engineering Aspects*, 1998, **142**, 219.
- Lanet, V. and Gandini, A., *Journal of Prepress and Printing Technology*, 1989, **3**.
- Larrondo, L. and St-Amour, S., *Tappi Coating Conference*, Tappi Press, Atlanta., 1992, 37.
- Larrondo, L. and St-Amour, S., *Tappi Coating Conference*, Tappi Press, Atlanta., 1995, 79.
- Laudone, G. M., Matthews, G. P. and Gane P. A. C., *Third International Symposium on Contact angle Wettability and Adhesion*, 2002, in press.
- Lee, L.-H., *Journal of Adhesion Science Technology*, 1993, **7**, 583.
- Lee, L.-H., *Journal of Colloid and Interface Science*, 1999, **64**.
- LeGrand, E. J. and Rense, W. A., *Journal of Applied Physics*, 1945, **16**, 843.
- Lepoutre, P., *Paper Technology and Industry*, 1978, **298**.
- Lepoutre, P., *Trends In Polymer Science*, 1995, **3**, 112.
- Leskinen, A. M., *Tappi Journal*, 1987, **70**, 101.
- Letelier, M. F. and Leutheusser, H. J., *Journal of Colloid and Interface Science*, 1979, **72**, 465.
- Levine S, Lowndes J, Watson, E. J. and Neale, G., *Journal of Colloid and Interface Science*, 1980, **73**, 136.
- Levine, S., Reed, P. and Shutts, G., *Powder Technology*, 1977, **163**.
- Levine, S., Reed, P., Watson, E. J. and Neale, G., *A Theory of the Rate of Rise of a Liquid in a Capillary*, Academic Press, New York, 1976, 403.
- Li, Z., Giese, R. F., van Oss, C. J., Kerch, H. M. and Burdette, H. E., *Journal of American Ceramic Society*, 1994, **77**, 2220.
- Ligenza, J. R. and Bernstein, R. B., *Journal of the American Chemical Society*, 1951, **73**, 4636.
- Lohmander, S., Martinez, M., Lason, L. and Rigdahl, M., *Advanced Coating Fundamentals*, Tappi Press, Atlanta, 1999, 43.
- Lu, T. X., Biggar, J. W. and Nielsen, D. R., *Water Resources Research*, 1994, **30**, 3275.
- Lu, T. X., Nielsen, D. R. and Biggar, J. W., *Water Resources Research*, 1995, **31**, 11.
- Lucas, R., *Kolloid Z.*, 1918, **23**, 15.
- Lucassen, J., Lucassen-Reynders, E. H., Prins, A. and Sams, P. J., *Langmuir*, 1992, **3093**.

- Ma, S. X., Mason, G. and Morrow, N. R., *Colloids and Surfaces*, 1996, 273.
- Macosko, C. W., *Rheology: Principles, measurements and applications*, VCH Publishers, New York, 425, 1994.
- Maisch, E., Renzow, D., Sell, P.-J. and Walitza, E., *Zeitschrift für Flugwissenschaften und Weltraumforschung*, 1981, 5, 189.
- Maisch, E., Sell, P.-J. and Siekmann, E., *Ingenieur-Archiv*, 1986, 56, 281.
- Maloney, T. and Paulapuro, H., *The Science of papermaking*, Pulp and Paper Fundamental Research Society, Bury, 2001, 897.
- Marmur, A., *Journal of Colloid and Interface Science*, 1988, 122, 209.
- Marmur, A., *Advances in Colloid and Interface Science*, 1992, 13.
- Marmur, A. and Cohen, R. D., *Journal of Colloid and Interface Science*, 1997, 189, 299.
- Martic, G., Gentner, F., Seveno, D., Coulon, D. and DeConinck, J., *6th International Symposium on Evaluation of Reservoir Wettability and Its Effect on Oil Recovery*, Socorro, Mexico, 2000.
- Mason, G. and Morrow, N. R., *Journal of Colloid and Interface Science*, 1994, 168, 130.
- Mathews, G. P., *Nordic Pulp and Paper Research Journal*, 2000, 15, 476.
- Mathews, G. P., Moss, A. K., Spearing, M. C. and Volland, F., *Powder Technology*, 1993, 76, 95.
- Mathews, G. P., Ridgway, C. J. and Spearing, M. C., *Journal of Colloid and Interface Science*, 1995, 171, 8.
- Miller, B. and Tyomkin, I., *Journal of Adhesion Science Technology*, 1992, 6, 1371.
- Miller, B. and Tyomkin, I., *Textile Research Journal*, 1994b, 64, 55.
- Miller, B. and Tyomkin, I., *Journal of Colloid and Interface Science*, 1994a, 162, 163.
- Miller, R., Bree, M. and Fainerman, F. B., *Colloids and Surfaces A: Physicochemical and Engineering Aspects*, 1998, 142, 237.
- Minayoshi, Shiro, Saito, Naofumi, Hanazaki, Minoru, Nishioka, Hidehiko, Kuroda, Sakae, Takahashi, Masako, Shimizu, Seiya, and Maida, Norimasa. *Monodisperse vaterite type CaCO<sub>3</sub>, its manufacturing method and method of controlling growth of particles and shape thereof*. Maruo Calcium Company Limited, Japan. Patent 706,423(5,275,651). 4-1-1994. United States of America, Japan. 28-5-1991.
- Moir, W. W., *JOCCA-Surface Coatings International*, 1994, 77, 221.
- Moshinskii, A. I., *Colloid Journal*, 1997, 59, 62.
- Mumley, T. E., Radke, C. J. and Williams, M. C., *Journal of Colloid and Interface Science*, 1986, 109, 398.
- Nederveen, C. J., *Tappi Journal*, 1994, 77, 174.
- Nielsen, D. R., van Genuchten, M. Th. and Biggar, J. W., *Water Resources Research*, 1986, 22, 895.

- Niskanen, K. J., Rasi, M., Aaltosalmi, U., Timonen, J. and Jataja, M., *Tappi International Paper Physics Conference*, 1999, 297.
- Pan, S. X., Davis, H. T. and Scriven, L. E., *Tappi Journal*, 1995, **78** (8), 127.
- Papirer, E., Schultz, J. and Turchi, C., *Eur. Polym. J.*, 1984, **20**, 1155.
- Peat, D. M. W., Matthews, G. P., Worsfold, P. J. and Jarvis, S. C., *European Journal of Soil Science*, 2000, **51**, 65.
- Peek, R. L. and McLean, D. A., *Analytical Edition Industrial and Engineering Chemistry*, 1934, **6**, 85.
- Pennanen, M., *A contribution to the understanding of coating layers*, Abo Akademi, Department of Paper Chemistry, 1996.
- Petzold, A. and Hinz, W., *Silikatchemie - Einführung in die Grundlagen*, Ferdinand Enke Verlag Stuttgart, 1979.
- Pezron, I., Bourgain, G. and Quere, D., *Journal of Colloid and Interface Science*, 1995, **173**, 319.
- Philip, J. R., *J. Chem. Phys.*, 1977, **66**, 5069.
- Pickett, G., *Jour. App. Phys.*, 1944, **15**, 623.
- Picollet, M., Piette, P., Morin, V. and Le Nest, J. F., *Tappi Coating Conference*, Tappi Press, Atlanta, 1998, 383.
- Quere, D., *Europhysics Letters*, 1997, **39**, 533.
- Ransohoff, T. C. and Radke, C. J., *Journal of Colloid and Interface Science*, 1988, **121**, 392.
- Rideal, E. K., *Phil. Mag. Series 6*, 1922, **44**, 1152.
- Ridgway, C. J., PhD Thesis, University of Plymouth, 1995.
- Ridgway, C. J. and Gane, P. A. C., *Colloids and Surfaces A: Physicochemical and Engineering Aspects*, 2002, **206**, 217.
- Ridgway, C. J., Ridgway, K. and Matthews, G. P., *Journal of Pharmacy and Pharmacology*, 1997, **49**, 377.
- Ridgway, C. J., Schoelkopf, J., Matthews, G. P., Gane, P. A. C. and James, P. W., *Journal of Colloid and Interface Science*, 2001, **239**, 417.
- Robin, M., *Oil & Gas Science and Technology*, 2001, **56**, 55.
- Rousu, S. M., Gane, P. A. C. and Eklund, D. E. *The Science of Papermaking*, Pulp and Paper Fundamental Research Society, Bury, 897, 2001b, 1115.
- Rousu, S. M., Gane, P. A. C., Spielmann, D. C. and Eklund, D., *Nordic Pulp and Paper Research Journal*, 2001a, **15**, 527.
- Rousu, S. M., Gane, P. A. C., Spielmann, D. C. and Eklund, D. E., *International Printing and Graphic Arts Conference, Savannah, Georgia*, Tappi Press, Atlanta, 2000, 55.

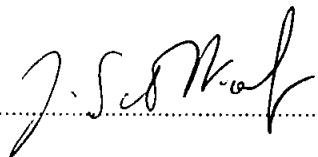
- Rousu, S. M., Grankvist, T. and Eklund, D., *2001 Advanced Coating Fundamentals Symposium Proceedings*, Tappi, San Diego, California USA, 2001c.
- Salminen, P., PhD Thesis, Laboratory of Paper Chemistry, Department of Chemical Engineering Abo Akademi, 1988.
- Sangl, R. and Weigl, J., *Forschungsbericht Inkjet*, Papiertechnische Stiftung, 1997, PTS-FB 23/97
- Schoelkopf, J., Gane, P. A. C., Ridgway, C. J., Spielmann, D. C. and Matthews, G. P., *Tappi 2001 Advanced Coating Fundamentals Symposium Proceedings, San Diego*, Tappi, Atlanta, 2001, 1.
- Schoelkopf, J., Ridgway, C. J., Gane, P. A. C., Matthews, G. P. and Spielmann, D. C., *Journal of Colloid and Interface Science*, 2000, **227**, 119.
- Seebergh, J. E. and Berg, J. C., *Chemical Engineering Science*, 1992, **47**, 4455.
- Seguin, D., Montillet, A. and Comiti, J., *Chemical Engineering Science*, 1998b, **53**, 3751.
- Seguin, D., Montillet, A., Comiti, J. and Huet, F., *Chemical Engineering Science*, 1998a, **53**, 3897.
- Sell, P.-J., Maisch, E. and Siekmann, J., *Acta Astronautica*, 1984, **11**, 577.
- Sell, P.-J., Maisch, E. and Siekmann, J., *Acta Astronautica*, 1986, **13**, 87.
- Senden, T. J., Knackstedt, M. A. and Lyne, M. B., *Nordic Pulp and Paper Research Journal*, 2000, **15**, 554.
- Sharma, R. and Ross, D. S., *J. Chem. Soc. Faraday Trans.*, 1991, **87**, 619.
- Shiryayeva, N. I., Gerasimov, V. K. and Vyatkin, G. P., *Colloid Journal*, 1995, **57**, 725.
- Siegrist, J., *K+E Druckfarben PRINT*, 1994, 1.
- Sorbie, K. S., Wu, Y. Z. and McDougall, S. R., *Journal of Colloid and Interface Science*, 1995, **174**, 289.
- Spielmann, D. C., 2002, Personal Communication.
- Stipp, S. L. S., Gutmannsbauer, W. and Lehmann, T., *American Mineralogist*, 1996, **81**, 1.
- Szekely, J., Neumann, A. W. and Chuang, Y. K., *Journal of Colloid and Interface Science*, 1971, **35**, 273.
- Tang, L.-H. and Tang, Y., *Journal De Physique II*, 1994, **4**, 881.
- Taylor, S. C., Hall, Ch., Hoff, W. D. and Wilson, M. A., *Journal of Colloid and Interface Science*, 2000, 351.
- Theiler, M., *Print*, 1994, 20.
- Toivakka, M., Eklund, D. and Bousfield, D. W., *Tappi Coating Conference*, Tappi Press, Atlanta, 1992, 403.
- Toivakka, M. and Nyfors, K., *Tappi Coating Conference-Washington DC, 2000*, Tappi Press, Atlanta, 197.
- Toivakka, M. and Nyfors, K., *Tappi Journal*, 2001, **84**, 1.
- Troeger, J., Lunkwitz, K., Grundke, K. and Buerger, W., *Colloids and Surfaces A: Physicochemical and Engineering Aspects*, 1998, **134**, 299.
- Tuller, M., Or, D. and Dudley, L. M., *Water Resources Research*, 1999, **35**, 1949.

- Unertl, W. N., *Langmuir*, 1998, 2201.
- van Brakel, J., *Powder Technology*, 1975, 11, 205.
- van der Zanden, A. J. J. and Chesters, A. K., *Int. J. Multiphase Flow*, 1994, 20, 775.
- van Gilder, R. L. and Purfeerst, R. D., *Tappi Journal*, 1994, 77, 230.
- van Oss, C. J., Giese, R. F., Li, Z., Murphy, K., Norris, J., Chaudhury, M. K. and Good, R. J., *Journal of Adhesion Science and Technology*, 1992, 413.
- van Oss, C. J., Good, R. J. and Chaudhury, M. K., *Journal of Colloid and Interface Science*, 1986, 111, 378.
- van Oss, C. J., Good, R. J. and Chaudhury, M. K., *Langmuir*, 1988, 884.
- van Oss, C. J., Ju, L., Chaudhury, M. K. and Good, R. J., *Journal of Colloid and Interface Science*, 1989, 128, 313.
- Washburn, E. W., *Physical Review*, 1921, 17, 273.
- Weislogel, M. M., *AIChE Journal*, 1997, 43, 645.
- Weislogel, M. M. and Lichter, S., *Journal of Fluid Mechanics*, 1998, 373, 349.
- Wilhelmy, L., *Ann. Physik*, 1863, 119, 177.
- Xiang, Y. and Bousfield, D. W., *PanPacific and International Printing and Graphic Arts Conference*, CPPA, 1998, 93.
- Xiang, Y., Bousfield, D. W., Desjumeaux, D. and Forbes, M. F., *PanPacific and International Printing and Graphic Arts Conference*, CPPA, 1998.
- Yang, Y.-W. and Zografis, G., *Journal of Pharmaceutical Sciences*, 1986b, 75, 719.
- Yang, Y.-W., Zografis, G. and Miller, E. E., *Journal of Colloid and Interface Science*, 1988, 122, 35.
- Yang, Y.-W. and Zografis, G., *Journal of Pharmaceutical Sciences*, 1986a, 75, 719.
- Yoldas, B. E., *J. Mater. Res.*, 1999, 14, 2594.
- Yost, F. G., Rye, R. R. and Mann, J. A., *Acta mater*, 1997, 45, 5337.
- Zang, Y. H. and Aspler, J. S., *Journal of Pulp and Paper Science*, 1998, 24, 141.
- Zhang, B. and Nakajima, A., *Journal of Colloid and Interface Science*, 1999, 211, 114.

## Copyright Statement

This copy of the thesis has been supplied on condition that anyone who consults it is understood to recognise that its copyright rests with its author and that no quotation from the thesis and no information derived from it may be published without the author's prior written consent.

Signed.....

A handwritten signature in black ink, appearing to read 'J. Schoelkopf', written over a horizontal dotted line.

Joachim Schoelkopf